Analytical and Spectro-Spatial Analyses of Nonlinear Metamaterials for Vibration Control, Energy Harvesting, and Acoustic Non-reciprocity.

Mohammad A. Bukhari

Dissertation submitted to the Faculty of the

Virginia Polytechnic Institute and State University

in partial fulfillment of the requirements for the degree of

Doctor of Philosophy

in

Mechanical Engineering

Oumar R. Barry, Chair

Lei Zuo

Ling Li

Robert Parker

Masoud Agah

May 26, 2021

Blacksburg, Virginia

Keywords: Nonlinear Metamaterials, Spectro-Spatial Analyses, Self-Tuning Mechanisms, Energy Harvesting

Analytical and Spectro-Spatial Analyses of Nonlinear Metamaterials for Vibration Control, Energy Harvesting, and Acoustic Nonreciprocity.

Mohammad A. Bukhari

(ABSTRACT)

This dissertation investigates the nonlinear wave propagation phenomena in nonlinear metamaterials with nonlinear chains and nonlinear resonators using analytical and spectro-spatial analyses. In the first part of the thesis, the nonlinear metamaterials are modeled as a chain of masses with multiple local resonators attached to each cell. The nonlinearity stems from the chain's stiffness in one case and the local resonator's stiffness in another. Analytical approximates solutions are obtained for each case using perturbation techniques. These results are validated through numerical simulations and the results show good agreement. To further demonstrate the nonlinear wave propagation characteristics, spectro-spatial analyses are conducted on the numerical integration data sets. The wave profiles, short-term Fourier transform spectrograms, and contour plots of 2D Fourier transform show the presence of solitary waves for both sources of nonlinearity. In addition, spectro-spatial features demonstrate the presence of significant frequency shifts at different wavelength limits.

The second part of the thesis studies a nonlinear electromechanical metamaterial and examines how the electromechanical coupling in the local resonator affects the wave propagation. Numerical examples indicate that the system can be used for simultaneous energy harvesting and vibration attenuation without any degradation in the size of bandgaps. Spectro-spatial analyses conducted on the electromechanical metamaterial also reveal the

presence of solitons and frequency shifts. The presence of solitary wave in the electrome-chanical metamaterial suggests a significant improvement in energy harvesting and sensing techniques. The obtained significant frequency shift is employed to design an electrome-chanical diode, allowing voltage to be sensed and harvested only in one direction. Design guidelines and the role of different key parameters are presented to help designers to select the type of nonlinearity and the system parameters to improve the performance of acoustic diodes.

The last part of this thesis studies the passive self-tuning of a metastructure via a beam-sliding mass concept. The governing equations of motions of the holding structure, resonator, and sliding mass are presented and discretized into a system of ODEs using Galerkin's projection. Given that the spatial parameters of the system continuously change over time (i.e., mode shapes and frequencies), instantaneous exact mode shapes and frequen-cies are determined for all possible slider positions. The numerical integration is conducted by continuously updating the spatial state of the system. The obtained exact mode shapes demonstrate that the resonance frequency of the resonator stretches over a wide frequency band. This observation indicates that the resonator can attenuates vibrations at a wide frequency range. Experiments are also conducted to demonstrate the passive self-tunability of the metastructure and the findings colloborate the analytical results.

Analytical and Spectro-Spatial Analyses of Nonlinear Metamaterials for Vibration Control, Energy Harvesting, and Acoustic Nonreciprocity.

Mohammad A. Bukhari

(GENERAL AUDIENCE ABSTRACT)

Metamaterials are artificially engineered structures that can offer incredible dynamical properties, which cannot be found in conventional homogeneous structures. Consequently, the global metamaterials market is expected to display a 23.6% compound annual growth rate through 2027. Some of these exciting properties include, but not limited to, negative stiffness, negative mass, negative Poisson's ratio. The unique dynamic properties show the importance of metamaterials in many engineering applications, such as vibration reduction, noise control, and waveguiding and localization. However, beyond the linear characteristics of metamaterials, nonlinear metamaterials can exhibit more interesting nonlinear wave propagation phenomena, such as solitons, cloaking, tunable bandgaps, and wave non-reciprocity.

This research work investigates wave propagation characteristics in nonlinear locally resonant metamaterials using analytical, numerical, and signal processing techniques. The nonlinearity stems from the chain in one case and from the local resonator in another. Numerical examples show the presence of solitary waves in both types of nonlinearity and significant frequency shift in certain frequency/wavenumber regions. The obtained significant frequency shift can be utilized to design mechanical diodes, where its operation range can be increased by introducing nonlinearity in the resonator.

For simultaneous energy harvesting and vibration attenuation, integrating the local resonator with piezoelectric energy harvesters is also investigated in this research work with the

presence of both types of nonlinearities. For weak electromechanical coupling, the results demonstrate that the band structure of the system is not affected by the electromechanical coupling. Therefore, the system can also be used for energy harvesting without any degradation in the vibration attenuation performance. This observation is also validated experimentally for the linear limit. Spectro-spatial analyses also reveal the presence of solitary output voltage waves, which can enhance the energy harvesting and sensing. The obtained significant frequency shift can be utilized to design an electromechanical diode where the wave can propagate and be harvested only in one direction. Numerical examples show that the performance of the electromechanical diode can be significantly improved by including nonlinearities in the local resonator.

Another goal of this research work is the introduction of passive self-tuning mechanism to design self-tuning metastructure. The design of such a metastructure is motivated by the need for broadband devices that can adapt to changing environment. The passive self-tuning concept is achieved by a sliding mass coupled with a resonator. Analytical and experimental results show the ability of this system to tune itself to the excitation frequency, and hence, can control vibrations over a significantly wider frequency band as compared to conventional resonators.

Dedication

To my parents, siblings, and teachers.

Acknowledgments

First of all, I would like to thank GOD for the blessings and gifts he has bestowed upon me. After all, it is because of his love and guidance that I made it so far in my life. Indeed, his first message to Prophet Mohammad was my motivation to learn and work hard in getting higher-education.

I am deeply grateful to my Advisor, Professor Barry, for his guidance, support, encouragement, and insights throughout my work. Professor Barry has not only been a great academic advisor; but, he helped me to enhance my communication skills significantly. I still remember the first few months working with him in the United States. It was really difficult for me to communicate with anyone in English; however, Professor Barry was always supportive, understanding, and encouraging. His communication and dealing with me gave me great confidence and made English language not a barrier anymore. In addition, he provided me endless flexibility during my studies, which made me love my research work more than anything else and helped me in being productive. Professor Barry knows when to be an advisor, a friend, and even an elder brother. It helped me to enjoy my time here in the United States although I am around 7000 miles away from my family.

I would also like to offer my sincere thanks to the members of my Ph.D. committee, Professor Zuo, Professor Parker, Professor Li, and Professor Agah. Special thanks goes to Professor Zuo, who helped me in learning experimental skills and collaborated with me on several projects. He was always easy to reach and very kind whenever I needed any help.

My endless gratitude goes to my parents (Abdulbaqi Mohammad Bukhari, and Naeimah Qawasmi) and my siblings (Ahmed, Asmaa, Fouad, Maha, Maisoon, Muna, and Zeinab) for their unconditional love and support throughout my studies. Their encouragement convinced

Contents

List of Figures

List of Tables

Chapter 1

Introduction

1.1 Overview

Due to their incredible unique dynamical properties, researchers have recently drawn their attention to the study of mechanical metamaterials. Earlier considerations of metamaterials were performed within the electromagnetic and optical wave propagation communities [33, 187]. These concepts were later extended for elastic wave propagation [84] and acoustics [120]. Instead of homogeneous structures, metamaterials are fabricated in special engineered configurations, patterns, and constitutions. These engineered structures can offer negative stiffness, negative mass, negative Poisson's ratio, and many others [14, 48, 84, 111, 116]. Consequently, metamaterials show a great potential for being used in a wide pool of engineering applications. Examples on these applications include vibration isolation or reduction [15, 51, 53, 71, 82, 83, 146, 150], noise control and sound absorption [72, 122, 152, 156], non-destructive testing [155], waveguiding and localization [87, 92, 93, 161, 162, 177], micro scale signal sensing [54, 127, 128], wave demultiplexers−passive devices [19, 81, 126, 142, 170], liquid properties sensing [113, 114, 183], mass sensing [132], sound collimation [39, 43, 56, 158], negative refraction [59, 77, 88, 103, 149, 169, 188, 193], positive refraction [36, 66, 176], wave focusing [8, 17, 20, 42, 65, 102, 164, 168, 196], directional-biased wave propagation [16, 104, 106, 107, 143], cloaking [21, 38, 46, 47, 124, 136, 137, 138, 139, 141, 147], and many others. This doctoral dissertation focuses on investigating nonlinear wave propagation phe-

nomena in nonlinear metamaterials and how we can implement these observation in many engineering applications. In addition, it proposes a novel self-tuning locally resonant metamaterials using sliding mass mechanism for broad band vibration attenuation. Section 1.2 describes phononic, locally resonant, nonlinear metamaterials, and electromechanical metamaterials for vibration reduction and energy harvesting. Section 1.3 states the scientific and engineering motivations for utilizing sliding mass mechanism in novel self-tuning metamaterials. Section 1.4 summarize the research objectives and contributions. Finally, the dissertation layout is provided in Section 1.5.

1.2   Linear, nonlinear, locally resonant, and electromechanical metamaterials

Within elastic media, earlier investigations for metamaterials were conducted on periodic structures (phononic crystals) [97, 98, 99, 159, 160, 178]. Periodicity in phononic crystals can be represented by material, geometry, and boundary conditions periodicity. Periodic structures offer a frequency bandgap, where the wave is attenuated instead of propagating through the structure. Due to Bragg scattering, this bandgap occurs at wavelengths close to the cell lattice constant. Therefore, low frequency waves can be banned from propagating through the structure, thus achieving significant vibration attenuation. However, since the Bragg scattering is restricted to certain lattice constants, only large structures can be controlled. On the other hand, by introducing local resonators into metamaterials (resulting in locally resonant metamaterials), wave propagation can be controlled in systems with much smaller lattice constants [110]. This results from the hybridization of the local resonances even in the absence of periodicity [4]. Therefore, applications of vibration attenuation can be extended to much smaller structures and engineering applications (e.g., MEMS, sensors, and

energy harvesters). Based on the local resonator parameters, the presence of local resonators in periodic patterns can develop bandgaps due to Bragg scattering or mode hybridization [109].

The evolved bandgaps can be enhanced by inserting multiple resonators inside the cell to obtain multiple bandgaps at different frequencies [78, 197] or using nonlinear metamaterials to obtain tunable bandgap limits [117]. The latter revealed many other interesting nonlinear wave propagation phenomena such as gap solitons [95], wave non-reciprocity [16, 104, 106, 107, 115, 129], dark and enveloped solitons [131], and cloak [50, 58, 147]. Previous study of nonlinear metamaterials was focused on obtaining the band structure analytically or numerically. The former uses perturbation techniques [134, 135] (e.g., Lindstedt–Poincare [133], multipe scales [119]) and homotopy analysis [1]. On the other hand, analytical or approximate analytical solutions may not yield accurate results or deduce the interesting the interesting nonlinear wave characteristics. Therefore, numerical analyses should be conducted. These analyses can further be analyzed by different signal processing techniques to obtain the spectro-spatial features of the propagating waves in addition to the temporal space analyses [63, 195]. These analytical and numerical studies of nonlinear metamaterials were limited to diatomic chains or locally resonant metamaterials with single resonator. However, there is a gap in the literature for obtaining an analytical solution and investigating the spectro-spatial features of nonlinear metamaterials with multiple local resonators. Moreover, the study of spectro-spatial features in [63, 195] showed long-wavelength waves are not affected by the nonlinearity in the chain, while the effect of local resonator in the nonlinearity in this region has not been explored yet.

Take away 1: Perturbation techniques can be used to obtain an approximate analytical solutions for deispersion curves in the case of weakly nonlinear metamaterials. However, applying these techniques in the literature is limited to the simple case of metamaterials in

the absence of local resonator or the presence of single resonator. In addition, the effect of local resonator nonlinearity on nonlinear propagation phenomena need to investigated to explore its cabability to extend the effect to the long-wavelength limit.

Increasing the mass added by the local resonators increases the bandgap size in locally resonant metamaterials. Consequently, this limits the application of locally resonant metamaterial in weight restricted systems (e.g., vibration reduction in aerospace applications). However, attaching piezoelectric patches on periodic structures can manipulate the added stiffness to the system. This leads to developing an electromechanical bandgap [5, 13, 34, 173, 194]. The electromechanical bandgap is realized due to the electromechanical coupling The piezoelectric can also be used for energy harvesting and sensing. This is inspired by the flat frequency band in metamaterials and can be realized by shunting the piezoelectric material to a load resistor [74, 75, 76, 105, 157]. Beside the obtained interesting dynamical properties, electromechanical metamaterials can be employed to enhance energy harvesting and sensing[74]. This is motivated by a metamaterial's flat frequency band, which has been observed experimentally in locally resonant plates [157] and 3D printed structures [105]. Further theoretical demonstrations were reported in the literature for discrete [74] and continuous structures [75, 76]. In addition, 2D metamaterials have shown the ability to concentrate energy at the energy harvester location, thus significantly improving the energy harvesting [108, 174, 175, 184]. The benefits of electromechanical metamaterials (i.e., vibration reduction and energy harvesting) were realized and investigated in the literature without considering the nonlinearity. Although, both nonlinear metamaterials and nonlinear energy harvesters have shown significant enhancements on the wave propagation and energy harvesting, respectively.

Take away 2: Elechtromechanical metamaterials can be used for simultaneous energy harvesting. However, for prior studies in the literature, the interesting nonlinear wave prop-

agation characteristics were not employed to enhance the electromechanical metamaterials performance.

The nonlinearity in metamaterials can lead to a significant wave distortion. This wave distortion results in frequency conversion, enabling output wave to appear at frequencies different from the input wave frequency. Indeed, when the nonlinear metamaterial is coupled to a linear metamaterial (i.e., the linear metamaterial has a bandgap tuned to the frequency conversion region in the nonlinear metamaterial), the energy content with shifted frequency can propagate in the forward configuration. However, waves propagating from the linear metamaterial side (backward configuration) will be tuned inside the linear metamaterial's bandgap. This is an indication that directional-biased wave propagation can be realized [16, 104, 106, 107, 115]. This wave non-reciprocity can also be observed in nonlinear granular structures [16] or nonlinear hierarchical internal structures [129]. Spectro-spatial analyses can be employed to examine the frequency conversion in nonlinear metamaterials. The spectro-spatial features can show a significant frequency shift at the medium-wavelength limit in both nonlinear chain and nonlinear local resonators metamaterials [26, 27, 195]. Unlike the case of nonlinear chain, nonlinear local resonator metamaterials can also show significant frequency shift at the long-wavelength limit in addition to the medium-wavelength limit [27], [23]. Models of acoustic diodes are limited to the use of local mechanical resonators embedded within the periodic structure or simple coupling between linear and nonlinear metamaterials. To the best of our knowledge, there are no works in the literature investigating the use of electromechanical resonators in nonlinear metamaterials for designing electromechanical diodes. In addition, works in the literature did not harness the significant frequency shift at long wavelength limit for the case of nonlinear resonator to broaden the operation frequency of the electromechanical diode. Consequently, the asymmetric and transmission ratios are not relatively high for diodes reported in the literature.

Take away 3: Investigating the spectro-spatial features of nonlinear metamaterials with nonlinear resonators demonstrated a significant frequency shift at the long-wavelength limit. Therefore, it is worthy to investigate employing this shift to broaden the operation range of the mechanical diode. In addition, extending these observing phenomena to design an electromechanical diode cannot be found in the literature.

1.3   Self-tuning metamaterials using sliding mass mechanisims

In the prior section, the aforementioned examples have shown a great potential for vibration isolation and energy harvesting with passive metamaterials systems. Yet further significant enhancements in vibration mitigation can be obtained by active and adaptive (programmable) metamaterials [84]. For instance, active control for tunable bandgaps can be obtained by manipulating cell orientations [64]. Moreover, metamaterials can be actively controlled by piezoelectric materials [5, 13, 34, 73, 100, 153, 173, 194], colloidal crystals [11], electrorheological materials subjected to an electric field [189], temperature dependent materials (e.g., shape memory alloy) [154], thermal tuning [79, 86], and magnetism [144, 151, 180, 181]. Due to the required external energy source, active metamaterials are not practical in most applications. However, researchers have suggested adaptive tuning techniques to control the structure bandgap independent of any external power sources. These include bistable structures [61, 68, 121, 185], piezoelectric patches shunted to negative-capacitance [12, 41, 44], resistive-inductive [5, 34, 40], or negative-inductance [41]. However, these techniques can only tune the bandgap in limited regions near the linear frequency, with improvement appearing as a significant increase in the attenuation constant depending on the excitation amplitude in the structures. In addition, piezoelectric based metamaterials face limitations

in tunability of bandgap that are confined by narrow size and positions [41].

Take away 4: Adaptive metamaterials are capable of changing the size and locations of their bandgap without external power source; however, for the mechanisms studied in prior literature, this capability is limited by bandgap positions, size, and practicality.

Tuned resonators have shown great potential for both vibration mitigation [163] and energy harvesting applications [55, 148]. Moreover, they can provide a wide frequency bandgap if embedded within metamaterials [110]. When tuned properly, their performance can be maximized. Unfortunately, environmental excitation frequencies are time varying and therefore not likely to meet the narrow frequency band of the resonators, thus making the resonators ineffective [10, 35, 37, 130, 145, 148, 165, 166, 167, 171, 198]. Consequently, the seeking of mechanisms that can widen the operational frequency band has been a focus of researchers for many years. For instance, researchers have investigated nonlinear resonators as an alternative solution, due to their wide bandwidth compared to linear resonators and the presence of secondary resonances [45, 49, 69, 112, 135, 179]. Still, nonlinear resonators succeeded in enhancing frequency matching only in specific regions. More effective frequency matching can be obtained using active tuning. However, active tuning is usually less practical and reliable due to its dependence on external power sources. Indeed, this often makes employing active resonators in energy harvesting applications infeasible [7]. On the other hand, a sliding mass moving along a beam can continuously vary the resonator frequency based on the excitation frequency, thus improving its performance [37, 94, 96, 123, 130, 145, 166, 167, 190, 191]. The nonlinear dynamics interactions between the sliding mass and the beam (i.e., Coriolis and centrifugal forces) drive the slider to settle on a vibration anti-node, and thus causing the resonator to be in-resonance with the excitation frequency. Therefore, such resonators can self-tune, resulting in dramatic performance enhancement. Self-tuning resonators have been investigated

for systems ranging from strings [18] to beams [123, 125, 172] and plates [182]. Moreover, experimental demonstrations of this significant performance enhancement were reported in [37, 123, 125, 130, 145, 190, 191]. Beam-based self-tuning resonator has been examined in the literature for various resonator boundary conditions. These variations include clamped-clamped resonator [94, 123, 145, 190, 191], clamped-free resonator [37, 91, 125, 130], and even more complicated arrays of resonators [165, 166, 167].

Take away 5: Self-tuning resonators have demonstrated better frequency tuning than other passive systems at wide frequency range. Therefore, embedding these resonators may offer enhanced tunable bandgap as compared to other mechanisms. However, no study has examined the concept of self-tuning via a sliding mass in locally resonant metamaterials.

1.4   Research objectives and contributions

In this dissertation, we will study different nonlinear metamaterials models to reveal interesting nonlinear wave propagation phenomena and obtain wide band vibration attenuation. The specific research objectives are to:

- Gain better understanding of nonlinear wave propagation phenomena of nonlinear metamaterials with different sources and types of nonlinearities through analyzing the spectro-spatial features.

- Derive general approximate analytical solutions for nonlinear locally resonant metamaterials with any number of embedded local resonators.

- Gain fundamental understanding of the nonlinear dynamic interactions within such an electromechanical metamaterial.

- Provide design guidelines for a broadband electromechanical diode with high asymmetry ratio.

- Test a self-tuning single resonator using sliding mass mechanism for better energy harvesting and vibration attenuation.

- Develop an adaptive feedback technique for self-tuning system for better prediction to the evolved dynamic.

- Integrate the self-tuning resonator within locally resonant metamaterials to obtain a system that tunes its bandgap to the applied excitation frequency.

In addition, this dissertation makes many significant contributions to the literature. These contributions include novel methods to analyze nonlinear metamaterials, design broadband electromechanical diode, and obtain novel self-tuning metamaterials. Specifically, the contributions of this dissertation can be summarized as follows:

- Prior derivations of approximate analytical dispersion dispersion relations in the literature were limited to diatomic chains and single resonator locally resonant metamaterials. Therefore, this dissertation uses the method of multiple scales to obtain a generalized approximate analytical expressions for the dispersion relations of nonlinear metamaterials with any number of local resonators.

- Significant wave distortion in nonlinear metamaterials were only reported for the medium/short wavelength limits since only the case of nonlinear chain was investigated in the literature. This dissertation shows that significant wave distortion can also be realized in the long-wavelength limit for nonlinear metamaterials with nonlinear resonators. This is tackled by analyzeing the spectro-spatial features of the propagating waves through the structure.

- The study of electromechanical metamaterials in the literature were limited to linear electromechanical metamaterials. However, nonlinear metamaterials and nonlinear energy harvesting have shown interesting wave propagation phenomena and significant improvement in widening the harvester bandwidth, respectively. Therefore, this dissertation study nonlinear electromechanical metamaterials to harness the benefits of nonlinear wave propagation phenomena to enhance simultaneously energy harvesting and vibration reduction.

- Adaptive metamaterials are capable of changing the size and locations of their bandgap without external power source; however, for the mechanisms studied in prior literature, this capability is limited by bandgap positions, size, and practicality. In addition, self-tuning resonators have demonstrated better frequency tuning than other passive systems at wide frequency range. Therefore, this dissertation proposes novel self-tuning metamaterials by embedding these resonators in locally resonant metamaterials to obtain enhanced tunable bandgap as compared to other mechanisms.

1.5   Dissertation layout

After the introduction chapter, which describes the background, problem statement, dissertation objectives, and dissertation contributions, we present in Chapter 2 the analyses for nonlinear metamaterials with multiple local resonators. The computational study for validation of this system is detailed in Chapter 3. Next, Chapters 4 and 5 illustrates the effect of electromechanical coupling in metamaterilas with chain and resonator nonlinearity, respectively. Experimental validation of the effect of electromechanical coupling on the band structure is presented in Chapter 6. Chapter 7 investigates the design of an electromechanical diode for biased energy harvesting and wave propagation. Next, a self-tuning resonator

is investigated for vibration reduction applications in Chapter 8. Finally, the main findings and future insights are summarised in the conclusion.

Chapter 2

Spectro-Spatial Analyses of a Nonlinear Metamaterial with Multiple Nonlinear Local Resonators

This chapter is an edited version of: Bukhari, Mohammad, and Oumar Barry. "Spectro-spatial analyses of a nonlinear metamaterial with multiple nonlinear local resonators." *Nonlinear Dynamics* 99, no. 2 (2020): 1539-1560 [27].

Recent focus has been given to spectro-spatial analysis of nonlinear metamaterials since they can predict interesting nonlinear phenomena not accessible by spectral analysis (i.e., dispersion relations). However, current studies are limited to a nonlinear chain with single linear resonator or linear chain with nonlinear resonator. There is no work that examines the combination of nonlinear chain with nonlinear resonators. This chapter investigates the spectro-spatial properties of wave propagation through a nonlinear metamaterials consisting of nonlinear chain with multiple nonlinear local resonators. Different combinations of softening and hardening nonlinearites are examined to reveal their impact on the traveling wave features and the band structure. The method of multiple scales is used to obtain closed form expressions for the dispersion relations. Our analytical solution is validated via numerical simulation and results from the literature. The numerical simulation is based on

12

spectro-spatial analysis using signal processing techniques such as spatial-spectrogram, wave filtering, and contour plots of 2D Fourier Transform. The spectro-spatial analysis provides a detailed information about wave distortion due to nonlinearity and classify the distortion into different features. The observations suggest that nonlinear chain with multiple nonlinear resonators can affect the waveform at all wavelength limits. Such nonlinear metamaterials are suitable for broadband vibration control and energy harvesting, as well as other applications such as acoustic switches, diodes, and rectifiers, allowing wave propagation only in a pre-defined direction.

2.1   Introduction

The study of metamaterials has gained lots of attention in recent years due to their exceptional material properties characteristics and their wider engineering applications. Metamaterials are a new class of artificial composites that derive their unique dynamic properties from both engineered local configurations and material constituents [84]. They were originally developed for electromagnetic and optical wave propagation and later the technology was extended to acoustic and elastic waves[33]. Metamaterials can be constructed as periodic structures (i.e., phononic crystals in the presence or absence of local resonator) or in random arrangements (usually in the presence of local resonator). However, locally resonant metamaterials draw their interesting dynamic phenomena because of the presence of local resonators rather than periodicity [4]. These interesting dynamic features can be judiciously employed for suppressing noise and vibration, harvesting energy, non-destructive testing structures for defects, improving image resolution, and ameliorating the performance of antennas and many other engineering structures and devices [14].

The study of periodic structures reveals the development of a frequency bandgap where the wave does not propagate through the structure instead it get reflected [97, 98, 99, 159, 160, 178]. These frequencies are associated with wavelength near the size of lattice constant. The wave attenuation is caused by Bragg scattering and offers a good vibration control in low frequency region. However, the restriction on the lattice size limits the advantage of Bragg scattering to large structures applications.

Due to the crucial need for extending this phenomena to control much smaller size structures (e.g., MEMS), Liu et al. [110] suggested embedding smaller resonators inside crystals

to form locally resonant metamaterials. Locally resonant metamaterials form a bandgap at wave lengths much larger than the lattice constant. Indeed, the bandgap formation results from the combination of Bragg scattering and local resonance when the frequency of the local resonator is not very low. Nevertheless, the parameters of the resonator govern the dominant effect of the bandgap formation [109]. Yet, very low frequency local resonators can still be excited by long wavelength waves and hence bandgap can be formed due to hybridization of the local resonances only and without the need for Bragg scattering [4]. Controlling different frequency regions requires using different resonators inside the lattice [78, 197], such that wave attenuation can be observed in the vicinity of different local resonances. Intentionally introducing nonlinearity can reveal additional interesting wave propagation phenomena which widens the applications of metamaterials. Some of those, but not limited to, are gap solitons [95], envelope and dark solitons [131], asymmetric wave propagation [107], and adjusting band structure limits [117].

Based on the magnitude of nonlinearity, the metamaterial can be classified as a strongly or weakly nonlinear. The latter may be asymptotically converging and an explicit approximate solution can be presented by perturbation techniques [134, 135]. For instance, dispersion relation of nonlinear chain (metamaterial) can be obtained by Lindstedt-Poincare method [133]. However, for more complicated or interacting nonlinear systems, the method of multiple scales is more convenient since the associated algebra requires much less effort [101, 119]. Yet dispersion curves in nonlinear continuous metamaterials can be approximated by using the transfer matrix method [90]. Studying nonlinear dispersion curves can reveal important information about the effect of nonlinearity on the wave propagation (e.g. dispersive and solitary waves) [85].

Recent trends in nonlinear metamaterials focus on wave non-reciprocity such that uni-direction wave propagation can be utilized to passively develop acoustic diodes, switches, and rectifiers. For example, acoustics diodes can be obtained by coupling nonlinear and linear chains [104, 106, 107]. This requires tuning the secondary resonances of nonlinear chain to the passband of a linear chain. For instance, exciting weakly nonlinear oscillator with cubic nonlinearity can develop a signal with subharmonic resonance. If this secondary resonance lies in the passband of coupled wave while the the original excitation frequency lies in the bandgap, waves can only propagate in the direction from nonlinear to linear chain [115]. Similarly, bifurcation due to defects in granular chains can allow the wave to propagate only in one direction [16]. Nonlinear energy sink can also form wave non-reciprocity in hierarchical internal structures [129].

Nonlinear metamaterials are often analyzed by tracking the change in the temporal state properties and discussing the existence of solitary waves, and dispersion characteristics. Dispersion relations do not, however, reveal enough detailed information on the wave distortion features. On the other hand, spectro-spatial analyses can provide better understanding of the physical features of wave propagation such as frequency shift and wave localization or dispersion in a nonlinear medium. Ganesh and Gonella [63] were the first to study the spectro-spatial wave packet propagation features of nonlinear periodic chains using signal processing tools to highlight new important nonlinear wave propagation properties. Their analysis provided more detailed information about the wave distribution; such as conditions related to the birth or inhalation of solitary wave at different wavelengths. Their work was extended by Zhou et al. [195], who investigated the spectro-spatial features of nonlinear acoustics metamaterials consisting of nonlinear cell with a linear local resonator. Their study showed that nonlinearity gives rise to nondispersive features in wave

propagation. The spectro-spatial features in [63, 195] revealed that nonlinear phenomena affect only short wavelength domain. This is because the nonlinearity was limited to the springs connecting the cells only. None of the aforementioned studies included nonlinearities in the local resonators. Recently, we presented for the first time the spectral analysis (i.e., dispersion relations only) of a nonlinear metamaterials consisting of nonlinear (or linear) chain with linear (or nonlinear) multiple local resonators [30]. Our work indicated that the dispersion relations for nonlinear chain with linear resonator and linear chain with nonlinear resonator are different. Particularly, the former affects the waveform only in the short wavelength limit while the latter can be tuned to affect the waveform in the long wavelength limit. These findings were also confirmed by the spectro-spatial analysis of such a nonlinear metamaterial presented in [24]. Note that both papers were limited to the study of the nonlinearity attributed to either the chain only or local resonator only. We did not examine the combination of both nonlinearities.

In this chapter, we extend our work in [24, 30] by combining both chain nonlinearity and local resonators nonlinearity, and thoroughly study the relation between topological (i.e., space-time domain) and spectral (dispersion relations) features of a wave propagating in such a nonlinear metamaterial. We derive analytical expressions for the dispersion relations by the method of multiple scales. Our analytical results are validated through numerical simulation. Parametric studies are carried out to examine the role of both hardening and softening nonlinearities in the chain and local resonators. The results show very interesting characteristics of wave propagation in all wavelength limits.

The remainder of the chapter is organized as follows. Section 2 presents the mathematical modeling of the proposed nonlinear metamaterial. We address the spectral analysis in Section 3 and the spectro-spatial analysis in Section 4. Section 5 summarizes the findings and provides suggestion for future work.
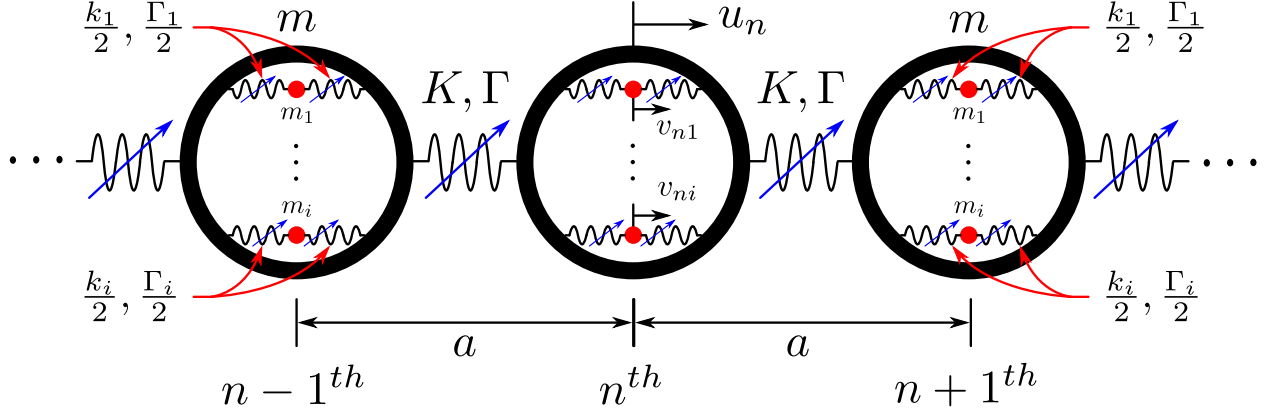
Figure 2.1: A schematic diagram for the nonlinear acoustics metamaterials with nonlinear resonators

2.2   Mathematical Modeling

This section presents the mathematical derivation for the dispersion equation for a nonlinear chain with nonlinear resonators depicted in Fig. 2.1. Each unit cell consists of a rigid mass, m, connected to other cells through a nonlinear spring with linear coefficient, k and nonlinear coefficient Γ. Inside each cell, there are multiple resonators with mass, m_i, attached by nonlinear spring with linear spring coefficient, k_i and nonlinear spring coefficient, Γ_i. The free oscillation equations for each cell with s number of resonators can be expressed as

$$m\ddot{u}_n + K(2u_n - u_{n-1} - u_{n+1}) + \epsilon\Gamma((u_n - u_{n-1})^3 + (u_n - u_{n+1})^3) +$$
$$\sum_{i=1}^{s} k_i(u_n - v_{ni}) + \sum_{i=1}^{s} \epsilon\Gamma_i(u_n - v_{ni})^3 = 0 \tag{2.1}$$

$$m_i\ddot{v}_{ni} + k_i(v_{ni} - u_n) + \epsilon\Gamma_i(v_{ni} - u_n)^3 = 0 \tag{2.2}$$

For convenience, we introduce the following dimensionless parameters

$$\tau = \omega_n t; \bar{\Gamma} = \frac{\Gamma}{K}; \bar{\Gamma}_i = \frac{\Gamma_i}{K}; \bar{k}_i = \frac{k_i}{K} \tag{2.3}$$

where $\omega_n = \sqrt{K/m}$ and $\omega_{di} = \sqrt{k_i/m_i}$.

Introducing these parameters in Eqs. (2.1)-(2.2) leads to

$$\ddot{u}_n + 2u_n - u_{n-1} - u_{n+1} + \epsilon\bar{\Gamma}((u_n - u_{n-1})^3 + (u_n - u_{n+1})^3)+$$
$$\sum_{i=1}^{s} \bar{k}_i(u_n - v_{ni}) + \sum_{i=1}^{s} \epsilon\bar{\Gamma}_i(u_n - v_{ni})^3 = 0 \tag{2.4}$$

$$\frac{\omega_n^2}{\omega_{di}^2}\ddot{v}_{ni} + (v_{ni} - u_n) + \epsilon\frac{\bar{\Gamma}_i}{\bar{k}_i}(v_{ni} - u_n)^3 = 0 \tag{2.5}$$

We assume expansions for the displacements in the form

$$u_n(t, \epsilon) = u_{n0}(T_0, T_1) + \epsilon u_{n1}(T_0, T_1) + o(\epsilon^2) \tag{2.6}$$

$$v_{ni}(t, \epsilon) = v_{ni0}(T_0, T_1) + \epsilon v_{ni1}(T_0, T_1) + o(\epsilon^2) \tag{2.7}$$

where $T_0 = \tau$ is the fast time scale and $T_1 = \epsilon\tau$ is the slow time scale. Since the time is expressed in two independent variables, the time derivative can be presented by using the chain role as

$$(\ddot{}) = D_0^2 + 2\epsilon D_0 D_1 + ... \tag{2.8}$$

where $D_n = \frac{\partial}{\partial T_n}$. Substituting Eqs. (2.6)-(2.8) into Eqs. (2.4)-(2.5) and collecting the similar coefficients of ϵ, one can get

Order ϵ^0

$$D_0^2 u_{n0} + 2u_{n0} - u_{(n-1)0} - u_{(n+1)0} + \sum_{i=1}^{s} \bar{k}_i(u_{n0} - v_{ni0}) = 0 \tag{2.9}$$

$$\frac{\omega_n^2}{\omega_{di}^2} D_0^2 v_{ni0} - (u_{n0} - v_{ni0}) = 0 \tag{2.10}$$

Order ϵ

$$D_0^2 u_{n1} + 2u_{n1} - u_{(n-1)1} - u_{(n+1)1} + \sum_{i=1}^{s} \bar{k}_i(u_{n1} - v_{ni1}) = -2D_0D_1u_{n0} -$$

$$\bar{\Gamma}((u_{n0} - u_{(n-1)0})^3 + (u_{n0} - u_{(n+1)0})^3) - \sum_{i=1}^{s} \bar{\Gamma}_i(u_{n0} - v_{ni0})^3 \qquad (2.11)$$

$$\frac{\omega_n^2}{\omega_{di}^2}D_0^2 v_{ni1} - (u_{n1} - v_{ni1}) = -2\frac{\omega_n^2}{\omega_{di}^2}\epsilon D_0D_1v_{ni0} - \frac{\bar{\Gamma}_i}{\bar{k}_i}(v_{ni0} - u_{n0})^3 \qquad (2.12)$$

2.2.1   Linear Dispersion Relation

At order ϵ^0 the problem is linear; therefore, the solution can be expressed as [119]

$$u_n = Ae^{j(nk-\omega T_0)} + c.c \qquad (2.13)$$

$$v_{ni} = B_i e^{j(nk-\omega T_0)} + c.c \qquad (2.14)$$

where $c.c$ refers to complex conjugate, $k = qa$ denotes the dimensionless wave number, and q represents the wave number. A and B_i stand for the wave amplitude of the outer and inner masses, respectively. By substituting Eqs. 2.13-2.14 into Eqs. 2.9-2.10 and following [119], the linear dispersion equation can be expressed as

$$-\omega^2 + (2 - 2\cos k) + \sum_{i=0}^{s} \bar{k}_i(1 - K_{\omega i}) = 0 \qquad (2.15)$$

where $K_{\omega i} = \frac{\omega_{di}^2}{\omega_{di}^2 - \omega_n^2 \omega^2}$.

2.2.2 Approximate Analytical Solution for the Nonlinear Dispersion Relation

For small values of nonlinear spring coefficients, Γ and Γ_i, Eqs. (2.4)-(2.5) are classified as weakly nonlinear. For such a system, the nonlinear dispersion relations can be derived approximately by perturbation techniques. For system with multiple coupled equations, it is more convenient to employ the method of multiple scales since it has advantages over other methods in terms of the required efforts and associated algebra. By rearranging equations at order ϵ, we obtain

$$
X(D_0^2 u_{n1} + 2u_{n1} - u_{(n-1)1} - u_{(n+1)1}) + \sum_{i=1}^{s} \frac{X\bar{k}_i \omega_n^2/\omega_{di}^2}{1 - \omega_n^2 \omega^2/\omega_{di}^2} D_0^2 u_{n1} =
$$
$$
\sum_{i=1}^{s} \frac{X\bar{k}_i}{1 - \omega_n^2 \omega^2/\omega_{di}^2}(-2\omega_n^2/\omega_{di}^2 D_0 D_1 v_{ni0} + \frac{\bar{\Gamma}_i}{\bar{k}_i}(u_{n0} - v_{ni0})^3) +
$$
$$
X(-2D_0 D_1 u_{n0} - \sum_{i=1}^{s} \bar{\Gamma}_i (u_{n0} - v_{ni0})^3 - \bar{\Gamma}((u_{n0} - u_{(n-1)0})^3 + (u_{n0} - u_{(n+1)0})^3))
$$

$$(2.16)$$

where $X = \prod_{i=1}^{s}(\omega_n^2/\omega_{di} D_0^2 + 1)$.

Introducing Eqs. (2.13)-(2.14) into Eq. (2.16) leads to

$$
X(D_0^2 u_{n1} + 2u_{n1} - u_{(n-1)1} - u_{(n+1)1}) + \sum_{i=1}^{s} \frac{X\bar{k}_i \omega_n^2/\omega_{di}}{1 - \omega_n^2 \omega^2/\omega_{di}^2} u_{n1} =
$$
$$
[2j\omega \sum_{i=1}^{s} \frac{X\bar{k}_i \omega_n^2/\omega_{di}^2}{1 - \omega_n^2 \omega^2/\omega_{di}^2} A' K_{\omega i} + 2jX\omega A' - 12\bar{\Gamma} X A^2 \bar{A}(1 - \cos k)^2 +
$$
$$
3A^2 \bar{A}(\sum_{i=1}^{s}[\frac{X(1 - k_{\omega_i})^3}{1 - \omega_n^2 \omega^2/\omega_{di}^2}\bar{\Gamma}_i - X(1 - k_{\omega_i})^3 \bar{\Gamma}_i])]e^{j(nk - \omega T_0)} + NST
$$

$$(2.17)$$

where NST denotes non-secular terms, $A' = \frac{dA}{dT_1}$, and $\bar{A}$ is the complex conjugate of A. We note here that X becomes $X = \prod_{i=1}^{s}(1 - \omega^2 \omega_n^2/\omega_{di})$

The left hand side of Eq. (2.17) has a nontrivial solution while the secular terms on the

right hand side must be eliminated for bonded solution by solving the following solvability condition [134]

$$
\begin{aligned}
[2j\omega \sum_{i=1}^{s} \frac{X\bar{k}_i\omega_n^2/\omega_{di}^2}{1 - \omega_n^2\omega^2/\omega_{di}^2}A'K_{\omega i} + 2jX\omega A' - 12\bar{\Gamma}XA^2\bar{A}(1 - \cos k)^2 + \\
3A^2\bar{A}(\sum_{i=1}^{s}[\frac{X(1 - k_{\omega_i})^3}{1 - \omega_n^2\omega^2/\omega_{di}^2}\bar{\Gamma}_i - X(1 - k_{\omega_i})^3\bar{\Gamma}_i]] = 0
\end{aligned}
\tag{2.18}
$$

Substituting the polar form

$$
A = \frac{1}{2}\alpha e^{j\beta}
\tag{2.19}
$$

into the solvability condition and separating the real and imaginary parts, the modulation equations for the amplitude and phase can be expressed as

$$
\omega \sum_{i=1}^{s} \frac{\bar{k}_i X\omega_n^2/\omega_{di}^2}{1 - \omega_n^2\omega^2/\omega_{di}^2}\alpha'K_{\omega i} + X\omega\alpha' = 0
\tag{2.20}
$$

$$
\begin{aligned}
-\omega \sum_{i=1}^{s} \frac{\bar{k}_i X\omega_n^2/\omega_{di}^2}{1 - \omega_n^2\omega^2/\omega_{di}^2}\alpha\beta'K_{\omega i} - X\omega\alpha\beta' - \frac{3}{2}X\bar{\Gamma}\alpha^3(1 - \cos k)^2 - \\
\sum_{i=1}^{s}[\frac{3}{8}\alpha^3(1 - k_{\omega_i})^3 X\bar{\Gamma}_i(\frac{1}{1 - \omega_n^2\omega^2/\omega_{di}^2} - 1)] = 0
\end{aligned}
\tag{2.21}
$$

By solving the modulation equations, the amplitude and phase can be expressed as

$$
\alpha = \alpha_0
\tag{2.22}
$$

$$
\beta = \frac{\sum_{i=1}^{s}[\frac{3}{8}\alpha^2(1 - K_{\omega_i})^3\bar{\Gamma}_i(\frac{1}{1 - \omega_n^2\omega^2/\omega_{di}^2} - 1)] - \frac{2}{3}\bar{\Gamma}\alpha^2(1 - \cos k)^2}{\omega(1 + \sum_{i=1}^{s}\frac{\bar{k}_i\omega_n^2/\omega_{di}}{1 - \omega_n^2\omega^2/\omega_{di}^2}K_{\omega i})}T_1
\tag{2.23}
$$

Since $T_1 = \epsilon\tau$, the nonlinear frequency , ω_{nl} associated with k is

$$
\omega_{nl} = \omega + \epsilon\beta'
\tag{2.24}
$$

The nonlinear dispersion relation presented by Eq. (2.24) includes the effect of both non-linearity in the chain $\bar{\Gamma}$ and in the resonators $\bar{\Gamma}_i$). This expression is also valid for the cases of nonlinear chain only (i.e., $\Gamma_i = 0$) and nonlinear resonator only (i.e., $\Gamma = 0$). It can also be observed that only the effect of nonlinearity of the chain varies explicitly with the wavenumber. Moreover, The nonlinear correction coefficient $\epsilon\beta'$ is a function of vibration amplitude α, the nonlinear spring coefficient $\epsilon\Gamma$ (for the nonlinear chain) and $\epsilon\Gamma_i$ (for the nonlinear resonator). It is noteworthy here that we assume the system is weakly nonlinear (i.e., $\epsilon << 1$), set $\alpha = 1$ in all subsequent sections, and vary the magnitude of nonlinear stiffness.

2.3 Predicting Band Structure Boundaries by Analytical Dispersion Relations

2.3.1 Validating the current model

To check the accuracy of the derived expression, we validate our results by using two different techniques. First, for nonlinear chain with single linear resonator case, we compare our results with those obtained by Lindstedt-Poincare method in the literature. Second, we compare our results for nonlinear resonator case and multiple resonators case by direct numerical integration. For the numerical integration, we simulate 500 cells with Perfectly match layers (PML) to omit wave reflections [133]. The system is excited by a transient wave packet applied at the beginning of the structure and propagating to the other end of the structure. The velocity of the wave packets is selected to force the wave to travel in one direction only and suppress any wave propagating in the opposite direction. This wave packet excitation

can be defined as:

$$u_m(0) = \frac{1}{2}(H(m-1) - H(m-1-N_{cy}2\pi/k))(1 - \cos(mk/N_{cy}))\sin(mk) \qquad (2.25)$$

$$\dot{u}_m(0) = \frac{1}{2}(H(m-1) - H(m-1-N_{cy}2\pi/k))(-\omega_n\omega/N_{cy}\sin(mk/N_{cy})\sin(mk)-$$
$$\omega_n\omega(1 - \cos(mk/N_{cy}))\cos(mk)) \qquad (2.26)$$

$$v_{mi}(0) = K_{\omega i}u_m(0) \qquad (2.27)$$

$$\dot{v}_{mi}(0) = K_{\omega i}\dot{u}_m(0) \qquad (2.28)$$

where N_{cy} is the number of cycles and in our numerical simulations we set $N_{cy} = 7$, and $H(x)$ is the Heaviside function. For these initial conditions, we integrate the system by MATLAB built in integrator ODE45.

To obtain numerical dispersion curves, we collect the time response resulting from the numerical integration in the displacement matrix at a specific wave number. The displacement matrix is then transformed to the frequency-wave number domain by 2D Fast Fourier transform (2D FFT). We next pick the point with maximum power density. The frequency and wavenumber corresponding to this point are a point on the reconstructed dispersion curve. To construct the full curve, the wave number is swept along the first Brillouin zone.

The parameters of the system are selected as $\omega_n = \omega_{d1} = 1000$ rad/sec, and $\bar{k}_1 = 1$ for single resonator system (i.e., s=1), and for two resonators case (i.e., s=2) and we select the parameters as $\omega_n = \omega_{d1} = 1000$ rad/sec, $\omega_{d2} = 1.5\omega_n$, $\bar{k}_1 = 1$, and $\bar{k}_2 = 1.5$.

Validation for the nonlinear chain and single linear resonator is presented in Fig. 2.2-(a). It is observed that our multiple scale results show a good agreement with those obtained by Lindstedt-Poincare method [195] and numerical results except inside the Pseudo-bandgap. In the Pseudo-bandgap region (as we will show in the subsequent sections), there is a significant

frequency shift for wave packets excitation [195]. This significant frequency shift cannot be captured by our approximate solution. It is noteworthy here that we highlighted the bandgap, optical mode, and acoustic mode for single resonator system in Fig. 2.2 and Fig. 2.3.
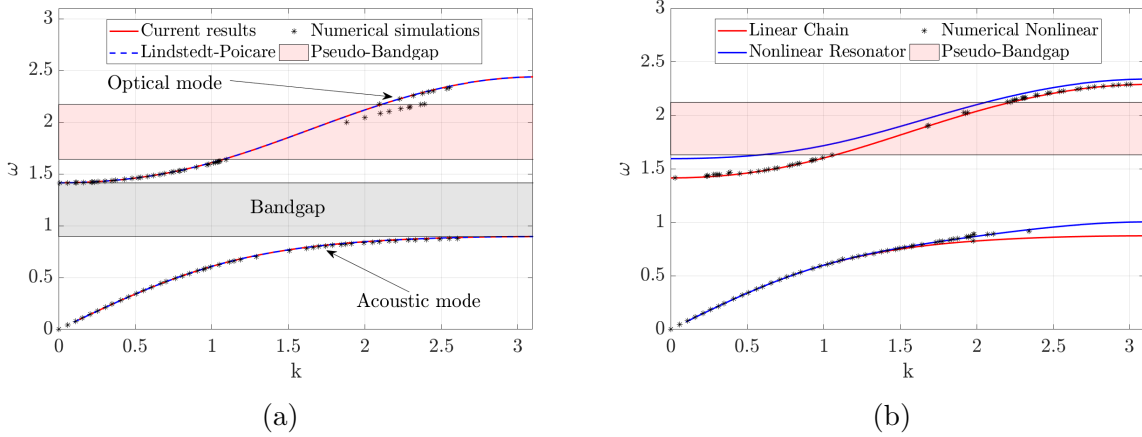
Figure 2.2: (a) Validating the results of a nonlinear chain with single resonator $\alpha^2\epsilon\bar{\Gamma} = 0.06$, $\alpha^2\epsilon\bar{\Gamma}_1 = 0.$; (b) Validating the results of a linear chain with single nonlinear resonator $\alpha^2\epsilon\bar{\Gamma} = 0$, $\alpha^2\epsilon\bar{\Gamma}_1 = 0.06$.
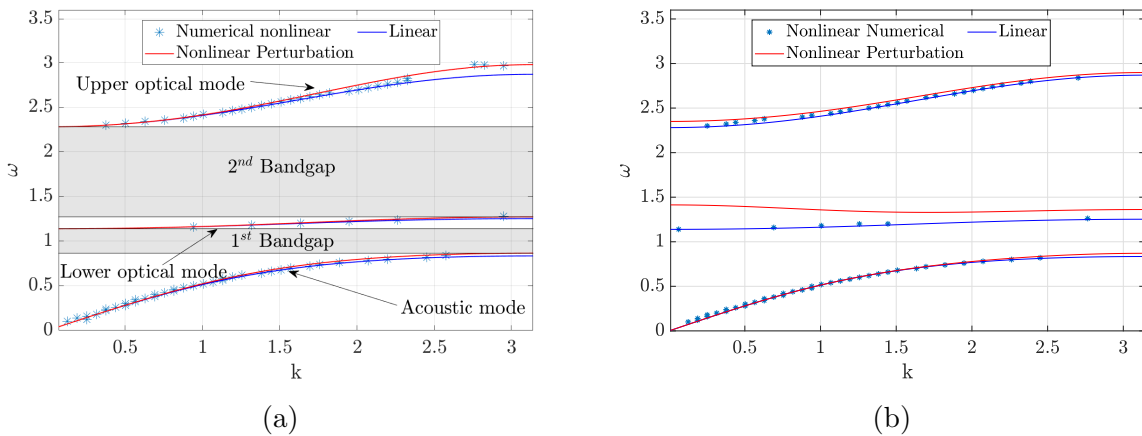
Figure 2.3: (a) Validating the results of a nonlinear chain with multiple resonator $\alpha^2\epsilon\bar{\Gamma} = 0.06$, $\alpha^2\epsilon\bar{\Gamma}_1 = \alpha^2\epsilon\bar{\Gamma}_2 = 0.$; (b) Validating the results of a linear chain with multiple nonlinear resonator $\alpha^2\epsilon\bar{\Gamma} = \alpha^2\epsilon\bar{\Gamma}_2 = 0$, $\alpha^2\epsilon\bar{\Gamma}_1 = 0.06$.

For the cases of nonlinear resonators, the results are validated only numerically. The
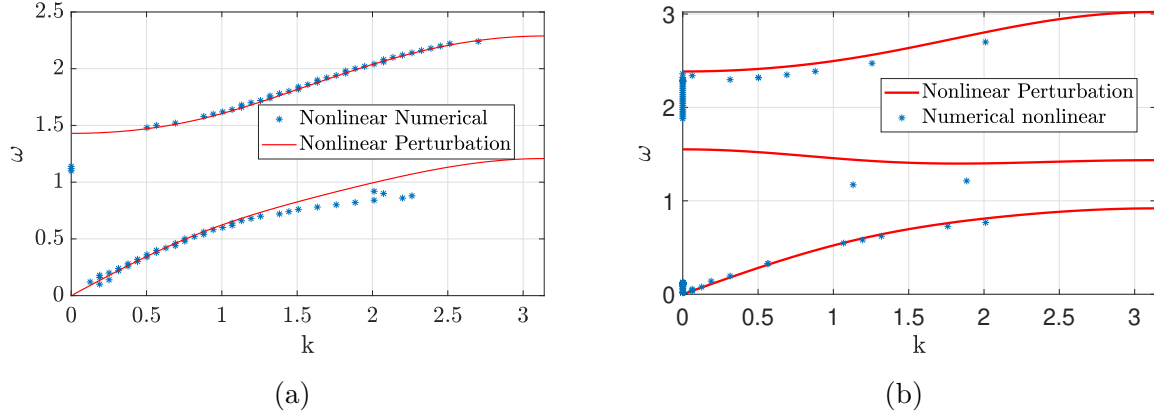
Figure 2.4: (a) Validating the results of a nonlinear chain with single nonlinear resonator $\alpha^2\epsilon\bar{\Gamma} = \alpha^2\epsilon\bar{\Gamma}_1 = 0.06$.; (b) Validating the results of a linear chain with multiple nonlinear resonators $\alpha^2\epsilon\bar{\Gamma} = \alpha^2\epsilon\bar{\Gamma}_1 = \alpha^2\epsilon\bar{\Gamma}_2 = 0.06$.

results of a chain with single nonlinear resonator are shown in Fig. 2.2-(b). The numerical results show a good agreement with the analytical results in the acoustic mode. However, a significant error is observed near the resonator frequency. This error results from the significant frequency shift. Indeed, points in the long wavelength limit ($k \sim 0$ since $\lambda = 2\pi/k$ where λ is the wavelength) belong to a signal with wavelength inside the Pseudo-bandgap (at medium wavelength limit $k \sim \pi/2$); however, due to the significant frequency shift, they appear in the long wavelength limit.

For multiple resonators, the results for nonlinear chain and nonlinear resonators are presented in Fig. 2.3. We note here that reconstructing the dispersion curves by wave packets excitation is not possible due to the significant frequency shift. Therefore, we reconstruct the dispersion curves using a plane waves excitation. For a nonlinear metamaterial with linear local resonators (i.e., Fig. 2.3-(a)), the perturbation results can accurately predict the cut-off frequencies. On the other hand, in the case of linear chain with nonlinear resonators, the perturbation results can only predict cut-off frequencies away from the surrounding region of nonlinear resonator frequency. Hence, higher order perturbations or other nonlinear

analytical tools may be required to provide better approximations.

Validation of results for a metamaterial with combined nonlinearity in both cells and resonators is presented in Fig. 2.4. The results show very good agreement between our analytical and numerical methods. However, similar observation can be revealed about the failure in predicting the dispersion curves near the frequency of nonlinear resonator. This is clearly demonstrated in Fig. 2.4-(a) in the short wavelength ($k \sim \pi$) limit of the acoustic branch and long wavelength limit of the optical branch. The points in these regions cannot be captured numerically. For multiple resonators case (Fig. 2.4-(b)), a significant frequency shift is observed in the middle branch. This region of frequency shift is confined between the frequencies of both nonlinear resonators.

2.3.2   Analytical Band Structure for Different Sources and Types of Nonlinearities

The numerical validation in section 2.3.1 revealed that the analytical dispersion curves can predict the regions of wavelength that are affected by nonlinearity although they fail in accurately estimating the band structure limits. In addition to Fig. 2.2, Fig. 2.3, and Fig. 2.4, dispersion curves for different sources and types of nonlinearities are depicted in Figs. 2.5 and Fig. 2.6.

For single resonator system, the effect of softening nonlinearity on the band structure is depicted in Fig. 2.5-(a). It is observed that the dispersion curves shift due to nonlinear resonator is more pronounced at frequencies close to the bandgap. This means that the short wavelength region in the acoustical mode and the long wavelength region in the optical mode are significantly affected by the nonlinear resonator. On the other hand, the dispersion curves shift for the nonlinear chain is confined in the short wavelength regions in both modes. This
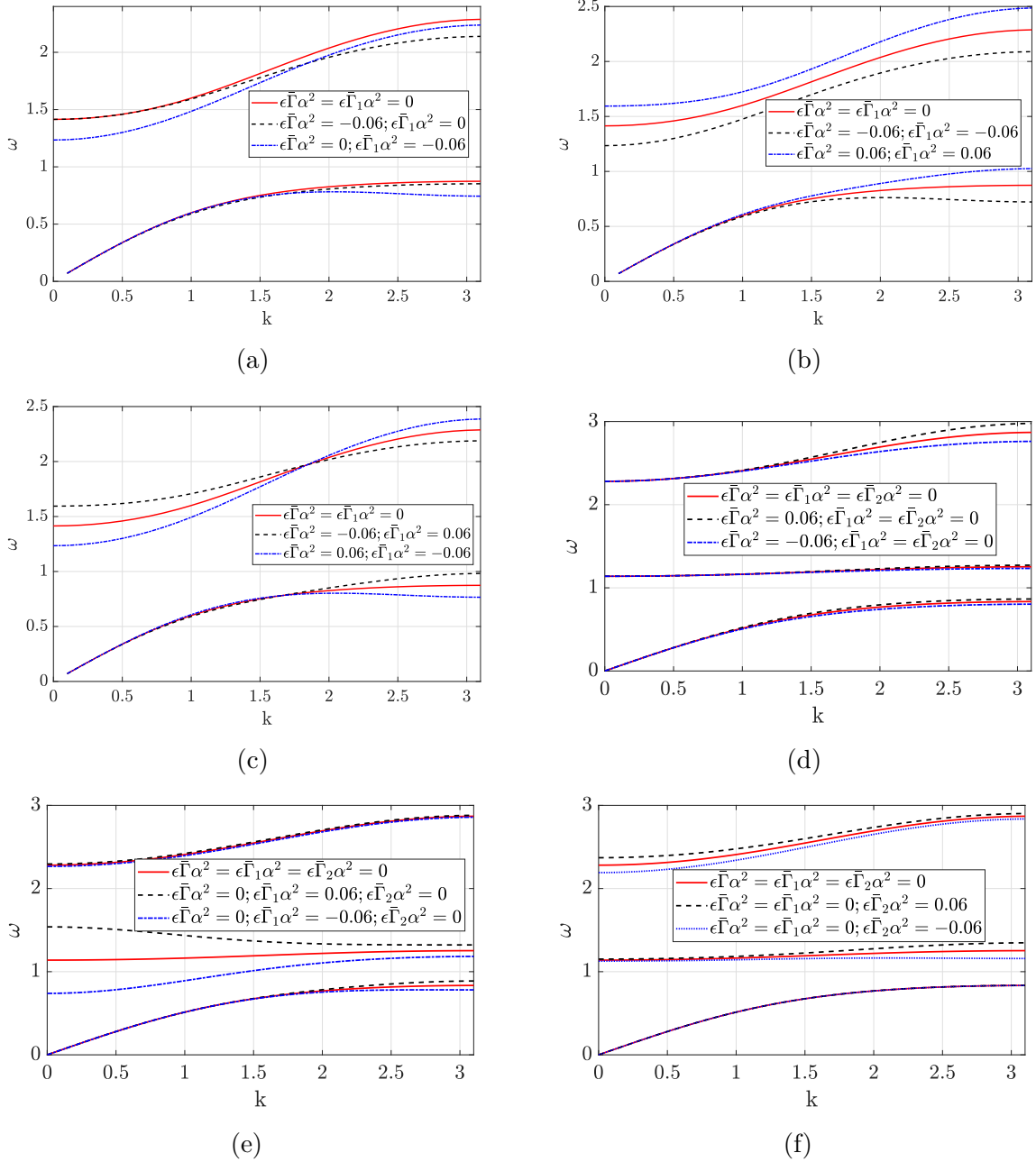
Figure 2.5: Analytical band structure for a system with single and multiple resonators and different sources and types of nonlinearities. (a)-(c): single resonator; (d)-(f) two resonators.

is not surprising since the nonlinear correction term β' explicitly depends on the wave number for the case of nonlinear chain unlike the case of nonlinear resonator. It is noteworthy here that softening chain increases the size of the bandgap; however, the softening resonator does
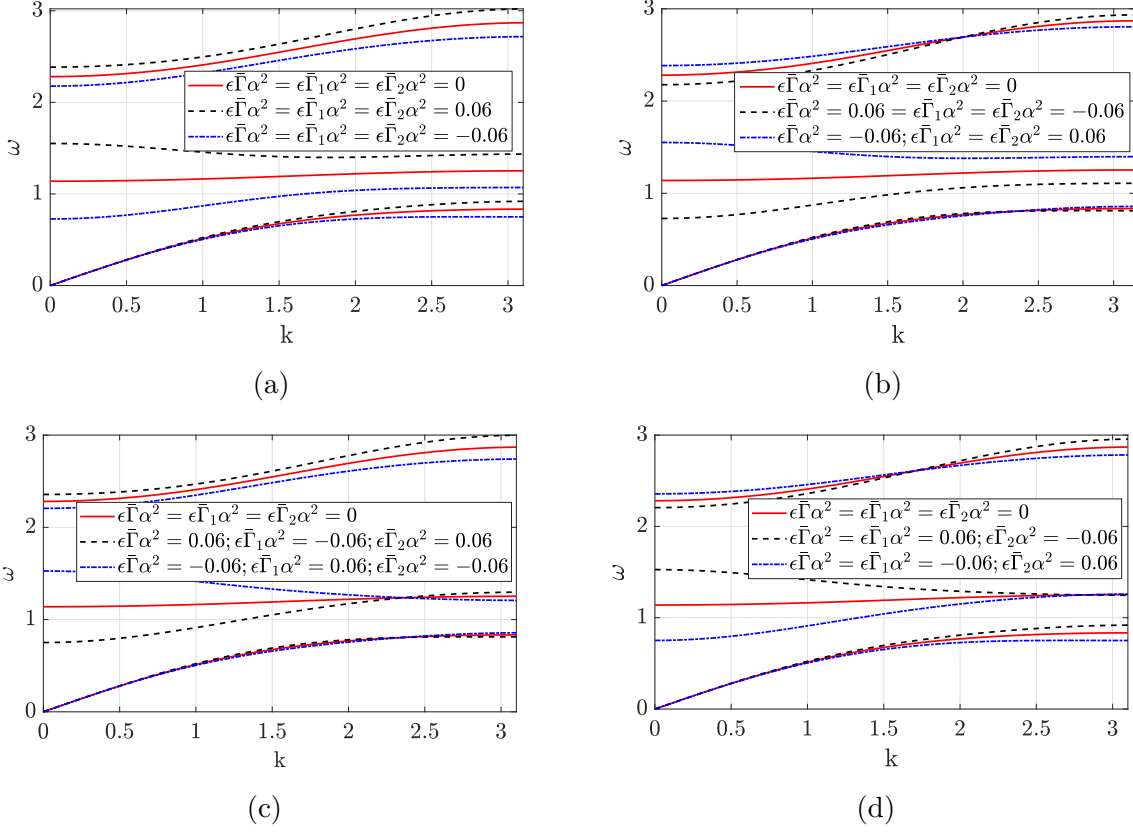
Figure 2.6: Analytical band structure for a system with single and multiple resonators and different sources and types of nonlinearities.

not.

The dispersion curves for a system with nonlinear chain and nonlinear local resonators with the same type of nonlinearity are plotted in Fig. 2.5-(b). When the type of nonlinearity is hardening, the dispersion curves are significantly shifted up. However, the dispersion curves are shifted down for softening type of nonlinearity. This shift is concentrated in the short wavelength region in the acoustic mode. The resonators nonlinearities equally shift the optical mode in all wavelength regions. This shift in the optical mode in the short wavelength limit can be attributed to the chain nonlinearity; whereas that in long wavelength limit is due to resonator nonlinearity.

To clarify the affected wavelength regions, we assign different types of nonlinearities for the chain and local resonators as depicted in Fig. 2.5-(c). It is demonstrated that the local resonator nonlinearity is more dominant than chain nonlinearity in the acoustic mode. However, there are different effects on the dispersion curves shifts in the optical mode. This difference is demonstrated by domination of the local resonance nonlinearity in the long wavelength region and domination of the chain nonlinearity in the short wavelength region. Furthermore, there is an interaction between both sources of nonlinearites in medium wavelength ($k \sim \pi/2$) region since the nonlinear curves intersect the linear curve in Fig. 2.5-(c).

For the multiple resonators case, the effect of each source and type of nonlinearity on the dispersion curves is shown in Fig. 2.5-(d), Fig. 2.5-(e), and Fig. 2.5-(f). The shift attributable to nonlinear chain is pronounced in the short wavelength regions similar to the single resonator case as shown in Fig. 2.5-(d). However, the impact of nonlinear resonators on the dispersion curves is not concentrated at the bandgap boundaries. Instead, it is related to the tuned frequency of the nonlinear resonator. For instance, if the resonator with $\omega_{d1} = \omega$ is nonlinear, we observe a substantial dispersion curves shift near $\omega = 1$ as shown in Fig. 2.5-(e). Similarly, the dispersion curves shift is observed at frequencies close to $\omega = 1.5$ when the nonlinear resonator is the second resonator $\omega_{d2} = 1.5\omega$ as shown in Fig. 2.5-(f).

To further illustrate the effect of nonlinearity on dispersion curves for the case of multiple local resonators, we investigate the nonlinear system when the chain and all local resonators are both nonlinear. The results are depicted in Fig. 2.6. When the chain and local resonators have all the same type of nonlinearity (softening or hardening), the dispersion curves are shifted up in all modes as demonstrated in Fig. 2.6-(a). This shift is quantitatively variant; however, its trend is not.

Next, we assign different types of nonlinearity to the chain and local resonators. The

results are shown in Fig. 2.6-(b) and reveal that the impact of nonlinearity in the chain can be observed only in the second optical mode at the short wavelength limit. This is not surprising since that zone is away from the local resonators frequencies; therefore, the effect of nonlinear local resonators is not dominant there.

Finally, the effect of each nonlinear local resonators on wavelength zones can be obtained from Fig. 2.6-(c) and Fig. 2.6-(d). The figures show that when one of the nonlinear local resonators has a nonlinearity type different than the nonlinearity of the chain and the other local resonator, the impact of that resonator is dominant in the short wavelength limit in the mode just below its frequency and in the long wavelength limit in the upper branch. The results here suggest that for the case of multiple resonators the dispersion curves shift due to nonlinear local resonator is dominant in frequency zones near its tuned frequency. Therefore, tuning the nonlinear resonator is crucial in determining the zones affected by nonlinearity. Solitary waves, wave non-reciprocity, and other nonlinear phenomena can be observed in these zones. On the other hand, zones at short wavelength limit and away from the resonator frequency are only affected by nonlinear chain.

2.4   Spectro-Spatial Analysis

Although the cut-off frequencies (boundaries of the nonlinear band structure)can be predicted by the method of multiple scales, other nonlinear wave propagation features (e.g., solitons, secondary resonances, dispersive waves) cannot be characterized. This suggests the use of spectro-spatial analysis to characterize the wave propagation in the proposed metamaterial. It should be noted that all the following simulations are based on the optical (upper branch) wave mode because we find this mode to be more affected by nonlinearity than the acoustic mode. In particular, there is no significant frequency shift observed in the acoustics

branch (also defined as Pseudo-Bandgap in Sec. 3.1) and it is hard to tune the nonlinear resonator to the long wavelength region in this mode. Otherwise, the observation in the optical mode should be similar to those in the acoustic mode. Also the numerical simulation for the optical mode is much faster. The simulation in this mode lasted for 8 sec, while the wave packet defined in Eqs. (25)-(28) was used as an input signal.

2.4.1 Spatial Profile of the Wave Packet

At the end of the simulation, the spatial profiles of the wave packet are plotted in Fig. 2.7 and Fig. 2.8. To investigate how each source of nonlinearity alters the input signal, we first present the wave profile of a metamaterial with a single source of nonlinearity in Fig. 2.7. The wave profile for a signal propagating in a linear chain is shown in Fig. 2.7-(a). The results show that the wave is not distorted in the long wavelength limit. However, the wave becomes gradually dispersive with increasing wavenumber (i.e., the amplitude of the wave becomes lower at high wave number since waves of different frequencies travel with different phase speed. We refer the reader to Figure. 9 in [85] for more information).

It should be noted that the terms distortion and dispersive are not exactly the same although they both indicate deformation in the input wave. We used the former mainly when the wave is split into multiple components and/or when there are other forms of deformation resulting from nonlinearity in the system. The latter is used when the wave get stretched and the wave amplitude becomes smaller.

For nonlinear chain only, there is no effect on the wave profile in the long wavelength range and the nonlinear chain behaves like the linear chain as shown in Fig. 2.7-(b) and Fig. 2.7-(c). This is not surprising since inspecting Eq. (23) when $\bar{\Gamma}_i = 0$ demonstrates that for small values of wavenumbers, β is negligible. In the meantime, increasing the wavenumber

(a) Linear chain: $\epsilon\bar{\Gamma}\alpha^2 = \epsilon\bar{\Gamma}_1\alpha^2 = \epsilon\bar{\Gamma}_2\alpha^2 = 0$
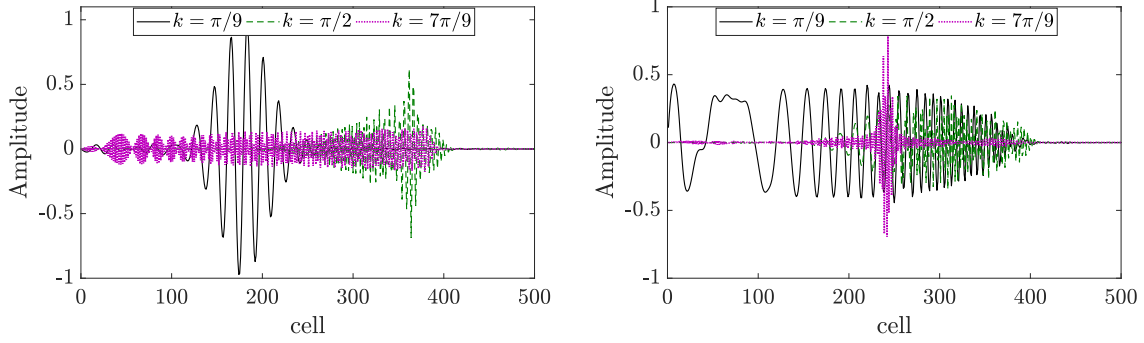
(b) Hardening chain nonlinearity $\epsilon\bar{\Gamma}\alpha^2 = 0.03$, $\epsilon\bar{\Gamma}_1\alpha^2 = \epsilon\bar{\Gamma}_2\alpha^2 = 0$

(c) Softening chain nonlinearity $\epsilon\bar{\Gamma}\alpha^2 = -0.03$, $\epsilon\bar{\Gamma}_1\alpha^2 = \epsilon\bar{\Gamma}_2\alpha^2 = 0$

(d) Hardening resonator nonlinearity $\epsilon\bar{\Gamma}_2\alpha^2 = 0.03$, $\epsilon\bar{\Gamma}_1\alpha^2 = \epsilon\bar{\Gamma}\alpha^2 = 0$
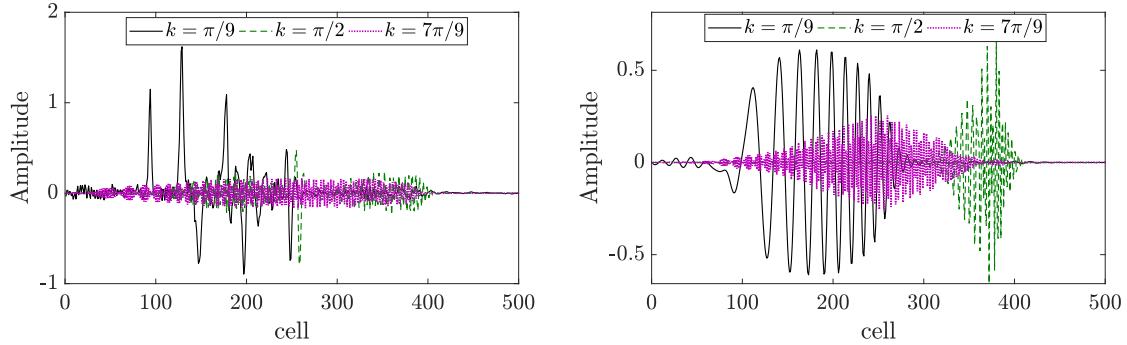
(e) Softening resonator nonlinearity $\epsilon\bar{\Gamma}_2\alpha^2 = -0.03$, $\epsilon\bar{\Gamma}_1\alpha^2 = \epsilon\bar{\Gamma}\alpha^2 = 0$

(f) Hardening resonator nonlinearity $\epsilon\bar{\Gamma}_1\alpha^2 = 0.03$, $\epsilon\bar{\Gamma}_2\alpha^2 = \epsilon\bar{\Gamma}\alpha^2 = 0$

Figure 2.7: Spatial profile of the wave packet for different types and sources of nonlinearities at frequencies in the upper branch of dispersion curve.

gradually shows different types of wave distortion due to nonlinear chain. For instance, hardening chain distorts the wave into a low amplitude dispersive signal and high amplitude

localized signal. The latter indicates the birth of solitary wave due to nonlinearity unlike the pure dispersive signal in the linear case. This can be explained by changing the shape of the variable slope dispersion curve to linear (fixed slope) dispersion curve similar to those of nondispersive mediums in homogeneous structures [85] (see Sec. 4.3). On the other hand, softening chain stretches the signal further to lower amplitudes components with the absence of any localized high amplitude signals. In other words, the shape of the variable slope dispersion curve of linear metamaterial becomes more nonlinear (variable slope), thus more dispersive [85].

The effect of some nonlinear phenomena in the long wavelength limit can be observed only when the nonlinearity is assigned in the resonator as depicted in Fig. 2.7-(d), Fig. 2.7-(e), and Fig. 2.7-(f). If the resonator with a frequency near the upper dispersion curve is nonlinear, a significant distortion in the wave profile is observed in the vicinal frequencies. Therefore, nonlinearity in the local resonator can affect the long wavelength limit unlike the nonlinear chain case. For instance, we set the second resonator ($\omega_{d2} = 1.5\omega$) to be nonlinear and plot the wave profile in Fig. 2.7-(d) and Fig. 2.7-(e). The results indicate that both hardening and softening nonlinearity in the resonator distort the wave shape at all wavelength limits. However, this distortion (w.r.t linear case in Fig. 2.7-(a)) becomes less significant with increasing wavenumber. The hardening nonlinearity stretches the wave in the long wavelength limit while it develops a localized signal in addition to the dispersive signal with decreasing wavelength as shown in Fig. 2.7-(d). The softening nonlinearity stretches the wave profile more substantially at all wavelengths limits as shown in Fig. 2.7-(e). This dispersive signal is associated with multiple high amplitude localized features with increasing wavelength. Finally, we set the first resonator ($\omega_{d1} = \omega$) to be nonlinear and plot the wave profile in Fig. 2.7-(f). Since this resonator's frequency is away from the upper branch of dispersion curve, the effect of nonlinearity is insignificant. Fig. 2.7-(f) also shows

the existence of a minor distortion in the wave profile at the long wavelength limit. This distortion becomes negligible with increasing wavenumber.
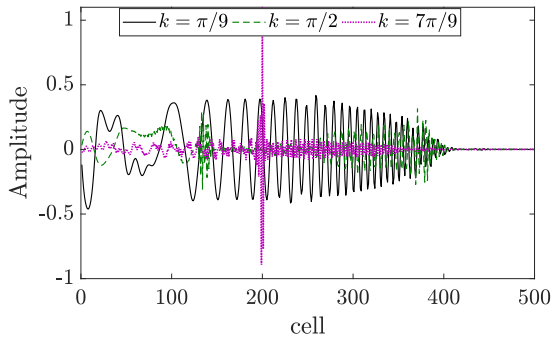
(a) $\epsilon\bar{\Gamma}\alpha^2 = \epsilon\bar{\Gamma}_1\alpha^2 = \epsilon\bar{\Gamma}_2\alpha^2 = 0.03$; (b) $\epsilon\bar{\Gamma}\alpha^2 = 0.03$

(b) $\epsilon\bar{\Gamma}\alpha^2 = 0.03$, $\epsilon\bar{\Gamma}_1\alpha^2 = \epsilon\bar{\Gamma}_2\alpha^2 = -0.03$
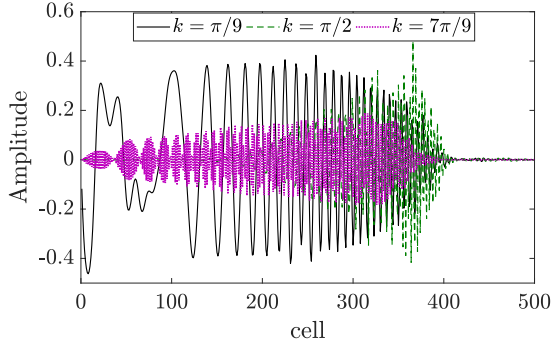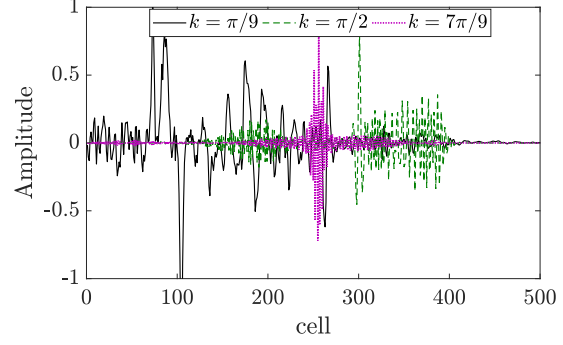
(c) $\epsilon\bar{\Gamma}\alpha^2 = -0.03$, $\epsilon\bar{\Gamma}_1\alpha^2 = \epsilon\bar{\Gamma}_2\alpha^2 = 0.03$
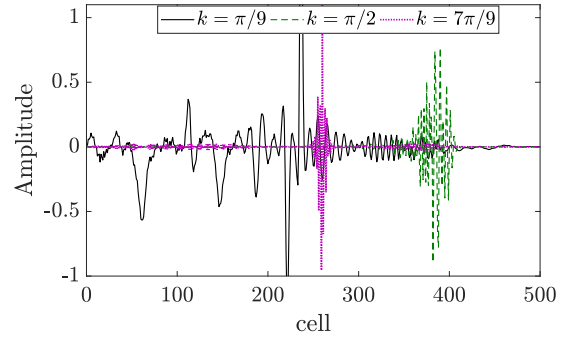
(d) $\epsilon\bar{\Gamma}\alpha^2 = 0.03$, $\epsilon\bar{\Gamma}_1\alpha^2 = 0.03$, $\epsilon\bar{\Gamma}_2\alpha^2 = -0.03$
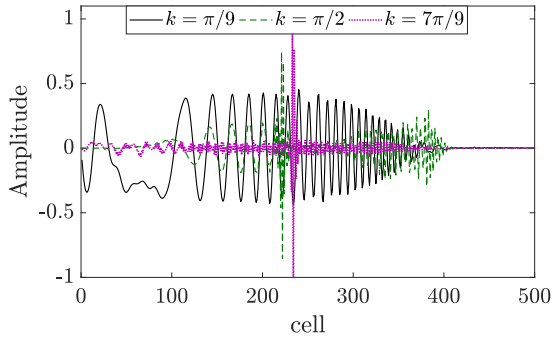
(e) $\epsilon\bar{\Gamma}\alpha^2 = 0.03$, $\epsilon\bar{\Gamma}_1\alpha^2 = -0.03$, $\epsilon\bar{\Gamma}_2\alpha^2 = 0.03$
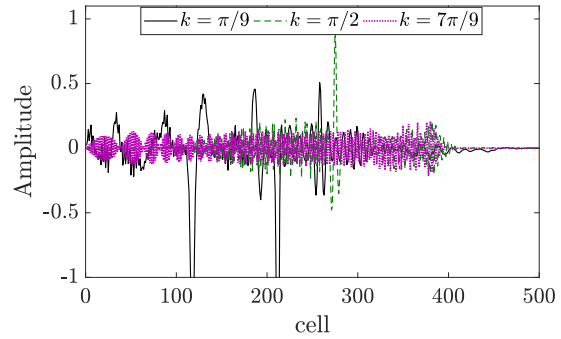
(f) $\epsilon\bar{\Gamma}\alpha^2 = -0.03$, $\epsilon\bar{\Gamma}_2\alpha^2 = 0.03$, $\epsilon\bar{\Gamma}\alpha^2 = -0.03$

Figure 2.8: Spatial profile of the wave packet for different types and sources of nonlinearities at frequencies in the upper branch of dispersion curve.

After analyzing each type of nonlinearity individually, we analyze the effect of different combinations of nonlinearities as depicted in Fig. 2.8. When the chain and both resonators have hardening nonlinearity, waves at short wavelength limit form a solitary wave (localized signal) with a small amplitude dispersive signal as shown in Fig. 2.8-(a). However, distortion at long wavelength limit is not negligible anymore since the nonlinear resonators stretches the wave with medium vibration amplitude. Between the long and short wavelength limits, there is a transition in the wave profile behavior, such that the wave has a dispersive feature (with amplitude in between the two limits) and localized feature with medium amplitude. Severe distortions in the wave profile are observed when the nonlinearity of both resonators are changed to softening as shown in Fig. 2.8-(b). Signals at all wavelength limits are more dispersive, particularly, waves with low wavenumbers. However, one can still recognize localized features at short wavelength limit due to hardening chain. The latter can completely disappear if the chain has softening nonlinearity (see Fig. 2.8-(c)), even though, both resonators have hardening nonlinearity. Yet hardening nonlinear resonators reduce the wave stretching.

Next, we assign for the first resonator a type of nonlinearity different from the second resonator, which has a frequency near the upper optical mode in Fig. 2.8-(d) and Fig. 2.8-(e). It is observed that the behavior of the wave profile for the cases in Fig. 2.8-(d) is similar to the wave profile in Fig. 2.8-(b) and signals in Fig. 2.8-(e) and Fig. 2.8-(a) are also similar. Though the distortion in the mid and long wavelength limits is less dominant by the nonlinearity of the second resonator. One can hypothesize that the effect of nonlinearity in the first resonator is less pronounced than that of the second resonator in the upper branch of the dispersion curves. Finally, we can also observe that the nonlinearity type in the first resonator does not distort the wave profile in the short wavelength limit since the frequency of this resonator is away from frequencies of the system in this region and the effect of other

sources of nonlinearity are more dominant as shown in Fig. 2.8.

2.4.2   Spatial Spectrograms of the Wave Packet

After investigating wave propagation through the metamaterial in the spatial domain, we now examine the wave profile in the wavenumber domain. Here, we use Short Term Fourier Transform (STFT) instead of simple Fourier Transform (FT) to investigate the signal as it changes over time. We apply a Hann window with the size of initial wave profile to divide the time signal into shorter segments. The spectrograms for different types and sources of nonlnearities at different wavelengths are plotted in Fig. 2.9 and Fig. 2.10.

Figure. 2.9-(a) shows that the input signal is the same as the output signal for the case of nonlinear chain. This is not surprising since it was observed in the previous analysis that at long wavelength limit, the system with nonlinear chain has similar performance to the linear system. This does not hold in the nonlinear resonator case. It is revealed for Fig. 2.9-(b) and Fig. 2.9-(c) that the input signal is severely distorted in the long wavelength limit. If the nonlinearity is hardening, the input signal becomes stretched over the chain with high amplitude as shown in Fig.2.9-(b). On the other hand, softening nonlinearity distorts the input signal into low amplitude dispersive component and multiple high amplitude localized components. Indeed, some of the energy content of the input signal appears at wavenumbers outside the input signal window. This implies that this energy content appears at frequencies different than the input signal frequencies since wavenumber and frequency are related in Eq. (24). Therefore, we will refer to any shift in the wavenumber of the output signal as frequency shift in the subsequent discussion. However, if only the first resonator is nonlinear, the observed distortion is less significant at long wavelength limit as shown in Fig. 2.9-(d). Beyond the long wave length limit, the effect of nonlinearity in the case of nonlinear

(a) Hardening chain nonlinearity $\epsilon\bar{\Gamma}\alpha^2 = 0.03$,

(b) Hardening resonator nonlinearity

(c) Softening resonator nonlinearity

(d) Hardening resonator nonlinearity

(e) Hardening resonator nonlinearity
$\epsilon\bar{\Gamma}_2\alpha^2 = 0.03$, $\epsilon\bar{\Gamma}_1\alpha^2 = \epsilon\bar{\Gamma}\alpha^2 = 0$, $k = 7\pi/9$

(f) Hardening resonator nonlinearity
$\epsilon\bar{\Gamma}_1\alpha^2 = 0.03$, $\epsilon\bar{\Gamma}_2\alpha^2 = \epsilon\bar{\Gamma}\alpha^2 = 0$, $k = 7\pi/9$
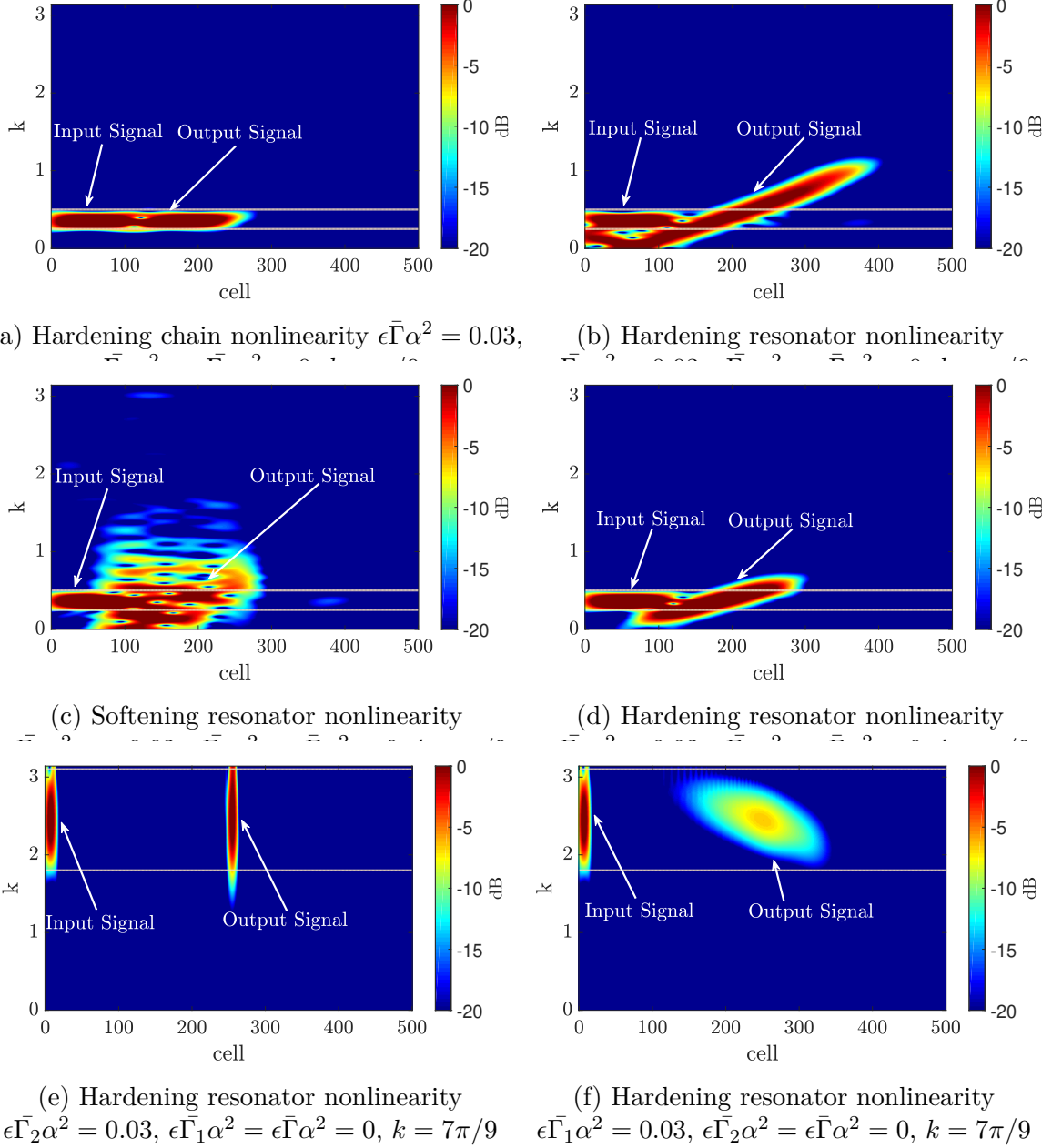
Figure 2.9: Spatial spectrograms of the wave packet for different types and sources
of nonlinearities at frequencies in the upper branch of dispersion curve.
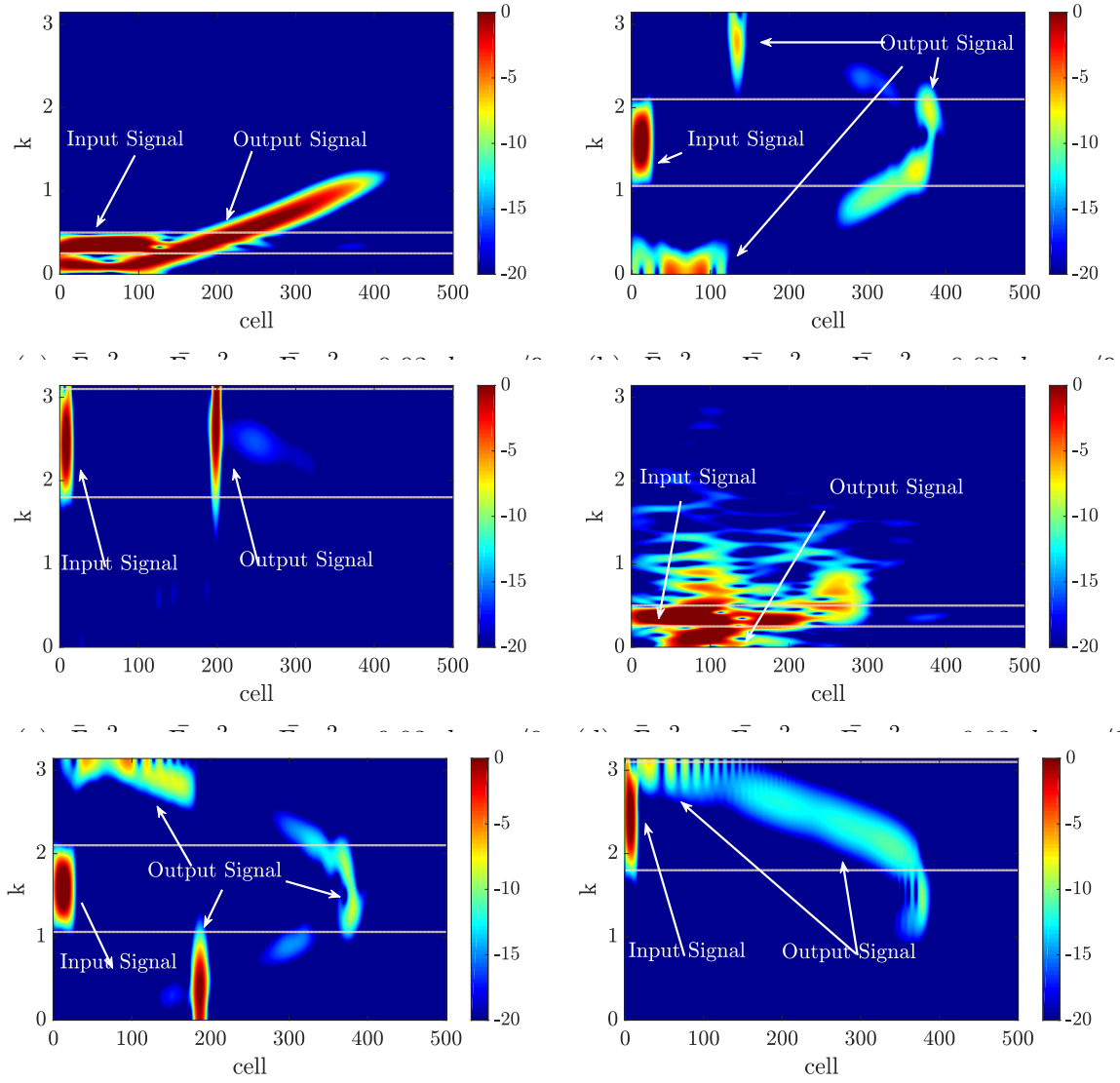
(e) $\epsilon\bar{\Gamma}\alpha^2 = \epsilon\bar{\Gamma}_1\alpha^2 = \epsilon\bar{\Gamma}_2\alpha^2 = -0.03$, $k = 7\pi/9$ (f) $\epsilon\bar{\Gamma}\alpha^2 = \epsilon\bar{\Gamma}_1\alpha^2 = \epsilon\bar{\Gamma}_2\alpha^2 = -0.03$, $k = 7\pi/9$

Figure 2.10: Spatial spectrograms of the wave packet for different types and sources of nonlinearities at frequencies in the upper branch of dispersion curve.

resonator is also demonstrated in the short wavelength limit as shown in Fig. 2.9-(e). We can observe that the nonlinear hardening resonator acts like the nonlinear hardening chain in the short wavelength limit, such that it distorts the signal into localized component unlike the dispersive signal in the linear chain. Since the short wavelength limit frequencies in the upper optical mode are away from the first resonator frequency, the effect of nonlinearity in this resonator is insignificant in this zone. For instance, we assign a hardening nonlinearity for this resonator in Fig. 2.9-(f), yet the wave is dispersive like the linear case.

To investigate how different types and sources of nonlinearities interact in the metamaterial, we assign different types of nonlinearity to the chain and resonators and plot them in Fig.2.10. When all sources of nonlinearity are of hardening type, the system performs like the hardening resonator (ω_{d2}) in the long wavelength limit as depicted in Fig. 2.10-(a). Therefore, this zone can be controlled fully by the second resonator regardless of the nonlinearity in the chain, and partially by the first resonator as observed in Fig. 2.9-(d). In Fig. 2.10-(b), the output signal is distorted severely and brakes down into multiple components. Most of the energy content of the output signal appears at wavenumbers away from the input signal wavenumbers. Therefore, a significant frequency shift is observed at medium wavelength limit when all sources of nonlinearities are hardening. This frequency shift forms a Pseudo-bandgap [195], which can be utilized to design acoustics diode. However, there is no frequency shift at short wavelength limit for hardening chain and hardening resonators, instead, the signal is concentrated in a main component forming a solitary wave as depicted in Fig. 2.10-(c).

In order to generate a significant frequency shift in all wavelengths limits, we assign softening nonlinearity to both the resonators and the chain. This can generate a significant frequency shift in wavelength zones; therefore, it can widen the Pseudo-bandgap, thus resulting in a wider operating frequency range for acoustics diodes for example. These plots are

presented in Fig. 2.10-(d) and Fig. 2.10-(e). A significant frequency shift is observed in all of these figures. In particular, the signal at long and medium wavelengths shift the dominant component in the signal to very low values of wavenumber/frequency. This indicates that a wider Pseudo-bandgap can be established at these wavelength zones, since any input signal with wavenumber/frequency in this range will be distorted and shifted significantly to low wavenumber. Even though this frequency shift is less significant at short wavelength limit and at higher values of wavenumber/frequency (Fig. 2.10-(f)), it can be used to construct acoustic diodes.

2.4.3 2-D Fourier Transform of the Response

After studying the wave form evolution in spatial and wavenumber domains, we present the contour of 2D Fast Fourier transform (2D-FFT) or 2D power spectrum of the signal in both frequency and wavenumber domains (see Fig. 2.11 and Fig. 2.12). Contour plots allow us to reconstruct the dispersion curves especially inside the Pseudo bandgap. Moreover, these plots can be used to detect the birth of solitary waves based on the shape and distribution of frequency-wavenumber component. At long wavelength limit, the hardening nonlinear chain does not distort the traveling wave as depicted in Fig. 2.11-(a). We note here that the contour plots for the linear signal is exactly the same as the signal plot in Fig. 2.11-(a). Thus confirming that the nonlinear chain has no effect in this zone. However, frequency shift and distortion are observed for nonlinear resonator (ω_{d2}) with hardening nonlinearity (Fig. 2.11-(b)) and softening nonlinearity (Fig. 2.11-(c)). It is noteworthy that the frequency shift is more significant and the wave distortion is more severe in the case of softening nonlinearity. To demonstrate the importance of tuning the nonlinear resonator, we present the contour plot for the first resonator in Fig. 2.11-(d). It can be observed that the distortion in this case is less significant comparing to the plot in Fig. 2.11-(b).

(a) Hardening chain nonlinearity $\epsilon\bar{\Gamma}\alpha^2 = 0.03$,

(b) Hardening resonator nonlinearity

(c) Softening resonator nonlinearity

(d) Hardening resonator nonlinearity

(e) Linear chain and resonators
$\epsilon\bar{\Gamma}_2\alpha^2 = \epsilon\bar{\Gamma}_1\alpha^2 = \epsilon\bar{\Gamma}\alpha^2 = 0$, $k = 7\pi/9$

(f) Hardening resonator nonlinearity
$\epsilon\bar{\Gamma}_2\alpha^2 = 0.03$, $\epsilon\bar{\Gamma}_1\alpha^2 = \epsilon\bar{\Gamma}\alpha^2 = 0$, $k = 7\pi/9$
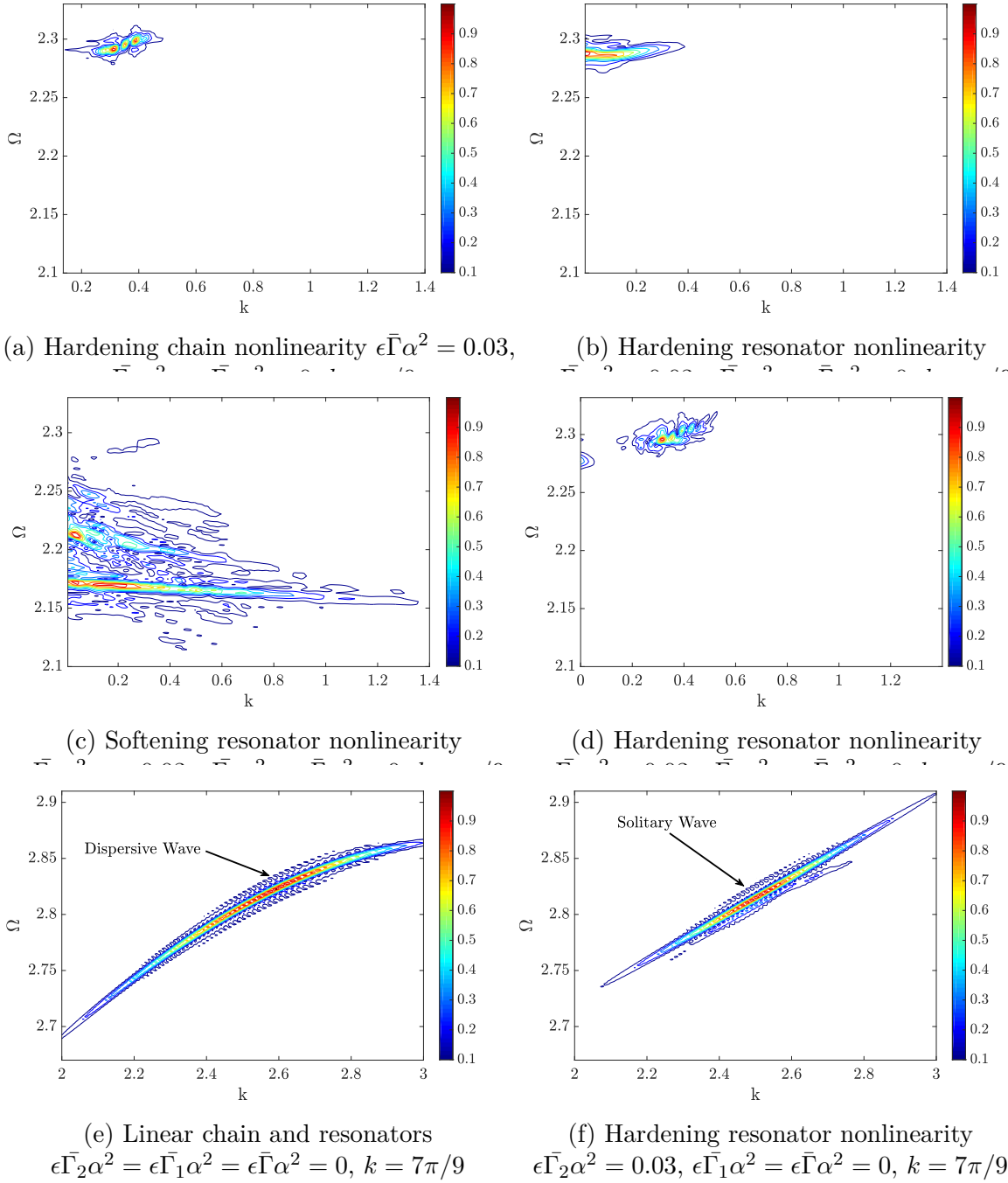
Figure 2.11: 2-D Fourier transform contour of the response for different types and sources of nonlinearities at frequencies in the upper branch of dispersion curve.
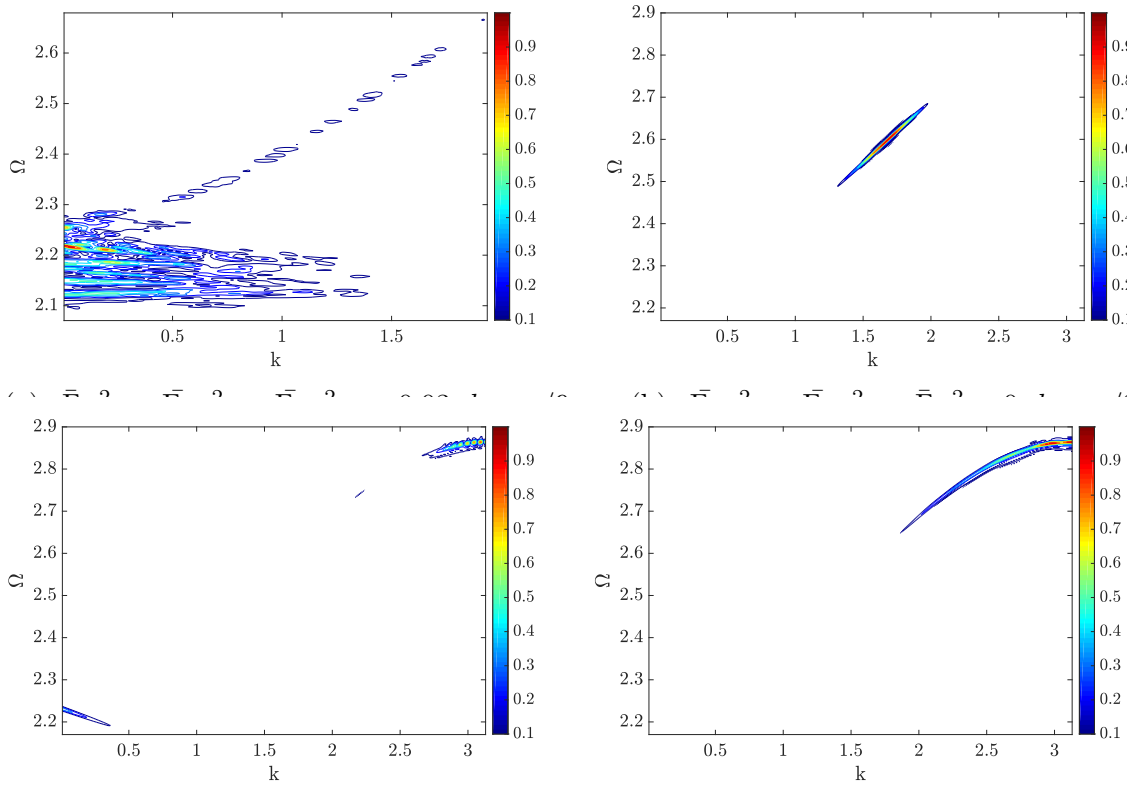
(c) $\epsilon\bar{\Gamma_2}\alpha^2 = \epsilon\bar{\Gamma_1}\alpha^2 = \epsilon\bar{\Gamma}\alpha^2 = -0.03$, $k = \pi/2$ (d) $\epsilon\bar{\Gamma_1}\alpha^2 = \epsilon\bar{\Gamma_2}\alpha^2 = \epsilon\bar{\Gamma}\alpha^2 = -0.03$, $k = 7\pi/9$

Figure 2.12: 2-D Fourier transform contour of the response for different types and sources of nonlinearities at frequencies in the upper branch of dispersion curve.

At short wavelength limit, the contour plots for the linear traveling wave is plotted in Fig. 2.11-(e). We can observe that the signal density is stretched over wide range of frequencies. Moreover, the power spectrum of this signal has a variable slope dispersion curve , hence suggesting that the wave is dispersive in this case [85]. However, the stretching of the dispersive wave becomes narrower and the signal tends to become localized when nonlinear hardening resonator is used as depicted in Fig. 2.11-(f). We can also observe that the presence of some low amplitude dispersive signals in the surrounding of the localized wave. These dispersive signals were also observed in Section. 4.1 for hardening nonlinearity in both the resonator and chain. It is obvious here that the localized signal represents a solitary wave since the power spectrum has a linear dispersion curve (constant slope) [85].

Finally, we demonstrate the concept of significant frequency shift by using softening chain and softening resonators at all wavelength limits (Fig. 2.12). In Fig. 2.12-(a), a significant frequency shift is observed at the long wavelength limit. This shift locates the dominant frequency component at frequencies much lower than the predicted frequencies in the linear case (see Fig.2.11-(a) for comparison). At medium wavlength limit, the frequency shift is more significant comparing to the other cases as shown in Fig. 2.12-(c). The original signal (Fig. 2.12-(b)) is completely distorted and shifted to frequencies in the maximum and minimum level of the upper dispersion curve. At short wavelength limit (Fig. 2.12-(d)), a frequency shift can also be observed. Although this shift is less significant comparing to other wavelength limits, the initial frequency bands is clearly shifted to the end of the dispersion curve. Furthermore, the dispersion curve tends to be more nonlinear, thus the wave is more dispersive [85]. The aforementioned frequency shifts reveal that a wider Pseudo-bandgap can be formed by using softening chain and softening resonators. This Pseudo-bandgap can be utilized for constructing acoustics diodes with wide range of operational frequencies.

2.5 Limitation of the approximate analytical solution by contour plots

After analyzing the spectro-spatial analysis of the wave propagating in a nonlinear meta-material and showing the possibility of predicting the nonlinear dispersion curves from the contour plots, we now study the limitations of the approximate analytical solution by increasing the strength of nonlinearity. This can be done by comparing the analytical results with their corresponding contour plots.

For the case of nonlinear chain, we compare our solution derived by the method of multiple scales to the dispersion curves obtained by the contour plots of the 2D-FTT of the numerical simulations for different strength of nonlinearity as shown in Fig. 2.13. This comparison is done in the short wavelength limit (in the upper optical branch of the dispersion curves) since this region is the most affected by nonlinearity as we showed in Sec. 3. For small value of nonlinearity ($\alpha^2 \epsilon \Gamma \leq 0.06$), our approximate analytical solution shows a good agreement with the contour plots of the numerical simulations as shown in Fig. 2.13-(a) and Fig. 2.13-(b). It can also be observed that the other wave with linear profile coincide with the linear dispersion curves. Increasing the nonlinearity further results in an additional weak nonlinear wave, which lies between the linear and nonlinear dispersion curves as shown in Fig. 2.13-(c)-Fig. 2.13-(f). The energy content in this wave increases with increasing nonlinearity. Yet, Fig. 2.13-(c)-Fig. 2.13-(e) indicate that our approximate analytical solution can still predict the upper boundaries of the dispersion curve for ($\alpha^2 \epsilon \Gamma \leq 0.015$). Beyond this value ($\alpha^2 \epsilon \Gamma \geq 0.15$), we observe that our approximate analytical solution fails to accurately predict the upper boundary of the dispersion curve as shown in Fig. 2.13-(f).

As for the case of nonlinear resonators, the comparison of the approximate solution and the 2D-FTT contour plot of the numerical simulation is shown in Fig. 2.14. Considering

(a) $\epsilon\bar{\Gamma}\alpha^2 = 0.03$, $k = \pi/9$

(b) $\epsilon\bar{\Gamma}\alpha^2 = 0.06$, $k = \pi/9$

(c) $\epsilon\bar{\Gamma}\alpha^2 = 0.09$, $k = \pi/9$

(d) $\epsilon\bar{\Gamma}\alpha^2 = 0.12$, $k = \pi/9$

(e) $\epsilon\bar{\Gamma}\alpha^2 = 0.15$, $k = \pi/9$

(f) $\epsilon\bar{\Gamma}\alpha^2 = 0.18$, $k = \pi/9$
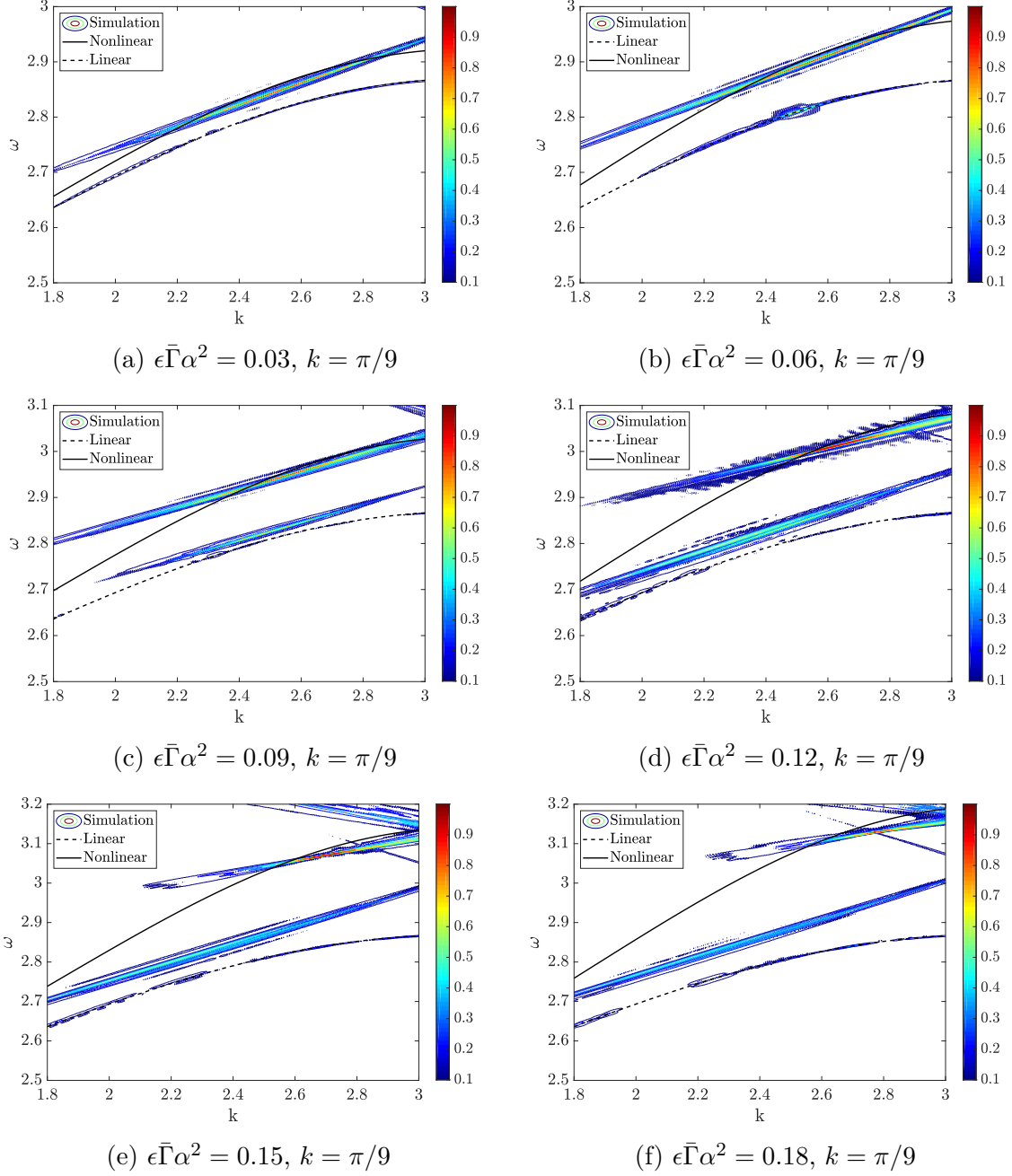
Figure 2.13: Comparison between approximate analytical solution and contour plots of 2D-FFT of the numerical simulations for nonlinear chain case.

frequencies closer to the nonlinear resonator frequency and focusing on the long wavelength limit, Fig. 2.14-(a) and Fig. 2.14-(b) show that our approximate analytical solution cannot

(a) $\epsilon\bar{\Gamma}_2\alpha^2 = 0.03$, $k = \pi/9$

(b) $\epsilon\bar{\Gamma}_2\alpha^2 = 0.06$, $k = \pi/9$

(c) $\epsilon\bar{\Gamma}_2\alpha^2 = 0.06$, $k = 7\pi/9$

(d) $\epsilon\bar{\Gamma}_2\alpha^2 = 0.15$, $k = 7\pi/9$
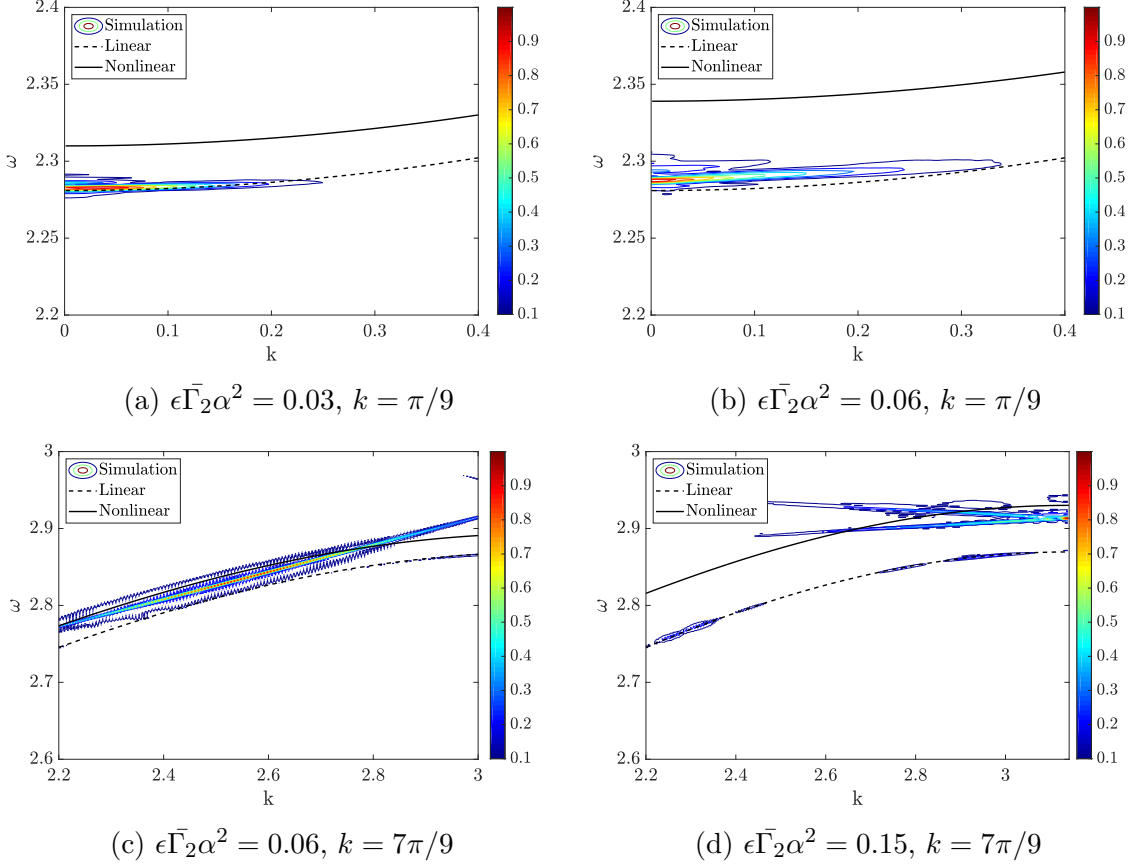
Figure 2.14: Comparison between approximate analytical solution and contour plots of 2D-FFT of the numerical simulations for nonlinear resonator case.

accurately predict the dispersion curve of the system even for small values of nonlinearity. However, when considering the region away from the nonlinear resonator frequency and focusing on the short wavelength limit, Fig. 2.14-(c) and Fig. 2.14-(d) demonstrate that our approximate analytical solution can accurately predict the nonlinear dispersion curve for small values of nonlinearity. This accuracy vanishes for larger value of nonlinearity ($\epsilon\bar{\Gamma}_2\alpha^2 \geq 0.15$).

2.6   Conclusion and Future Work

In this chapter, we investigated a nonlinear metamaterial consisting of a nonlinear chain with multiple nonlinear local resonators. Using the method of multiple scales, we obtained explicit expressions for the nonlinear dispersion relations for a nonlinear chain with multiple nonlinear resonators. These expressions were validated by numerical simulations and results in the literature. The validation indicated that our analytical solution can accurately predict the cut-off frequencies of the dispersion curves and the boundaries of the bandgaps. However, the analytical results failed to predict the behavior of the nonlinear system in region near the frequency of the nonlinear local resonator and the Pseudo-bandgap for wave packet input signal simulations. The Pseudo-bandgap has a unique feature since a significant frequency shift can be observed inside this zone. Nevertheless, analytical expressions can still reveal the wavelength zones affected by nonlinearity. The nonlinearity only affected the short wavelength limit for the case of nonlinear chain. However, for the case of nonlinear resonators, this nonlinear affected all wavelengths, particularly when the resonator was properly tuned. This observation was consistent with the topological analysis.

In the spectro-spatial analysis, the results showed the existence of solitary wave with hardening nonlinearity and dispersive wave with softening nonlinearity. This wave distortion cannot be observed at long wavelength limit in the nonlinear chain case. However, nonlinear local resonators stretch the wave in this zone with both type of nonlinearities. The amplitude of this dispersive wave was much higher with hardening nonlinearity. This wave distortion depends on the nonlinear resonator frequency and how close it is to the input wave frequency. These observations were also confirmed by spectrograms and contour plots of 2-D Fourier Transform. For different combinations of nonlinearities, the spectrograms demonstrated significant frequency shift in the medium wavelength limit when the chain and resonator have

both hardening nonlinearity. However, this frequency shift can be observed at all wavelength limits when we change the nonlinearity type to softening. Finally, the contour plots showed a wide Pseudo-bandgap demonstrating a significant frequency shift at all wavelength limits. the implication is that this Pseudo-bandgap can be utilized to design and construct acoustics diodes with wide range of operation frequencies. For future work, the authors plan to experimentally demonstrate the benefits of the revealed phenomena.

Chapter 3

Spectro-spatial wave features in nonlinear metamaterials: Theoretical and computational studies

Considerable attention has been given to nonlinear metamaterials because they offer some interesting phenomena such as solitons, frequency shifts, and tunable bandgaps. However, only little is known about the spectro-spatial properties of a wave propagating in nonlinear periodic chains, particularly, a cell with multiple nonlinear resonators. This problem is investigated here. Our study examines both hardening and softening nonlinearities in the chains and in the local resonators. Explicit expressions for the nonlinear dispersion relations are derived by the method of multiple scales. We validate our analytical results using numerical simulations. The numerical simulation is based on spectro-spatial analysis using signal processing techniques such as spatial-spectrogram and wave filtering. The spectro-spatial analysis provides detailed information about the interactions of dispersive and nonlinear phenomena of waveform in both short and long-wavelength domains. Furthermore, we val-

idate and demonstrate the theoretically obtained bandgaps, wave distortion, and birth of solitary waves through a computational study using finite element software, ANSYS. The findings, in both theoretical and computational analyses, suggest that nonlinear resonators can have more effect on the waveform than the nonlinear chains. This observation is valid in both short and long wavelength limits.

3.1   INTRODUCTION

Introducing unique dynamic properties artificially from engineering configurations and material constituent leads to promising materials with exceptional characteristics in different engineering applications. These materials, which are called metamaterials, have attracted many researchers because of their wider applications in different fields. They were first introduced in electromagnetic and optical wave propagation and later extended to mechanical waves applications[14, 84].

Mechanical metamaterials are often fabricated from periodic cells arranged carefully. The earliest study of periodic structure was in the 1900s [97, 98, 99, 159, 160, 178]. These structures form bandgaps due to Bragg scattering at wavelengths near their lattice constant. This enables, for example, vibration attenuation at low frequencies located inside the bandgap. However, the condition associated with Bragg scattering makes this application limited to large structures.

Attaching local resonators on the crystal allows a bandgap formation at wavelengths much larger than the lattice constant [110]. This enables the vibration control of small structures at low frequencies, thus widening the possible applications of metamaterials. Further investigation on the comparison between local resonator and Bragg scattering concepts can be found in [109]. Multiple bandgaps at different frequency ranges can also be developed by using multiple resonators with different parameters [78, 197].

Beyond vibration suppression, nonlinear metamaterials offer a wide pool of applications including gap solitons [95], dark solitons, envelope and dark solitons [131], wave non-reciprocity [107], and altering band structure limits [117].

Weakly nonlinear acoustics metamaterials were investigated analytically by using different perturbation techniques [134, 135]. For instance, Narisetti et al. [133], employed the Lindstedt-Poincare method in deriving the dispersion relations for nonlinear chain and vali-
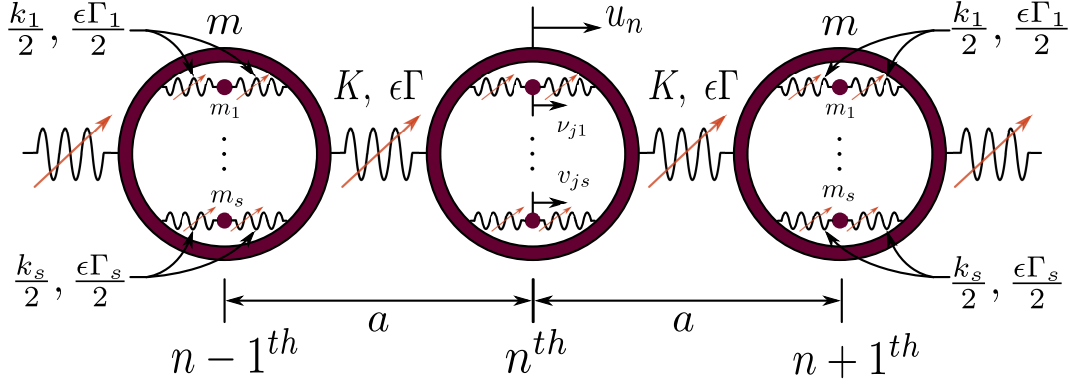
Figure 3.1: A schematic diagram for the nonlinear acoustics metamaterial

dated the results numerically. The method of multiple scales can deal with more complicated nonlinear systems like multiple waves interaction or nonlinear resonators [101, 119].

Early considerations of nonlinear continuum phononic media can be found in [85, 90]. Furthermore, enhancing the vibration attenuation performance can be realized using chains with two coupled nonlinear resonators [57, 186].

Wave non-reciprocity can be used in uni-directional acoustic wave propagation (e.g. acoustics diode). This can be obtained by coupling linear and nonlinear mediums [104, 106, 107], bifurcation in granular structures [16], or nonlinear hierarchical internal structures [129]. Moreover, an acoustic rectifier can be obtained by a cubic weakly nonlinear oscillator attached to a linear periodic lattice such that the operation frequencies of the rectifier coincide with the secondary resonances of the nonlinear oscillator [115].

Analyzing nonlinear metamaterials is often performed by tracking the change in the temporal state properties and discussing the existence of solitary waves, and dispersion characteristics. However, Ganesh and Gonella [63] have studied the spectro-spatial wave packet propagation features of nonlinear periodic chains by utilizing some signal processing tools. This allows detecting wave localization (birth of solitons), and reconstructing dispersion curves. However, although their analytical expressions could predict the shift in dispersion curves, many other nonlinear phenomena could not be inferred. Zhou et al. [195],

extended Ganesh and Gonella's work by including local linear resonators and studying the spectro-spatial wave features of nonlinear acoustic metamaterial. In both studies [63, 195], the effect of nonlinearity in the chain was limited to short wavelength region only. None of the studies included the nonlinearity in local resonators or determined how nonlinear resonators affect dispersion characteristics or propagation of solitary waves in both long and short-wavelength domains. None of the past works included the nonlinearity in the local resonators to study their effect on the wave propagation in both long and short-wavelength domains. The goal of the current study is to fill this knowledge gap by studying a nonlinear metamaterial consisting of nonlinear chains with multiple local resonators. The present study is performed using different analytical and computational techniques in order to show the ability of obtaining interesting nonlinear wave propagation phenomena at all wavelength limits.

Seeking a nonlinear system that offers interesting wave propagation phenomena in all wavelength regions, which is a rare find, we recently investigated the nonlinear vibration of a nonlinear chain with multiple nonlinear local resonators analytically and numerically [24, 27, 30?]. In order to validate the observed nonlinear wave propagation features, we extend our conference paper in [24] by reporting a thorough theoretical and computational studies. The nonlinearity is assumed to be weakly cubic type with softening or hardening nonlinear coefficients. In one case, we study the effect of nonlinearity attributed to the nonlinearity in the chain only. In another case, we examine the nonlinearity effect caused by the local resonator only. We employ the method of multiple scales to generate approximate close form expressions for the dispersion curves of a nonlinear (or linear) chain with any number of linear (or nonlinear) resonators. We follow this by numerical simulations of the metamaterial subjected to a wave packet input impulse. The results are used to check our analytical model in predicting the cut-off frequency. We then use multiple signal processing tools in order to investigate the spectro-spatial properties of the nonlinear acoustic metamaterial.

Furthermore, we study the effect of both hardening and softening nonlinearities in the chain and in the local resonators. Finally, we conduct a computational study using finite element software ANSYS to validated the bandgaps, birth of solitary waves, and other spectro-spatial properties. The findings suggest that very interesting dispersion characteristics and propagation of solitary wave can be realized in both long-wavelength and short-wavelength domains using nonlinear chain with multiple nonlinear local resonators. These interesting wave propagation characteristics can be employed to design superior vibration isolation and acoustic diode devices.

The remainder of the chapter is organized as follows. The next section describes the system of interest and presents explicit expressions for the nonlinear dispersion relations. The obtained analytical expressions are validated through direct numerical simulations and results from the literature. Spectro-spatial analysis is then carried out to explain the relation between topological/physical (space-time domain) and spectral domains. Finally, we present a computational study using ANSYS to further validate and demonstrate the interesting wave characteristics observed from the analytical and numerical results. Our findings are then summarized in the conclusion.

3.2 SYSTEM DESCRIPTION AND MATHEMATICAL MODELING

A schematic diagram for the acoustic metamaterial chain is depicted in Fig. 3.1. The chain consists of periodic cells. Each cell is represented by a mass, m, and it is connected to the other cells by a linear or nonlinear spring with linear coefficient, k, and nonlinear coefficient $\epsilon\Gamma$. There are s number of local resonators in each cell. The ith resonator consists of a mass, m_i and connected to the nth cell by a linear or nonlinear spring with linear coeficient, k_i,

and a nonlinear coefficient, $\epsilon\Gamma_i$. It is noteworthy here that the system is reduced to a linear system if $\epsilon = 0$.

The equations of motion for the nth cell can be expressed as follows [133, 195]

$$
\begin{aligned}
m\ddot{u}_n + K(2u_n - u_{n-1} - u_{n+1}) + \\
\epsilon\Gamma((u_n - u_{n-1})^3 + (u_n - u_{n+1})^3) + \\
\sum_{i=1}^{s} k_i(u_n - v_{ni}) + \sum_{i=1}^{s} \epsilon\Gamma_i(u_n - v_{ni})^3 = 0
\end{aligned}
\tag{3.1}
$$

$$
m_i\ddot{v}_{ni} + k_i(v_{ni} - u_n) + \epsilon\Gamma_i(v_{ni} - u_n)^3 = 0
\tag{3.2}
$$

For the case of nonlinear chain only, we set $\Gamma_i = 0$ while we set $\Gamma = 0$ in the case of nonlinear resonator only.

Eqns. (1)-(2) can be written in the non-dimensional form as

$$
\begin{aligned}
\ddot{u}_n + 2u_n - u_{n-1} - u_{n+1} + \epsilon\bar{\Gamma}((u_n - u_{n-1})^3 + \\
(u_n - u_{n+1})^3) + \sum_{i=1}^{s} \bar{k}_i(u_n - v_{ni}) + \sum_{i=1}^{s} \epsilon\bar{\Gamma}_i(u_n - v_{ni})^3 = 0
\end{aligned}
\tag{3.3}
$$

$$
\frac{\omega_n^2}{\omega_{di}^2}\ddot{v}_{ni} + (v_{ni} - u_n) + \epsilon\bar{\Gamma}_i(v_{ni} - u_n)^3 = 0
\tag{3.4}
$$

where the dots here denote the derivative in terms of the non-dimensional time $\tau = \omega_n t$, $\bar{\Gamma} = \frac{\Gamma}{\omega_n^2 m}$, $\bar{k}_i = \frac{k_i}{\omega_n^2 m}$, $\omega_n^2 = K/m$, and $\omega_{di}^2 = k_i/m_i$.

3.2.1 Approximate Analytical Solution by the Method of Multiple Scales

For weakly nonlinear systems like the one presented in Eqns. (3)-(4), perturbation techniques can be employed to obtain approximate analytical solution of the dispersion curves. Here we use the method of multiple scales to present explicit expressions for the dispersion relations. The method of multiple scales is advantageous over other techniques due to the simplicity of handling and collecting the secular terms in multiple equations or complicated systems. The approximate solution can be represented up to second order approximation as [135]

$$u_n(t, \epsilon) = u_{n0}(T_0, T_1) + \epsilon u_{n1}(T_0, T_1) \tag{3.5}$$

$$v_{ni}(t, \epsilon) = v_{ni0}(T_0, T_1) + \epsilon v_{ni1}(T_0, T_1) \tag{3.6}$$

where $T_0 = \tau$ is the fast time scale and $T_1 = \epsilon \tau$ is the slow time scale. The system can now be represented by two independent variables (scales) and applying the full derivative is not valid any more. Instead, we can represent the time derivative by the chain rule as

$$(\ddot{\ }) = D_0^2 + 2\epsilon D_0 D_1 + ... \tag{3.7}$$

where $D_n = \frac{\partial}{\partial T_n}$.

Using Bloch theory for infinite periodic medium [?] (also known as Floquet theory for 1-dimensional medium [?]), the solution of the linear system can be expressed as

$$u_n = A e^{j(n\bar{k} - \omega T_0)} + c.c \tag{3.8}$$

$$v_{ni} = B_i e^{j(n\bar{k} - \omega T_0)} + c.c \tag{3.9}$$

where $\bar{k} = aq$ is the nondimensional wavenumber, and $c.c$ is the complex conjugate. For convenience, we drop the bar from $\bar{k}$ in the subsequent analysis since the linear stiffness of the chain k does not appear any more in the normalized parameters.

Substituting Eqns. (5)-(7) into Eqns. (3)-(4), collecting the coefficients of $\epsilon^0 \& \epsilon$, and then substituting Eqns. (8)-(9), one can write the linear dispersion relation for all cases of nonlinearity as

$$-\omega^2 + (2 - 2\cos k) + \sum_{i=1}^{s} \bar{k}_i (1 - K_{\omega i}) = 0 \tag{3.10}$$

where $K_{\omega i} = \frac{1}{1 - \omega_n^2 \omega^2 / \omega_{di}^2}$. To derive the nonlinear solution, the vibration amplitude should be written in the polar form as

$$A = \frac{1}{2}\alpha e^{i\beta} \tag{3.11}$$

Solving for the amplitude α, reveals that $\alpha = \alpha_0$, where α_0 is a constant, for both cases of nonlinearity. The phase can be written for each case as [30?]

- Nonlinear chain $\bar{\Gamma} \neq 0$

$$\beta = -\frac{3\bar{\Gamma}\alpha^2(1 - \cos k)^2}{2\omega(1 + \sum_{i=0}^{s} \frac{\bar{k}_i \omega_n^2 / \omega_{di}^2}{1 - \omega_n^2 \omega^2 / \omega_{di}^2} K_{\omega i})} T_1 \tag{3.12}$$

- Nonlinear resonator $\bar{\Gamma}_i \neq 0$

$$\beta = -\frac{\sum_{i=1}^{s} [\frac{3}{8}\alpha^2(1 - K_{\omega i})^3 \bar{\Gamma}_i (\frac{\bar{k}_i}{1 - \omega_n^2 \omega^2 / \omega_{di}^2} - 1)]}{\omega(1 + \sum_{i=1}^{s} \frac{\bar{k}_i \omega_n^2 / \omega_{di}}{1 - \omega_n^2 \omega^2 / \omega_{di}^2} K_{\omega i})} T_1 \tag{3.13}$$

Therefore, the nonlinear dispersion curves can be written as

$$\omega_{nl} = \omega + \epsilon\beta' \tag{3.14}$$

where β' is the derivative in terms of the slow time scale.

From Eqn. (12), it can be observed that the nonlinear frequency in the nonlinear chain case is a function of wavenumber. In fact, the correction factor $\beta \sim 0$ when k is very small and hence the effect of chain nonlinearity (β) is negligible for long wavelength limit $(k \sim 0)$ at both acoustic and optical modes. On the other hand, for the case of the nonlinear resonator (Eqn. (13)), the wavenumber does not explicitly appear in the expression of the correction factor and hence the only wavenumber dependence in this case is through the linear dispersion relation (i.e. Eqn. (10)). Also note the appearance of a new term $(1 - K_{\omega i})^3$ in the numerator of Eqn. (13), which can have a significant effect on the correction factor β and hence on the nonlinear frequency when the resonator is tuned to the excitation frequency regardless of the wavenumber. It is noteworthy here that the derived expression for, β in Eqn. (13), is correct and different from that obtained in [117], since the latter omitted the contribution of the resonators on the left hand side from the equations at order ϵ [119, 133] (for more information refer to [118]).

3.3   VALIDATING ANALYTICAL RESULTS

To validate the dispersion relations obtained by the method of multiple scale, we compare the current results with those obtained in the literature for a nonlinear chain single linear resonator system obtained by Lindstedt-Poincare methods and with those obtained numerically. For this part, we select $\omega_n = \omega_{d1} = 1000$ rad/sec, $\bar{k}_i = 1$, $s = 1$, $\epsilon\bar{\Gamma}\alpha^2 = 0.06$, and $\epsilon\bar{\Gamma}_i\alpha^2 = 0$.
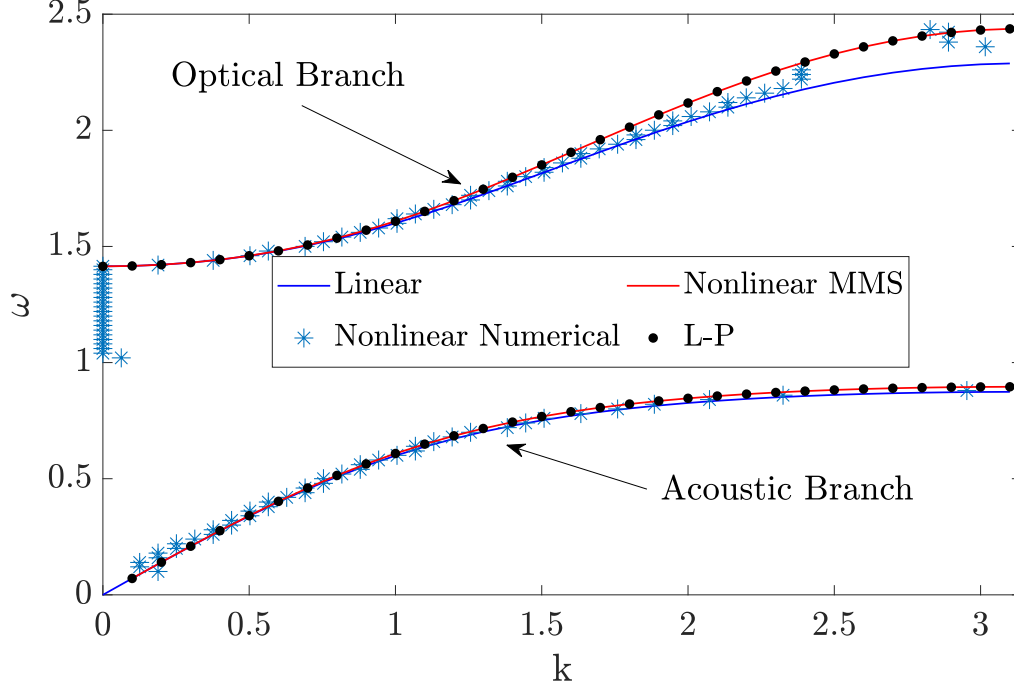
Figure 3.2: Validating the results of nonlinear chain with single linear resonator, $\epsilon \bar{\Gamma} \alpha^2 = 0.06$, $\epsilon \bar{\Gamma}_1 \alpha^2 = 0$.

For numerical simulations, we simulate a chain consisting of 500 cells and attached to it s number of resonators (e.g. $s = 1$ in the first part of the validation, then we set $s = 2$). The boundaries of the chain are assumed to be a perfectly matched layer (PML) in order to absorb and dissipate incoming waves, as well as, to minimize wave reflections at each end [133]. The system is excited by a transient wave packets signal at different wavenumbers. The velocity of the wave packet is selected to limit the motion of the signal in one direction and suppress any waves traveling in the opposite direction [63]. The numerical integration is carried out using MATLAB built in integrator ODE45 (Runge-Kutta). After running the simulation at a specific wavenumber, 2-D Fast Fourier Transform is applied on the displacement matrix and the frequency and wavenumber corresponding to the maximum amplitude value are collected. These values represent the point in the dispersion curve corresponding to the wavenumber of excitation signal [119]. The wavenumber is then swept to reconstruct other
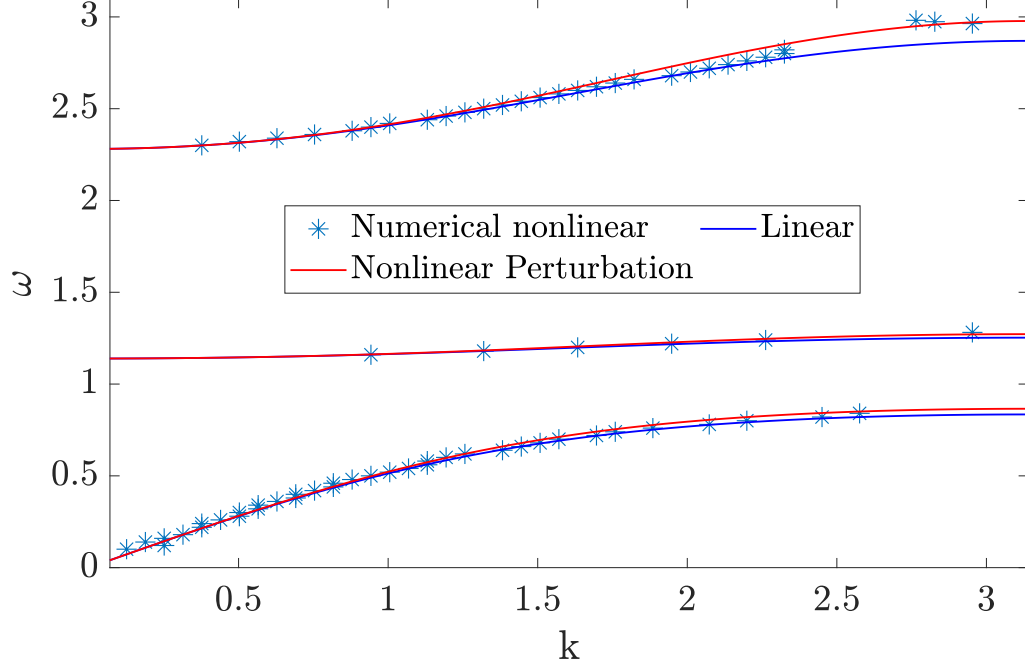
Figure 3.3: Validating the results of nonlinear chain with two linear resonators, $\epsilon \bar{\Gamma} \alpha^2 = 0.06$, $\epsilon \bar{\Gamma}_1 \alpha^2 = \epsilon \bar{\Gamma}_2 \alpha^2 = 0$.

points in the dispersion curves. These wave packets excitation can be defined as:

$$u_m(0) = \frac{1}{2}(H(m-1) - H(m-1-N_{cy}2\pi/k))(1- \tag{3.15}$$

$$\cos(mk/N_{cy}))\sin(mk)$$

$$\dot{u}_m(0) = \frac{1}{2}(H(m-1) - H(m-1-N_{cy}2\pi/k))$$

$$(-\omega_n\omega/N_{cy}\sin(mk/N_{cy})\sin(mk) - \omega_n\omega(1- \tag{3.16}$$

$$\cos(mk/N_{cy}))\cos(mk))$$

$$v_{mi}(0) = K_{\omega i}u_m(0) \tag{3.17}$$

$$\dot{v}_{mi}(0) = K_{\omega i}\dot{u}_m(0) \tag{3.18}$$

where $H(x)$ is the heaviside function and N_{cy} is the cycles number and set in the current
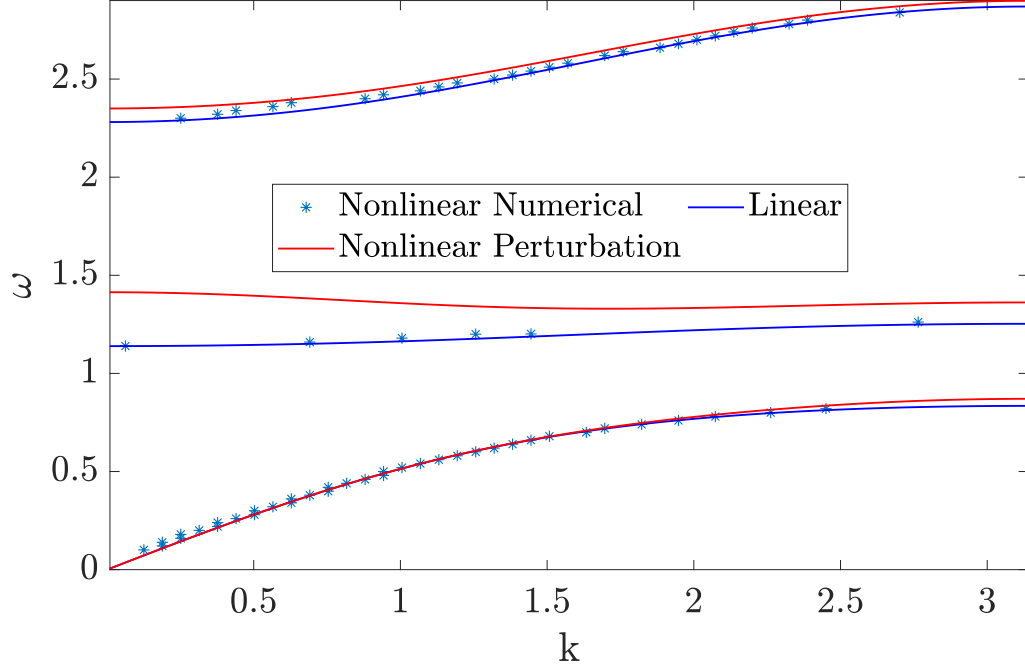
Figure 3.4: Validating the results of linear chain with two nonlinear resonators, $\epsilon\bar{\Gamma}\alpha^2 = 0$, $\epsilon\bar{\Gamma}_1\alpha^2 = 0.06$, $\epsilon\bar{\Gamma}_2\alpha^2 = 0$.

study to $N_{cy} = 7$.

Fig. 3.2 presents a comparison between our results, the literature results, and the numerical results. Our multiple scales results show very good agreement for the case of nonlinear chain with single linear resonator.

For the case of nonlinear chain with multiple linear resonators, we validate our analytical results using numerical simulation only since the literature lacks simulations for similar nonlinear systems. The results are shown in Fig. 3.3 for the case of two resonators where $\omega_{d1} = \omega_n$ and $\omega_{d2} = 1.5\omega_n$. The results show that the method of multiple scales can accurately predict, in general, dispersion curves and the trend of this type of nonlinearity. However, it fails to predict any other nonlinear dynamics phenomena such as solitons and the presence of secondary resonances as we will show in the following sections.
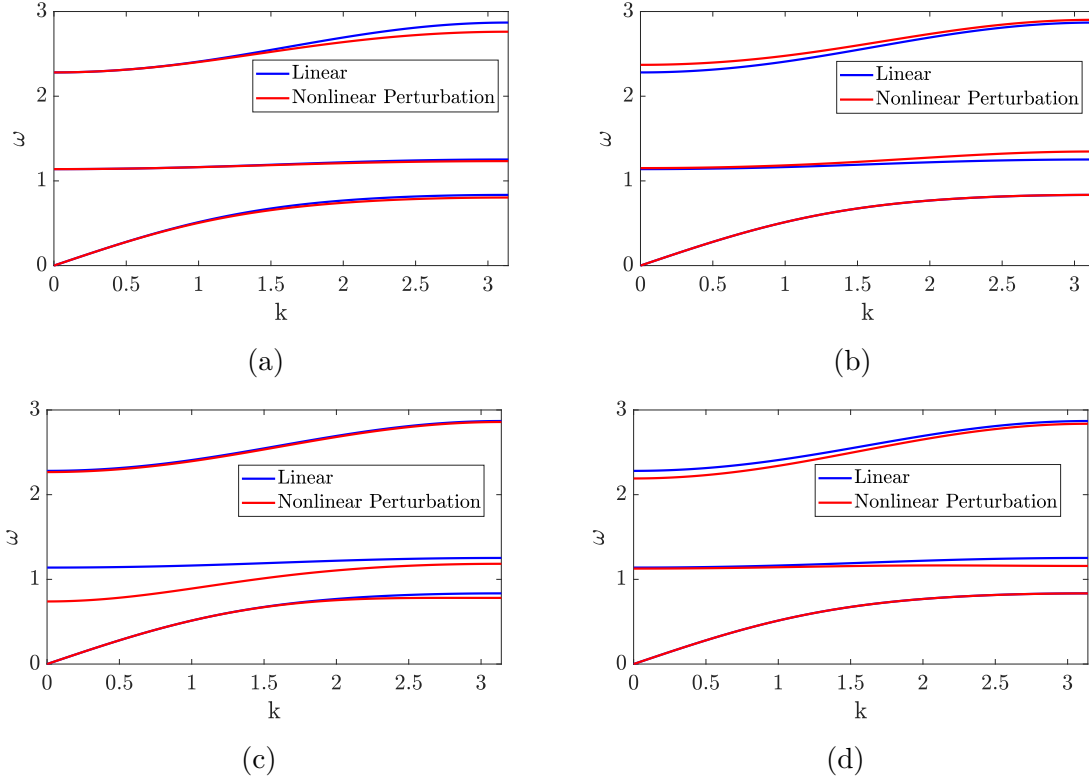
Figure 3.5: Analytical dispersion curves for acoustics metamaterial and two local resonators with different types and sources of nonlinearities: (a) Softening chain nonlinearity $\epsilon\bar{\Gamma}\alpha^2 = -0.06$, $\epsilon\bar{\Gamma}_1\alpha^2 = \epsilon\bar{\Gamma}_2\alpha^2 = 0$; (b) Hardening resonator nonlinearity $\epsilon\bar{\Gamma}_2\alpha^2 = 0.06$, $\epsilon\bar{\Gamma}_1\alpha^2 = \epsilon\bar{\Gamma}\alpha^2 = 0$; (c) Softening resonator nonlinearity $\epsilon\bar{\Gamma}_1\alpha^2 = -0.06$, $\bar{\Gamma}\alpha^2 = \epsilon\bar{\Gamma}_2\alpha^2 = 0$; (d) Softening resonator nonlinearity $\epsilon\bar{\Gamma}_2\alpha^2 = -0.06$, $\epsilon\bar{\Gamma}_1\alpha^2 = \epsilon\bar{\Gamma}\alpha^2 = 0$.

Furthermore, the numerical and analytical results of the nonlinear resonator are plotted in Fig. 3.4. We can observe that the method of multiple scales is a good predictor of the upper and lower branches of the dispersion curve, but a poor predictor of the middle branch when the natural frequency of the system is $\omega_{d1} = \omega_n$. Therefore, this region should be handled by a different approach.
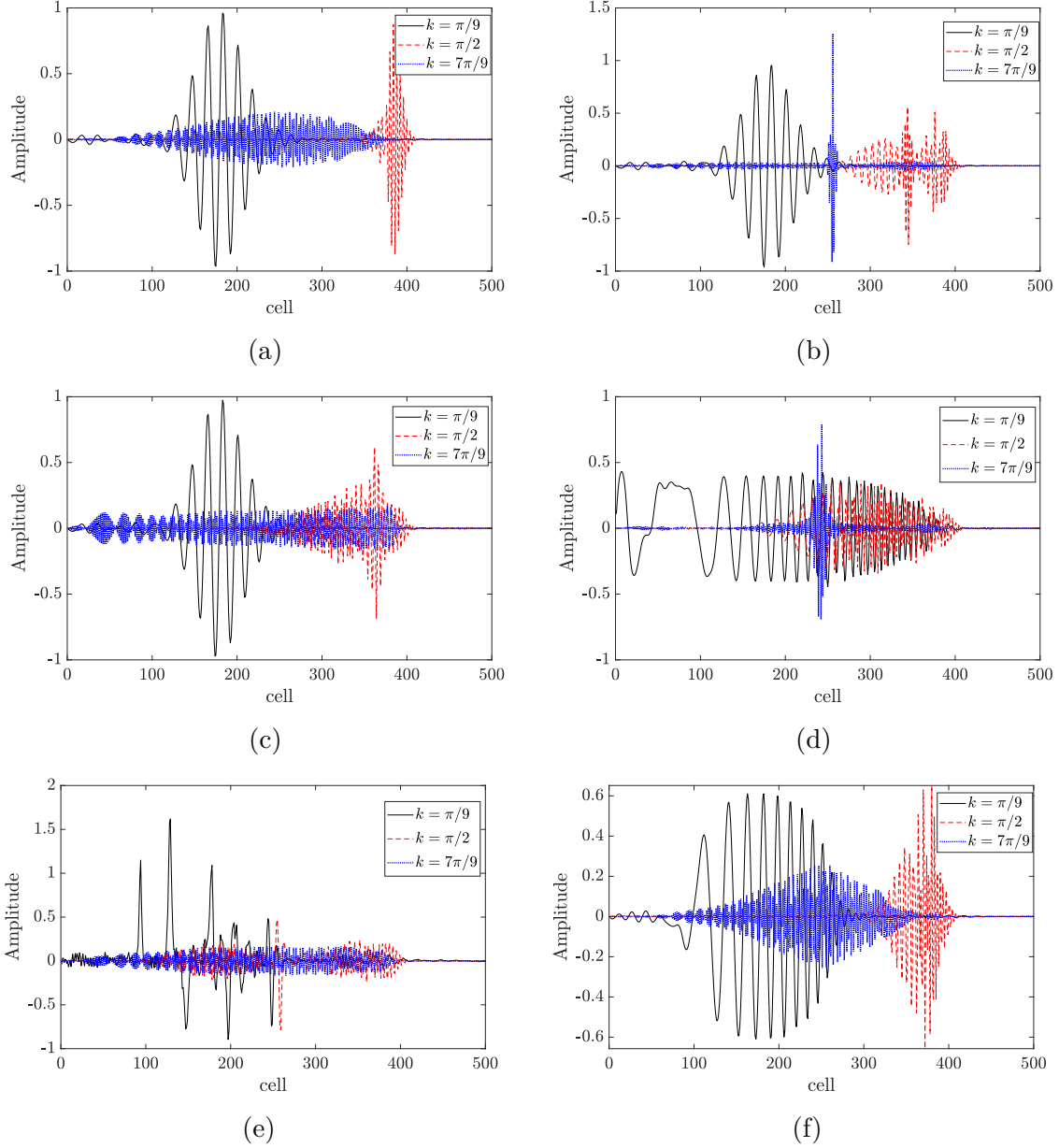
Figure 3.6: Spatial profile of the wave packet for different types and sources of nonlinearities at frequencies in the upper branch of dispersion curve: (a) Linear chain $\epsilon\bar{\Gamma}\alpha^2 = \epsilon\bar{\Gamma}_1\alpha^2 = \epsilon\bar{\Gamma}_2\alpha^2 = 0$; (b) Hardening chain nonlinearity $\epsilon\bar{\Gamma}\alpha^2 = 0.03$, $\epsilon\bar{\Gamma}_1\alpha^2 = \epsilon\bar{\Gamma}_2\alpha^2 = 0$; (c) Softening chain nonlinearity $\epsilon\bar{\Gamma}\alpha^2 = -0.03$, $\epsilon\bar{\Gamma}_1\alpha^2 = \epsilon\bar{\Gamma}_2\alpha^2 = 0$; (d) Hardening resonator nonlinearity $\epsilon\bar{\Gamma}_2\alpha^2 = 0.03$, $\epsilon\bar{\Gamma}_1\alpha^2 = \epsilon\bar{\Gamma}\alpha^2 = 0$; (e) Softening resonator nonlinearity $\epsilon\bar{\Gamma}_2\alpha^2 = -0.03$, $\epsilon\bar{\Gamma}_1\alpha^2 = \epsilon\bar{\Gamma}\alpha^2 = 0$; (f) Hardening resonator nonlinearity $\epsilon\bar{\Gamma}_1\alpha^2 = 0.03$, $\epsilon\bar{\Gamma}_2\alpha^2 = \epsilon\bar{\Gamma}\alpha^2 = 0$.

Figure 3.7: Spatial spectrograms of the wave packet for different types and sources of nonlinearities at frequencies in the upper branch of dispersion curve: (a) Hardening chain nonlinearity $\epsilon\bar{\Gamma}\alpha^2 = 0.03$, $\epsilon\bar{\Gamma}_1\alpha^2 = \epsilon\bar{\Gamma}_2\alpha^2 = 0$, $k = \pi/9$; (b) Hardening resonator nonlinearity $\epsilon\bar{\Gamma}_2\alpha^2 = 0.03$, $\epsilon\bar{\Gamma}_1\alpha^2 = \epsilon\bar{\Gamma}\alpha^2 = 0$, $k = \pi/9$; (c) Softening resonator nonlinearity $\epsilon\bar{\Gamma}_2\alpha^2 = -0.03$, $\epsilon\bar{\Gamma}_1\alpha^2 = \epsilon\bar{\Gamma}\alpha^2 = 0$, $k = \pi/9$; (d) Hardening resonator nonlinearity $\epsilon\bar{\Gamma}_1\alpha^2 = 0.03$, $\epsilon\bar{\Gamma}_2\alpha^2 = \epsilon\bar{\Gamma}\alpha^2 = 0$, $k = \pi/9$; (e) Hardening resonator nonlinearity $\epsilon\bar{\Gamma}_2\alpha^2 = 0.03$, $\epsilon\bar{\Gamma}_1\alpha^2 = \epsilon\bar{\Gamma}\alpha^2 = 0$, $k = 7\pi/9$; (f) Hardening resonator nonlinearity $\epsilon\bar{\Gamma}_1\alpha^2 = 0.03$, $\epsilon\bar{\Gamma}_2\alpha^2 = \epsilon\bar{\Gamma}\alpha^2 = 0$, $k = 7\pi/9$.

3.4   THE EFFECT OF DIFFERENT TYPES OF NON-
LINEARITIES ON THE BANDGAP BOUNDARIES

After checking the obtained solution for each case, we examine the effect of nonlinearity on the wave propagation in various wavelength regions. In addition to Figs. 3.3-3.4, we present the analytical dispersion curves for different kind and source of nonlinearities in Fig. 3.5.

We can observe from Fig. 3.3 and Fig. 3.5.(a) that the nonlinear chain affects mainly the short wavelength region ($k \sim \pi$). The effect of nonlinearity in the long wavelength region ($k \sim 0$) is almost negligible; however, a significant shift of the dispersion curves is observed at high wavenumbers. On the other hand, Fig. 3.4 and Figs. 3.5.(b)-(d) show that systems with nonlinear resonators have significant impact on the dispersion curves in the long wavelength region.

Moreover, it is demonstrated that the effect of nonlinear resonators becomes more pronounced at frequencies near the resonator frequency. For instance, in Fig. 3.4 and Fig. 3.5.(c), a significant shift occurs near the resonance frequency of the nonlinear resonators $\omega_{d1} = \omega_n$. However, making the second resonators $\omega_{d2} = 1.5\omega_n$ nonlinear, shifts the effect of nonlinearity to other frequency regions.

It is also demonstrated that tuning the bandgap can be done by changing the type of nonlinearity. In Fig. 3.5.(a) and Figs. 3.5.(c)-(d), softening nonlinearity shifts the dispersion curves lower, thus increasing the size of the bandgap. On the other hand, hardening nonlinearity shifts the dispersion curves up as shown in Figs. 3.3-3.4 and Fig. 3.5.(b).

3.5 SPECTRO-SPATIAL ANALYSIS

Although the cut-off frequencies can be predicted by the method of multiple scales, other nonlinear wave propagation features cannot be characterized. This merits the use of spectro-spatial analysis to characterize the wave propagation in the proposed metamaterial. It should be noted that all the following simulations are based on the optical branch because this branch is more affected by nonlinearity than the acoustic branch. Also the numerical simulation for the optical mode is much faster. Moreover, Figs. 3.6-3.7 are plotted at the end of the numerical simulations. The numerical simulations lasted for $t = 8$ sec.

The spatial profile of the wave packet is depicted in Fig. 3.6 for different types of nonlinearities. For the linear case (Fig. 3.6 (a)), the output profile of the long wavelength limit is a mirror image of the input signal profile. However, increasing the wavenumber gradually turns the input wave into a dispersive wave (i.e, the output wave get stretched over the chain and the wave amplitude becomes smaller). In addition, we observe that the nonlinear chain gives rise to travelling localized wave (i.e. solitary waves) with increasing wavenumber when the nonlinearity is hardening (Fig. 3.6.(b)) and wave dispersive (i.e., the wave is stretched over the chain) when the nonlinearity is softening (Fig. 3.6.(c)). This can be explained by the change in the dispersion curve slope (i.e., see discussions on Fig. 3.8). For instance, hardening nonlinear chain has a fixed linear slope instead of a variable slope in the dispersion curve. This is an indication of solitary (localized) waves [85]. On the other hand, Figs. 3.6.(a)-(c) indicate that nonlinear hardening chain has no effect on the wave profile in long wavelength region for both types of nonlinearities (i.e., the input signal has the same profile as the output signal at long wave length region). The opposite is observed in Figs. 3.6.(d)-(f) when the system is changed to linear chains with nonlinear local resonators. It is evident that the wave profile is distorted in all wavelength domains unlike the nonlinear chain case. In Fig. 3.6.(d), a hardening resonator exhibits dispersive

wave at long wavelength and travelling localized wave at short wavelength. On the other
hand, a softening resonator shows an interesting behavior at long wavelength limit since
the wave profile has travelling localized and dispersive components. However, the travelling
localized component vanishes with reducing wavelength (i.e. increasing wavenumber) as
shown in Fig. 3.6.(e). Therefore, unlike the case of nonlinear chain, wave distortion can be
obtained at all wavelength limits in the case of nonlinear resonator. This effect of resonator
nonlinearity depends significantly on the frequency of the nonlinear resonator. For example,
tuning the nonlinear resonator away from the upper dispersion curve results in significant
reduction in the effect of nonlinear wave propagation phenomena, specifically, in the short
wavelength region as shown in Fig. 3.6.(d). It is noteworthy that, albeit the analytical
dispersion curves fail to predict the cut-off frequency and other important wave propagation
features, they accurately predict how the nonlinearities in both the chains and resonators
affect the wave propagation across all wavelength domains. In that, their predictions about
the effect of nonlinearities agree with the spatial profile plots. For example, both Fig. 3.3
and Fig. 3.6.(b) show hardening chains to have no effect in long-wavelength domain and
significant effect in short wavelength domain.

Fig. 3.7 shows the spectrograms of the wave propagating through the metamaterial in
both short and long-wavelengths. As we observed before, the nonlinear chain has no effect on
the structure in the long wavelength limit. This is clearly shown in Fig. 3.7.(a), the output
wave profile is exactly the same as the input signal. However, as shown in Figs. 3.7.(b)-
(c), a significant distortion (i.e., the output wave is split into multiple components and/or
there are other forms of deformation resulting from resonator and chain nonlinearity) to the
input signal is observed when we change the nonlinearity from chain to local resonator. The
signal becomes clearly dispersive (i.e, the output wave get stretched over the chain) along
the chain with significant equal amplitude when the nonlinearity is hardening as shown in
Fig. 3.7.(b). When the nonlinearity is of softening type, we observe multiple localized signals,

as well as, dispersive components (Fig. 3.7.(c)). The dispersive components are generated at a wide range of wavenumbers outside the initial signal wavenumber content. In the short wavelength region, the effect of nonlinear resonator is similar to that of nonlinear chain: the output signal is localized unlike in the linear case where the signal at this limit is completely dispersive. As we will show in the below discussions, this indicates that soliton formation is also possible in the case of nonlinear resonator as shown in Fig. 3.7.(e). In Fig. 3.7.(d) and Fig. 3.7.(f), it is observed that a nonlinear resonator with frequency away from the excitation frequency has less effect on the wave profile, specifically in the short wavelength limit where it is completely linear. Therefore, a properly tuned nonlinear resonator can distort the output wave at all wavelength limits. The output signal appears at frequencies different than the input frequency. This indicates that nonlinear resonators can be utilized in designing acoustics diodes that can be operated at all wavelength limits.

Furthermore, we present the effect of nonlinear resonators in the image of 2-D fast Fourier transform depicted in Fig. 3.8. The linear signal is similar to the nonlinear signal as shown in Fig. 3.8.(a), thus confirming that the nonlinear chain has no effect in this limit. In Fig. 3.8.(b)-(c), the nonlinear resonator shows a wider distribution of the signal along both the frequency and wavenumber ranges in the long wavelength limit for both types of nonlinearity. This observation suggests that such nonlinear acoustic metamaterial can be suitable for applications such as acoustic diode. Fig. 3.8.(e) demonstrates that the nonlinear resonator is also effective in the short wavelength limit since it localizes the signal and stretches it over a wider region. Moreover, the results indicate that the energy content is concentrated in fixed slope dispersion curve unlike the case of linear chain. This is an indication that solitary localized waves can be observed at this wavelength limit with properly tuned hardening resonators. However, it is also demonstrated in Fig. 3.8.(d) and Fig. 3.8.(f) that the effect of nonlinear resonator vanishes when it is not tuned carefully. Overall, both spec-

tral (wavenumber-frequency domain) and topological/physical (space-time domain) analyses provide good insight about the nonlinear effect on wave propagation across all wavelength regions. But only the topological analysis can provide detail information about the physical features of wave propagation such as solitons formation.

Finally, we check the limitation of our analytical solution in weakly nonlinear systems for nonlinearity in the chain and the resonator. In Fig. 3.9, we plot the analytical solution for the linear and nonlinear dispersion curves against the images of 2D FFT for the numerical simulations. For the nonlinear chain case, our solution shows a good agreement with the numerical results for small value of nonlinearity ($\epsilon \bar{\Gamma} \leq 0.06$) as shown in Fig. 3.9 (a). The figure also indicates that the solitary nonlinear component with high energy content (shown in Fig. 3.8 (e)) coincides with the nonlinear dispersion curve while the linear component with low energy content coincides with the linear dispersion curves. Increasing the nonlinearity further ($\epsilon \bar{\Gamma} \geq 0.06$) gives rise to a new component between the linear and nonlinear dispersion curves in addition to the previously observed linear and nonlinear components. Nevertheless, the nonlinear component still coincides with the nonlinear dispersion curves, which indicates that the analytical solution is still accurate in terms of the bandgap boundaries. This new component has a fixed slope with energy content lower than the energy content of the main nonlinear component. Yet its energy content increases with increasing nonlinearity. However, for values beyond ($\epsilon \bar{\Gamma} \geq 0.15$), a discrepancy between the analytical and numerical solutions can be observed although the main numerical nonlinear component is still closer to the analytical nonlinear dispersion curve than the linear dispersion curves as shown in Fig. 3.9 (c). Moreover, the new component is more dominant and has higher energy content due to the increase of nonlinearity. For the nonlinear resonator case, Fig. 3.9 (d) demonstrates that the analytical solution fails to predict the nonlinear dispersion curve at frequencies close to the nonlinear resonator frequency and the numerical results completely
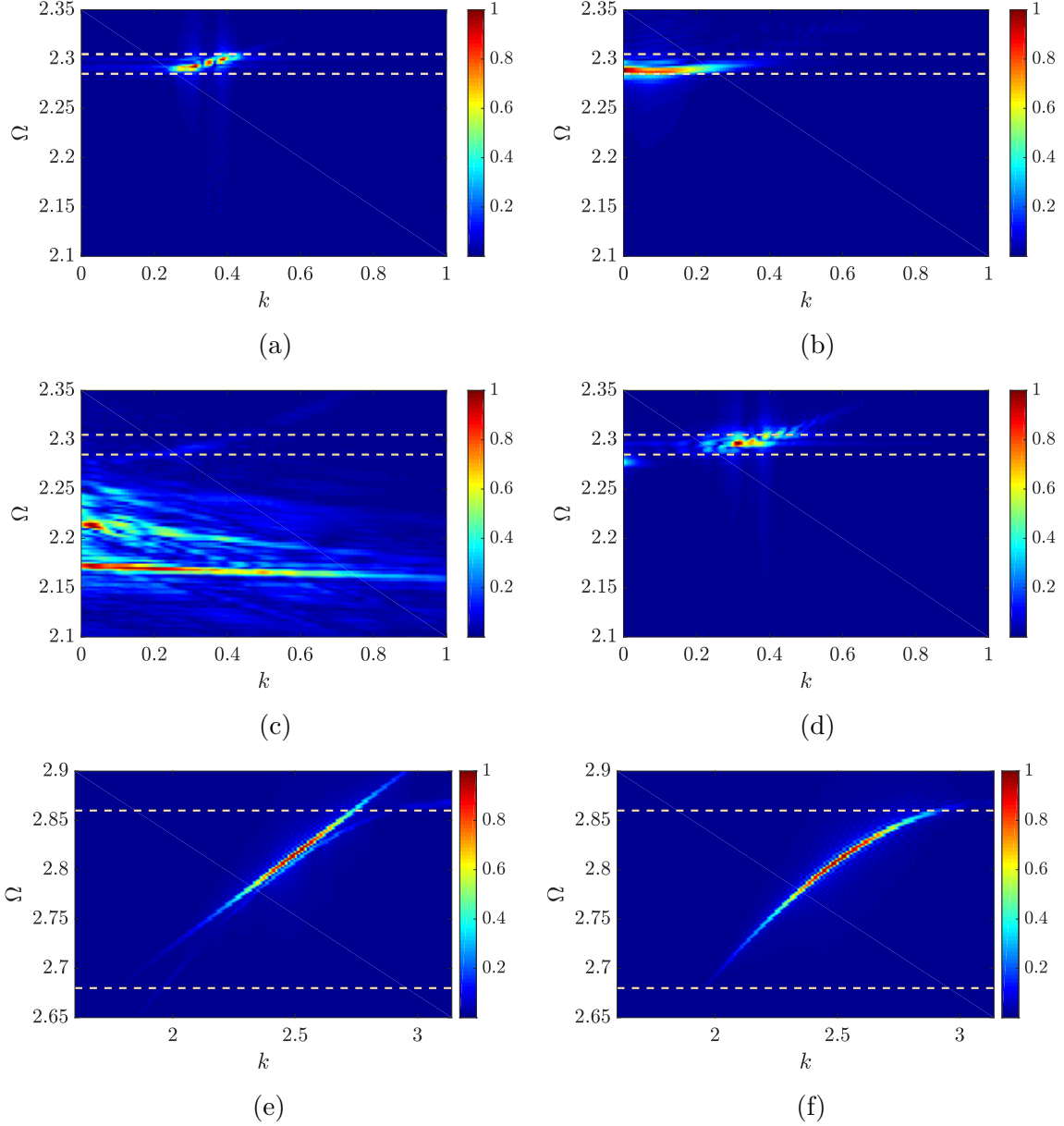
Figure 3.8: 2-D Fourier transform of the response for different types and sources of nonlinearities at frequencies in the upper branch of dispersion curve: (a) Hardening chain nonlinearity $\epsilon\bar{\Gamma}\alpha^2 = 0.03$, $\epsilon\bar{\Gamma}_1\alpha^2 = \epsilon\bar{\Gamma}_2\alpha^2 = 0$, $k = \pi/9$; (b) Hardening resonator nonlinearity $\epsilon\bar{\Gamma}_2\alpha^2 = 0.03$, $\epsilon\bar{\Gamma}_1\alpha^2 = \epsilon\bar{\Gamma}\alpha^2 = 0$, $k = \pi/9$; (c) Softening resonator nonlinearity $\epsilon\bar{\Gamma}_2\alpha^2 = -0.03$, $\epsilon\bar{\Gamma}_1\alpha^2 = \epsilon\bar{\Gamma}\alpha^2 = 0$, $k = \pi/9$; (d) Hardening resonator nonlinearity $\epsilon\bar{\Gamma}_1\alpha^2 = 0.03$, $\epsilon\bar{\Gamma}_2\alpha^2 = \epsilon\bar{\Gamma}\alpha^2 = 0$, $k = \pi/9$; (e) Hardening resonator nonlinearity $\epsilon\bar{\Gamma}_2\alpha^2 = 0.03$, $\epsilon\bar{\Gamma}_1\alpha^2 = \epsilon\bar{\Gamma}\alpha^2 = 0$, $k = 7\pi/9$; (f) Hardening resonator nonlinearity $\epsilon\bar{\Gamma}_1\alpha^2 = 0.03$, $\epsilon\bar{\Gamma}_2\alpha^2 = \epsilon\bar{\Gamma}\alpha^2 = 0$, $k = 7\pi/9$. Dashed lines represents linear frequency bands.

coincide with the analytical linear dispersion curve instead of the nonlinear dispersion curve. However, at frequencies away from the nonlinear resonator frequency, the analytical solution can accurately predict the numerical results for small values of nonlinearity ($\epsilon\bar{\Gamma} < 0.15$) as shown in Fig. 3.9 (e). Beyond that both solutions start departing from each other as shown in Fig. 3.9 (f) and the analytical solution does not predict the actual dispersion curves accurately.

3.6   COMPUTATIONAL STUDY USING ANSYS APDL

In order to further validate and demonstrate the analytical bandgaps and the interesting nonlinear wave propagation phenomena obtained by the theoretical analysis, we conduct a computational study using finite element software, ANSYS. This computational analysis is based on a long nonlinear chain with linear resonator, as well as, a long linear chain with nonlinear resonator.

The geometry of the metamaterials is first created by a group of nodes and elements in the preprocessor section of ANSYS Parametric Design Language (APDL). The number of nodes is equal to the number of cells. Three types of elements are defined as: COMBIN14 for the stiffness of the linear spring, MASS21 for the mass of the chain and resonator, and COMBIN39 for the stiffness of the nonlinear spring. The values of the linear spring and mass are assigned to their elements by command "R". For the nonlinear spring (in the nonlinear chain or the nonlinear resonator cases), we define the weak nonlinearity by a force-displacement curve. These values were then assigned to the element COMBIN39 by command "R".

Each rigid chain and resonator is created by one node using commands "N" and "*RE-PEAT". Next, element MASS21 is assigned to its corresponding node using commands
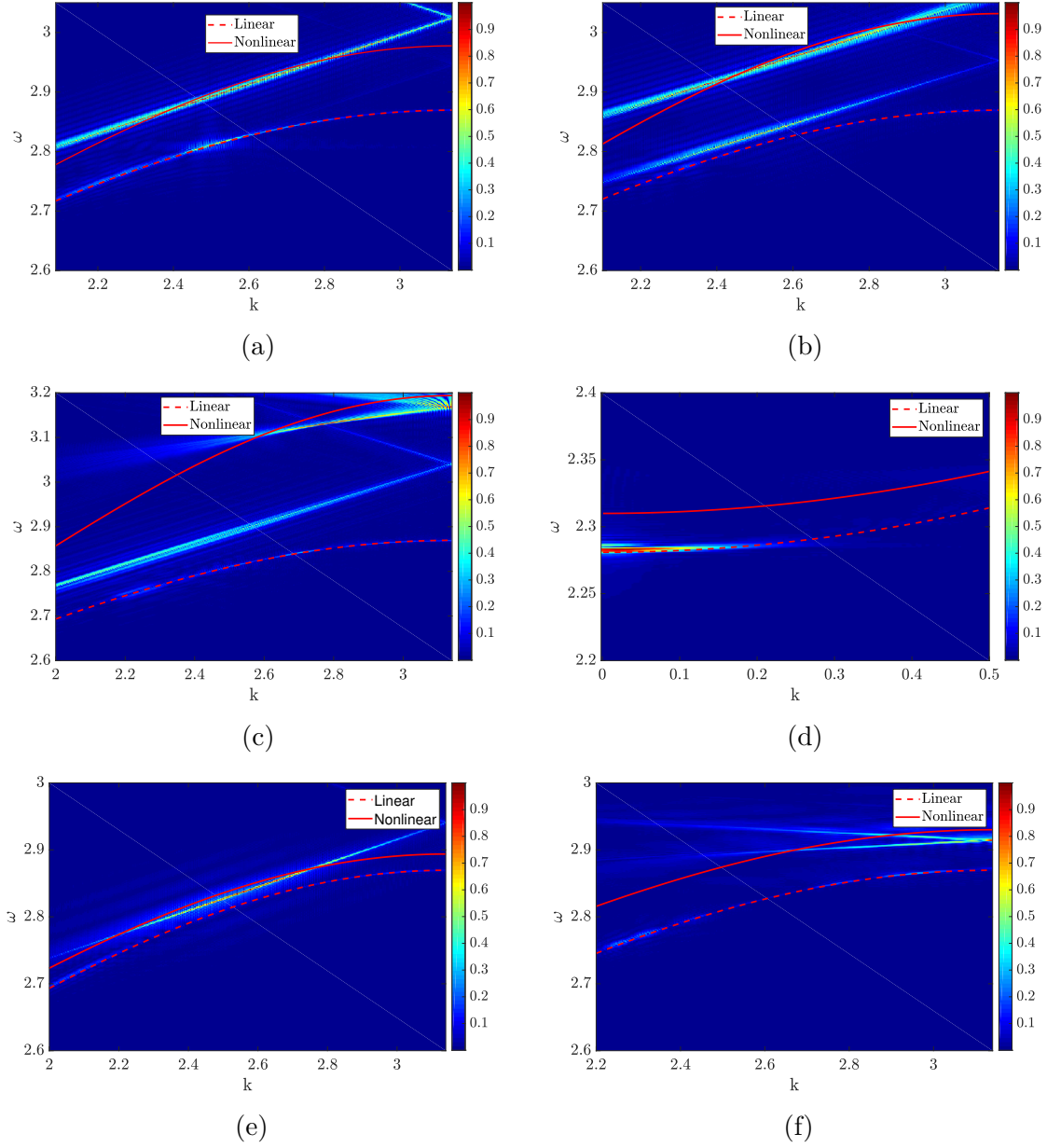
Figure 3.9: Comparison between the analytical solution and images of 2D FFT of the numerical simulations for a chain with two resonators: (a) Hardening chain nonlinearity $\epsilon\bar{\Gamma}\alpha^2 = 0.06$, $\epsilon\bar{\Gamma}_1\alpha^2 = \epsilon\bar{\Gamma}_2\alpha^2 = 0$, $k = 7\pi/9$; (b) Hardening chain nonlinearity $\epsilon\bar{\Gamma}\alpha^2 = 0.09$, $\epsilon\bar{\Gamma}_1\alpha^2 = \epsilon\bar{\Gamma}_2\alpha^2 = 0$, $k = 7\pi/9$; (c) Hardening chain nonlinearity $\epsilon\bar{\Gamma}\alpha^2 = 0.18$, $\epsilon\bar{\Gamma}_1\alpha^2 = \epsilon\bar{\Gamma}_2\alpha^2 = 0$, $k = 7\pi/9$; (d) Hardening resonator nonlinearity $\epsilon\bar{\Gamma}_2\alpha^2 = 0.03$, $\epsilon\bar{\Gamma}_1\alpha^2 = \epsilon\bar{\Gamma}\alpha^2 = 0$, $k = \pi/9$; (e) Hardening resonator nonlinearity $\epsilon\bar{\Gamma}_2\alpha^2 = 0.06$, $\epsilon\bar{\Gamma}_1\alpha^2 = \epsilon\bar{\Gamma}\alpha^2 = 0$, $k = 7\pi/9$; (f) Hardening resonator nonlinearity $\epsilon\bar{\Gamma}_2\alpha^2 = 0.15$, $\epsilon\bar{\Gamma}_1\alpha^2 = \epsilon\bar{\Gamma}\alpha^2 = 0$, $k = 7\pi/9$.
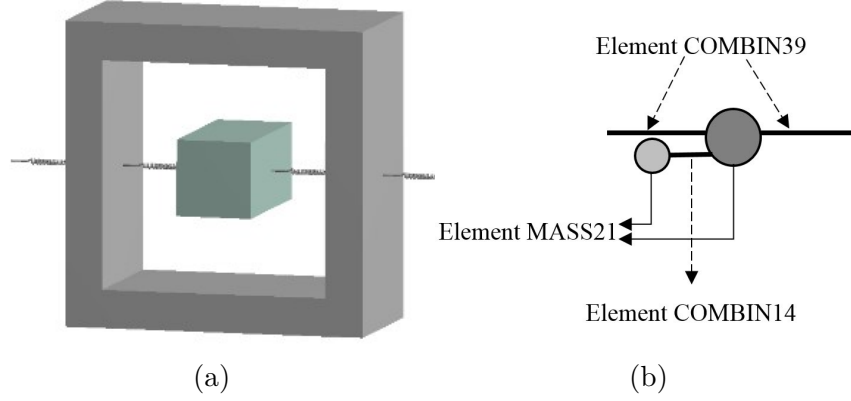
Figure 3.10: (a) A schematic of a cell in ANSYS Workbench; (b) equivalent diagram in APDL.

"TYPE" and "REAL". Fig. 3.10 shows the schematic of a cell in ANSYS workbench (Fig. 3.10. (a)) and its equivalent diagram in ANSYS APDL (Fig. 3.10. (b)). In Fig. 3.10.(a), two linear springs each with a stiffness of $k_1/2$ connect in parallel the chain to the resonator. These two springs are merged into one element defined as COMBIN14 with an equivalent stiffness of k_1.

3.6.1 Band Structures

In order to determine the passband and bandgap, we excite the metamaterial by a harmonic force and monitor the output amplitude at each frequency in the frequency sweep range. Following [76], we excite the second chain in the metamaterial and record the response of the last cell of the chain at the other end.

For the single resonator case, we plot the frequency response curve for different sources of nonlinearities in Fig. 3.11. (a)-(c). In Fig. 3.11. (a)-(b), the results indicate that the wave does not propagate through the structure for frequencies inside the bandgap in the linear and nonlinear chain cases. These frequency limits show a very good agreement with those obtained analytically (marked by the dashed lines in Fig. 3.11). Moreover,

the results demonstrate that both methods (i.e., computational and analytical) can capture the shift in the bandgap boundaries due to the nonlinearity in the chain. On the other hand, the wave propagates in the passband (outside the bandgap) since the amplitude of the system is much higher as compared to the amplitude inside the bandgap. However, for the nonlinear resonator case (Fig. 3.11. (c)), the results indicate that our analytical solution over estimates the bandgap boundaries. This error in bandgap appears mainly close to the nonlinear resonator frequency within the end of the acoustics branch and at the beginning of the optical branch.

For the case of two resonators, we plot the frequency response curve of the system for different types of nonlinearities in Fig. 3.11 (d)-(f). The computational results obtained by ANSYS reveal a good agreement with the analytical solution for the linear and nonlinear chain cases as shown in Fig. 3.11 (d)-(e). However, the analytical results fails again in matching the computational results for the nonlinear resonator case, especially at the nonlinear resonator frequencies, as shown in Fig. 3.11. (f). The different regions (i.e., passband and bandgap) between the dashed lines separate the regions of high amplitude response and the zero amplitude response in the system.

3.6.2 Spectro-Spatial Analysis of ANSYS Results

In this section, we demonstrate the presence of solitary waves based on ANSYS computational simulations. We excite the chain by a wave packet and plot the spatial profile of the output wave, the spectrograms of the wave propagation, and the 2DFFT images in Figs. 3.12- 3.14.

For the spatial profile, we observe that a nonlinear chain has no effect on the wave profile at long wavelength limit while the nonlinear resonator distorts the signal significantly
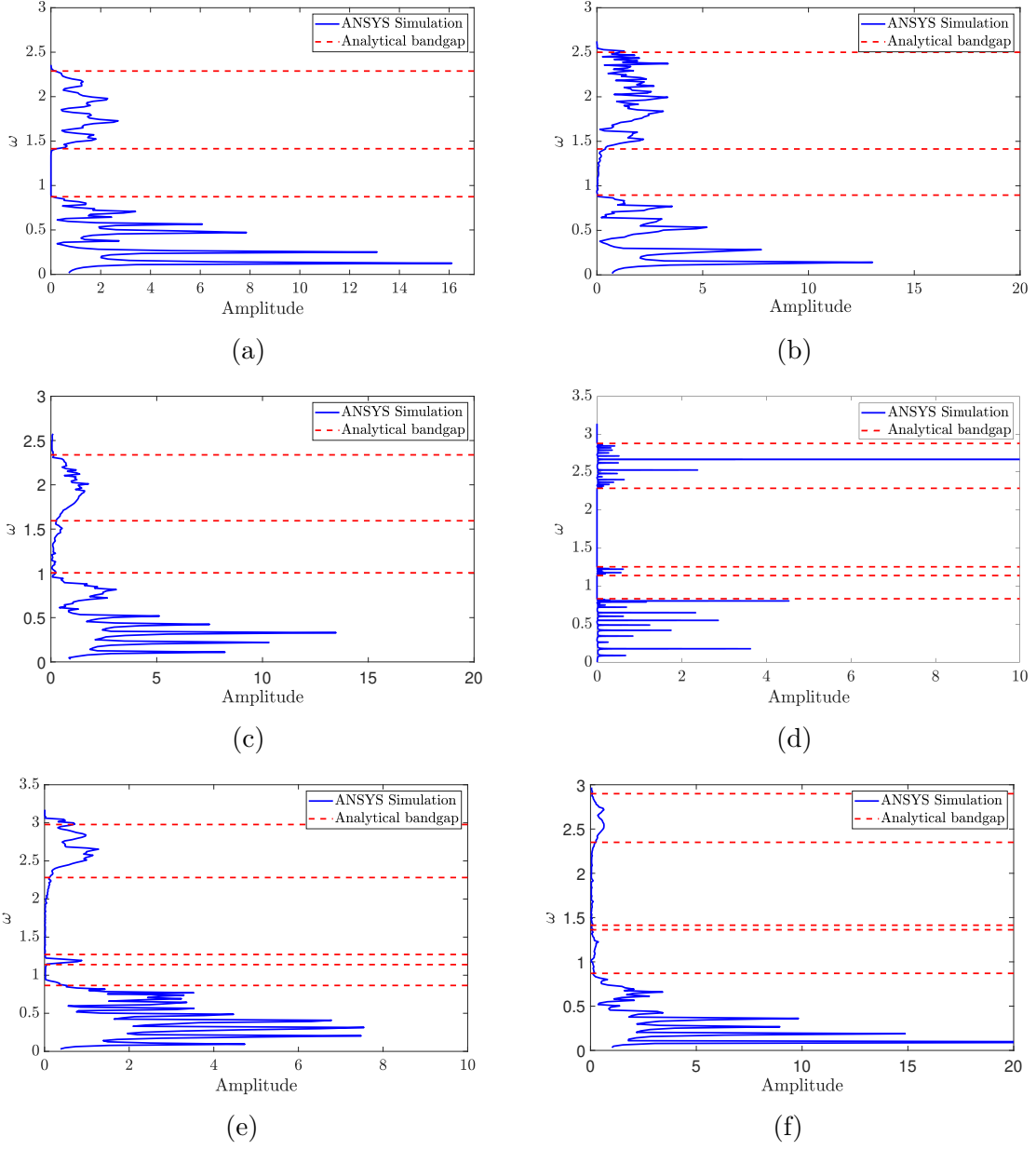
Figure 3.11: Frequency response curves for a linear and nonlinear metamaterial with marking the boundaries of the analytical bandgaps by dashed lines: (a) Linear chain single resonator $\epsilon\bar{\Gamma}\alpha^2 = \epsilon\bar{\Gamma_1}\alpha^2 = 0$; (b) Nonlinear chain single resonator $\epsilon\bar{\Gamma}\alpha^2 = 0.06; \epsilon\bar{\Gamma_1}\alpha^2 = 0$; (c) Nonlinear resonator single resonator $\epsilon\bar{\Gamma}\alpha^2 = 0; \epsilon\bar{\Gamma_1}\alpha^2 = 0.06$; (d) Linear chain two resonators $\epsilon\bar{\Gamma}\alpha^2 = \epsilon\bar{\Gamma_1}\alpha^2 = \epsilon\bar{\Gamma_2}\alpha^2 = 0$; (e) Nonlinear chain two resonators $\epsilon\bar{\Gamma}\alpha^2 = 0.06; \epsilon\bar{\Gamma_1}\alpha^2 = \epsilon\bar{\Gamma_2}\alpha^2 = 0$; Nonlinear resonator two resonators $\epsilon\bar{\Gamma}\alpha^2 = \epsilon\bar{\Gamma_2}\alpha^2 = 0; \epsilon\bar{\Gamma_1}\alpha^2 = 0.06$.
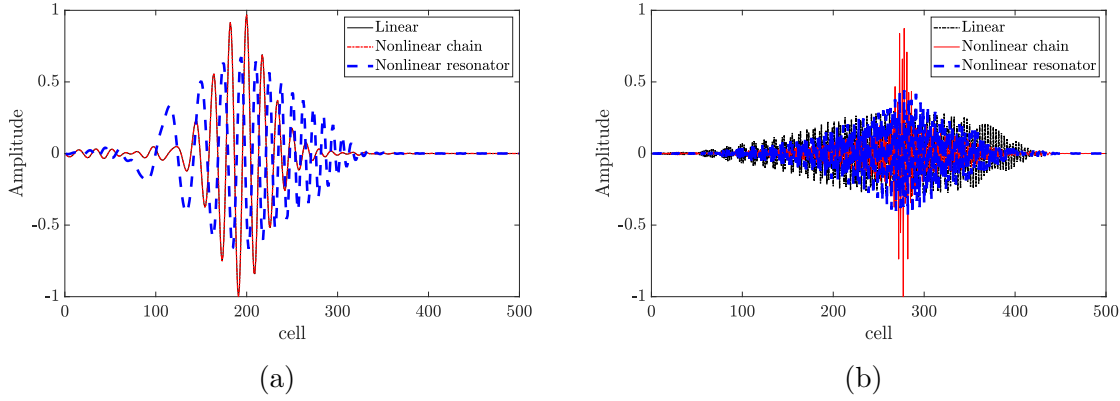
Figure 3.12: Spatial profile in short and long wavelength limits in the upper optical mode (a chain with two resonators) for linear chain, nonlinear chain, and nonlinear resonator: (a) $k = \pi/9$; (b) $k = 7\pi/9$.

as shown in Fig. 3.12. (a). This distortion can lead to a significant frequency shift (i.e., the output signal appears at frequencies different than the frequency of the input signal) and shows a good agreement with the theoretical results obtained in the previous section. The wave profile for the linear chain is a mirror image of the nonlinear chain case. On the other hand, in Fig. 3.12. (b), the nonlinearity in the chain and resonator shows a birth of localized solitary waves at short wavelength limit and the profile of the linear chain is different from that of the nonlinear chain since it is completely dispersive. These findings were also observed in the numerical analysis in the previous section, except that in the computational simulation the localized component in the nonlinear resonator case is not sharp as compared to the numerical results.

In Fig. 3.13 (a)-(b), spatial spectograms further demonstrate the wave distortion and wave number/frequency shift due to the nonlinear resonator at long wavelength limit. In particular, some of the energy content for the output signal appears outside the input wavenumber/frequency band as shown in Fig. 3.13 (b). This distortion cannot be obtained in the nonlinear chain case (Fig. 3.13 (a)) since its spectrogram is a mirror image of the linear chain case. On the other hand, the spatial spectrogram plots in Fig. 3.13 (c)-(d) indicate
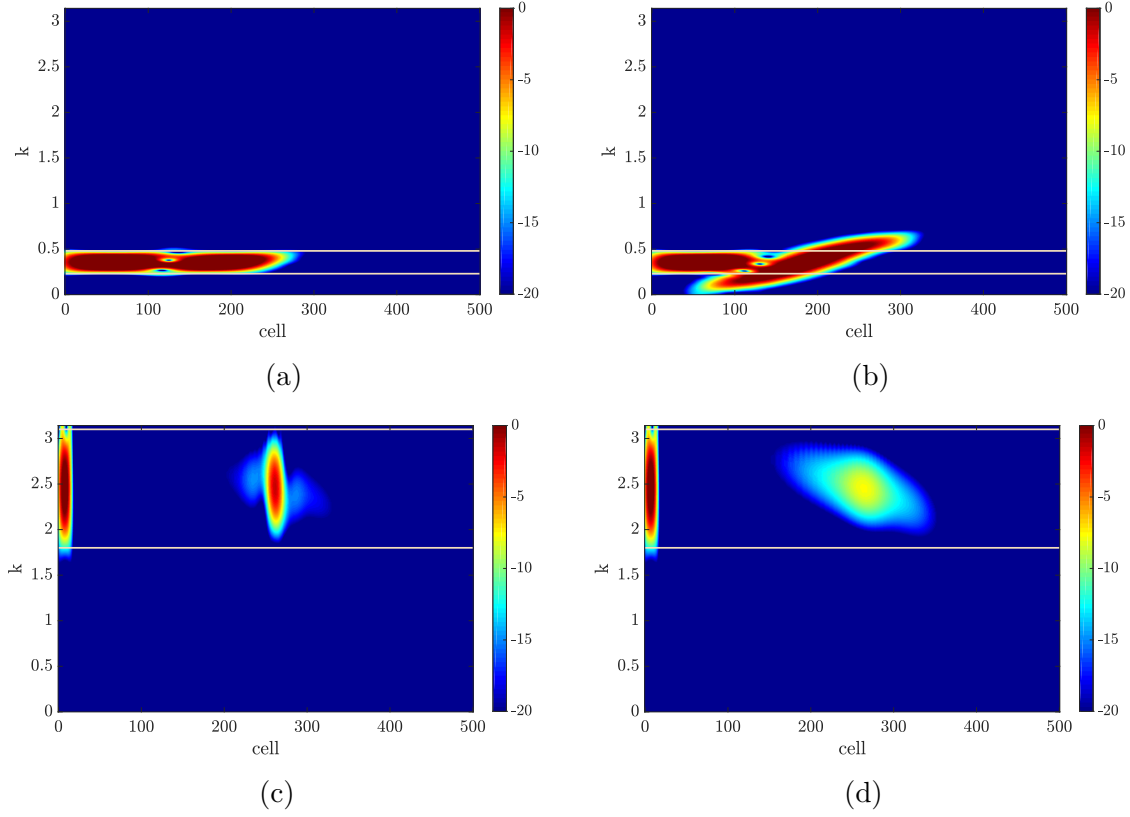
Figure 3.13: Spatial spectrograms for nonlinear metamaterial with two local resonators in short and long wavelength limits: (a) Nonlinear chain, $\epsilon\bar{\Gamma}\alpha^2 = 0.03$, $\epsilon\bar{\Gamma}_1\alpha^2 = \epsilon\bar{\Gamma}_2\alpha^2 = 0$, $k = \pi/9$; (b) Nonlinear resonator, $\epsilon\bar{\Gamma}_2\alpha^2 = 0.03$, $\epsilon\bar{\Gamma}_1\alpha^2 = \epsilon\bar{\Gamma}\alpha^2 = 0$, $k = \pi/9$; (c) Nonlinear chain, $\epsilon\bar{\Gamma}\alpha^2 = 0.03$, $\epsilon\bar{\Gamma}_1\alpha^2 = \epsilon\bar{\Gamma}_2\alpha^2 = 0$, $k = 7\pi/9$; (d) Nonlinear resonator, $\epsilon\bar{\Gamma}_2\alpha^2 = 0.03$, $\epsilon\bar{\Gamma}_1\alpha^2 = \epsilon\bar{\Gamma}\alpha^2 = 0$, $k = 7\pi/9$.

that all energy content of the output wave is concentrated in one component inside the input wavenumber/frequency band with high energy. This observation suggests the birth of localized wave at short wavelength limit. Although, the wave in Fig. 3.13 (d) looks dispersive, the wave still has localized component that preserves high energy content.

Finally, we show the images of 2DFFT in Fig. 3.14 to demonstrate the effect of nonlinearity on the dispersion curve based on the results obtained in ANSYS. In the long wavelength limit, the results indicate that the nonlinearity in the chain doe not distort the wave since its profile (shown in Fig. 3.13 (a)) is exactly the same as the profile of the linear chain. On
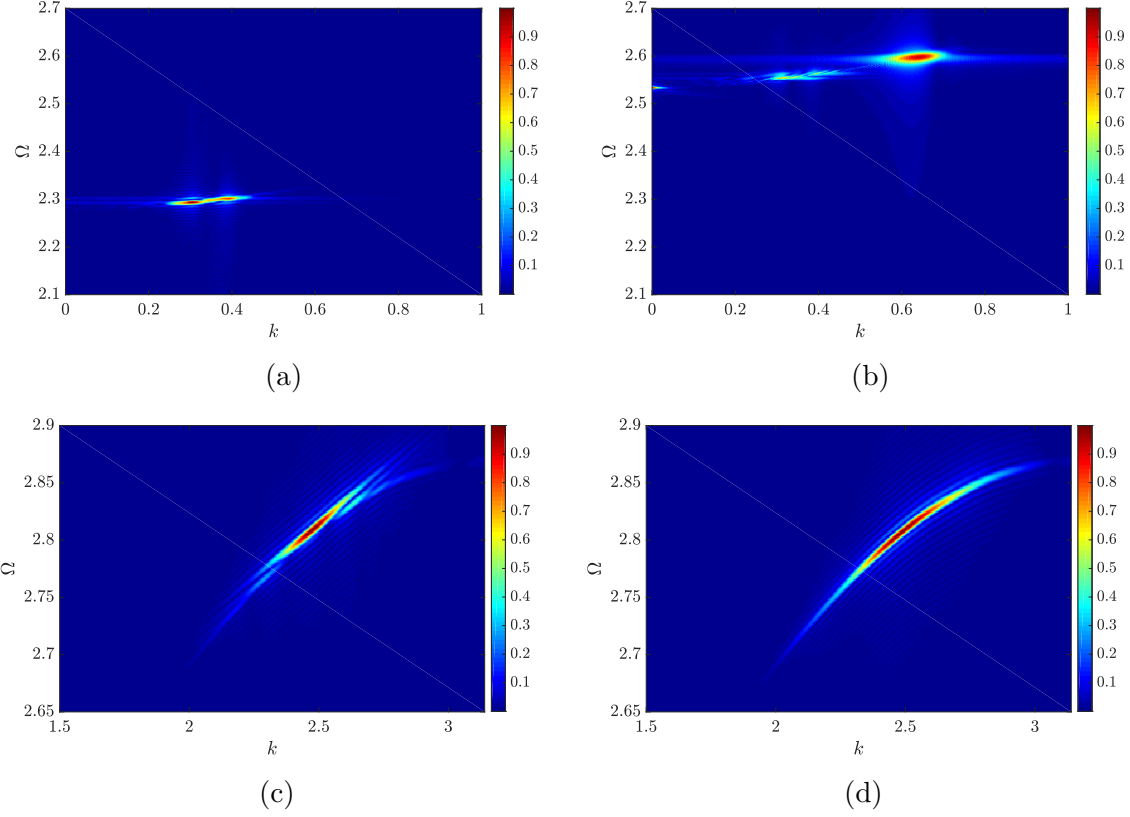
Figure 3.14: Images of 2-D Fourier transform and nonlinear metamaterial with two local resonators in short and long wavelength limits : (a) Nonlinear chain, $\epsilon \bar{\Gamma} \alpha^2 = 0.03$, $\epsilon \bar{\Gamma}_1 \alpha^2 = \epsilon \bar{\Gamma}_2 \alpha^2 = 0$, $k = \pi/9$; (b) Nonlinear resonator, $\epsilon \bar{\Gamma}_2 \alpha^2 = 0.03$, $\epsilon \bar{\Gamma}_1 \alpha^2 = \epsilon \bar{\Gamma} \alpha^2 = 0$, $k = \pi/9$; (c) Nonlinear chain, $\epsilon \bar{\Gamma} \alpha^2 = 0.03$, $\epsilon \bar{\Gamma}_1 \alpha^2 = \epsilon \bar{\Gamma}_2 \alpha^2 = 0$, $k = 7\pi/9$; (d) Nonlinear resonator, $\epsilon \bar{\Gamma}_2 \alpha^2 = 0.03$, $\epsilon \bar{\Gamma}_1 \alpha^2 = \epsilon \bar{\Gamma} \alpha^2 = 0$, $k = 7\pi/9$.

the other hand, the nonlinearity in the resonator distorts the output wave since the wave (Fig. 3.14. (b)) appears at frequency different than the input frequency which is identical to the undistorted wave of the linear and nonlinear chain shown in Fig. 3.13 (a). In the short wavelength limit, the image of the nonlinear chain (Fig. 3.14. (c)) shows that the energy content of the output wave appears on two main components. One with variable slope and coincides with the linear dispersion curve, the other has fixed slope and appears above the linear dispersion curve due to the type of hardening nonlinearity. The latter represents a solitary wave [85]. For the nonlinear resonator case (Fig. 3.14. (d)), distinguishing the two

energy components is harder since the this region is not affected by the resonator nonlinearity as compared to the nonlinear chain. Yet the hardening resonator nonlinearity shifts the dispersion curves up toward the fixed slope case which indicates the birth of solitary wave.

3.7 CONCLUSION

In this chapter, a nonlinear acoustics metamaterial with multiple local resonators was investigated theoretically and computationally. In one case, we examined the nonlinearity in the chains and in another we investigated the nonlinearity in the resonators. Closed-form expressions were presented for the nonlinear dispersion relations using the method of multiple scales. These expressions are more general since they can be applied for nonlinear chains with any number of nonlinear local resonators. The analytical results were validated via comparison with those in the literature, those obtained numerically, and those obtained by finite element software, ANSYS. The validation revealed that the analytical results can predict the cut-off frequency in both cases; however, the analytical approach fails to predict the dispersion curve near the resonator frequency. This failure suggests that higher perturbation or more robust analytical techniques may be required to accurately predict the dispersion relations of such a nonlinear metastructure. The analytical dispersion equation for the case of nonlinear resonator shows a significant frequency shift at all wavelength limits, particularly when the excitation frequency is near the resonator frequency. This finding is an indication that nonlinear resonators in the present system, unlike nonlinear chains, affect wave propagations in the long wavelength domain. This observation was consistent with the topological (space-time domain) analysis conducted based on numerical and computational simulations. In the spectro-spatial analysis, we demonstrated that the effect of hardening nonlinearity appears as localizing the wave, whereas, that of softening nonlinearity appears

as dispersing the wave. This effect depends on the nonlinear resonator frequency and how close it is to the input wave frequency. Spectrograms and images of 2-D short term Fourier transform also confirmed these observations. They also showed that the nonlinear resonator has output signal stretching over a wider range of frequencies and wavenumbers in the long wavelength region. In addition, the nonlinear resonators and nonlinear chains exhibited similar waveform characteristics in short wavelength region when the nonlinear resonator was tuned properly. These observations suggest that such a nonlinear metamaterial (i.e, metamaterial investigated in the current study), consisting of a nonlinear (or linear) chain and multiple linear (or nonlinear) resonators, are suitable for various applications including acoustic diodes and broadband vibration isolation and energy harvesting. The current findings can be further supported or generalized upon investigating similar systems using various analytical and experimental techniques and employing these observations in various applications like acoustics diode in the future.

Chapter 4

Simultaneous energy harvesting and vibration control in a nonlinear metastructure: a spectro-spatial analysis

This chapter is an edited version of: Bukhari, Mohammad, and Oumar Barry. "Simultaneous energy harvesting and vibration control in a nonlinear metastructure: A spectro-spatial analysis." *Journal of Sound and Vibration* 473 (2020): 115215. [26].

Considerable attention has recently been given to the study of simultaneous energy harvesting and vibration attenuation in metastructures. However, only linear metastructures were investigated although nonlinear metastructures and nonlinear electromechanical devices offer superior interesting wave propagation phenomena (e.g., birth of solitary waves, tunable bandgap, acoustic nonreciprocity) and broadband energy harvesting. In this paper, we investigate the wave propagation in a weakly nonlinear metastructure with electromechanical resonators. Explicit expressions are derived for the nonlinear dispersion relations using the method of multiple scales. These expressions are validated via direct numerical integration. We carried out parametric studies to investigate the role of different parameters of the

electromechanical resonators on the linear and nonlinear band structure. To obtain further detailed information on the nonlinear wave propagation, we employ spectro-spatial analyses on the numerical simulations. This spectro-spatial analysis can reveal the output voltage distortion due to different types of nonlinearities. The results indicate that nonlinear chain can enhance energy harvesting through the birth of solitary wave and without degrading the boundary of the bandgap. The results also suggest that such a system is suitable for designing electromechanical diodes and rectifiers.

4.1   Introduction

Metastructures are artificially engineered structures offering exceptional and unique proper-
ties that are not present in conventional homogeneous structures [84]. They were originally
developed for optical wave propagation (also known as metamaterials) and then they were
extended to enhance elastic and wave propagation properties [33]. Some of these properties
are negative mass, negative density, and negative Poisson's ratio [14]. These unique features
suggest that metastructures can be beneficial in vibration and noise control, non-destructive
testing, energy harvesting, and acoustic rectifiers.

Metastructures are usually arranged in specific patterns that exhibit exotic function-
alities. Earlier consideration of metastructures studied periodic structures [97, 98, 99, 159,
160, 178]. Periodic structures prevent the wave from propagating through the structure at
range of frequencies known as bandgap and caused by Bragg scattering. These frequencies
have wavelengths close to the lattice constant. This bandgap formation can be employed in
low-frequency vibration attenuation.

The limitation on the lattice size in Bragg scattering restricts the application of metama-
terials to only large structures; however, many engineering applications require controlling
smaller size components. Inspired by smaller size systems, Liu et al. [110] introduced lo-
cal resonators in metastructures to control vibrations at wavelengths much smaller than
the lattice constant. These structures are called locally-resonant metamaterials and they are
capable of widening the original bandgap developed by Bragg scattering. Indeed, the param-
eters of the local resonator determine the dominant cause of the bandgap [109]. Moreover,
multiple bandgaps can be obtained by using multiple resonators with different parameters
[78, 197].

For large wave amplitudes in inherently nonlinear mediums, linear theory cannot ad-

equately represent the problem; thus higher-order nonlinear terms need to be considered. Nonlinear metastructures exhibit some interesting wave propagation phenomena that do not develop in linear metastructures. Some of those are gap solitons [95], envelope and dark solitons [131], asymmetric wave propagation [107], and adjustable bandgap [117].

Nonlinear problems can be characterized based on the strength of nonlinearities. When the nonlinearity is weak, the problem can be handled by perturbation techniques [134, 135] and approximate analytical solution can be derived when the problem asymptotically converges. Weakly nonlinear metastructures were investigated by Narisetti et al. [133]. They employed Lindstedt-Poincare method to derive explicit expressions for the dispersion relations. However, when several nonlinear waves propagate and interact through the structure, the method of multiple scales is more suitable since the associated algebra requires less efforts [119]. Strongly nonlinear metastructures have gained less attention in the literature and they usually require other techniques such as the complexification-averaging or shooting methods to tackle the problem [2].

Analyzing the dispersion relation analytically does not provide adequate information about the nonlinear dynamical features in metastructures. Instead, it only presents the nonlinear shift in the dispersion curves. To reveal other interesting features, Ganesh and Gonella [63] employed spectro-spatial analysis to investigate the wave propagation through metastructures. Their analysis provided more detailed information about the wave distribution in the structure (i.e., localized or dispersive waves); therefore, the birth and inhalation of solitary waves can be predicted based on the wavelength and nonlinearity type. The use of spectro-spatial analyses were also extended in [27, 195] for locally resonant metastructures. They observed a significant frequency shift in the optical branch, and they then employed this shift to design acoustics diodes.

In recent years, many researchers investigated the bandgap formation due to electrome-

chanical coupling in metastructures with piezoelectric patches [5, 13, 34, 173, 194]. The electromechanical coupling generates piezoelectric locally bandgap where the dimension of the bandgap is controlled by the added stiffness to the system. Embedding piezoelectric materials in metastructures can also lead to simultaneous energy harvesting and vibration attenuation [74]. This is inspired by the flat band of frequencies in metastructures, which was experimentally demonstrated using a locally resonant phononic crystal plate with embedded spiral beams[157]. The problem was theoretically investigated later for a discrete structure in [74] and for a continuous structure in [75]. Moreover, Hu et al. [76] extended the problem by coupling the internal resonators. This showed an improvement in the energy harvesting and vibration suppression. Energy harvesting in metastructures was also experimentally demonstrated by testing a 3D printed 2D structure in [105]. Furthermore, traveling wave energy harvesting was also experimentally and numerically demonstrated in a 2D phononic crystal lens structure. The authors showed that a significance improvement in energy harvesting can be achieved when the acoustic metamaterial is designed to focus or properly localize the wave energy [174, 175].

The study of simultaneous energy harvesting and vibration attenuation in metastructures has so far been limited to linear metastructures. There is no study that investigates the effect of nonlinearity in metastructures for simultaneous energy harvesting and vibration control. In this chapter, we investigate the wave propagation and energy harvesting in a weakly nonlinear metastructure with local electromechanical resonators. We employ the method of multiple scales to derive explicit expressions for the dispersion relations. These relations are validated by direct numerical integration. Then, we study various nonlinear phenomena and their effects on the energy harvesting distribution and magnitude. This is done through studying the relation between topological (i.e., space-time domain) and spectral (dispersion relations) features of a wave propagating in such a nonlinear metastructure. Parametric

studies are conducted to investigate the effect of different parameters on the band structure, the role of nonlinearity on energy harvesting, and energy harvesting associated with solitary waves.

The rest of the chapter is outlined as follows: In Section 2, we model the nonlinear chain and electromechanical resonators. We then present an approximate closed form solution for the dispersion relations. These relations are discussed and validated numerically in Section 3. In Section 4, we investigate the topological features of the output voltage wave by spectro-spatial analysis to demonstrate more detailed information about nonlinear wave propagation phenomena. Finally, we discuss the obtained results in Section 5, and then summarize our findings in Section 6.

4.2   Mathematical Modeling

A schematic diagram for the proposed metastructure is shown in Fig. 4.1. The metastructure is presented by a chain of cells. Each cell consists of a rigid mass, M, and is connected to other cells by a nonlinear spring with linear coefficient, K, and nonlinear coefficient, $\bar{\alpha}$. The cell is also connected to a local electromechanical resonator with an effective mass, m_p, and an effective linear stiffness k_1. The resonator consists of a substrate covered by a piezoelectric layer. This piezoelectric layer is shunted to an external resistor R_{eq} and it harvests a voltage, v. The displacement of the nth cell is defined as u_n, while the absolute displacement of its local resonator is Y_n. Following [74] and [24] the coupled equation of motions for each cell can be written as

$$M\ddot{\bar{u}}_n + 2K\bar{u}_n - K\bar{u}_{n+1} - K\bar{u}_{n-1} + \bar{\alpha}(\bar{u}_n - \bar{u}_{n+1})^3 + \bar{\alpha}(\bar{u}_n - \bar{u}_{n-1})^3 + m_p(\ddot{\bar{y}}_n + \ddot{\bar{u}}_n) = 0 \quad (4.1)$$
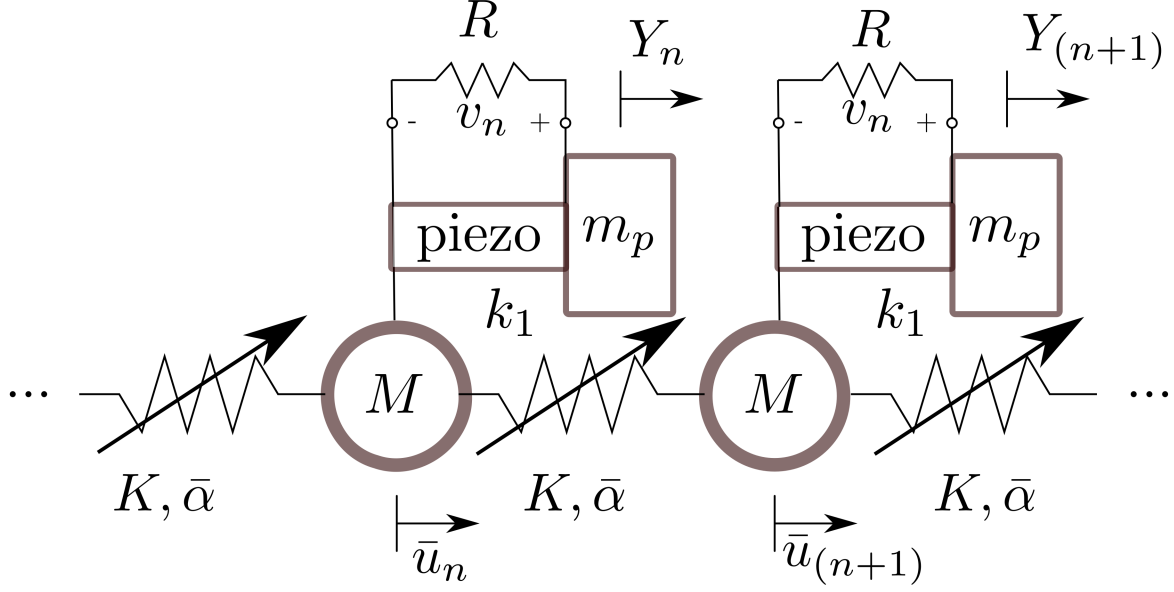
Figure 4.1: A schematic diagram for the nonlinear acoustics metastructure with linear electromechanical resonator resonators.

$$m_p \ddot{\bar{y}}_n + k_1 \bar{y}_n - \theta \bar{v}_n = -m_p \ddot{\bar{u}}_n \tag{4.2}$$

$$RC_p \dot{\bar{v}}_n + \bar{v}_n + R\theta \dot{\bar{y}}_n = 0 \tag{4.3}$$

where $\bar{y}_n = Y_n - \bar{u}_n$ is the relative displacement of the local resonator, θ is the electromechanical coupling coefficient, and C_p is the capacitance of the piezoelectric element. These equations can be written in normalized form as

$$\ddot{u}_n + 2u_n - u_{n+1} - u_{n-1} + \alpha(u_n - u_{n+1})^3 + \alpha(u_n - u_{n-1})^3 + \bar{k}\Omega_0^2(\ddot{y}_n + \ddot{u}_n) = 0 \tag{4.4}$$

$$\Omega_0^2 \ddot{y}_n + y_n - \alpha_1 v_n = -\Omega_0^2 \ddot{u}_n \tag{4.5}$$

$$\alpha_2 \dot{v}_n + v_n + \alpha_3 \dot{y}_n = 0 \tag{4.6}$$

where $\omega_n^2 = K/M$, $\omega_d^2 = k_1/m_p$, $\bar{k} = k_1/K$, $u_n = \bar{u}_n/U_0$, $y_n = \bar{y}_n/y_0$, $v_n = \bar{v}_n/V_0$, $\alpha = \bar{\alpha}U_0^2/K$, $\Omega_0 = \omega_n/\omega_d$, $\alpha_1 = \theta V_0/k_1$, $\alpha_2 = RC_p\omega_n$, $\alpha_3 = R\theta\omega_n y_0/V_0$, and the nondimensional time is $\tau = \omega_n t$. We express the solution for the system by power series. By ignoring the terms of second order and higher, the solution can be written in the form

$$u_n(t, \epsilon) = u_{n0}(T_0, T_1) + \epsilon u_{n1}(T_0, T_1) + o(\epsilon^2) \tag{4.7}$$

$$y_n(t, \epsilon) = y_{n0}(T_0, T_1) + \epsilon y_{n1}(T_0, T_1) + o(\epsilon^2) \tag{4.8}$$

$$v_n(t, \epsilon) = v_{n0}(T_0, T_1) + \epsilon v_{n1}(T_0, T_1) + o(\epsilon^2) \tag{4.9}$$

where $T_0 = \tau$ is the fast time scale and $T_1 = \epsilon\tau$ is the slow time scale. Since the time is expressed in two independent variables, the time derivative can be presented using the chain role as

$$(\dot{\ }) = D_0 + \epsilon D_1 + ... \tag{4.10}$$

$$(\ddot{\ }) = D_0^2 + 2\epsilon D_0 D_1 + ... \tag{4.11}$$

Introducing Eqs. (4.7)-(4.11) into Eqs. (4.4)-(4.6) and collecting the terms of similar coefficient leave us with the following sets of equations

order ϵ^0

$$D_0^2 u_{n0} + 2u_{n0} - u_{(n-1)0} - u_{(n+1)0} + \bar{k}\Omega_0^2 D_0^2(y_{n0} + u_{n0}) = 0 \tag{4.12}$$

$$\Omega_0^2 D_0^2 y_{n0} + y_{n0} - \alpha_1 v_{n0} = -\Omega_0^2 D_0^2 u_{n0} \tag{4.13}$$

$$\alpha_2 D_0 v_{n0} + v_{n0} + \alpha_3 D_0 y_{n0} = 0 \tag{4.14}$$

order ϵ^1

$$D_0^2 u_{n1} + 2u_{n1} - u_{(n-1)1} - u_{(n+1)1} + \bar{k}\Omega_0^2 D_0^2(y_{n1} + u_{n1}) = -2\bar{k}\Omega_0^2 D_0 D_1(y_{n0} + u_{n0}) -$$
$$2D_0 D_1 u_{n0} - \alpha(u_{n0} - u_{(n-1)0})^3 - \alpha(u_{n0} - u_{(n+1)0})^3 \tag{4.15}$$

$$\Omega_0^2 D_0^2 y_{n1} + y_{n1} - \alpha_1 v_{n1} = -\Omega_0^2 D_0^2 u_{n1} - 2\Omega_0^2 D_0 D_1 u_{n0} - 2\Omega_0^2 D_0 D_1 y_{n0} \tag{4.16}$$

$$\alpha_2 D_0 v_{n1} + v_{n1} + \alpha_3 D_0 y_{n1} = -\alpha_2 D_1 v_{n0} - \alpha_3 D_1 y_{n0} \tag{4.17}$$

4.2.1 Linear dispersion relations

At order ϵ^0, the problem is linear. The solution can be written as

$$u_n = Ae^{i(nk-\omega\tau)} \tag{4.18}$$

$$y_n = Be^{i(nk-\omega\tau)} \tag{4.19}$$

$$v_n = Ce^{i(nk-\omega\tau)} \tag{4.20}$$

Substituting Eqs. (4.19)-(4.20) into Eq. (4.14) yields

$$-i\alpha_2\omega C + C - i\alpha_3\omega B = 0 \tag{4.21}$$

Solving for C leaves us with

$$C = \Gamma B \tag{4.22}$$

where Γ is complex and can be written as

$$\Gamma = \frac{i\alpha_3\omega}{1 - i\alpha_2\omega} \tag{4.23}$$

Substituting Eqs. (4.18)-(4.19) and Eq. (4.22) into Eq. (4.13) leads to

$$B = K_\omega A \tag{4.24}$$

where K_ω is also complex and defined as follow

$$K_\omega = \frac{\Omega_0^2 \omega^2}{1 - \alpha_1 \Gamma - \Omega_0^2 \omega^2} \tag{4.25}$$

Finally, one can obtain the linear dispersion relation from Eqs. (4.12), (4.22), (4.24) as:

$$-\omega^2 + (2 - 2\cos k) - \bar{k}\Omega_0^2 \omega^2 (1 + K_\omega) = 0 \tag{4.26}$$

It is noteworthy here that Eq. (4.26) has five roots. Four of them are complex pairs with nonzero real part, while the fifth one is pure complex.

4.2.2 Nonlinear dispersion relation

At order ϵ the problem is nonlinear. We need to obtain the solvability condition in order to obtain a convergent approximate solution.

Equation. (4.17) can be written as (after multiplying by α_1)

$$(\alpha_2 D_0 + 1)\alpha_1 v_{n1} = \alpha_1 [-\alpha_3 D_0 y_{n1} - \alpha_2 D_1 v_{n0} - \alpha_3 D_1 y_{n0}] \tag{4.27}$$

Multiplying Eq. (4.16) by $(\alpha_2 D_0 + 1)$ and using Eq. (4.27) to eliminate v_{n1}, one can obtain

$$(\alpha_2 D_0 + 1)(\Omega_0^2 D_0^2 y_{n1} + y_{n1} + \Omega_0^2 D_0^2 u_{n1}) + \alpha_1 \alpha_3 D_0 y_{n1} = (\alpha_2 D_0 + 1)$$
$$(-2\Omega_0^2 D_0 D_1 u_{n0} - 2\Omega_0^2 D_0 D_1 y_{n0}) - \alpha_2 \alpha_1 D_1 v_{n0} - \alpha_1 \alpha_3 D_1 y_{n0} \tag{4.28}$$

Equation (4.28) can be written as

$$[(\alpha_2 D_0 + 1)(\Omega_0^2 D_0^2 + 1) + \alpha_1\alpha_3 D_0]y_{n1} = -(\alpha_2 D_0 + 1)\Omega_0^2 D_0^2 u_{n1} + (\alpha_2 D_0 + 1)$$
$$(-2\Omega_0^2 D_0 D_1 u_{n0} - 2\Omega_0^2 D_0 D_1 y_{n0}) - \alpha_2\alpha_1 D_1 v_{n0} - \alpha_1\alpha_3 D_1 y_{n0}$$

(4.29)

Multiplying Eq. (4.29) by $\bar{k}\Omega_0^2 D_0^2$ and substituting it in Eq. (4.15) yields

$$[(\Omega_0^2 D_0^2 + 1)(\alpha_2 D_0 + 1) + \alpha_1\alpha_3 D_0]((1 + \bar{k}\Omega_0^2)D_0^2 u_{n1} + 2u_{n1} - u_{(n-1)1} - u_{(n+1)1}) -$$
$$\bar{k}\Omega_0^2 D_0^2(\alpha_2 D_0 + 1)\Omega_0^2 D_0^2 u_{n1} = [(\Omega_0^2 D_0^2 + 1)(\alpha_2 D_0 + 1) + \alpha_1\alpha_2 D_0](-2D_0 D_1 u_{n0} -$$
$$-2\bar{k}D_0 D_1(u_{n0} + y_{n0}) - \alpha(u_{n0} - u_{(n-1)0})^3 - \alpha(u_{n0} - u_{(n+1)0})^3) + \bar{k}\Omega_0^2 D_0^2[-(\alpha_2 D_0 +$$
$$1)(-2\Omega_0^2 D_0 D_1 u_{n0} - 2\Omega_0^2 D_0 D_1 y_{n0})] + \alpha_1\alpha_2 D_1 v_{n0} + \alpha_1\alpha_3 D_1 y_{n0}]$$

(4.30)

To determine the solvability condition, one should substitute Eqs. (4.18)-(4.20) into Eq. (4.30) to obtain

$$[(\Omega_0^2 D_0^2 + 1)(\alpha_2 D_0 + 1) + \alpha_1\alpha_3 D_0]((1 + \bar{k}\Omega_0^2)D_0^2 u_{n1} + 2u_{n1} - u_{(n-1)1} - u_{(n+1)1}) -$$
$$\bar{k}\Omega_0^2 D_0^2(\alpha_2 D_0 + 1)\Omega_0^2 D_0^2 u_{n1} = ([[(-\Omega_0^2\omega^2 + 1)(-i\alpha_2\omega + 1) - i\alpha_1\alpha_2\omega](2i\omega A'$$
$$+2i\omega\bar{k}\Omega_0^2(1 + K_\omega)A' - 12\alpha A^2\bar{A}(1 - \cos k)^2) - \bar{k}\Omega_0^2\omega^2[(i\omega\alpha_2 - 1)(2i\Omega_0^2\omega A' + 2i\Omega_0^2\omega K_\omega A')$$
$$+\alpha_1\alpha_2 K_\omega\Gamma A' + \alpha_1\alpha_3 K_\omega A'])e^{i(nk-\omega t)} + NST$$

(4.31)

where NST denotes the non-secular terms.

The solvability condition can then be obtained as

$$[(-\Omega_0^2\omega^2 + 1)(-i\alpha_2\omega + 1) - i\alpha_1\alpha_2\omega](2i\omega A' + 2i\omega\bar{k}\Omega_0^2(1 + K_\omega)A' - 12\alpha A^2\bar{A}(1 - \cos k)^2) -$$
$$\bar{k}\Omega_0^2\omega^2[(i\omega\alpha_2 - 1)(2i\Omega_0^2\omega A' + 2i\Omega_0^2\omega K_\omega A') + \alpha_1\alpha_2 K_\omega\Gamma A' + \alpha_1\alpha_3 K_\omega A'] = 0$$

(4.32)

Substituting the polar form ($A = ae^{ib}$ where a and b are functions of the slow time scale, $K_\omega = \mathrm{Re}[K_\omega] + i\,\mathrm{Im}[K_\omega]$, and $\Gamma = \mathrm{Re}[\Gamma] + i\,\mathrm{Im}[\Gamma]$) in Eq. (4.32) yields

$$
\begin{aligned}
&-\frac{1}{2}\alpha_1\alpha_2\omega^2\Omega_0^2\bar{k}(\mathrm{Re}[\Gamma] + i\mathrm{Im}[\Gamma])\left(e^{ib}a' + iae^{ib}b'\right)(\mathrm{Re}[K_\omega] + i\mathrm{Im}[K_\omega]) \\
&+\alpha_2\omega^2\Omega_0^2\bar{k}\left(e^{ib}a' + iae^{ib}b'\right)(\mathrm{Re}[K_\omega] + i\mathrm{Im}[K_\omega]) \\
&+\frac{1}{2}\alpha_1\alpha_3\omega^2\Omega_0^2\bar{k}\left(e^{ib}a' + iae^{ib}b'\right)(\mathrm{Re}[K_\omega] + i\mathrm{Im}[K_\omega]) \\
&+i\omega\Omega_0^2\bar{k}\left(e^{ib}a' + iae^{ib}b'\right)(\mathrm{Re}[K_\omega] + i\mathrm{Im}[K_\omega]) + \alpha_2\omega^2\Omega_0^2\bar{k}\left(e^{ib}a' + iae^{ib}b'\right) \\
&+\alpha_1\alpha_3\omega^2\Omega_0^2\bar{k}\left(e^{ib}a' + iae^{ib}b'\right) + i\omega\Omega_0^2\bar{k}\left(e^{ib}a' + iae^{ib}b'\right) - \frac{3}{2}ia^3\alpha\alpha_2e^{ib}ccc\omega^3\Omega_0^2 \\
&+\frac{3}{2}a^3\alpha e^{ib}ccc\omega^2\Omega_0^2 + \frac{3}{2}ia^3\alpha\alpha_2e^{ib}ccc\omega + \frac{3}{2}ia^3\alpha\alpha_1\alpha_3e^{ib}ccc\omega \\
&-\frac{3}{2}a^3\alpha e^{ib}ccc - \alpha_2\omega^4\Omega_0^2\left(e^{ib}a' + iae^{ib}b'\right) + \alpha_2\omega^2\left(e^{ib}a' + iae^{ib}b'\right) \\
&+\alpha_1\alpha_3\omega^2\left(e^{ib}a' + iae^{ib}b'\right) - i\omega^3\Omega_0^2\left(e^{ib}a' + iae^{ib}b'\right) + i\omega\left(e^{ib}a' + iae^{ib}b'\right) = 0
\end{aligned}
\tag{4.33}
$$

where $ccc = 1 - \cos k$. Separating the real and imaginary parts reveals the following equations

$$
f + ga' + hab' = 0 \tag{4.34}
$$

$$
l - ha' + gab' = 0 \tag{4.35}
$$

where f, g, h, and l are defined as

$$
\begin{aligned}
g = -\frac{1}{2}\omega &\left(\alpha_2\omega\left(\Omega_0^2\left(\bar{k}\left(\alpha_1(-\mathrm{Im}[\Gamma])\mathrm{Im}[K_\omega] + (\alpha_1\mathrm{Re}[\Gamma] - 2)\,\mathrm{Re}[K_\omega] - 2\right) + 2\omega^2\right) - 2\right) \right. \\
&\left. + 2\Omega_0^2\bar{k}\mathrm{Im}[K_\omega] - \alpha_1\alpha_3\omega\left(\Omega_0^2\bar{k}\left(\mathrm{Re}[K_\omega] + 2\right) + 2\right)\right)
\end{aligned}
\tag{4.36}
$$

$$
h = \frac{1}{2}\omega\left(\Omega_0^2\left(\bar{k}\left(\mathrm{Re}[K_\omega]\left(\alpha_1\alpha_2\mathrm{Im}[\Gamma]\omega - 2\right) + \omega\mathrm{Im}[K_\omega]\left(\alpha_2\left(\alpha_1\mathrm{Re}[\Gamma] - 2\right) - \alpha_1\alpha_3\right) - 2\right) + 2\omega^2\right) - 2\right)
\tag{4.37}
$$

$$
f = \frac{3}{2}a^3\alpha ccc\left(\omega^2\Omega_0^2 - 1\right) \tag{4.38}
$$

$$l = \frac{1}{2}(-3)a^3 \alpha ccc\omega \left(\alpha_2 \left(\omega^2 \Omega_0^2 - 1 \right) - \alpha_1 \alpha_3 \right) \tag{4.39}$$

It is noteworthy here that only f and l are function of vibration amplitude. One can

solve Eqs. (4.34)-(4.36) to obtain

$$a' = \frac{lh - fg}{g^2 + h^2} \tag{4.40}$$

$$ab' = -\frac{gl + mh}{h^2 + g^2} \tag{4.41}$$

Therefore, the slow flow equations can be written in the following form

$$a' = c_0 a^3 \tag{4.42}$$

$$ab' = c_1 a^2 \tag{4.43}$$

where c_0 and c_1 are constants. These slow flow equations are nonlinear and need to be solved

in order to determine the correction term for the nonlinear frequency.

4.2.3   Approximate solution for slow flow equations

To obtain an approximate solution, we plot the values of c_0 and c_1 over the frequency range

in Fig. 4.2 for $\epsilon\alpha = 0.06$, $\bar{k} = 1$, $\omega_n = \omega_d = 1000$ rad/sec, $k_1 = 10^6$ N/m, $R = 100\Omega$,

$\theta = 171 \times 10^{-12}$ N/V, and $C_p = 13.3 \times 10^{-9}$ F. One can observe that the values of c_0 are

too small and almost negligible comparing to the values of c_1 in the acoustic and optical

modes. This indicates that one can safely assume that $a' = 0$ and as a result the amplitude

is constant $a = a_0$. Therefore, the correction factor can be written as

$$b' = c_1 a_0^2 \tag{4.44}$$
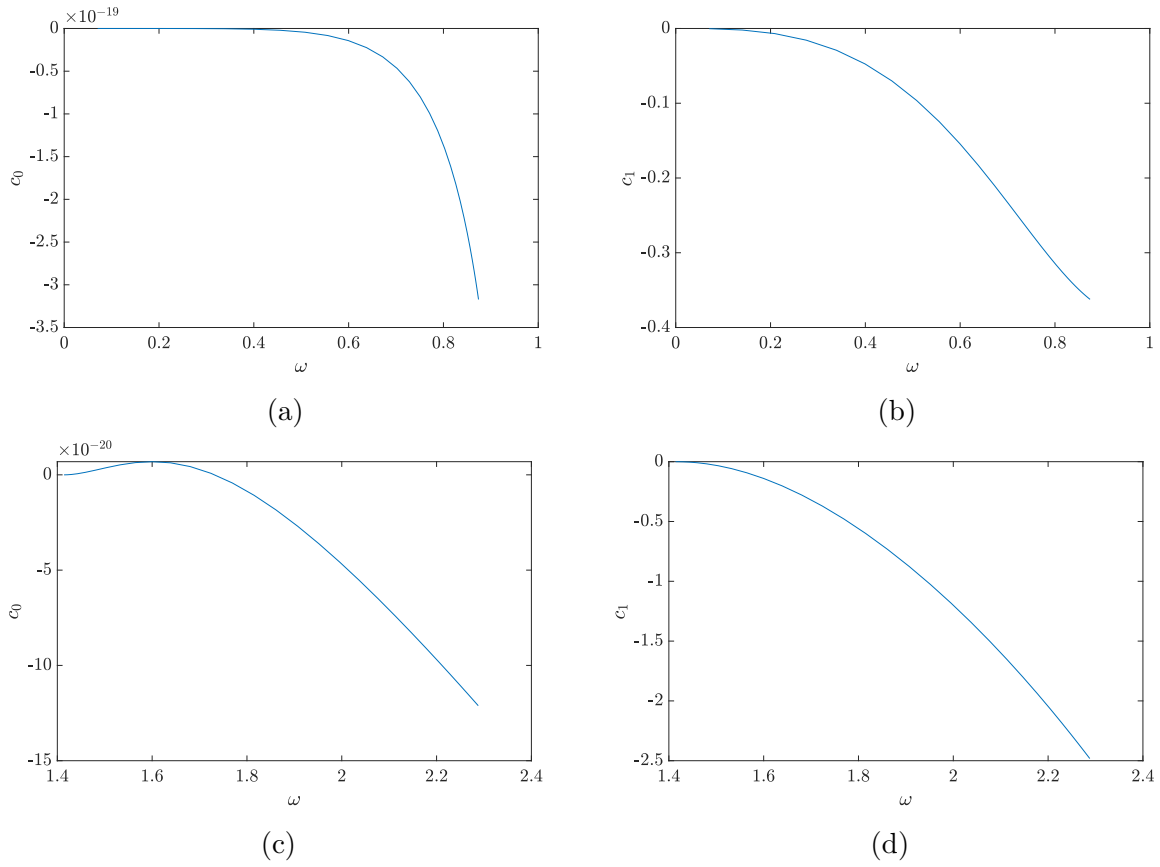
Figure 4.2: Values of c_0 and c_1 over the frequency range (a)-(b): acoustic mode; (c)-(d): optical mode.

Integrating the differential equation yields

$$b = c_1 a_0^2 T_1 \tag{4.45}$$

and the nonlinear frequency can be written as

$$\omega_{nl} = \omega - \epsilon b' \tag{4.46}$$
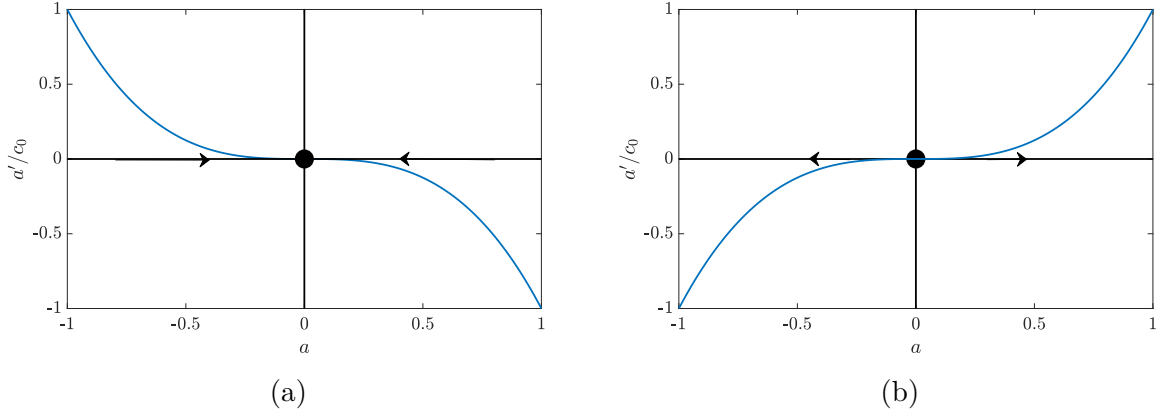
Figure 4.3: Phase portrait of a' and a for different values of c_0 (a): negative c_0; (b): positive c_0.

For large c_0, the amplitude can be determined as

$$a = \sqrt{\frac{-1}{2(c_0 T_1 + c)}} \tag{4.47}$$

where $c = \frac{-1}{2a_0^2}$. When c_0 is negative, the value under the square root is always positive; therefore, Eq. 4.47 is also a solution of the system for $T_1 > 0$. However, if c_0 is positive the square root has a solution only if $c_0 T_1 > \frac{1}{2a_0^2}$. Otherwise, the trivial solution is the only possible solution.

We plot the phase portrait for the first order system for positive and negative values of c_0 in Fig. 4.3. The results indicate that the stable solution associated with negative c_0 will reach 0 eventually; therefore, the trivial solution is always the only stable solution. On the other hand, the system departs from zero when c_0 is positive, which is not defined when $c_0 T_1 > \frac{1}{2a_0^2}$. Therefore, the system will also reach 0 eventually and only the trivial solution is stable.

4.3 Effect of electromechanical resonator on the band structure

In this section, we investigate the effect of the electromechanical coupling on the boundaries of the metastructure's bandgap. In particular, we fix the parameter of the metastructure and local resonator and we change the values of resistor if not mentioned otherwise. These parameter are defined as $\bar{k} = 1$, $\omega_n = \omega_d = 10^3$ rad/sec, $k_1 = 10^6$ N/m, and $C_p = 13.3 \times 10^{-9}$ F. These parameters are chosen based on similar studies in [195] and [55].

4.3.1 Validation of the approximate analytical solution

To check the accuracy of the current analytical solution derived by the method of multiple scales, we first compare our results with those obtained for nonlinear chain in the absence of electromechanical coupling using the Lindstedt-Poincare method. This can be obtained by setting the load resistor and piezoelectric constant to zero. Therefore, the problem is reduced to the classical chain with mechanical resonator instead of the electromechanical resonator. The comparison for both solutions are shown in Fig. 4.4-a. The results show a very good agreement with those in the literature.

Next, we consider the electromechanical coupling by shunting the system to a resistor. The analytical results here are validated numerically. We simulate a chain consisting of 500 cells, connected by nonlinear springs, and coupled to electromechanical resonators. The parameters of the chain are similar to those in the previous section. The simulation is conducted by integrating the governing equation numerically by Matlab built-in solver ODE45. To omit any reflective waves, we apply Perfectly Match Layers (PML) at each end of the chain [133]. The chain is excited by a transient wave packet. We select the velocity of the

wave packet to force the wave to propagate in one direction. Therefore, the wave packet is
defined as

$$u_m(0) = \frac{1}{2}(H(m-1) - H(m-1-N_{cy}2\pi/k))(1 - \cos(mk/N_{cy}))\sin(mk) \qquad (4.48)$$

$$\dot{u}_m(0) = \frac{1}{2}(H(m-1) - H(m-1-N_{cy}2\pi/k))(-\omega_n\omega/N_{cy}\sin(mk/N_{cy})\sin(mk)-$$
$$\omega_n\omega(1 - \cos(mk/N_{cy}))\cos(mk)) \qquad (4.49)$$

$$y_m(0) = K_\omega u_m(0) \qquad (4.50)$$

$$\dot{y}_m(0) = K_\omega \dot{u}_m(0) \qquad (4.51)$$

$$v = \Gamma K_\omega u_m(0) \qquad (4.52)$$

where N_{cy} is the number of cycles and in our numerical simulations we set $N_{cy} = 7$, and
$H(x)$ is the Heaviside function.

After simulating the system at any wavenumber, we determine the 2D Fourier trans-
form (2DFFT) of the data in the frequency and wavenumber domains. Then the natural
frequency of the system is the frequency associated with the maximum power density point.
By sweeping the wave number over the first Brillouin zone, one can numerically reconstruct
the dispersion curves from the obtained sets of wavenumbers and frequencies. It is notewor-
thy here that each of the optical and acoustic modes can be obtained separately by exciting
the system at frequencies close to the required mode frequencies.

We plot the numerical dispersion curves for different load resistors in Fig. 4.4-b. We
present only two values of resistor since other cases have similar dispersion curves. The
numerical results also show a good agreement with the analytical results in the presence of
the electromechanical coupling. However, the analytical solution fails to predict the middle
branch of the optical mode. In this region, there is a significant frequency shift (as we will

show in the subsequent sections) associated with transient wave packets excitation. This region is called Pseudo-bandgap [195].
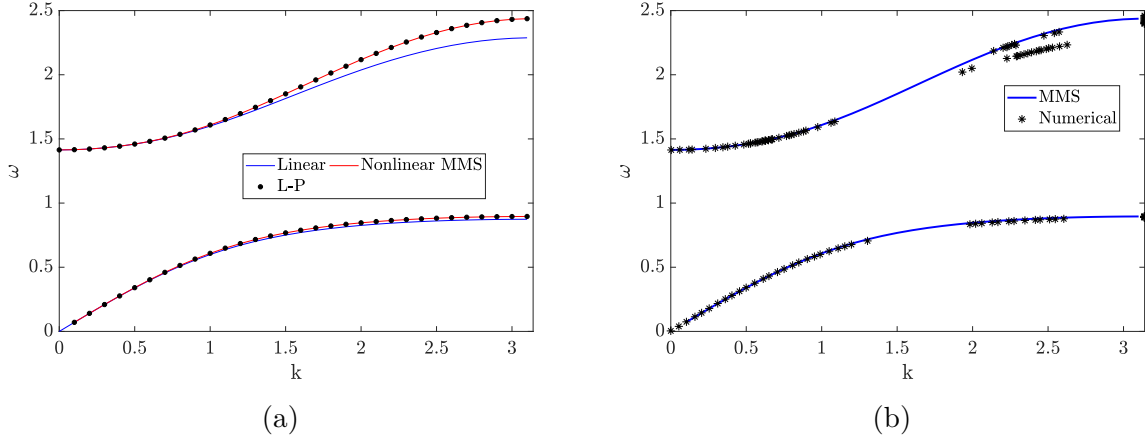
Figure 4.4: Validation of the analytical results (a): without electromechanical coupling using [195]; (b): with electromechanical coupling using numerical simulations for $\theta = 10^{-10}$ N/V, $R = 10^4\Omega$.

4.3.2   Linear band structure

When the problem is linear, we plot the dispersion curves with and without electromechanical coupling in Fig. 4.5. Unlike the chain with damping [80], it can be observed that shunting the electromechanical resonator to a load resistor does not affect the band structure of the metastructure for the weak electromechanical coupling case as shown in Fig. 4.5-a. Hence, harvesting the power has no role in controlling the boundary of the bandgap although it may change the attenuation level inside the bandgap (see Fig. 4.5-b). This indicates that metastructures can be used for simultaneous energy harvesting and vibration mitigation without degrading the bandgap boundary when the electromecanical coupling is weak.

For larger electromechanical coupling values up to $\theta = 10^{-3}$ N/V, the electromechanical coupling has also no noticeable effect on the band structure for different shunted load

resistors. However, for $\theta \geq 10^{-2}$ N/V the band structure starts deforming and emerging into one dispersion curve branch instead of two as shown in Fig. 4.5-c. Therefore, the bandgap disappears at this level of electromechanical coupling. Moreover, the shunted resistor has a significant role in the dispersion curve shape at this level of electromechanical coupling as shown in Fig. 4.5-d.
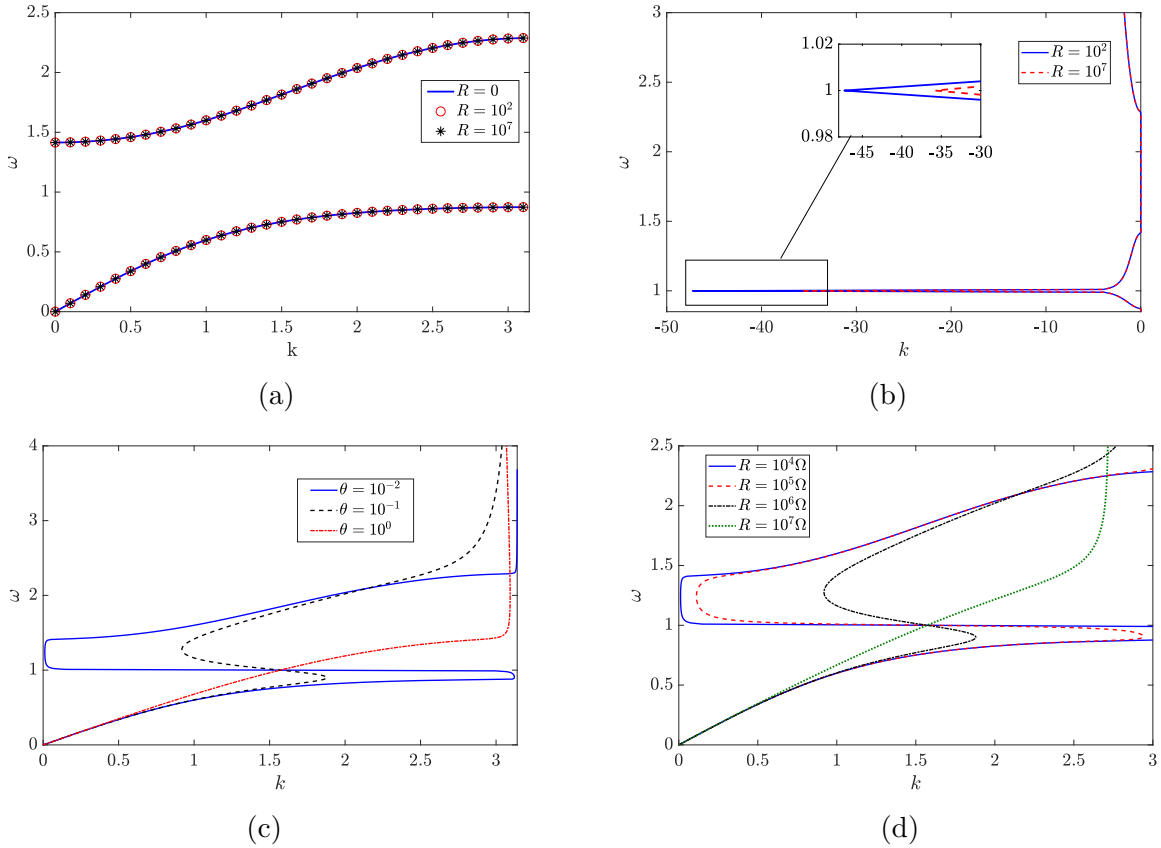
Figure 4.5: The effect of electromechanical coupling on the band structure in linear chain. (a): Weak electromechanical coupling $\theta = 10^{-10} N/V$; (b): Imaginary part of the band structure $\theta = 10^{-10}$ N/V; (c): Strong electromechanical coupling vlaues when $R = 10^2 \Omega$; (d): Effect of resistor on strong electromechanical coupling, $\theta = 10^{-2}$ N/V.
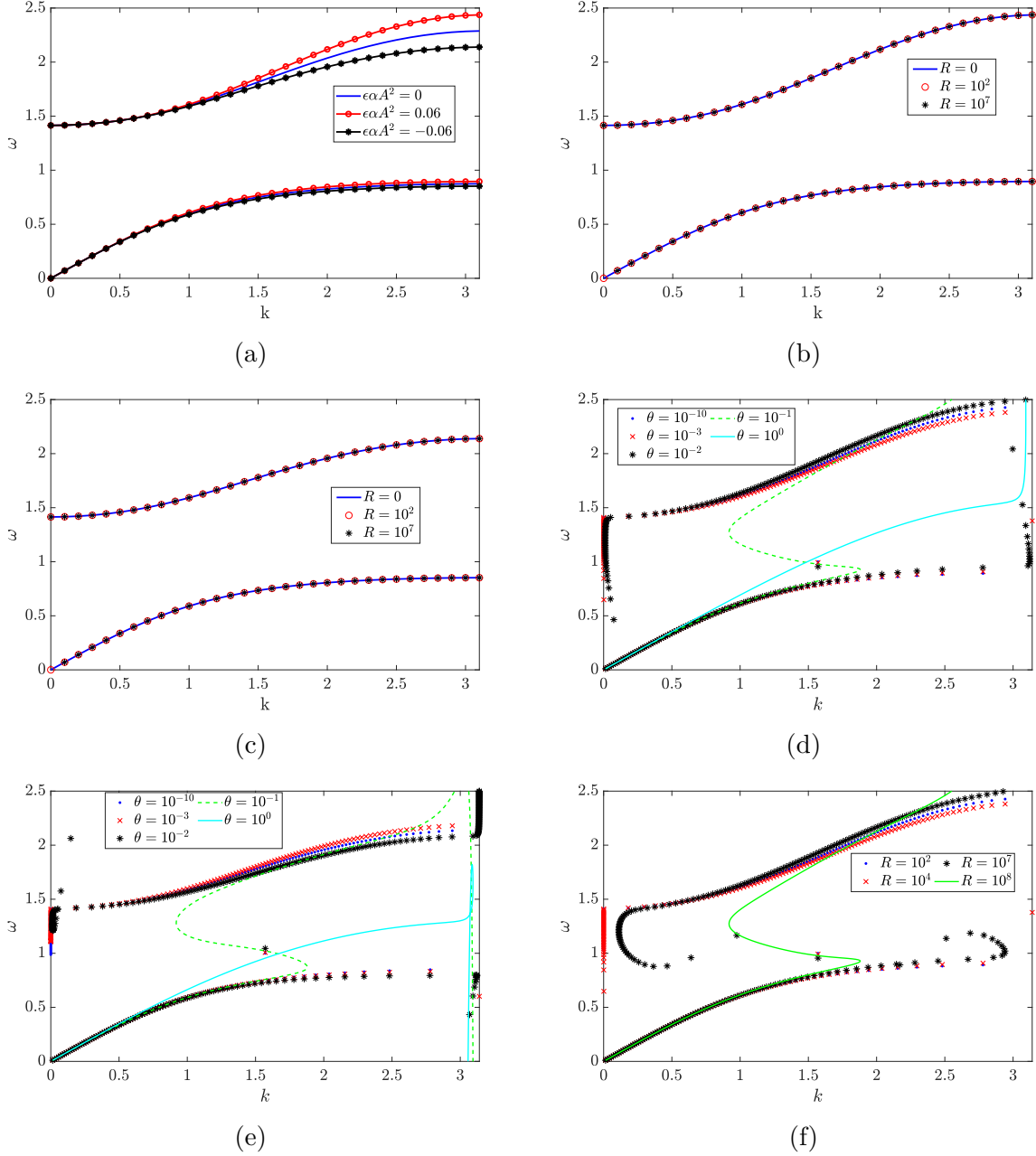
Figure 4.6: The effect of electromechanical coupling on the band structure in nonlinear chain. (a): In the absence of electromechanical coupling; (b): Hardening nonlinearity with weakly electromechanical coupling $\theta = 10^{-10} N/V$; (c): Softening nonlinearity with weakly electromechanical coupling $\theta = 10^{-10} N/V$; (d): Hardening nonlinearity with strong electromechanical coupling $R = 10^4 \Omega$; (e): Softening nonlinearity with strong electromechanical coupling $R = 10^4 \Omega$; (f): Effect of resistor on strong electromechanical coupling, $\theta = 10^{-3} N/V$.

4.3.3   Nonlinear band structure

When the problem is nonlinear, we first plot the dispersion curves in the absence of elec-tromechanical coupling for different types of nonlinearities in Fig. 4.6-(a). It can be observed that hardening nonlinearity shifts the dispersion curves up while softening nonlinearity shifts the curves down. Moreover, this shift is more significant in the optical mode. Next, we plot the dispersion curves with electromechanical coupling in Fig. 4.6-(b)-Fig. 4.6-(f). For both types of nonlinearities (hardening and softening) with weakly electromechanical coupling (Fig. 4.6-(b) and Fig. 4.6-(c)), it can be revealed that the effect of electromechanical cou-pling is negligible on the bandgap boundaries and only the nonlinearity in the chain shifts it. Therefore, one can also use metastructures for simultaneous energy harvesting and vibration reduction when the chain is nonlinear without affecting the bandgap boundaries. It is note-worthy here that these observations only hold for electromechanical coupling coefficient of $10^{-10} < \theta < 10^{-3}$ N/V. Similar to the linear case, stronger electromechanical coupling (i.e., $\theta \geq 10^{-3}$ N/V) also alters the band structure of nonlinear systems as shown in Fig. 4.6-(d) and Fig. 4.6-(e). Moreover, the band structure for θ ranging between 10^{-3} and 10^{0} N/V significantly depends on the shunted resistor unlike the case of weakly electromechanical coupling.

In the subsequent sections, our study will focus on the weakly electromechanical coupling case because θ depends on the piezoelectric constant which is usually at the order of 10^{-10} for most engineering applications [55].

4.4   Spectro-spatial analysis

In the previous section, we showed that weakly electromechanical coupling has no effect on the band structure in both linear and nonlinear chains. Nevertheless, the nonlinearity in the chain shifts the dispersion curves up or down depending on the type of nonlinearity. However, the dispersion characteristics do not reveal enough detailed information about nonlinear wave propagation phenomena except frequency shifts. Therefore, we employ the spectro-spatial analysis in this section to demonstrate other nonlinear wave propagation phenomena, particularly, wave distortion represented by wave localization or wave dispersion in nonlinear medium. This is done by analyzing the numerical data by different signal processing tools as it will be shown in the subsequent subsections.

4.4.1   Spatial profile of the wave packet

The wave profile of the output voltage and the voltage in the input cell is plotted in Figs. 4.7-4.8 for different load resistors and different wave limits. It should be noted that the input voltage is determined using Eq. (52) and the output voltage is calculated using numerical integration. Considering the acoustic-mode wave in the long wavelength region, Fig. 4.7-a shows that the harvested power decays through the chain for both linear and hardening nonlinear chains. This is not surprising since the frequency of the wave packet is away from the electromechanical resonator frequency. This figure is a mirror image of the wave profile of a wave propagating in a nonlinear chain since the effect of nonlinearity is negligible in the long wavelength limit. However, at frequencies close to the resonator frequency in the long wavelength limit (optical mode), the harvested voltage wave propagates through the structure as shown in Fig. 4.7-b. Yet the nonlinearity is negligible in this wavelength limit of the optical branch.

For the acoustic branch in the medium wavelength domain (Fig. 4.7-c), the dispersion curve is nonlinear (i.e., variable slope) and hence as expected, the wave is dispersive and its amplitude decreases significantly when the chain is linear. For the hardening nonlinear chain, the wave is split into two components; one is dispersive with low amplitude and the other is localized with high amplitude (solitary) wave. The solitary wave obtained from the nonlinear chain exhibits the highest output voltage as compared to the linear and softening nonlinear chains. The softening nonlinear chain stretches the dispersive wave, thus resulting in the lowest output voltage as compared to the linear and nonlinear hardening chains. Nevertheless, the number of cells engaged in energy harvesting at specific time are higher than those in the linear and hardening nonlinear chains.

For the optical mode in the medium wavelength limit, Fig. 4.7-d shows that the wave still has two different magnitude components for the hardening nonlinearity case, but the output voltage of the localized wave is not significantly higher that of the linear chain. Yet the higher amplitude component in hardening nonlinear chain in this case is more localized than that of the acoustic mode wave of Fig. 4.7-c. Fig. 4.7-d also shows that the softening nonlinear chain lowers the amplitude of the localized component and stretches the other wave component over more cells.

In the short wavelength region (Fig. 4.7-e for the acoustic mode and Fig. 4.7-f for the optical mode), it can be noted that the linear wave is more dispersive since the dispersion curve in this region is strongly nonlinear (refer to Section 4.3 for more details). However, the effect of nonlinearity is more significant in localizing the wave for the hardening nonlinearity case and stretching the wave for the softening nonlinearity case. These results suggest that higher power amplitude solitary waves are developed when the nonlinearity is hardening while more cells are engaged in energy harvesting when the nonlinearity is softening.

Finally, we show the spatial profile of the harvested voltage due to wave packet excitation

at lower electromechanical coupling in Fig. 4.8. The general observations discussed for the case of $R = 10^7\Omega$ and $\theta = 10^{-8}$ N/V holds here. However, some of the spatial profiles are slightly different, especially for the acoustic mode in the long wavelength limit. This indicates that the load resistor has a slight effect on the spatial profile of the wave propagation.

4.4.2 Spatial short term Fourier transform of wave motion

In this section, we plot the short term Fourier transform (STFT) to investigate the change in wave characteristics over time in the space domain as depicted in Fig. 4.9 and Fig. 4.10 for the acoustics and optical modes, respectively. We use a Hann window with the size of input burst to contain the short spatial components over time. This Hann window is represented by a signal between dashed lines in the figures. It is noteworthy here that we only consider medium and short wave lengths in this section since the previous section revealed that nonlinearity has no affect in the long wave length domain. These analyses are carried out on a chain coupled to $R = 10^7\Omega$ load resistors.

For the acoustic-mode wave propagating in a linear chain (Fig. 4.9-a for $k = \pi/2$ and Fig. 4.9-b for $k = 7\pi/9$), the voltage output is dispersive and has only one component with low amplitude. Moreover, it can be observed that the stretching of the wave is more severe at shorter wavelengths. It should be noted here that we plot the input signal in addition to the output signal; therefore, the reader can recognize the wave distortion. Furthermore, for better visualization of the output signal amplitude, we can compare the ratio between the output to the input signal to demonstrate the increase or decrease in wave amplitude. For instance, output voltage wave amplitude in Fig. 4.9-b is lower than that in Fig. 4.9-a since the input signal in the former case is lower.

For the nonlinear chain, two different behaviors are observed for different types of
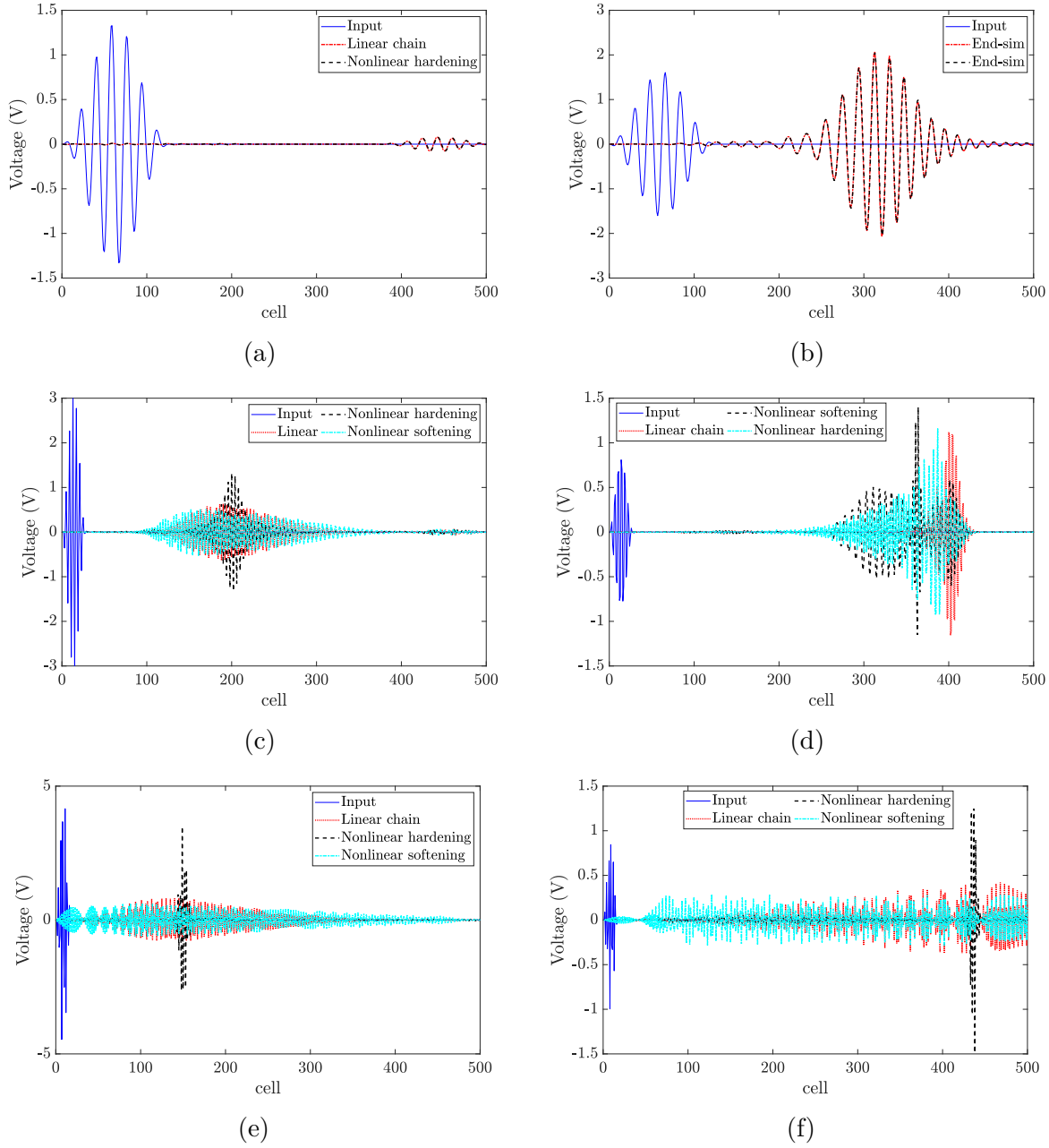
Figure 4.7: Spatial profile of the wave packet of harvested voltage from electromechanical resonator, $R = 10^7 \Omega$, $\theta = 10^{-8}$ N/V; (a): $k = \pi/9$ acoustic mode, (b): $k = \pi/9$ optical mode, (c): $k = \pi/2$ acoustic mode, (d): $k = \pi/2$ optical mode, (e): $k = 7\pi/9$ acoustic mode, (f): $k = 7\pi/9$ optical mode.

nonlinearities. For hardening nonlinearity (Fig. 4.9-c for $k = \pi/2$ and Fig. 4.9-d for $k = 7\pi/9$), solitary waves are developed, thus the output voltage is higher and localized within a
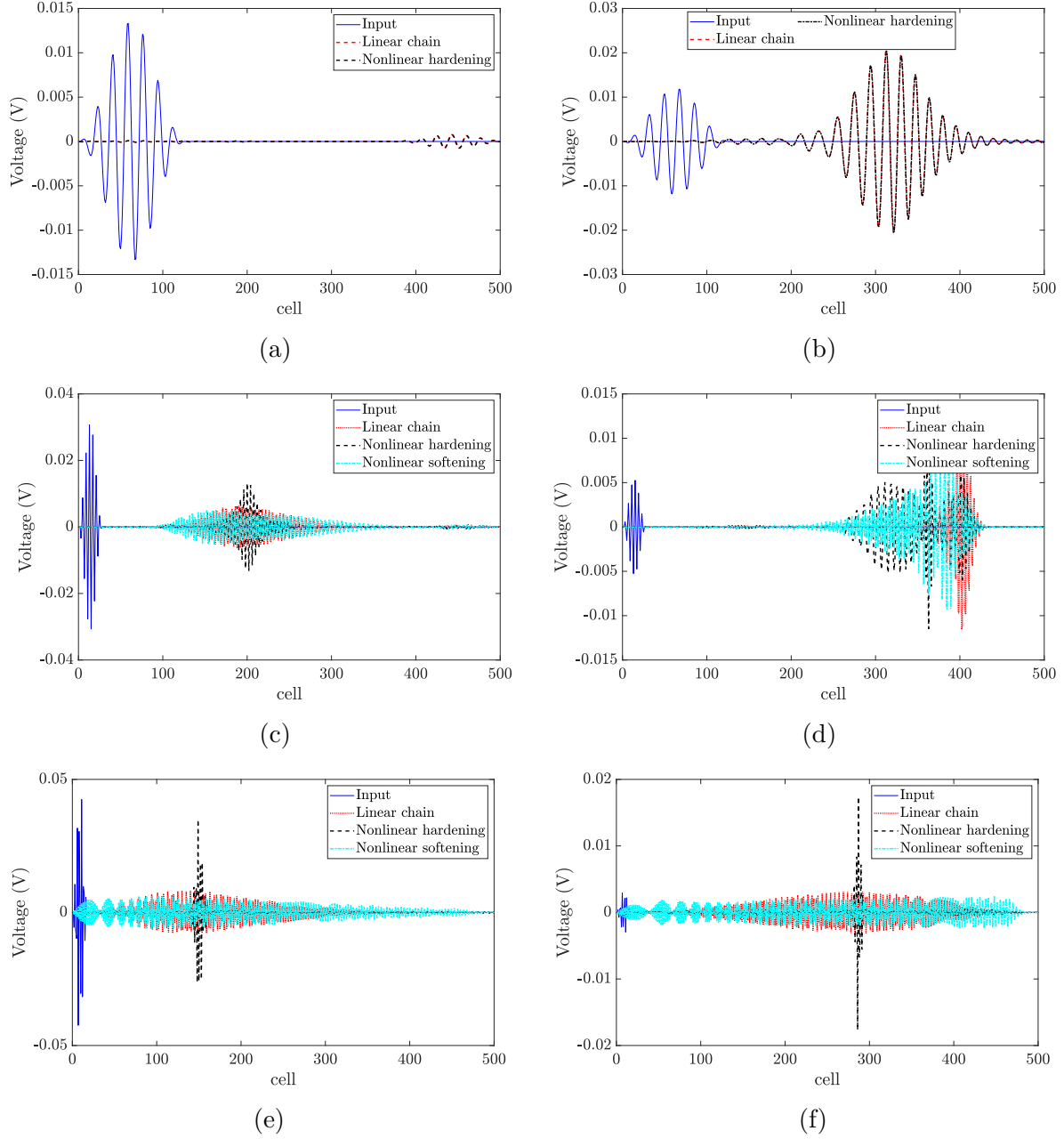
Figure 4.8: Spatial profile of the wave packet of harvested voltage from electromechanical resonator, $R = 10^7\Omega$, $\theta = 10^{-10}$ N/V; (a): $k = \pi/9$ acoustic mode, (b): $k = \pi/9$ optical mode, (c): $k = \pi/2$ acoustic mode, (d): $k = \pi/2$ optical mode, (e): $k = 7\pi/9$ acoustic mode, (f): $k = 7\pi/9$ optical mode.

few number of cells. However, the effect of hardening nonlinearity is more significant in the shorter wavelength limit and some of its energy is shifted outside the Hann window limits

as shown in Fig. 4.9-d. For softening nonlinearity (Fig. 4.9-e for $k = \pi/2$ and Fig. 4.9-f for $k = 7\pi/9$), the output voltage wave is stretched over the chain. This wave has lower amplitude than the linear case. It is also observed here that the effect of nonlineariy becomes more significant with reducing the wavelength. Moreover, some of the energy content is shifted below the Hann window limits. In general, we observe that the output voltage wave is attenuated through the chain at all wavelength regions of the acoustic mode; however, wave amplitude is almost at the same order of magnitude of the input wave amplitude in hardening nonlinear chain at short wavelength.

For the optical mode wave, we show STFT in Fig. 4.10. In general, the output voltage wave propagates at higher amplitudes through the chain in all wavelength limits. Yet this propagation depends significantly on the type of nonlinearity and wavelength. For a wave propagating in a linear chain at medium wavelength (Fig. 4.10-a), it can be observed that the wave is not dispersive and has a significant amplitude localized wave unlike the behavior observed in the same wavelength region of the acoustic mode. However, the wave is clearly dispersive at shorter wavelengths as depicted in Fig. 4.10-b for the linear chain.

For the optical branch in the medium wavelength region, (Fig. 4.10-c and Fig. 4.10-d), the output voltage wave is severely distorted and brakes down into multiple components. For hardening nonlinearity, the output wave has three components. The first component has low wavenumber and the wave is dispersive with low amplitude. The second component lies inside the Hann window (linear limit) and the wave is also dispersive. As for the third component, most of the energy content is shifted above the Hann window due to hardening nonlinearity. The latter represents a solitary wave. For softening nonlinearity (Fig. 4.10-d), the output voltage wave is broken into two components. The first component has a high wavenumber and the wave is dispersive with low amplitude. However, most of the energy of the linear wave is shifted significantly below the Hann window. In both types of nonlinearity,

we observe a significant frequency shift for the optical branch in the medium wavelength limit since most of the output energy dilates outside the input signal frequency confined within the Hann window.

Finally, we investigate the wave distortion for the optical branch in the short wavelength domain (Fig. 4.10-e and Fig. 4.10-f). The results indicate that the behavior of this mode is similar to that of the acoustic mode in the short wavelength limit. The hardening nonlinearity develops a localized solitary wave, which has a voltage amplitude much higher than the linear case as shown in Fig. 4.10-e. On the other hand, softening nonlinearity stretches the wave significantly in this wavelength limit. The resulting wave is dispersive with low amplitude. It is noteworthy here that, for the nonlinear chain, some of the energy content is shifted outside the limits of the input signal in the short wavelength region.

4.4.3   Contour plots of 2D Fourier transform

After analyzing the output voltage of the wave characteristics over time in the spatial domain, we investigate the frequency-wavenumber characteristics of the system in order to reconstruct the nonlinear dispersion curves and examine the Pseudo-bandgap observed in Fig. 4.4-b. This can be done by determining the 2D Fourier transform for the temporal and spatial components. We plot the contour lines of the results in frequency-wavenumber domain for the acoustic mode in Fig. 4.11 and optical mode in Fig. 4.12. To compare the distribution of the frequency-wavenumber component for different types of nonlinearity, we plot the output voltage power density with the same wavelength inside the same frequency-wavenumber band limit. We focus only on waves propagating in the medium and short wavelength regions since we have shown that the effect of nonlinearity is negligible in the long wavelength limit.

For the acoustic mode in the medium wavelength limit (Fig. 4.11-a, b, and c), it is
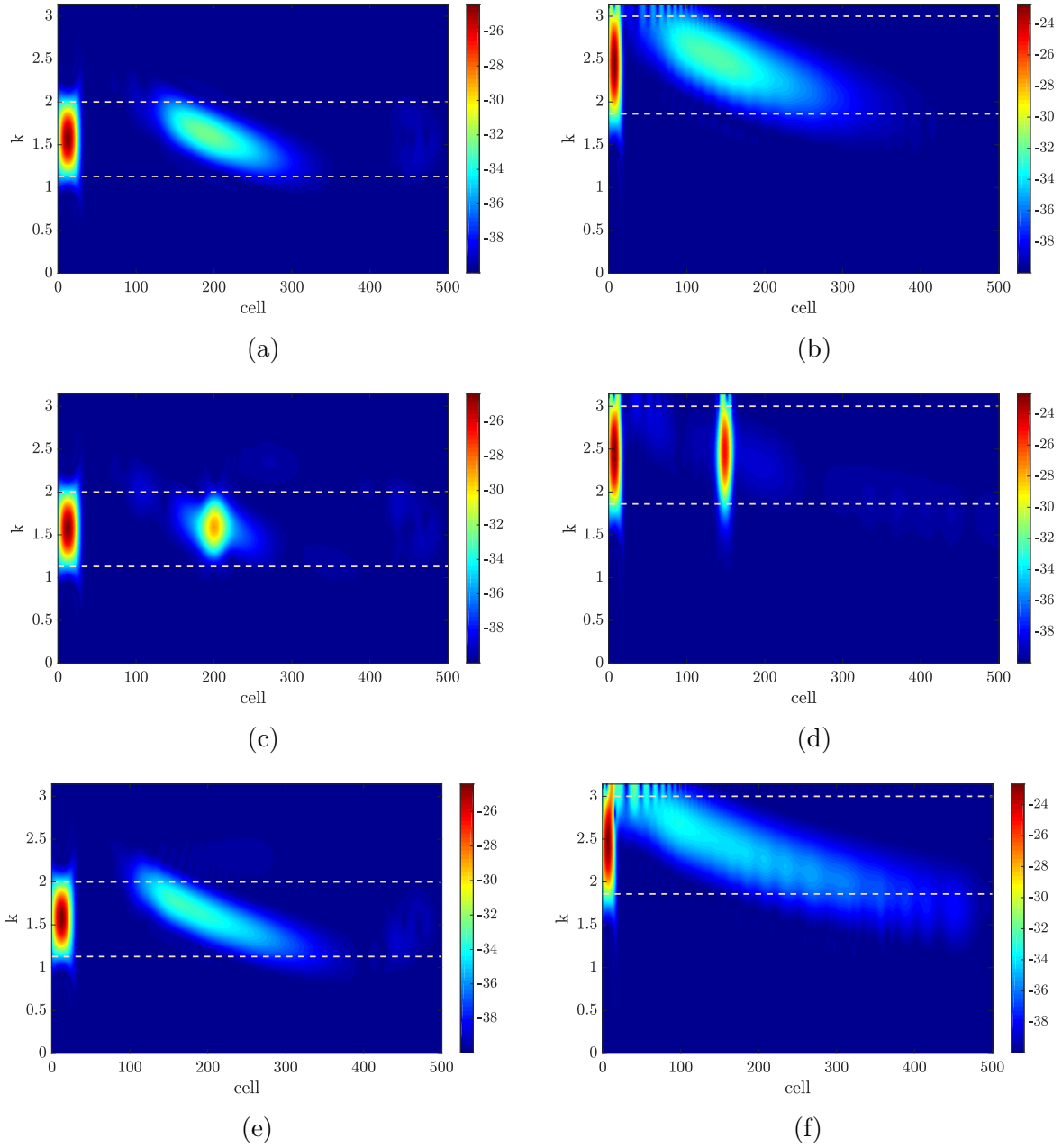
Figure 4.9: Short term Fourier transform for energy harvested in acoustic mode and for different types of nonlinearity, $R = 10^7\Omega$, $\theta = 10^{-10}$ N/V; (a): $k = \pi/2$, $\epsilon\alpha A^2 = 0$, (b): $k = 7\pi/9$, $\epsilon\alpha A^2 = 0$, (c): $k = \pi/2$, $\epsilon\alpha A^2 = 0.03$, (d): $k = 7\pi/9$, $\epsilon\alpha A^2 = 0.03$, (e): $k = \pi/2$, $\epsilon\alpha A^2 = -0.03$, (f): $k = 7\pi/9$, $\epsilon\alpha A^2 = -0.03$.

demonstrated that the hardening nonlinearity localized the output voltage power spectrum while the softening nonlinearity stretches it over a wider range of frequency-wavenumber.
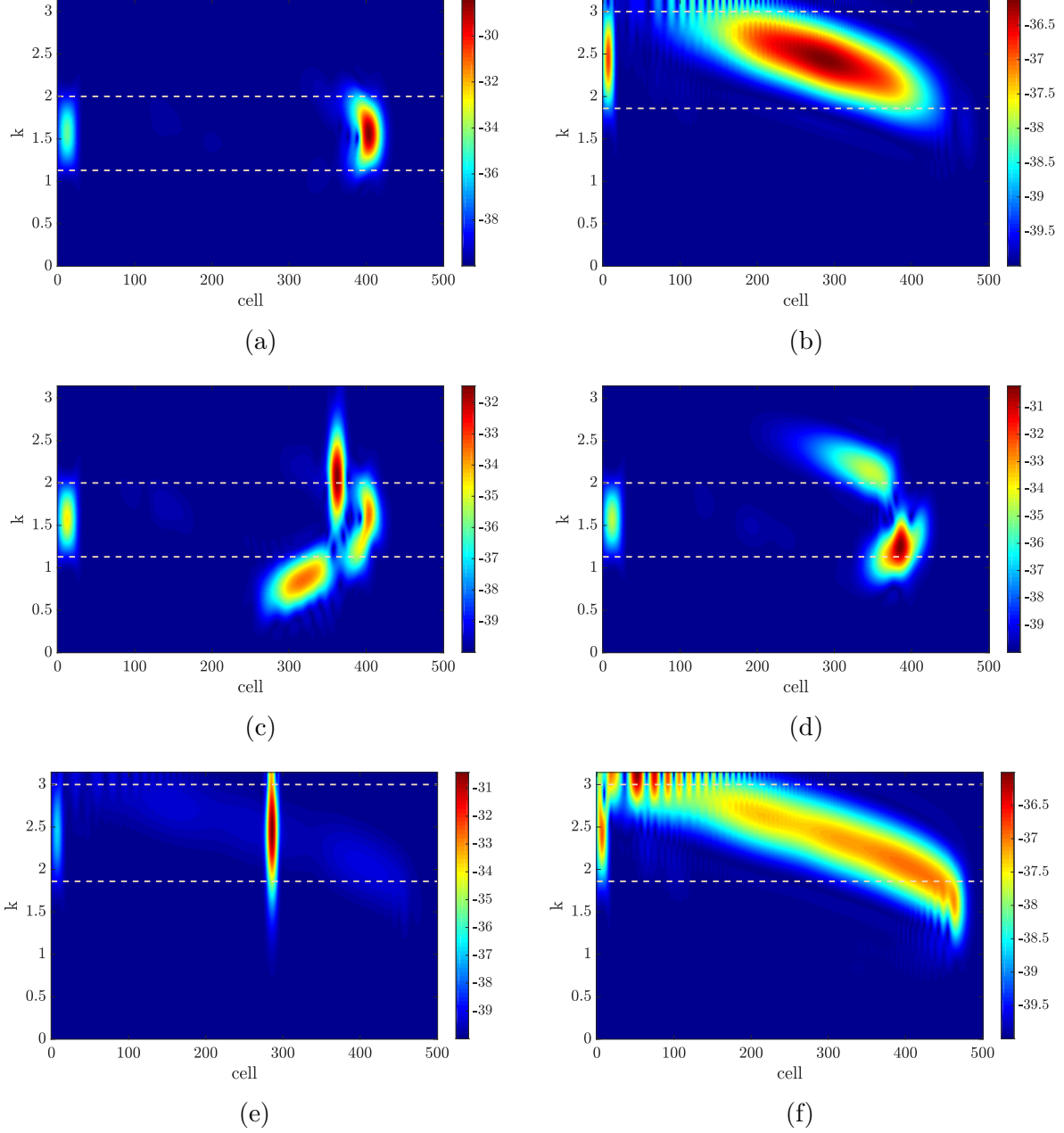
Figure 4.10: Short term Fourier transform for energy harvested in optical mode and for different types of nonlinearity, $R = 10^7\Omega$, $\theta = 10^{-10}$ N/V; (a): $k = \pi/2$, $\epsilon\alpha A^2 = 0$, (b): $k = 7\pi/9$, $\epsilon\alpha A^2 = 0$, (c): $k = \pi/2$, $\epsilon\alpha A^2 = 0.03$, (d): $k = \pi/2$, $\epsilon\alpha A^2 = -0.03$, (e): $k = 7\pi/9$, $\epsilon\alpha A^2 = 0.03$, (f): $k = 7\pi/9$, $\epsilon\alpha A^2 = -0.03$.

Moreover, it can be demonstrated that hardening nonlinearity bents the nonlinear dispersion curve (Fig. 4.11-a) to a less nonlinear dispersion curve while the softening nonlinearity bents
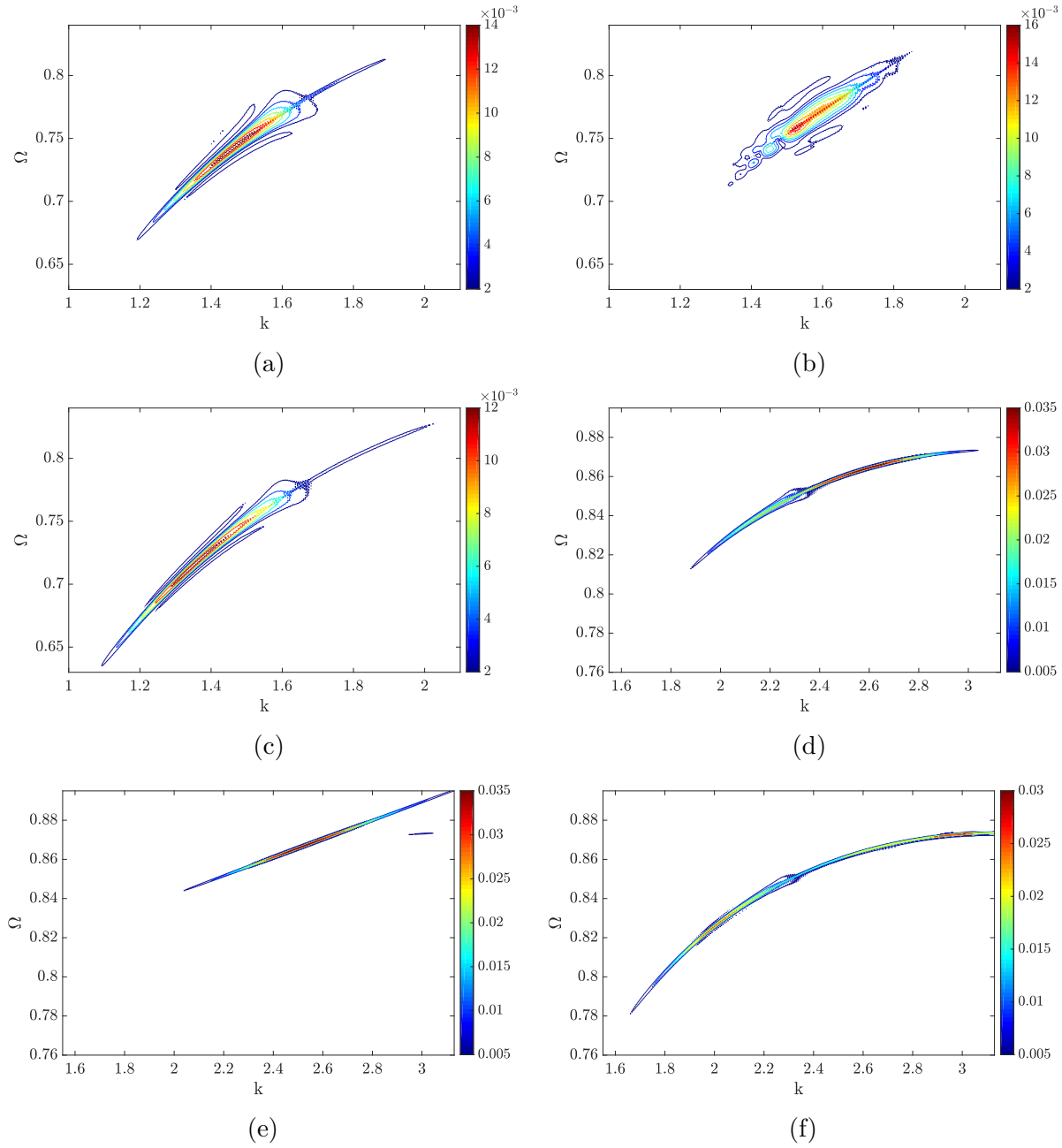
Figure 4.11: 2D Fourier transform for harvested voltage in acoustic mode, $\theta = 10^{-10}$ N/V, $R = 10^7 \Omega$; (a): $k = \pi/2$, $\epsilon \alpha A^2 = 0$, (b): $k = \pi/2$, $\epsilon \alpha A^2 = 0.03$, (c): $k = \pi/2$, $\epsilon \alpha A^2 = -0.03$, (d): $k = 7\pi/9$, $\epsilon \alpha A^2 = 0$, (e): $k = 7\pi/9$, $\epsilon \alpha A^2 = 0.03$, (f): $k = 7\pi/9$, $\epsilon \alpha A^2 = -0.03$.

the nonlinear dispersion curve to a more nonlinear dispersion curve; therefore, the wave becomes more dispersive. It is noteworthy that no significant frequency shift can be observed.
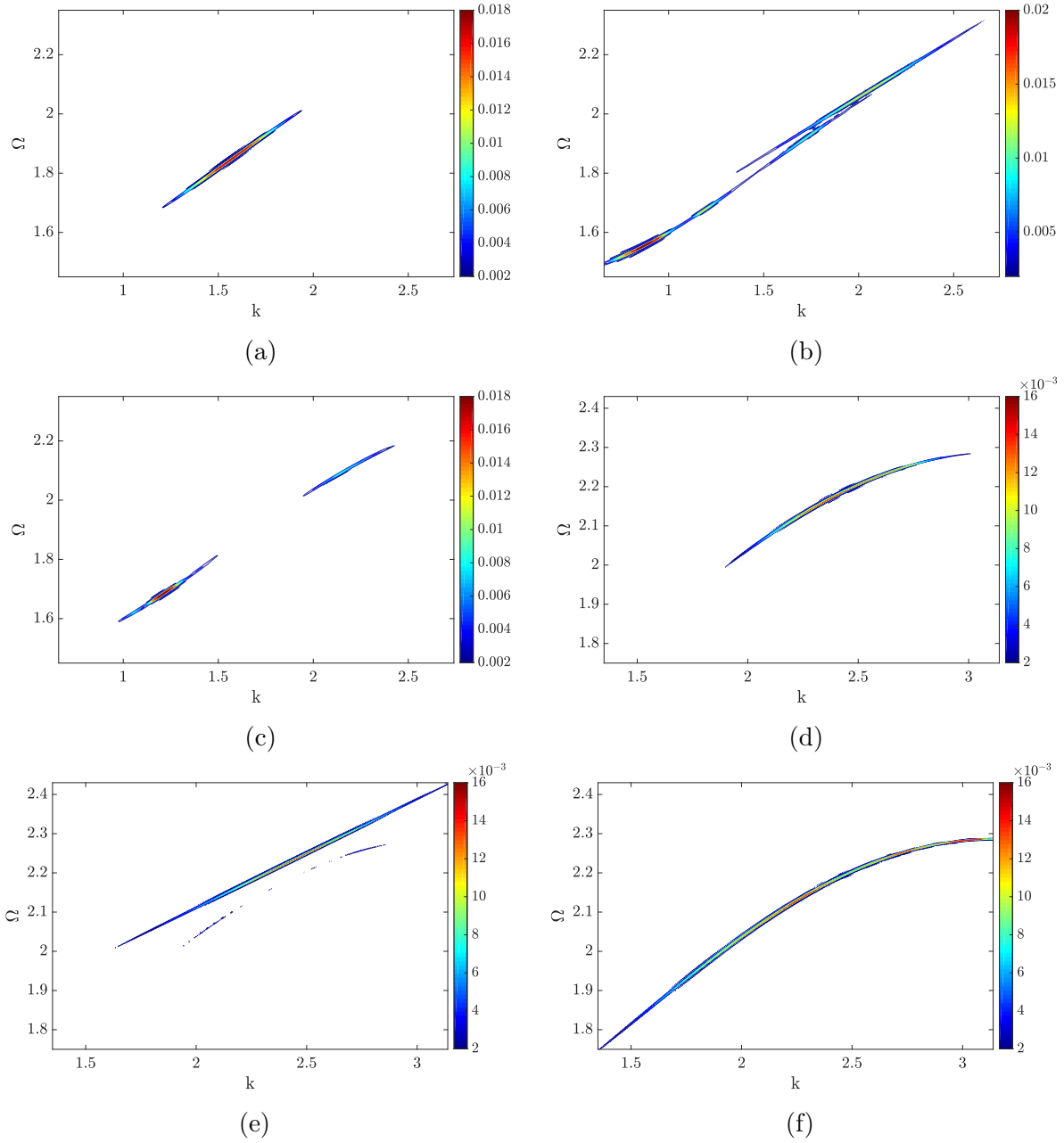
Figure 4.12: 2D Fourier transform for harvested voltage in optical mode, $\theta = 10^{-10}$ N/V, $R = 10^7 \Omega$; (a): $k = \pi/2$, $\epsilon\alpha A^2 = 0$, (b): $k = \pi/2$, $\epsilon\alpha A^2 = 0.03$, (c): $k = \pi/2$, $\epsilon\alpha A^2 = -0.03$, (d): $k = 7\pi/9$, $\epsilon\alpha A^2 = 0$, (e): $k = 7\pi/9$, $\epsilon\alpha A^2 = 0.03$, (f): $k = 7\pi/9$, $\epsilon\alpha A^2 = -0.03$.

For the same mode, but in the short wavelength region (Fig. 4.11-d, e, and f), similar behavior in localizing and stretching the power spectrum can be observed. However, the effect here

is more significant. For instance, the power spectrum in the case of hardening nonlinearity is almost linear which indicates the birth of solitons. On the other hand, power spectrum curves are more nonlinear in the case of softening nonlinear chain.

Next, we investigate the contour plots of 2D Fourier transform for the optical mode (Fig. 4.12). For the medium wavelength limit (Fig. 4.12-a, b, and c), we observe a significant frequency-wavenumber shift in the power spectrum contours for both types of nonlinearity. However, this shift is more pronounced in the case of hardening nonlinearity. It can be observed that the power spectrum is broken into mainly three components in the case of hardening nonlinearity while it is divided into two components in the case of softening nonlinearity. This is not surprising since we have observed this broken signal in STFT plots in the previous section. In Fig. 4.12-b, it is observed that the higher frequency component has most of the energy content; moreover, this component has a linear dispersion curve (i.e., constant slope), which indicates that there is a development of solitary wave. For the short wavelength limit (Fig. 4.12-d, e, and f), a frequency-wavenumber shift is also observed in the presence of nonlinearity; however, neither significant shift nor severe wave distortion is demonstrated in this wavelength region. When the chain has hardening nonlinearity (Fig. 4.12-e), the power spectrum of the output voltage is concentrated in a linear dispersion curve (strong soliton) and shifted to higher frequency values. Nevertheless, one can still observe some of the energy content appearing as nonlinear dispersion curves similar to those observed in the case of linear chain shown in Fig. 4.12-a. For softening nonlinearity Fig. 4.12-f, the power spectrum is shifted to lower frequency values. However, the energy content is not broken into multiple components, instead the signal is almost concentrated in one branch over wider band of frequency and wavenumber.

4.5   Discussion

Finally, we add some general comments about simultaneous energy harvesting or sensing and vibration attenuation in nonlinear metastructures based on the analyses carried out in the present study. The output voltage wave propagates to higher level through the chain only for the optical branch. However, the wave amplitude can be at the same level of input signal when the chain has hardening nonlinearity for the acoustic mode in the short wavelength limit. This is because solitary wave can be observed in this limit. The hardening nonlinearity can also convert the dispersive waves to solitary waves with higher voltage amplitude in the optical mode. On the other hand, softening nonlinearity stretches the voltage wave over the chain and reduces the amplitude. Therefore, higher voltage amplitude wave is predicted with hardening chain while low voltage amplitude is predicted with softening chain. However, the number of cells engaged in energy harvesting is higher in the latter case. Nonlinear chain also shifts the output signal frequency to higher or lower values at medium and short wavelengths when the nonlinearity is hardening or softening, respectively. However, this shift is significant for the optical mode in the medium wavelength limit. This significant shift is concentrated in shifting the higher power density component up or down while other lower value components can also be observed at different frequencies.

Nonlinear chains can be employed toward better simultaneous energy harvesting, sensing, and vibration attenuation. For instance, the significant increase in the voltage amplitude by hardening chain allows better and faster sensing of the input disturbance. In addition, the significant frequency shift can be utilized to design electromechanical rectifier [107]. This can be achieved by coupling such a nonlinear electromechanical chain with a linear electromechanical chain and tuning the frequency shift region to the bandgap of the linear chain. This will allow energy harvesting (sensing) and wave propagation in only one direction.

Finally, replacing some of the local electromechanical resonators by local mechanical resonators should preserve the performance of vibration attenuation in the structure. This is because the weak electromechanical coupling has no effect on the size of the bandgap. However, these local mechanical resonators must have equivalent dynamical properties as those of the local electromechanical resonators. Thus, only finite number of energy harvester can be considered. This will be more meaningful from the prospective of energy harvesting.

4.6   Conclusion

In this work, a nonlinear metastructure coupled to a linear electromechanical resonator was studied. The metastructure was modeled as a chain of masses connected by weakly nonlinear springs. The cells were coupled to electromechanical resonators which were also modeled as a spring-mass system and shunted to a load resistor. We employed the method of multiple scales to derive an analytical approximate solution for the nonlinear dispersion relations. These results were validated by direct numerical integration. The validation showed that the method of multiple scales can accurately predict the cut-off frequencies, but not the significant frequency shift in the medium wavelength limit of the optical branch. The analytical results indicated that neither the band structure of linear nor nonlinear chains were affected by the weakly electromechanical coupling. These findings suggest that energy harvesting does not degrade the vibration mitigation limits in metastructures. However, for very strong electromechanical coupling, the electromechanical coupling can alter the band structure. Nevertheless, these values of coupling coefficient are much higher than those in real life engineering applications.

We further investigated the nonlinear voltage output wave propagation by studying the spectro-spatial features using different signal processing techniques. This provided further

detailed information about different nonlinear phenomena based on the type of nonlinearity. The spatial profile of the output voltage wave demonstrated that the wave does not propagate for higher values comparing to input wave profile in linear chains. The effect of nonlinearity in nonlinear chains appeared as wave stretching in softening chain or wave localization in hardening chain. It was demonstrated that acoustic-mode wave in the short wavelength region can propagate with higher voltage amplitude only for the hardening nonlinear chain. Conversely, optical-mode wave in all wavelength regions can propagate with high voltage amplitude in both linear and nonlinear chains. Yet softening nonlinearity can stretch the wave while hardening nonlinearity can localize it. This wave distortion depends significantly on the wave length. The images of STFT demonstrated the output voltage wave distortion due to nonlinearity. The results indicated that there is a significant frequency shift at frequency-wavenumber located in the middle of the optical mode. Moreover, it was shown that the wave gets divided into multiple components in the medium wavelength limit. Furthermore, the spectro-spatial analysis revealed that the nonlinear dispersion curves can be reconstructed by contour of 2D Fourier transform. These contour plots demonstrated the birth of solitary waves in hardening nonlinear metastructures at medium and short wavelengths.

Finally, the observed significant frequency shift by spectro-spatial analysis in nonlinear metastructures can be employed to construct electromechanical diodes with simultaneous uni-direction energy harvesting and energy transfer.

Chapter 5

Substantial frequency conversion at long-wavelength limit in metamaterial with weakly nonlinear local electromechanical resonators: Analytical and computational study

Recent studies of nonlinear metatmaterials have shown interesting wave propagation phenomena including the birth of soliton, tunable bandgap, acoustic nonreciprocity and broadband energy harvesting. However, most studies are limited to nonlinear mechanical metamaterials and their applications in the short-wavelength limit. There is no study of nonlinear electromechanical metamaterials at the long-wavelength limit. The present work fills this gap through investigating a metamaterial with nonlinear local electromechanical resonators. An approximate analytical solution for the dispersion relations is obtained by

the method of multiple scales (MMS). This analytical solution is used to study the role of different system's mechanical and electromechanical parameters on the band structure. Other important nonlinear wave propagation characteristics are deduced by exploring the spectro-spatial features through different signal processing methods of the numerical results. The output voltage results demonstrate a significant wave distortion and frequency shift, particularly at the long-wavelength limit and other wavelength limits. Moreover, the results indicate an increase in the voltage output and the birth of solitary waves. Furthermore, the observed significant frequency shift at the long wavelength limit is demonstrated computationally using COMSOL Multiphysics. A nonlinear metamaterial is modeled and analyzed to demonstrate this phenomenon. These results suggest that such a system can enhance sensing and increase the operation range of electromechanical diode.

Chapter 5. Substantial frequency conversion at long-wavelength limit in metamaterial with weakly nonlinear local electromechanical resonators: Analytical and computational study

120

5.1   Introduction

Recent studies have shown that artificially engineered structures can offer exceptional properties that cannot be obtained by conventional homogeneous structures [84]. These structures are usually called metamaterials. The exciting properties of metamaterials include, but are not limited to: negative stiffness, negative mass, negative Poisson's ratio, and negative density (i.e., negative is associated with the effective parameter not to the parameter itself)[14]. The study of mechanical metamaterial was initially motivated by the development within the optics community [33]. Then, it was extended for acoustics [120] and elastic wave applications [84]. The unique characteristics of the mechanical metamaterial allow it to control noise and vibration, harvest energy, enable non-reciprocal wave propagation devices, and non-destructive testing.

For vibration attenuation applications, metamaterials draw their interesting properties from periodicity [160](i.e., phononic crystals) or through the embedded local resonators [110]. Periodic structures offer a low-frequency bandgap where waves with a wavelength near the lattice constant cannot propagate through the structure [97, 98, 99, 159, 160, 178]. This bandgap results from Bragg scattering. However, the limitations associated with the lattice dimension limit the application to large structures, and thus controlling smaller size structures requires different engineering configurations. This limitation can be overcome by embedding local resonators in locally resonant metamaterials by mode hybridization. This configuration showed the ability to attenuate waves with wavelengths much larger than the lattice constant [110]. Also, in the presence of periodicity, locally resonant metamaterials can form bandgap due to Bragg scattering and mode hybridization depending on the structure and local resonators parameters [109]. Yet bandgaps can be generated without Bragg scattering at a very low local resonator's frequency. Therefore, locally resonant metamaterials can also offer a frequency bandgap even in the absence of periodicity [4]. It is noteworthy

that multiple tuned frequency bandgaps can be obtained by utilizing different resonance frequency local resonators [78, 197].

With increasing amplitude of a wave propagating in an inherently nonlinear medium, the linear equation cannot adequately describe the problem, and nonlinear terms need to be considered. Nonlinear metamaterials can be handled using different techniques depending on the strength of nonlinearity. For weak nonlinearity, perturbation methods can be utilized to obtain an approximate converging closed-form solution [134, 135]. For example, Narisetti et al. utilized the Lindstedt-Poincare technique to obtain dispersion relation in discrete metastructure [133]. Moreover, the method of multiple scales (MMS) can handle more complex problems that include nonlinear interaction of multiple waves [119]. MMS can better address the problem due to reducing the required efforts associated with the algebra. Also, MMS is more convenient in handling higher-order perturbation [62]. On the other hand, strong nonlinearity in metamaterial can be treated by other techniques like homotopy analysis [1, 2, 90]. In addition to the accuracy obtained by considering nonlinear metamaterial, nonlinear metamaterials show interesting wave propagation phenomena beyond those observed in linear metamaterials, such as solitons [95, 131], non-reciprocal wave propagation [107], and tunable bandgaps [117].

The study of nonlinear metamaterials has been limited to obtaining the cut-off frequency through deriving the dispersion relations or investigating solitary waves at a short-wavelength limit. These investigations do not reveal the essential characteristics of the nonlinear wave propagation in metamaterials. Therefore, several studies in the literature employed spectro-spatial analysis to provide a better understanding of these essential properties [24, 27, 30, 63, 195]. Spectro-spatial features can provide detailed information on the local wave properties (e.g., solitary waves) or global wave properties (e.g., dispersion curves). Studies on spectro-spatial analyses have included studies on nonlinear periodic chains [63],

Chapter 5. Substantial frequency conversion at long-wavelength limit in metamaterial with weakly nonlinear local electromechanical resonators: Analytical and computational study

122

nonlinear locally resonant metamaterial [195], and locally resonant metamaterial with multiple local resonators with nonlinearity stemming from the chain or resonators [24, 27, 30]. These studies demonstrated the birth of solitary waves at short-wavelength limit, a significant frequency conversion at medium-wavelengths for transient excitation, and no effect of nonlinearity at long-wavelength limit in the case of the nonlinear chain [30]. Moreover, the investigations revealed that wave distortion could be obtained at all wavelength limits in the case of nonlinear resonator depending on the resonance frequency of the nonlinear local resonator [24, 27, 30]. These frequency shifts indicate that such nonlinear metamaterial can enable the design of acoustics diodes.

In addition to the superior performance of metamaterial in vibration attenuation, recent studies were motivated by the wide plateau band of frequencies in metamaterials to harvest energy [157]. The energy harvesting can be realized by installing electromechanical resonators instead of conventional local resonators for simultaneous energy harvesting and vibration attenuation [74]. Although earlier consideration of electromechanical coupling was to generate piezoelectric bandgap through the added stiffness [5, 13, 34, 173, 194], recent investigations showed the possibility of harvesting additional energy through this coupling [74, 75, 76, 157]. These investigations were conducted experimentally on locally resonant phononic plates [157] and 2D metamaterials [105], or theoretically on discrete systems [74], continuous systems [75], and coupled internal resonators [76].

To the best of our knowledge, recent studies on metamaterials for simultaneous energy harvesting and vibration mitigation were limited to investigating the linear problem. Only our previous work in [26] considered the effect of nonlinearity in such a problem. However, the nonlinearity in our previous work stems only from the nonlinear chain. This restricts the effect of nonlinearity for only short-wavelength limits, thus limiting the system applications to frequencies in this region (e.g., acoustics diodes, significant frequency shift). There is a

gap in the literature in extending nonlinear metamaterial's applications to frequencies at all wavelength limits in the presence of nonlinear electromechanical resonator for simultaneous energy harvesting and vibration reduction. Therefore, for the first time, we investigate a metamaterial with local electromechanical resonators with nonlinearity stemming from the resonator in the present study to fill this gap. This is also motivated by our previous work that has shown the possibility of significant frequency shifts at all wavelength limits in locally resonant metamaterial with nonlinearity in the conventional mechanical resonator [27]. In this paper, we employ analytical and different numerical signal processing techniques to investigate the local and global properties of the nonlinear wave features in the proposed metamaterial. The former is demonstrated through MMS to obtain a closed-form solution for the band structure. The latter is demonstrated through investigating the spectro-spatial features of the numerical results to reveal the birth of solitary waves, existing of significant frequency shift for non-reciprocal wave propagation applications, exploring the type of wave distortion, and validating the analytical results by reconstructing the band structure. These spectro-spatial analyses include spatial wave profile, spectrograms of Short term Fast Fourier Transform (STFT), and contours of 2D Fast Fourier transform (2D FFT). Parametric analyses are also conducted to study the effect of nonlinearity and electromechanical coupling parameters on the nonlinear wave propagation features in terms of wave amplitude and harvested power. Finally, we present the computational proof of this phenomenon: the presence of significant frequency shift at the long-wavelength limit in the proposed structure.

The rest of the current study is organized as follows: In Sec. 2, we present a mathematical model for the proposed metamaterial with nonlinear local electromechanical resonators. This is followed by the derivation of an analytical solution for the band structure. Then, we discuss the analytical findings in terms of the effect of different parameters on the bandgap size in Sec. 3. In Section 4, we study the spectro-spatial features of the output voltage wave
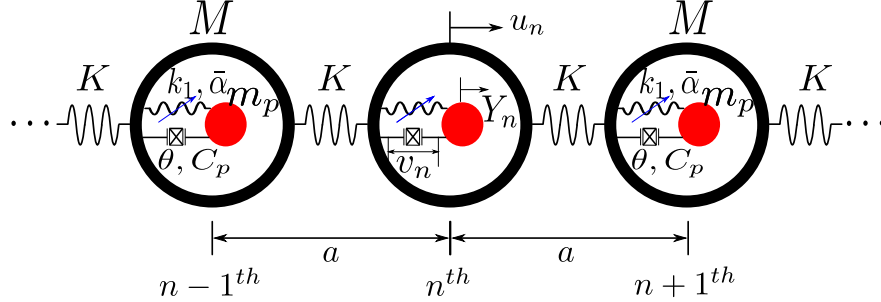
Figure 5.1: A schematic for the proposed metamaterial with nonlinear local electromechanical resonators.

by several signal processing techniques to reveal more important features of the nonlinear wave propagation phenomena in the proposed structure. Next, spectro-spatial analyses are used to validate our analytical solution in Section 5. The observed phenomenon is also validated computationally using COMSOL Multiphysics in Section 6. Finally, we summarize our findings in the conclusion section.

5.2   Mathematical model

The proposed metamaterial with embedded nonlinear electromechanical local resonators is depicted in Fig. 5.1. The metamaterial consists of an infinite chain of cells with mass M. These cells are connected by a linear spring with stiffness K. A local nonlinear electromechanical resonator with an effective mass m_p is embedded in each cell. The nonlinearity in the resonator stems from a nonlinear spring with an effective linear stiffness k_1, and cubic nonlinear stiffness $\bar{\alpha}$. The electromechanical local resonator is modeled as a beam sandwiched by piezoelectric layers with coupling coefficient θ and capacitance C_p. This resonator is shunted to a load resistor R, and it harvests a voltage, $\bar{v}_n$. If the displacement of the nth cell is defined as u_n, and the displacement of the electromechanical resonator is defined as Y_n, then the governing equations of motion for each cell with its local resonator can be

written as [24, 55, 74]

$$M\ddot{\bar{u}}_n + 2K\bar{u}_n - K\bar{u}_{n+1} - K\bar{u}_{n-1} + m_p(\ddot{\bar{y}}_n + \ddot{\bar{u}}_n) = 0 \,, \tag{5.1}$$

$$m_p\ddot{\bar{y}}_n + k_1\bar{y}_n - \theta\bar{v}_n + \bar{\alpha}\bar{y}^3 = -m_p\ddot{\bar{u}}_n \,, \tag{5.2}$$

$$RC_p\dot{\bar{v}}_n + \bar{v}_n + R\theta\dot{\bar{y}}_n = 0 \,, \tag{5.3}$$

where $\bar{y}_n = Y_n - \bar{u}_n$ is the relative displacement of the electromechanical resonator. The dimensionless version of these equations can be expressed as

$$\ddot{u}_n + 2u_n - u_{n+1} - u_{n-1} + \bar{k}\Omega_0^2(\ddot{y}_n + \ddot{u}_n) = 0 \,, \tag{5.4}$$

$$\Omega_0^2\ddot{y}_n + y_n - \alpha_1 v_n + \alpha y^3 = -\Omega_0^2\ddot{u}_n \,, \tag{5.5}$$

$$\alpha_2\dot{v}_n + v_n + \alpha_3\dot{y}_n = 0 \,, \tag{5.6}$$

where $\omega_n^2 = K/M$, $\omega_d^2 = k_1/m_p$, $\bar{k} = k_1/K$, $u_n = \bar{u}_n/U_0$, $y_n = \bar{y}_n/y_0$, $v_n = \bar{v}_n/V_0$, $\alpha = \bar{\alpha}U_0^2/K$, $\Omega_0 = \omega_n/\omega_d$, $\alpha_1 = \theta V_0/k_1$, $\alpha_2 = RC_p\omega_n$, and $\alpha_3 = R\theta\omega_n y_0/V_0$. It is noteworthy that the dots are related to the time derivative in the term of the nondimensional time, $\tau = \omega_n t$. To obtain an approximate analytical solution using MMS, we expand our solution by power series and keep only the first order terms as:

$$u_n(t,\epsilon) = u_{n0}(T_0, T_1) + \epsilon u_{n1}(T_0, T_1) + o(\epsilon^2) \,, \tag{5.7}$$

$$y_n(t,\epsilon) = y_{n0}(T_0, T_1) + \epsilon y_{n1}(T_0, T_1) + o(\epsilon^2) \,, \tag{5.8}$$

$$v_n(t,\epsilon) = v_{n0}(T_0, T_1) + \epsilon v_{n1}(T_0, T_1) + o(\epsilon^2) \,. \tag{5.9}$$

In addition, we keep the time scales T_0 and T_1 and neglect any higher time scales at

Chapter 5. Substantial frequency conversion at long-wavelength limit in
metamaterial with weakly nonlinear local electromechanical resonators: Analytical
126   and computational study

this order of perturbation where $T_0 = \tau$ is the fast time scale, and $T_1 = \epsilon\tau$ is the slow time scale. With the introduction of multiple time scales, the derivative operators will also get perturbed to

$$(\dot{\ }) = D_0 + \epsilon D_1 + \dots , \tag{5.10}$$

$$(\ddot{\ }) = D_0^2 + 2\epsilon D_0 D_1 + \dots , \tag{5.11}$$

where D_0 and D_1 denote the partial derivative with respect to the fast time scale and slow time scale, respectively. Substituting Eqs. (5.7)-(5.11) into Eqs. (5.4)-(5.6) and separating the coefficients of ϵ^0 and ϵ^1 yields

order ϵ^0

$$D_0^2 u_{n0} + 2u_{n0} - u_{(n-1)0} - u_{(n+1)0} + \bar{k}\Omega_0^2 D_0^2(y_{n0} + u_{n0}) = 0 , \tag{5.12}$$

$$\Omega_0^2 D_0^2 y_{n0} + y_{n0} - \alpha_1 v_{n0} = -\Omega_0^2 D_0^2 u_{n0} , \tag{5.13}$$

$$\alpha_2 D_0 v_{n0} + v_{n0} + \alpha_3 D_0 y_{n0} = 0 , \tag{5.14}$$

order ϵ^1

$$D_0^2 u_{n1} + 2u_{n1} - u_{(n-1)1} - u_{(n+1)1} + \bar{k}\Omega_0^2 D_0^2(y_{n1} + u_{n1}) = -2\bar{k}\Omega_0^2 D_0 D_1(y_{n0} + u_{n0}) - 2D_0 D_1 u_{n0} , \tag{5.15}$$

$$\Omega_0^2 D_0^2 y_{n1} + y_{n1} - \alpha_1 v_{n1} = -\Omega_0^2 D_0^2 u_{n1} - 2\Omega_0^2 D_0 D_1 u_{n0} - 2\Omega_0^2 D_0 D_1 y_{n0} - \alpha y_{n0}^3 , \tag{5.16}$$

$$\alpha_2 D_0 v_{n1} + v_{n1} + \alpha_3 D_0 y_{n1} = -\alpha_2 D_1 v_{n0} - \alpha_3 D_1 y_{n0} , \tag{5.17}$$

It can be noted from Eqs. 12-14 that $\mathcal{O}(\epsilon^0)$ equations are corresponding to linear equations and all the nonlinear terms appear at the equations corresponding to higher order of ϵ as

excitation terms. Therefore, there will not be any difficulty in handling of these equations. Having established these equations at different order of ϵ, next we present linear dispersion relations.

5.2.1 Linear dispersion relations

To obtain the linear dispersion relation, the equation set at order ϵ^0 is sufficient. The solution of this set can be expressed as

$$u_n = Ae^{i(nk-\omega\tau)}\,, \tag{5.18}$$

$$y_n = Be^{i(nk-\omega\tau)}\,, \tag{5.19}$$

$$v_n = Ce^{i(nk-\omega\tau)}\,. \tag{5.20}$$

Substituting Eqs. (5.19)-(5.20) into Eq. (5.14) leads to

$$-i\alpha_2\omega C + C - i\alpha_3\omega B = 0\,. \tag{5.21}$$

Rearranging Eq. (5.21) yields

$$C = \Gamma B\,, \tag{5.22}$$

where Γ is defined as

$$\Gamma = \frac{i\alpha_3\omega}{1 - i\alpha_2\omega}\,. \tag{5.23}$$

Similarly, one can solve for B by introducing Eqs. (5.18)-(5.19) and Eq. (5.22) into Eq. (5.13) to get

$$B = K_\omega A\,, \tag{5.24}$$

where K_ω can be expressed as

$$K_\omega = \frac{\Omega_0^2 \omega^2}{1 - \alpha_1 \Gamma - \Omega_0^2 \omega^2}, \tag{5.25}$$

From Eqs. (5.12), (5.22), (5.24), the dispersion relation of the metamaterial with local electromechanical resonator can be written as:

$$-\omega^2 + (2 - 2\cos k) - \bar{k}\Omega_0^2 \omega^2 (1 + K_\omega) = 0. \tag{5.26}$$

We emphasize that the above dispersion relation leads to 5 roots for ω with electromechanical coupling instead of 4 for the system without electromechanical coupling. Also, only 4 out of these 5 roots carry a nonzero real part.

5.2.2 Nonlinear dispersion relation

To obtain the approximate analytical solution (i.e., nonlinear frequency correction coefficient), we need to solve the nonlinear problem at order ϵ^1. In particular, the solvability condition should be determined in order to guarantee the convergence of our approximate solution.

Multiplying Eq. (5.17) by α_1 and collecting the coefficient of v_{n1} on the left-hand side yields

$$(\alpha_2 D_0 + 1)\alpha_1 v_{n1} = \alpha_1 [-\alpha_3 D_0 y_{n1} - \alpha_2 D_1 v_{n0} - \alpha_3 D_1 y_{n0}]. \tag{5.27}$$

To eliminate v_{n1} from Eq. (5.27), we multiply Eq. (5.16) by $(\alpha_2 D_0 + 1)$ and substitute Eq. (5.27). After rearrangement, Eq. 5.16 becomes

$$[(\alpha_2 D_0 + 1)(\Omega_0^2 D_0^2 + 1) + \alpha_1 \alpha_3 D_0] y_{n1} = -(\alpha_2 D_0 + 1)\Omega_0^2 D_0^2 u_{n1} + (\alpha_2 D_0 + 1)$$
$$(-2\Omega_0^2 D_0 D_1 (u_{n0} + y_{n0}) - \alpha y_{n0}^3) - \alpha_2 \alpha_1 D_1 v_{n0} - \alpha_1 \alpha_3 D_1 y_{n0}. \tag{5.28}$$

To eliminate v_{n1} and y_{n1} for Eq. (5.15), we multiply Eq. (5.28) by $\bar{k}\Omega_0^2 D_0^2$ and Eq. (5.15) by $[(\alpha_2 D_0 + 1)(\Omega_0^2 D_0^2 + 1) + \alpha_1 \alpha_3 D_0]$, and substitute the resulting equation into Eq. (5.15) yields

$$[(\Omega_0^2 D_0^2 + 1)(\alpha_2 D_0 + 1) + \alpha_1 \alpha_3 D_0]((1 + \bar{k}\Omega_0^2)D_0^2 u_{n1} + 2u_{n1} - u_{(n-1)1} - u_{(n+1)1}) -$$
$$\bar{k}\Omega_0^2 D_0^2 (\alpha_2 D_0 + 1)\Omega_0^2 D_0^2 u_{n1} = [(\Omega_0^2 D_0^2 + 1)(\alpha_2 D_0 + 1) + \alpha_1 \alpha_3 D_0](-2D_0 D_1 u_{n0} -$$
$$2\bar{k} D_0 D_1 (u_{n0} + y_{n0})) + \bar{k}\Omega_0^2 D_0^2[-(\alpha_2 D_0 +$$
$$1)(-2\Omega_0^2 D_0 D_1 (u_{n0} + y_{n0})) - \alpha y_{n0}^3 + \alpha_1 \alpha_2 D_1 v_{n0} + \alpha_1 \alpha_3 D_1 y_{n0}]. \tag{5.29}$$

The solvability condition can be obtained by substituting the linear solution Eqs. (5.18)-(5.20) into Eq. (5.29) as

$$[(\Omega_0^2 D_0^2 + 1)(\alpha_2 D_0 + 1) + \alpha_1 \alpha_3 D_0]((1 + \bar{k}\Omega_0^2)D_0^2 u_{n1} + 2u_{n1} - u_{(n-1)1} - u_{(n+1)1}) -$$
$$\bar{k}\Omega_0^2 D_0^2 (\alpha_2 D_0 + 1)\Omega_0^2 D_0^2 u_{n1} = ([[(-\Omega_0^2 \omega^2 + 1)(-i\alpha_2 \omega + 1) - i\alpha_1 \alpha_3 \omega](2i\omega A'$$
$$+2i\omega \bar{k}\Omega_0^2 (1 + K_\omega)A') - \bar{k}\Omega_0^2 \omega^2[(i\omega \alpha_2 - 1)(2i\Omega_0^2 \omega A'(1 + K_\omega)$$
$$-3A^2 \bar{A}) + \alpha_1 \alpha_2 K_\omega \Gamma A' + \alpha_1 \alpha_3 K_\omega A'])e^{i(nk-\omega\tau)} + \text{NST}. \tag{5.30}$$

where NST refers to the non-secular terms.

Next, to obtain a convergent solution, secular terms (i.e., coefficient of $e^{i(nk-\omega\tau)}$, which leads to unbounded solution) must be eliminated. Therefore, the solvability condition can

then be written as

$$
[(-\Omega_0^2\omega^2 + 1)(-i\alpha_2\omega + 1) - i\alpha_1\alpha_3\omega](2i\omega A'
$$

$$
+2i\omega\bar{k}\Omega_0^2(1 + K_\omega)A') - \bar{k}\Omega_0^2\omega^2[(i\omega\alpha_2 - 1)(2i\Omega_0^2\omega A'(1 + K_\omega)
$$

$$
-3A^2\bar{A}) + \alpha_1\alpha_2 K_\omega\Gamma A' + \alpha_1\alpha_3 K_\omega A'] = 0\,.
$$

(5.31)

Introducing the polar form ($A = \frac{1}{2}ae^{ib}$ where a and b are real functions of T_1) and the complex values in Cartesian form (i.e., $K_\omega = \mathrm{Re}[K_\omega] + i\,\mathrm{Im}[K_\omega]$, and $\Gamma = \mathrm{Re}[\Gamma] + i\,\mathrm{Im}[\Gamma]$) in Eq. (5.31) leads to

$$
\begin{aligned}
&\frac{3}{8}ia^3\alpha\alpha_2 e^{ib}\omega^3\Omega_0^2\bar{k}\,(\mathrm{Re}[K_\omega] + i\mathrm{Im}[K_\omega])^3\\
&\quad -\frac{3}{8}a^3\alpha e^{ib}\omega^2\Omega_0^2\bar{k}\,(\mathrm{Re}[K_\omega] + i\mathrm{Im}[K_\omega])^3\\
&\quad -\frac{1}{2}\alpha_1\alpha_2\omega^2\Omega_0^2\bar{k}(\mathrm{Re}[\Gamma] + i\mathrm{Im}[\Gamma])\left(e^{ib}a' + iae^{ib}b'\right)(\mathrm{Re}[K_\omega] + i\mathrm{Im}[K_\omega])\\
&\quad +\alpha_2\omega^2\Omega_0^2\bar{k}\left(e^{ib}a' + iae^{ib}b'\right)(\mathrm{Re}[K_\omega] + i\mathrm{Im}[K_\omega])\\
&\quad +\frac{1}{2}\alpha_1\alpha_3\omega^2\Omega_0^2\bar{k}\left(e^{ib}a' + iae^{ib}b'\right)(\mathrm{Re}[K_\omega] + i\mathrm{Im}[K_\omega])\\
&\quad +i\omega\Omega_0^2\bar{k}\left(e^{ib}a' + iae^{ib}b'\right)(\mathrm{Re}[K_\omega] + i\mathrm{Im}[K_\omega]) + \alpha_2\omega^2\Omega_0^2\bar{k}\left(e^{ib}a' + iae^{ib}b'\right)\\
&\quad +\alpha_1\alpha_3\omega^2\Omega_0^2\bar{k}\left(e^{ib}a' + iae^{ib}b'\right) + i\omega\Omega_0^2\bar{k}\left(e^{ib}a' + iae^{ib}b'\right)\\
&\quad -\alpha_2\omega^4\Omega_0^2\left(e^{ib}a' + iae^{ib}b'\right) + \alpha_2\omega^2\left(e^{ib}a' + iae^{ib}b'\right) + \alpha_1\alpha_3\omega^2\left(e^{ib}a' + iae^{ib}b'\right)\\
&\quad -i\omega^3\Omega_0^2\left(e^{ib}a' + iae^{ib}b'\right) + i\omega\left(e^{ib}a' + iae^{ib}b'\right) = 0\,.
\end{aligned}
$$

(5.32)

Upon separating the real and imaginary parts, the following equations can be obtained

$$
f + ga' + hab' = 0\,,
$$

(5.33)

$$
l - ha' + gab' = 0\,,
$$

(5.34)

where the coefficients of a' and ab' are

$$g = -\frac{1}{2}\omega \left(\alpha_2\omega \left(\Omega_0^2 \left(\bar{k} \left(\alpha_1(-\text{Im}[\Gamma])\text{Im}[K_\omega] + (\alpha_1\text{Re}[\Gamma] - 2) \text{Re}[K_\omega] - 2\right) + 2\omega^2\right) - 2\right) \quad (5.35)$$
$$+ 2\Omega_0^2\bar{k}\text{Im}[K_\omega] - \alpha_1\alpha_3\omega \left(\Omega_0^2\bar{k} \left(\text{Re}[K_\omega] + 2\right) + 2\right)\right) ,$$

$$h = \frac{1}{2}\omega \left(\Omega_0^2 \left(\bar{k} \left(\text{Re}[K_\omega] \left(\alpha_1\alpha_2\text{Im}[K_\omega]\omega - 2\right) + \omega\text{Im}[K_\omega] \left(\alpha_2 \left(\alpha_1\text{Re}[\Gamma] - 2\right) - \alpha_1\alpha_3\right) - 2\right) \quad (5.36)$$
$$+ 2\omega^2\right) - 2\right) ,$$

$$f = \frac{3}{8}a^3\alpha\omega^2\Omega_0^2\bar{k} \left(\alpha_2\omega\text{Im}[K_\omega]^3 - 3\alpha_2\omega\text{Im}[K_\omega]\text{Re}[K_\omega]^2 + 3\text{Im}[K_\omega]^2\text{Re}[K_\omega] - \text{Re}[K_\omega]^3\right) ,$$
$$(5.37)$$

$$l = \frac{1}{8}(-3)a^3\alpha\omega^2\Omega_0^2\bar{k} \left(3\alpha_2\omega\text{Im}[K_\omega]^2\text{Re}[K_\omega] + 3\text{Im}[K_\omega]\text{Re}[K_\omega]^2 - \text{Im}[K_\omega]^3 - \alpha_2\omega\text{Re}[K_\omega]^3\right) .$$
$$(5.38)$$

Among these coefficients, only l and f depends on the oscillation amplitude a. To obtain the slow-flow equations, one can solve Eqs. (5.33)-(5.34) to get

$$a' = \frac{lh - fg}{g^2 + h^2} , \quad (5.39)$$

$$ab' = -\frac{gl + mh}{h^2 + g^2} . \quad (5.40)$$

Consequently, the slow-flow equations of the system can be written as

$$a' = c_0 a^3 , \quad (5.41)$$

$$ab' = c_1 a^2 , \quad (5.42)$$

where c_0 and c_1 are constants and depend on the system parameters. It is to be noted here that these slow-flow equations are not linear functions of a. Consequently, determining the nonlinear frequency correction term for the nonlinear frequency is not straight forward. However, the value of c_1 is significantly larger than c_0 for common energy harvester parameters, as shown in Fig. 5.1. Therefore, one can safely assume the change in a with slow time scale T_1 is zero, which further implies $a' = 0$ and, consequently, the amplitude is constant $a = a_0$. Finally, the nonlinear frequency correction factor can be expressed as

$$b' = c_1 a_0^2 \,, \tag{5.43}$$

and integrating this factor with respect to the slow time scale T_1 yields

$$b = c_1 a_0^2 T_1 \,. \tag{5.44}$$

As a result, the nonlinear dispersion relation can be expressed as

$$\omega_{\mathrm{nl}} = \omega - \epsilon b' \,. \tag{5.45}$$

5.3   Analytical bandgap parametric study

To investigate the effect of resonator's nonlinearity in the presence of electromechanical coupling on the band structure, we vary some electromechanical and nonlinear parameters (i.e., $\epsilon \alpha a^2$, θ, and R) while other system parameters are held as constants. The fixed parameters are chosen based on [26, 55] as $\bar{k} = 1$, $\omega_n = \omega_d = 100$ rad/sec, $k_1 = 10^6$ N/m, and $C_p = 13.3 \times 10^{-9}$ F. It is noteworthy that we focus our analysis on the nonlinear band structure since the discussion about the linear band structure can be found in [26]. Moreover, we

validate our results in Sec. 5 by reconstructing the band structure from the 2D Fast Fourier Transform (2D-FFT).

The band structure of different system parameters is depicted in Fig. 5.2. The effect of weak nonlinearity on the band structure is demonstrated in Fig. 5.2 (a). The results indicate that softening nonlinearity shifts the dispersion curves down while hardening nonlinearity shifts the dispersion curves up. However, this shift varies over the wavelength and the different modes. For instance, the shift is more pronounced at the short-wavelength limit in the acoustics mode. On the other hand, the shift can be observed at all wavelength limits in the optical mode with more shift at the long-wavelength limit. This observation in the shift in the optical mode at the long-wavelength limit can only be observed in the case of a nonlinear resonator, unlike the nonlinear chain case where the nonlinearity has no effect at the long-wave length limit. Since the shift is more dominant at short-/long- wavelength limits in the acoustics/optical modes, one can deduce that the effect of nonlinearity is concentrated near the resonance frequency of the nonlinear electromechanical local resonator and degrades gradually with mistuning.

For typical weak electromechanical coupling ($\theta = 10^{-10}$ N/m), the electromechanical coupling has no effect (i.e., altering the band structure or the size of bandgap) on the band structure as demonstrated in Fig. 5.2 (b). This indicates that the proposed metamaterial can be employed for simultaneous energy harvesting and vibration reduction applications. However, the attenuation level inside the bandgap is degraded due to this coupling [26]. On the other hand, the band structure of the system changed significantly at very strong electromechanical coupling (i.e., $\theta \geq 10^{-2}$) as shown in Fig. 5.2 (c). In particular, the acoustics and optical modes start merging into a one dispersion curve with the increase in the electromechanical coupling. Moreover, some real frequencies appear at frequencies higher than the optical mode range in the absence of the electromechanical coupling. The strong

electromechanical coupling also affects the attenuation level inside the bandgap significantly, as shown in Fig. 5.2 (d). Also, the attenuation at higher frequencies increases with increasing the electromechanical coupling as both mode merges into one dispersion curve. Although with strong mechanical coupling the dispersion curves merge into one dispersion curve, the effect depends significantly on the shunted resistor. For instance, the dispersion curves gradually merge into one dispersion curve as the resistor increases at $\theta = 10^{-1}$, as shown in Fig. 5.2 (e). In addition, the resistor has a role in affecting the attenuation level inside the bandgap frequencies and at higher frequencies in the presence of strong electromechanical coupling as increasing the resistor's value leads to reduction in the attenuation level inside the bandgap frequencies as shown in Fig. 5.2 (f).

5.4 Spectro-spatial Analyses

The obtained analytical solutions are useful in determining the effect of nonlinearity on dispersion curves and obtaining the cut off frequency (i.e., the limit of acoustics/optical modes frequencies). However, it fails to get other important characteristics of propagating nonlinear waves. Therefore, we conduct spectro-spatial analyses to reveal more interesting features of the nonlinear waves that propagate through a metamaterial with nonlinear electromechanical resonator. In the present study, we focus our analyses on the harvested voltage from the nonlinear harvester. We numerically integrate a chain with 500 cells with the same parameters defined in the previous section. The chain is initially subjected to transient wave packets defined by the following set of equations

$$u_m(0) = \frac{1}{2}(H(m-1) - H(m-1-N_{cy}2\pi/k))(1 - \cos(mk/N_{cy}))\sin(mk), \qquad (5.46)$$
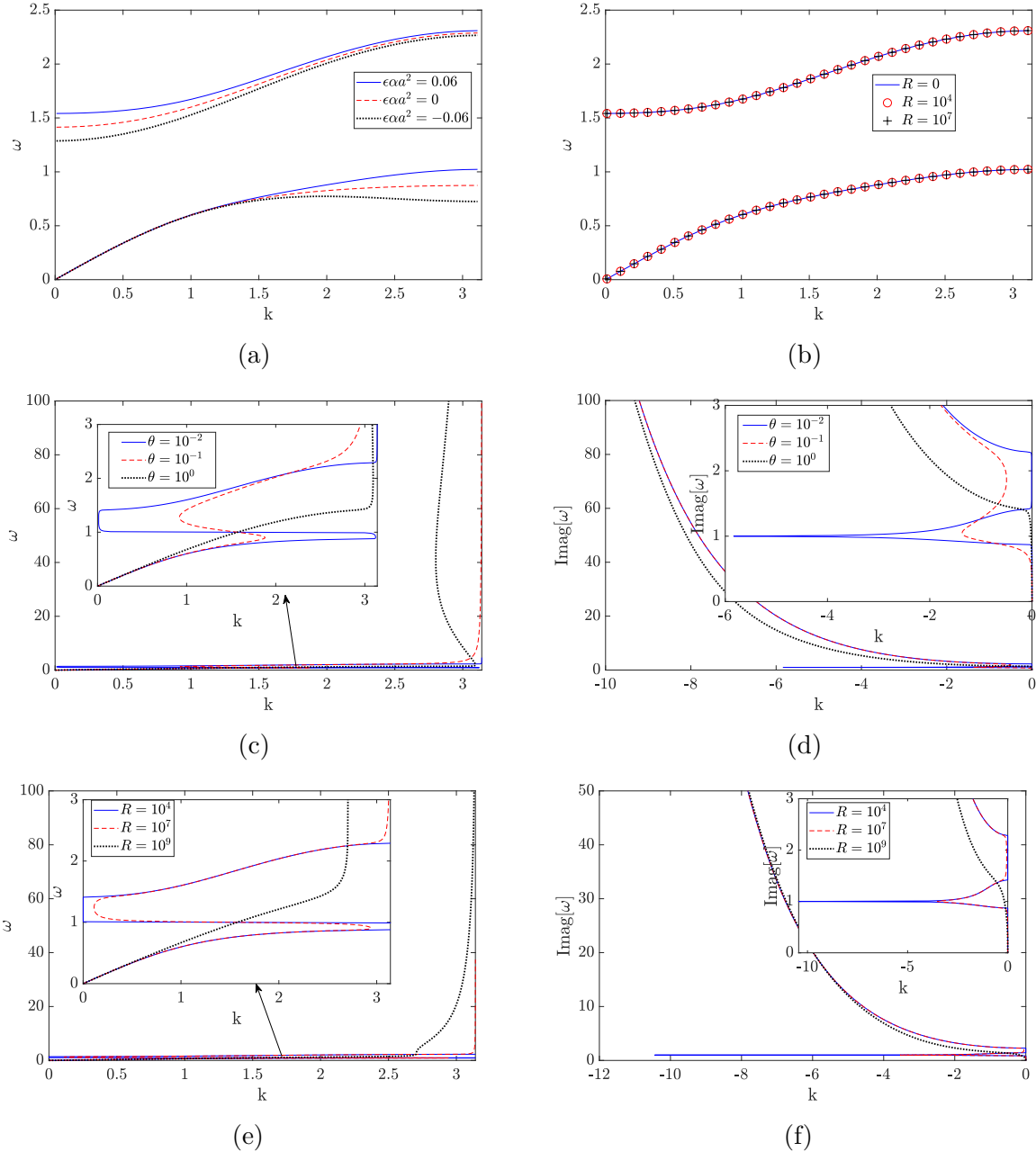
Figure 5.2: Effect of different parameters on the system band structure: (a) The effect of nonlinearity without electromechanical coupling; (b) The effect of weak electromechanical coupling with hardening nonlinearity; (c) The effect of strong coupling with hardening nonlinearity (real); (d) The effect of strong coupling with hardening nonlinearity (imaginary); (e) The effect of resistor with strong coupling with hardening nonlinearity (real); (f) The effect of resistor with strong coupling with hardening nonlinearity (imaginary).

$$\dot{u}_m(0) = \frac{1}{2}(H(m-1) - H(m-1-N_{cy}2\pi/k))(-\omega_n\omega/N_{cy}\sin(mk/N_{cy})\sin(mk)-$$
$$\omega_n\omega(1-\cos(mk/N_{cy}))\cos(mk)),$$
(5.47)

$$y_m(0) = K_\omega u_m(0),$$
(5.48)

$$\dot{y}_m(0) = K_\omega \dot{u}_m(0),$$
(5.49)

$$v_m(0) = \Gamma K_\omega u_m(0),$$
(5.50)

where the subscript m denotes the initial condition of the mth cell, N_{cy} is the number of cycles and it is set to 7 in the present study, and $H(x)$ is the Heaviside function.

5.4.1 Spatial profile of propagating waves

In this subsection, we investigate the output voltage spatial wave profile for different types of nonlinearities and at different wavelength limits, as depicted in Fig. 5.3. At the long-wavelength limit in the acoustics mode, the results indicate that the harvested voltage wave is not distorted by the nonlinearity (i.e., output wave has the same profile in the linear and nonlinear chains) as shown in Fig. 5.3 (a). Moreover, the output wave has a low amplitude since the excitation frequency is away from the resonance frequency of the local resonator/harvester. On the other hand, the wave gets severely distorted due to nonlinearity at the long-wavelength limit in the optical mode, as shown in Fig. 5.3 (b). For linear metamaterial, the wave is not distorted at all, although its amplitude gets amplified because the excitation frequency is close to the local resonator/harvester frequency. However, nonlinearity in the local resonator leads to a significant wave distortion for both, softening and hardening nonlinearities. This distortion leads to significantly frequency conversion, as we will show in the following sections. This observation raises attraction to metamaterial with nonlinear electromechanical harvester due to the achieved wave distortion at the long-

wavelength limit which cannot be obtained by other nonlinear systems like the nonlinear chain [195]. Indeed, this wave distortion can lead to a significant frequency shift (as we will show in the subsequent sections) and allow the use of the current system in designing mechanical or electromechanical diodes that can be operated at this wavelength limit. Although the harvested power by the nonlinear resonator is slightly lower than the harvested power by the linear resonator case, the amplitude of the nonlinear wave has a level similar to that of the input signal.

At medium wavelength limit in the acoustics mode (see Fig. 5.3 (c)), the output wave becomes dispersive (i.e., stretched over the cells with lower amplitude) for the linear local resonator case since the dispersion curve at this wavelength limit has a variable slope [85]. However, nonlinearity in the resonator results in distorting the output wave. This distortion appears as an increase in the amplitude due to hardening nonlinearity. Indeed, the wave has one dispersive component with low amplitude and one traveling localized amplitude with high amplitude, unlike the linear wave, where it has only one dispersive component. In addition, the wave becomes more dispersive in the case of softening nonlinearity. This distorted wave is even more dispersive than the linear wave in terms of lower amplitude and more stretching over the chain. In the optical mode (see Fig. 5.3 (d)), the nonlinearity distorts the wave in mainly three components for both, hardening and softening nonlinearity, unlike the linear case, which has only one component. It is noteworthy that the linear output voltage waves appear to have amplitude higher than the input amplitude in the presence of the energy harvester; however, the linear wave that propagates through the chain is usually dispersive at this wavelength limit and has amplitude lower than the input signal in the absence if the energy harvester[?].

At short wavelength limit in the acoustics mode (see Fig. 5.3 (e)), the effect of nonlinearity becomes more obvious in terms of stretching the linear dispersive wave further due to

the softening nonlinearity or the developed localized amplitude due to the hardening nonlinearity as compared to the medium wavelength limit in Fig. 5.3 (c). Moreover, one can also observe another traveling localized component with amplitude lower than the main localized component and higher than the dispersive component. However, this effect is not that significant in the optical mode at the same wavelength limit since the resonance frequency of the nonlinear resonator is away from this region [**?**]. Nevertheless, the wave is still more dispersive with lower amplitude in the case of softening nonlinearity while it has traveling localized high amplitude component in the case of the hardening chain.

5.4.2   Images of STFT of the propagating waves

In order to reveal more important characteristics of the propagating voltage wave through the proposed metamaterial, we monitor the change of the output voltage wave features over the spatial domain by determining the STFT of the signal. Then, we plot the spectrograms of the resulted signal after the processing, and the input signal with applying a Hann window with the size of the input burst. The window is applied to confine the short spatial components over the space. This window is highlighted on the spectrograms between two horizontal dashed lines.

For signals in the acoustics mode, we plot the spectrograms in Fig. 5.4. Since the nonlinearity has no effect on the output wave at long-wavelength limit in this mode, we did not show the spectrograms of this signal. At medium wavelength limit, the output voltage wave is dispersive in the linear metamaterial, as shown in Fig. 5.4 (a). Thus, the output wave has an amplitude significantly lower than the input signal and is stretched over the chain. However, the output signal has only one component. In the presence of the hardening nonlinearity Fig. 5.4 (b), the wave becomes severely distorted and is split
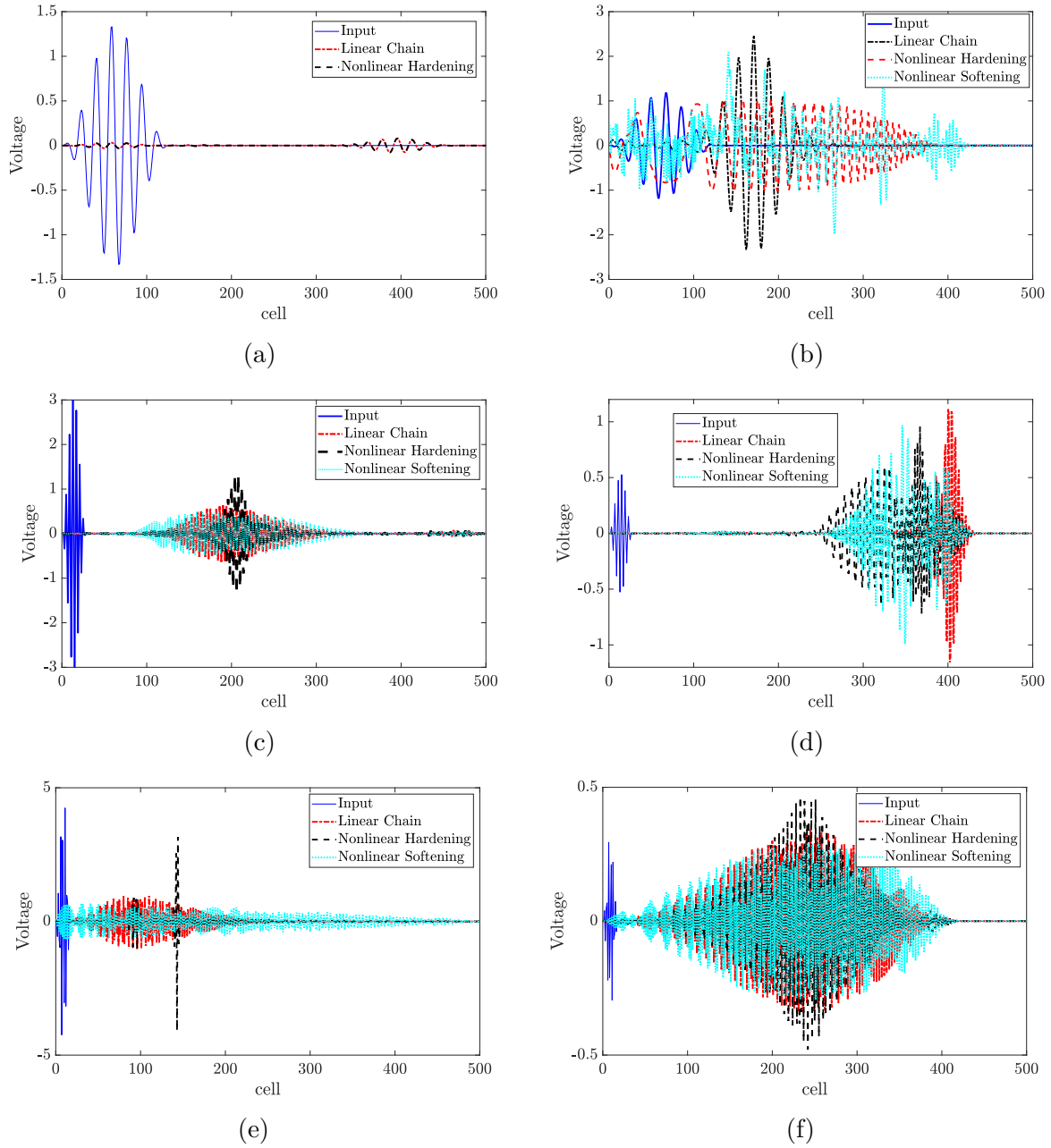
Figure 5.3: Spatial profile of output voltage, $R = 10^7 \Omega$, $\theta = 10^{-8}$ N/V: (a) Acoustics mode $k = \pi/9$; (b) Optical mode $k = \pi/9$; (c) Acoustics mode $k = \pi/2$; (d) Optical mode $k = \pi/2$; (e) Acoustics mode $k = 7\pi/9$; (f) Optical mode $k = 7\pi/9$.

into two components; one is localized and contains most of the energy content, and the other is stretched and has low energy content. On the contrary, the softening nonlinearity stretches the output wave further, as shown in Fig. 5.4 (c). The energy content of this wave is distributed over only one component. Furthermore, some of the energy content appears outside the Hann window that contains the input signal, which indicates the severity of the distortion resulted from the softening nonlinearity. For signals at a short-wavelength limit in the acoustics mode, the results indicate that the output voltage wave in the linear case has energy content higher than that at medium wavelength limit, as shown in Fig. 5.4 (c). This is because the excitation frequency is closer to the local electromechanical resonator frequency in the short wavelength limit case. This energy is confined within one component and stretches over the chain more severely than the case of medium wavelength limit. As of the case of the medium wavelength limit, similar distortion is observed for hardening and softening nonlinearities. However, this distortion is more severe at the short-wavelength limit. For instance, the hardening nonlinearity splits the output wave into three components (see Fig. 5.4 (e)); the first is localized and contains most of the energy content (Solitary wave), the second is dispersive (stretched over the cells) and has very low energy content, and the third is also localized with medium energy content. Although the latter can be observed at small values of resonator nonlinearity, it can only be observed at large values of nonlinearity in the case of the nonlinear chain [26] where a unique solitary wave is developed. On the contrary, the softening nonlinearity stretches the output voltage wave further over the chain (i.e., as compared to the linear case at the medium and short-wavelength limits and softening nonlinear case at medium wavelength limit), as shown in Fig. 5.4 (f). This stretch results in significant output wave energy content out on the window of the input signal.

We plot the spectrograms at the long-wavelength limit of the optical mode in Fig.
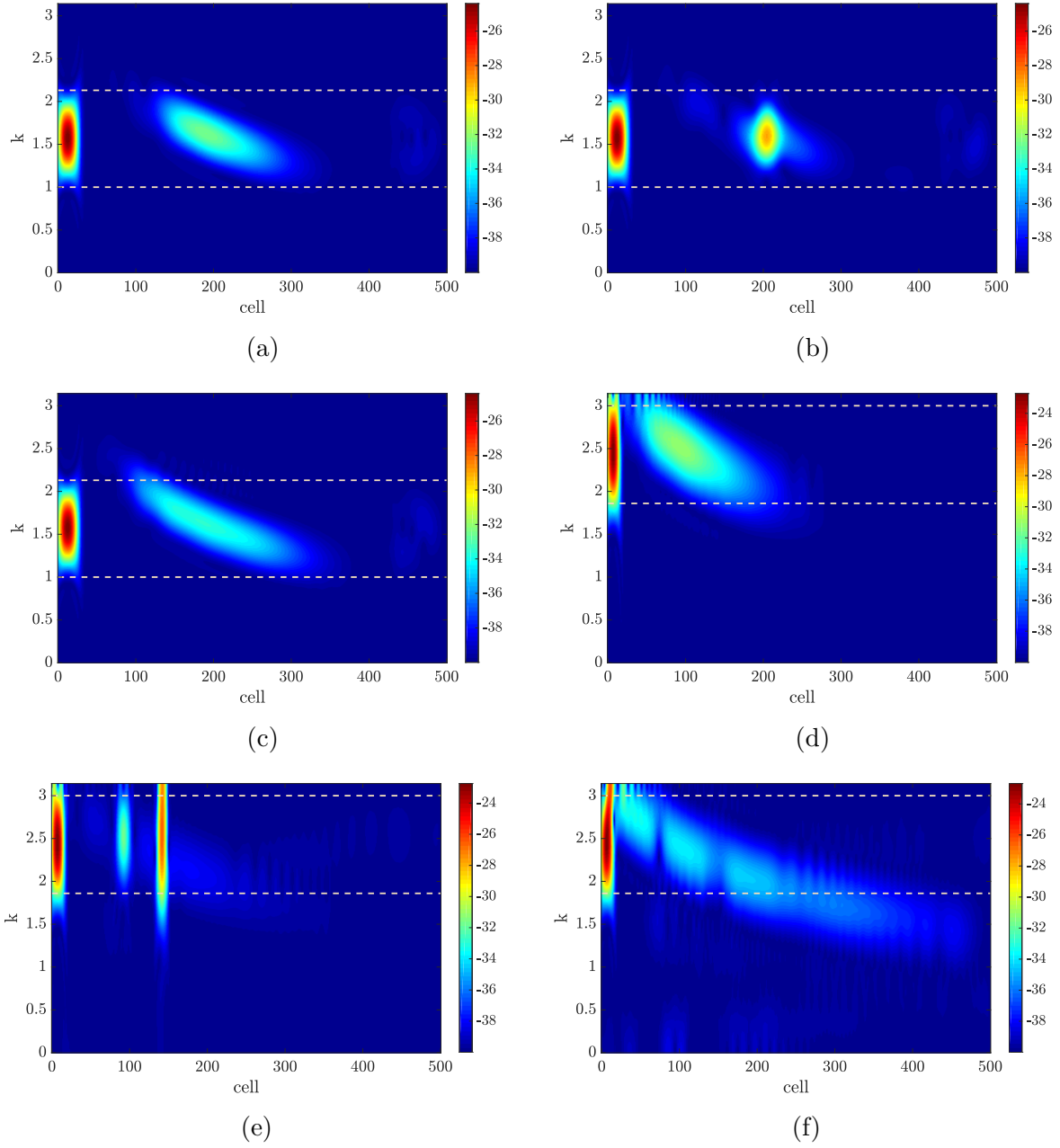
Figure 5.4: Spectrograms of the STFT for the output voltage in the acoustics mode $R = 10^7 \Omega$, $\theta = 10^{-8}$ N/V: (a) $k = \pi/2$, $\epsilon \alpha a^2 = 0$; (b) $k = \pi/2$, $\epsilon \alpha a^2 = 0.03$; (c) $k = \pi/2$, $\epsilon \alpha a^2 = -0.03$; (d) $k = 7\pi/9$, $\epsilon \alpha a^2 = 0$; (e) $k = 7\pi/9$, $\epsilon \alpha a^2 = 0.03$; (f) $k = 7\pi/9$, $\epsilon \alpha a^2 = -0.03$.

Chapter 5. Substantial frequency conversion at long-wavelength limit in metamaterial with weakly nonlinear local electromechanical resonators: Analytical and computational study

142

5.5. We focus on this region since one of the interesting characteristics of the proposed metamaterial is to realize severe distortion and significant frequency shift of the output signal by the nonlinearity in this region. For the linear case (see Fig. 5.5 (a)), although the output voltage wave is amplified due to the tuning between the excitation frequency and the resonance frequency of the local resonator, the wave is not distorted since it is completely confined within the window of the input signal. However, the presence of nonlinearity in the local resonator distorts the output wave significantly. For instance, softening nonlinearity splits the wave into multiple components with different energy content distribution, as shown in Fig. 5.5 (b). Most of these components lie outside the Hann window of the input signal. This indicates that a significant frequency/wavenumber shift can be obtained by softening nonlinearity in the local resonator at the long-wavelength limit. Hardening nonlinearity also results in severe wave distortion at the long-wavelength limit, as shown in Figs. 5.5 (c) and (d). The results demonstrate that the output signal is stretched over a wide range of frequency/wavenumber and distributed mainly within two main components. The energy content of these components is distributed almost equally with high energy content in both components. It is noteworthy that the energy content of components in the case of hardening nonlinearity is higher than the case of softening nonlinearity. Increasing the nonlinearity (see Fig. 5.5 (d)) results in stretching (distorting) the output voltage wave further; however, the energy content becomes lower. The observed significant frequency shift at the long-wavelength limit in the optical mode indicates that the proposed system can be used in designing electromechanical diode. This interesting frequency conversion cannot be achieved by other sources of nonlinearities, as the nonlinearity stems from the stiffness between the chain's cells [26, 195].

Finally, we study the effect of nonlinearity on the output voltage wave at medium and short wavelength limits in the optical mode. The spectrograms of these cases are depicted in
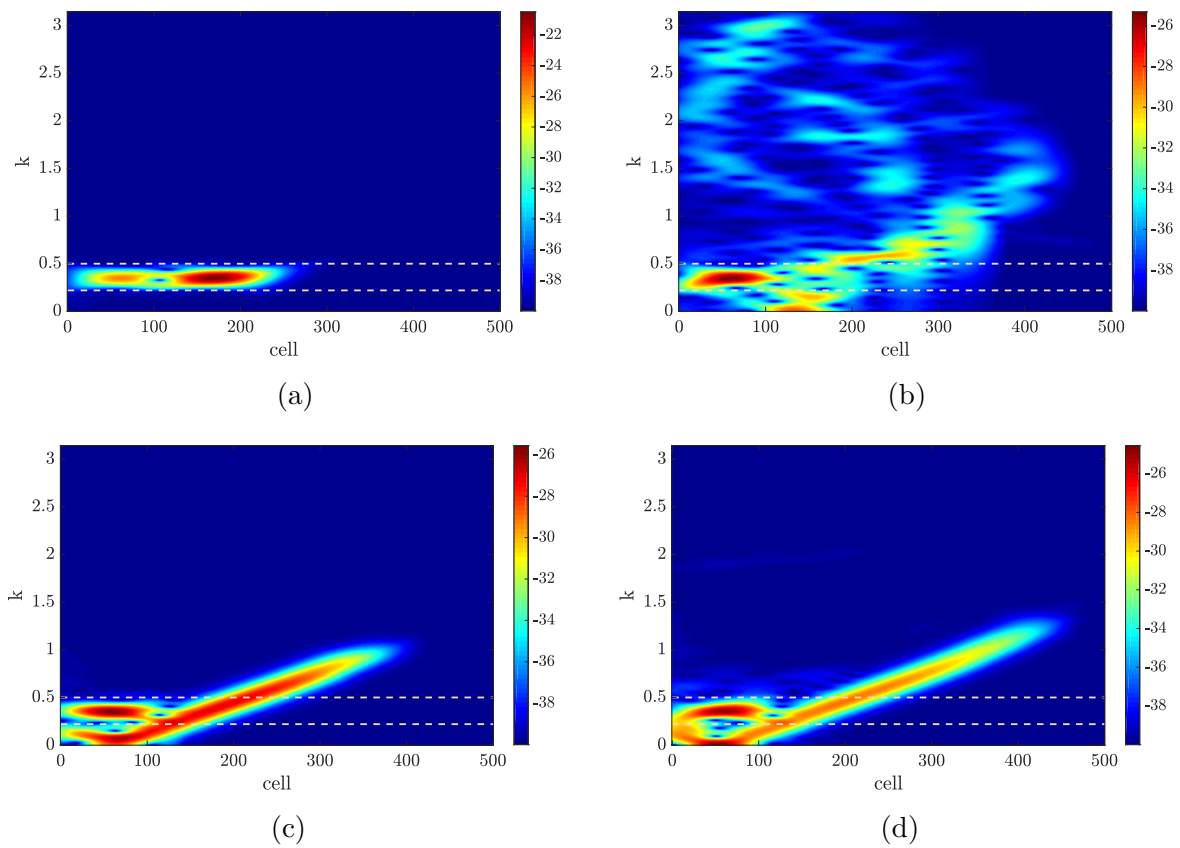
Figure 5.5: Spectrograms of the STFT for the output voltage at the long-wavelength limit in the optical mode $k = \pi/9$, $R = 10^7 \Omega$, $\theta = 10^{-8}$ N/V: (a) $\epsilon \alpha a^2 = 0$; (b) $\epsilon \alpha a^2 = -0.03$; (c) $\epsilon \alpha a^2 = 0.03$; (d) $\epsilon \alpha a^2 = 0.06$.

Fig. 5.6. At medium wavelength limit, we observe that the wave is not distorted in the linear case, and its component lies completely inside the window of the input signal, as shown in Fig. 5.6 (a). However, nonlinearity of the local resonator results in a severe wave distortion; thus a significant frequency/wavenumber shift happens, as shown in Figs. 5.6 (b) and (c). Moreover, nonlinearity splits the output wave into three main components; one is completely inside the window of the input signal with low energy content, and two outside this window. One of those two components having most of the energy content is observed above/below the input frequency range in the case of hardening/softening nonlinearity while the other has low energy content, but it is still higher than the energy content of the first component inside the window. This component lies below/above the window in the case of hardening/-softening nonlinearity. The significant frequency shift at this wavelength limit (i.e., medium wavelength limit) demonstrates that the proposed metamaterial can also be used in designing electromechanical diode that operates within the medium wavelength limit. Therefore, the proposed structure can be used at the long and medium-wavelength limits, unlike the case of nonlinear chain where it can only be utilized at medium wavelength limit. At the short-wavelength limit in the optical mode, the output voltage wave is stretched over the chain in the linear case, as depicted in Fig. 5.6 (d). Indeed, the wave is dispersive, although it has a high amplitude resulting from frequency tuning. The effect of the nonlinearity at this wavelength limit appears as localizing the wave in the case of hardening nonlinearity (see Fig. 5.6 (e)), and further stretching of the output signal in the case of the softening nonlinearity (see Fig. 5.6 (f)). However, this effect is not significant (i.e., as compared to results at the same wavelength in the acoustics mode) since the frequency in this region is away from the resonance frequency of the nonlinear local electromechanical resonator [?].
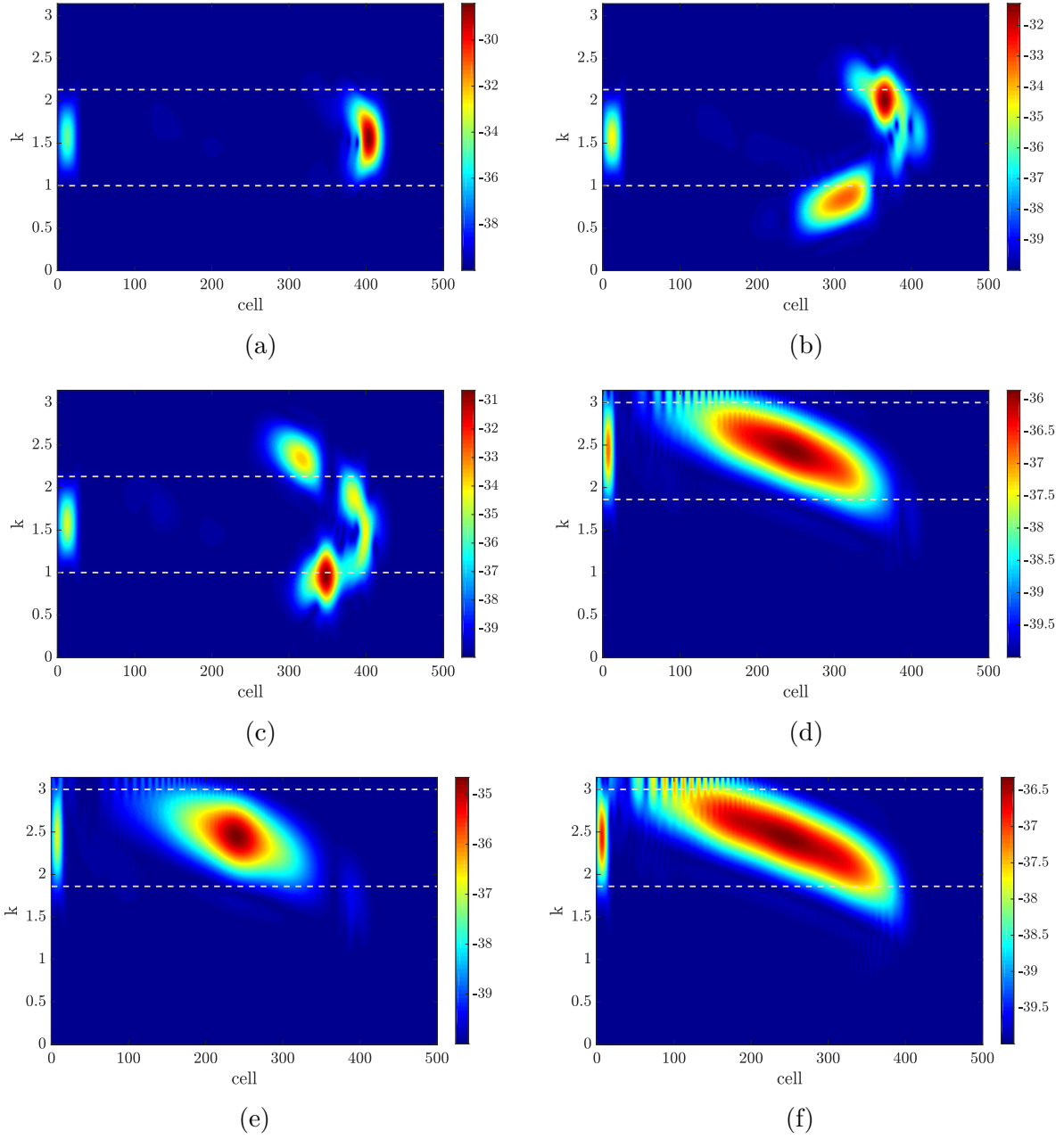
Figure 5.6: Spectrograms of the STFT for the output voltage in the optical mode $R = 10^7 \Omega$, $\theta = 10^{-8}$ N/V: (a) $k = \pi/2$, $\epsilon \alpha a^2 = 0$; (b) $k = \pi/2$, $\epsilon \alpha a^2 = 0.03$; (c) $k = \pi/2$, $\epsilon \alpha a^2 = -0.03$; (d) $k = 7\pi/9$, $\epsilon \alpha a^2 = 0$; (e) $k = 7\pi/9$, $\epsilon \alpha a^2 = 0.03$; (f) $k = 7\pi/9$, $\epsilon \alpha a^2 = -0.03$.

5.4.3   Contour plots of 2D FFT of the propagating wave

In order to reconstruct the band structure, demonstrate the role of nonlinearity on the dispersion curves, demonstrate the frequency shift further, and investigate the birth of solitary waves, we plot the contour plots of 2D FFT of the propagating wave in Figs. 5.7-5.9.

For the acoustics mode, we only show the results at short and medium-wavelength limits since the nonlinearity has no effect on the results at the long-wavelength limit in this mode. For the linear case at the medium-wavelength limit (see Fig. 5.7 (a)), the contour plot indicates that the dispersion curve has a non-constant slope (nonlinear curve), and thus the wave is dispersive [85]. Hardening nonlinearity changes the dispersion curve significantly and makes its slope almost constant (linear curve), as shown in Fig. 5.7 (b). This indicates the birth of solitary wave due to hardening nonlinearity [85]. On the other hand, softening nonlinearity bends the dispersion curve further to make the slope more nonlinear; therefore, the resulting wave is more dispersive, as depicted in Fig. 5.7 (c). At the short-wavelength limit in the acoustics mode, the contour plot of the linear case indicates that the dispersion curves have a variable slope (nonlinear curve), and the wave is dispersive, as shown in Fig. 5.7 (d). However, the bend is more pronounced in this case as compared to the medium-wavelength limit case, and thus the curve is more nonlinear and the stretch of this wave is more severe. Figure 5.7 (e) presents the contour plots in the case of hardening nonlinearity. The results demonstrate the birth of solitary localized wave due to bending the curve toward fixed slope curve. Moreover, the results indicate the birth of another solitary wave below the main solitary localized wave with lower energy content. Figure 5.7 (f) shows the contour plot in the case of softening nonlinearity. It can be deduced that softening nonlinearity bends the dispersion curve to become more nonlinear (variable slope), and thus the output wave is more stretched over the chain. It is noteworthy that although the effect of nonlinearity at short wavelength limit is similar to the effect at medium wavelength limit, the effect in the

case of short wavelength limit is more severe. This can also be deduced from the analytical results in the previous section and can be explained by the closest of the frequencies within short wavelength limit from the resonance frequency of the nonlinear local resonator.

Unlike the acoustics mode, the nonlinearity distorts the output wave at the long wavelength limit in the optical mode. We present the contour plots of 2D FFT at small wavenumers (i.e., long wavelength limit) in the optical mode in Fig. 5.8. Figure 5.8 (a) shows the contour plot for the linear case. The results indicate that the energy of the contour plot is concentrated within the frequency of the input signal. Therefore, no wave distortion is observed in the linear case. However, softening nonlinearity results in sever distortion since the energy content in the contour plot of the signal appears over a wide range of frequencies other than the input excitation frequency (i.e., appears at wide portion of the dispersion curve) as plotted in Fig. 5.8 (b). Moreover, hardening nonlinearity results also in significant frequency conversion at this wavelength limit. For instance, the results in Fig. 5.8 (c) show that the corresponding dispersion curve is stretched over wide range of frequencies. Therefore, the propagating wave appears at frequencies different than the input frequency. The effect of increasing nonlinearity on the contour plots is shown in Fig. 5.8 (d). The results indicate that increasing the nonlinearity increases the stretch of frequency component over a wider range of frequencies.

Next, we show the contour plots of 2D FFT at medium and short wavelength limits in the optical mode. Figure. 5.9 (a) show the contour plot of the linear case at medium wavelength limit. The results indicate that the frequency content of the contour plot is concentrated around the input frequency. Therefore, no frequency shift is observed in the linear case. However, hardening nonlinearity in the local resonator results in significant frequency shift since the energy of the contour plots is mainly concentrated in three regions as shown in Fig. 5.9 (b). This is not surprising since we have already observed these three component

Chapter 5. Substantial frequency conversion at long-wavelength limit in metamaterial with weakly nonlinear local electromechanical resonators: Analytical and computational study

148
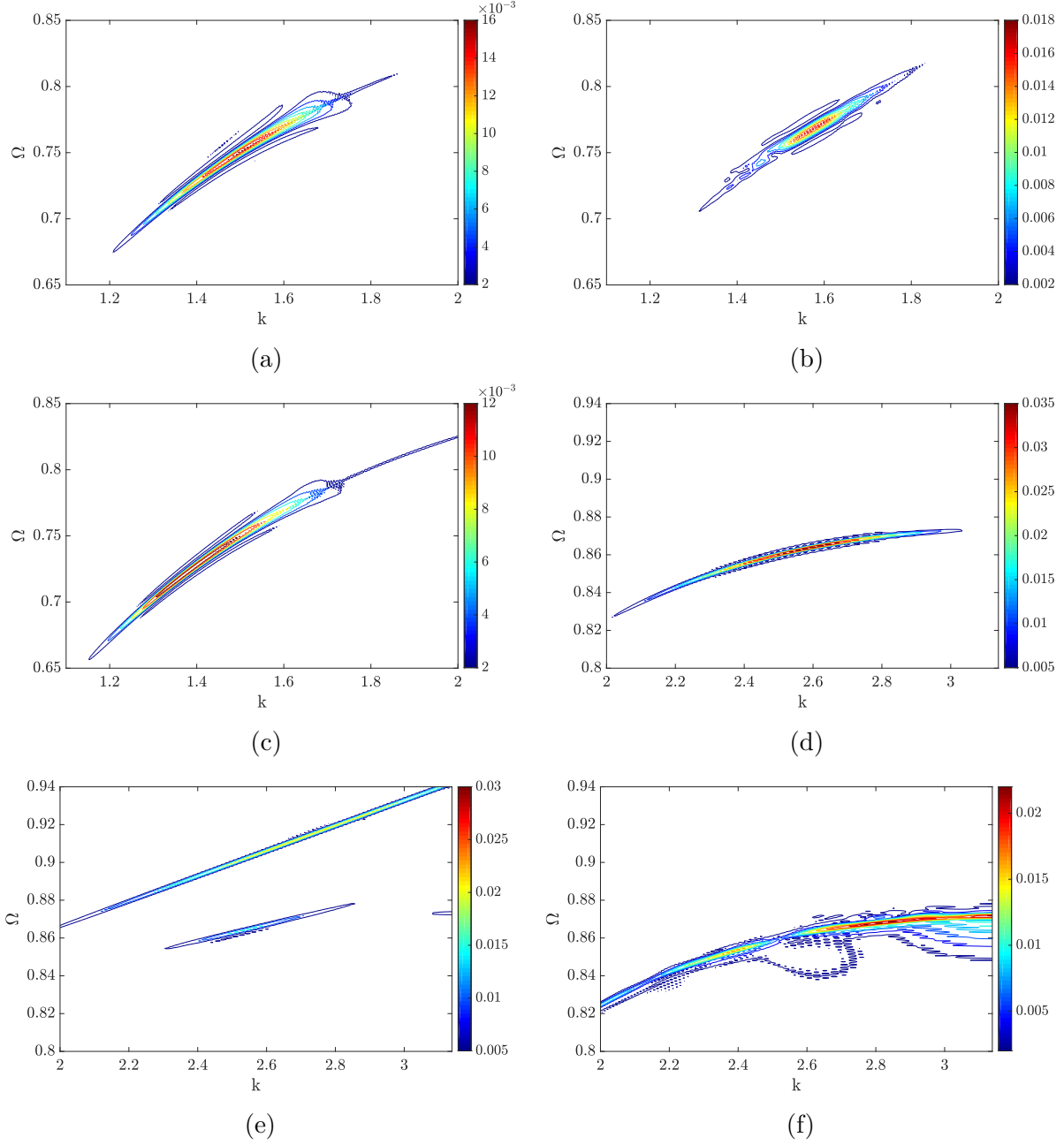
Figure 5.7: Contour plots of the 2D FFT for the output voltage in the acoustics mode $R = 10^7\Omega$, $\theta = 10^{-8}$ N/V: (a) $k = \pi/2$, $\epsilon\alpha a^2 = 0$; (b) $k = \pi/2$, $\epsilon\alpha a^2 = 0.03$; (c) $k = \pi/2$, $\epsilon\alpha a^2 = -0.03$; (d) $k = \pi/9$, $\epsilon\alpha a^2 = 0$; (e) $k = \pi/9$, $\epsilon\alpha a^2 = 0.03$; (f) $k = \pi/9$, $\epsilon\alpha a^2 = -0.03$.
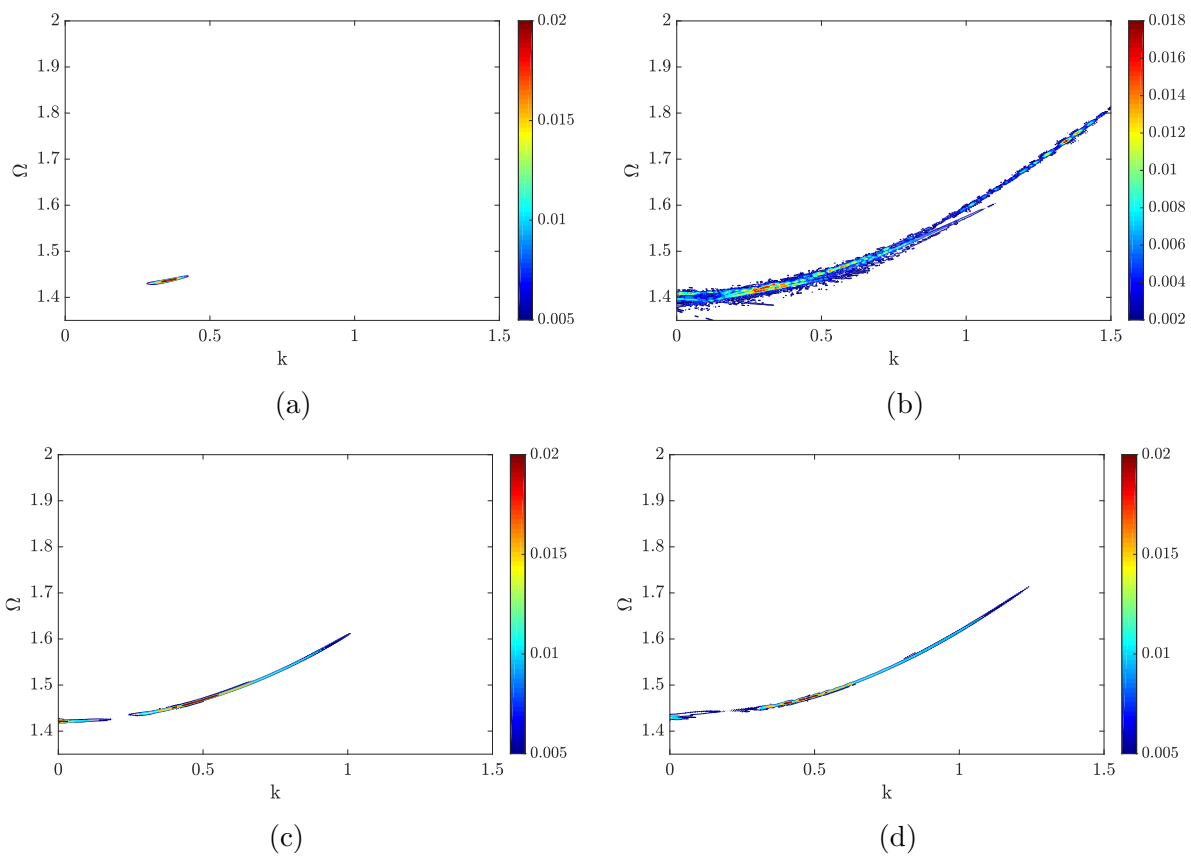
Figure 5.8: Contour plots of the 2D FFT for the output voltage at the long-wavelength limit in the optical mode $k = \pi/9$, $R = 10^7\Omega$, $\theta = 10^{-8}$ N/V: (a) $\epsilon\alpha a^2 = 0$; (b) $\epsilon\alpha a^2 = -0.03$; (c) $\epsilon\alpha a^2 = 0.03$; (d) $\epsilon\alpha a^2 = 0.06$.

in Fig. 5.6 (b). Two of these regions appear away from the original frequency of the input signal and have energy content higher than the energy content of the component within the input frequency range. Moreover, the upper component has a fixed slope; therefore, it represents a localized (solitary) wave. Similar frequency shift is also observed in the case of softening nonlinearity as shown in Fig. 5.9 (c). The energy content is also split into three components; however, the component of most energy content exists near the lowest point of the dispersion curve unlike the case of hardening nonlinearity. For waves at short wave length limit, the contour plots of the linear case (depicted in Fig. 5.9 (d)) demonstrate that the dispersion curve has a variable slope. therefore, the wave is dispersive and stretched over the chain. Since this frequency region is away from the resonance frequency of the local electromechanical resonator, the effect of nonlinearity is not significant in this region as compared to the short wavelength limit in the acoustics mode. Yet, the slight effect appears as localizing the energy component in the case of hardening nonlinearity (Fig. 5.9 (e)) and stretching the energy coponent over the dispersion curve (i.e., the output signal has frequency components other than the input signal frequency) in the case of softening nonlinearity as shown in Fig. 5.9 (f).

5.5 Analytical results validation using reconstructed dispersion curves from 2D FFT of the numerical results

In the previous section, we have shown that nonlinear dispersion curves can be reconstructed from the contour plots of 2D FFT of the numerical results. In this section, the numerical dispersion curves are used to check the validity of the obtained analytical solution and
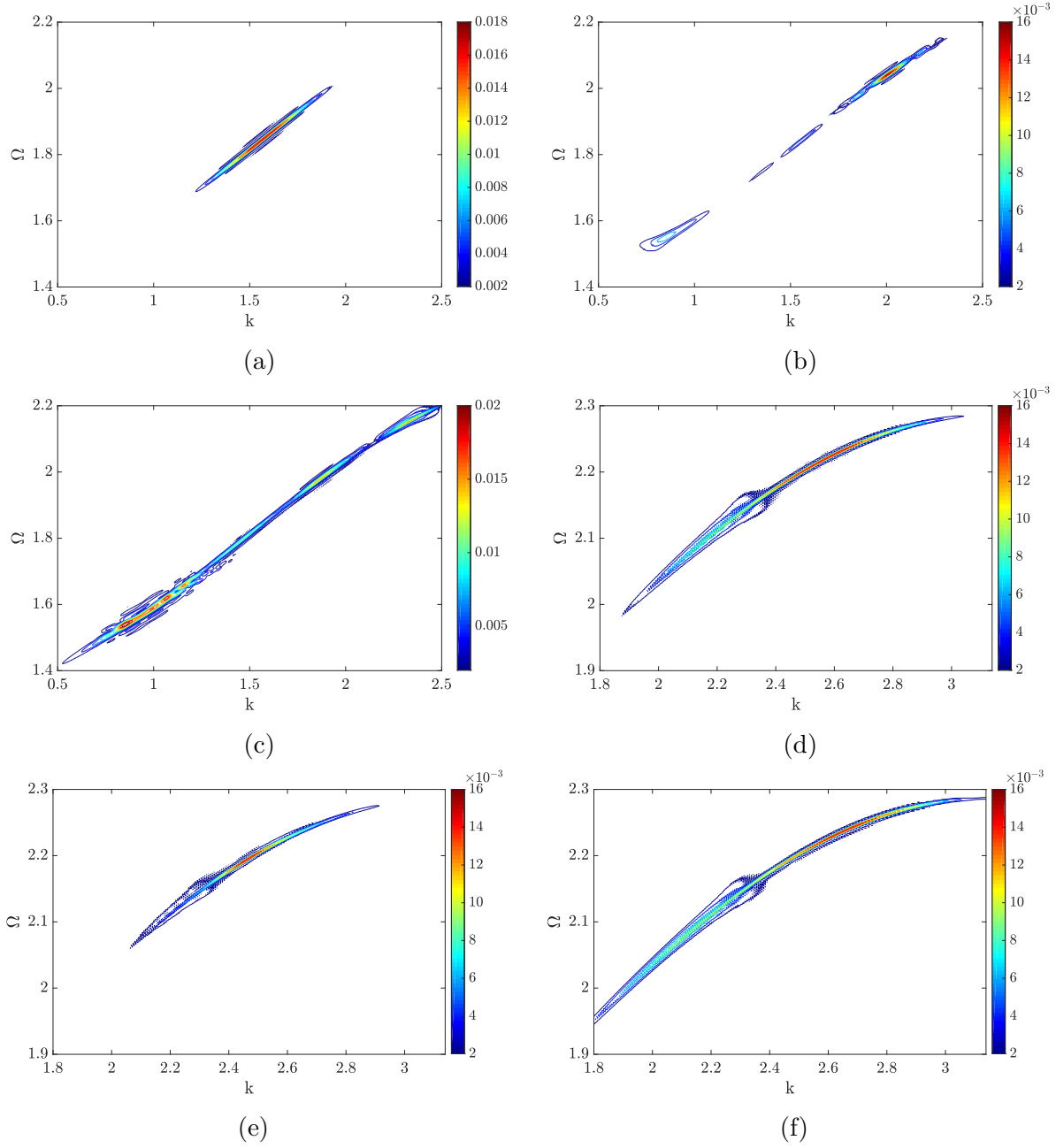
Figure 5.9: Contour plots of the 2D FFT for the output voltage in the optical mode $R = 10^7\Omega$, $\theta = 10^{-8}$ N/V: (a) $k = \pi/2$, $\epsilon\alpha a^2 = 0$; (b) $k = \pi/2$, $\epsilon\alpha a^2 = 0.03$; (c) $k = \pi/2$, $\epsilon\alpha a^2 = -0.03$; (d) $k = \pi/9$, $\epsilon\alpha a^2 = 0$; (e) $k = \pi/9$, $\epsilon\alpha a^2 = 0.03$; (f) $k = \pi/9$, $\epsilon\alpha a^2 = -0.03$.

ascertain its limitation. At short wavelength limit in the acoustics mode, the analytical results indicate that the effect of nonlinearity is the highest in this mode. The contour plot in this region indicates that the analytical results can predict the cut-off frequency for $\epsilon \alpha a^2 \leq 0.03$, as shown in Fig. 5.10 (a). In particular, the main solitary wave (which has most of the energy content) is almost confined within the analytical nonlinear dispersion curve. It is noteworthy that the dispersive component of the signal (which has low energy content) coincides with the linear dispersion curve. The error becomes more significant with increasing nonlinearity and our analytical solution fails to predict the cut-off frequency in this region with stronger nonlinearity, as depicted in Fig. 5.10 (b). For better prediction of the cut-off frequency, higher order perturbation should be considered. The analytical results also indicate that the effect of nonlinearity is more pronounced at long wavelength limit in the optical mode. In this region, our approximate solution also fails to predict the exact cut-on frequency, as shown in Figs. 5.10 (c) and (d). This can be explained by the significant frequency shift observed at the long-wavelength limit and discussed in the previous sections. In the short-wavelength limit in the optical mode, the analytical results slightly overestimate the cut-off frequency, as shown in Figs. 5.10 (e) and (f). This error increases with increasing nonlinearity although the effect of nonlinearity is minimal at this wavelength limit in the optical mode as demonstrated in the analytical and spectro-spatial results. It is noteworthy that although our analytical solution fails to predict the exact cut-off frequencies at some regions, it can provide an indication about the regions most affected by nonlinearity. This conclusion was supported by the spectro-spatial analyses discussed in the previous section. For instance, the analytical results show that the effect of nonlinearity is more pronounced at the long-wavelength limit in the optical mode. Similarly, the spectro-spatial analyses of the numerical results demonstrated that the effect of nonlinearity in this region is the most significant due to the severe wave distortion.
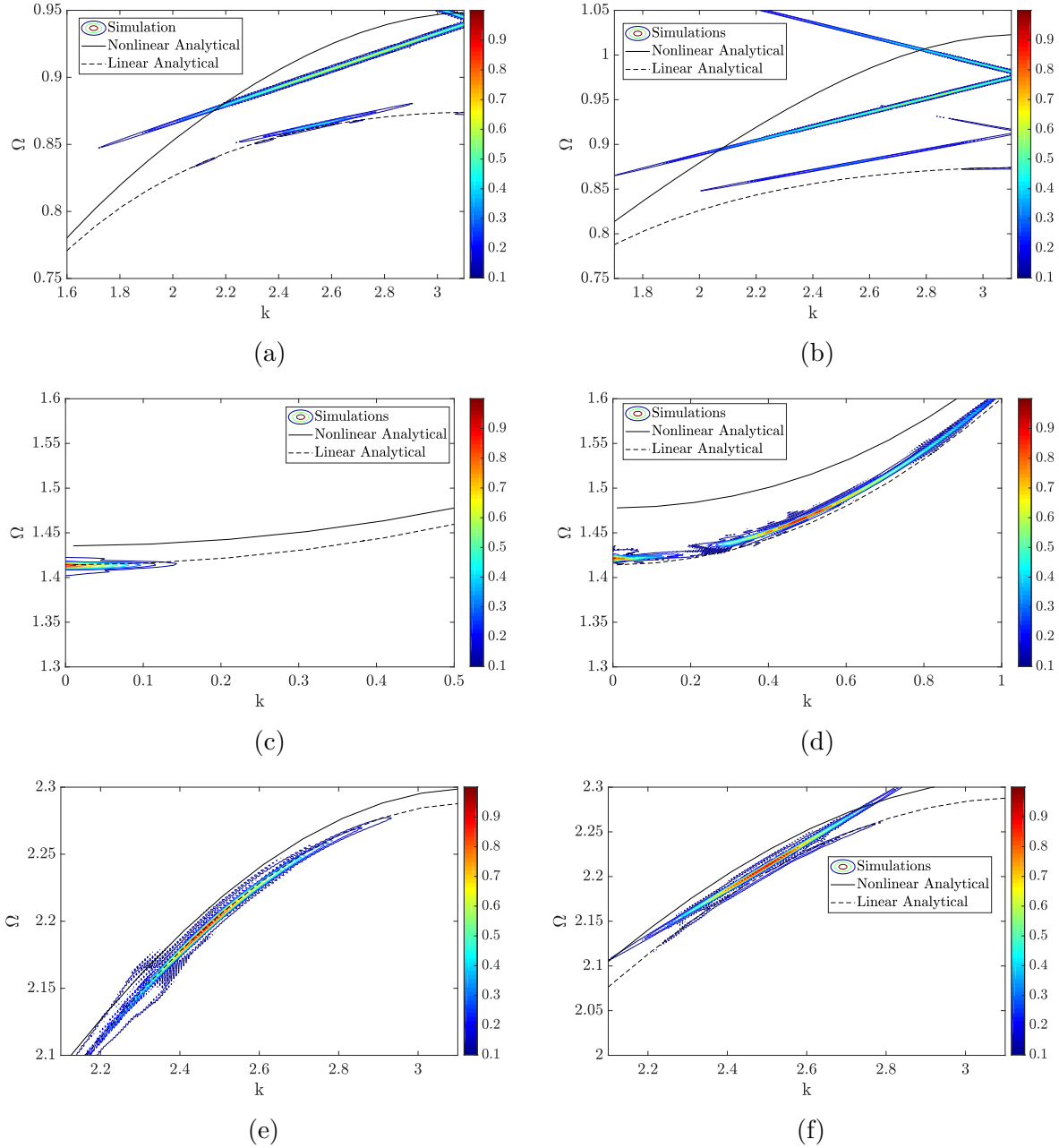
Figure 5.10: Validation of the analytical results using the reconstructed dispersion curves from 2D FFT $R = 10^7\Omega$, $\theta = 10^{-8}$ N/V: (a) Acoustics mode, $k = 7\pi/9$, $\epsilon\alpha a^2 = 0.03$; (b) Acoustics mode, $k = 7\pi/9$, $\epsilon\alpha a^2 = 0.06$; (c) Optical mode, $k = \pi/9$, $\epsilon\alpha a^2 = 0.01$; (d) Optical mode, $k = \pi/9$, $\epsilon\alpha a^2 = 0.03$; (e) Optical mode, $k = 7\pi/9$, $\epsilon\alpha a^2 = 0.03$; (f) Optical mode, $k = 7\pi/9$, $\epsilon\alpha a^2 = 0.06$.

5.6 Computational demonstration of significant frequency shift using COMSOL Multiphysics

In order to further demonstrate the significant frequency shift observed at the long-wavelength limit, we simulate a nonlinear periodic structure using COMSOL Multiphysics. We followed [192] in modelling our nonlinear structure; we model our resonator as unbuckled beam instead of buckled (curved) beam since we focus on studying cubic nonlinearity only. A schematic diagram of the unit cell is depicted in Fig. 5.11. The unit cell is assumed to be excited in the longitudinal direction (e.g., 1D model). First, we conduct stationary analyses to check the nonlinear stiffness of the local resonator in our model. We apply a static force at the middle point of the resonator and record the displacement as the force varies. The material is selected to be Aluminum which has a density of 2700 kg/m^3 and a modulus of elasticity of 69 GPa. The out of plane thickness for the proposed structure is 4.8 mm. The displacement-force curve obtained by COMSOL is plotted in Fig. 5.12. To obtain the stiffness coefficient, we fit the data using MATLAB curve fitting tool. Using a formula with a linear and cubic term, we obtain the linear stiffness as 18.19 N/mm and the nonlinear cubic stiffness as 12.01 N/mm^3 with **R-squared** value near 1. This indicates that our assumption about weak cubic nonlinearity in the proposed model is valid. It is noteworthy that we neglect the piezoelectric layer in the model since we only consider the weak electromechanical coupling case where its effect was shown to be negligible through this paper and in the literature [26]. However, the piezoelectric layer will be considered in the experimental demonstration in the next section.

We obtain first the linear band structure of the unit cell using COMSOL Multiphysics and plot it in Fig. 5.13. The waves propagating in the longitudinal direction are plotted in red stars. The bandgap for the longitudinal waves is observed around the linear in-plane
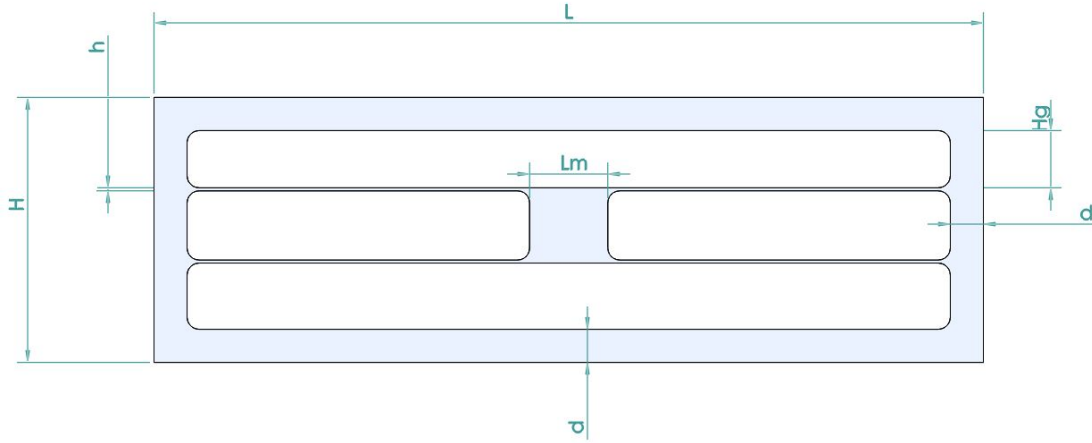
Figure 5.11: A schematic for unit cell model simulated in COMSOL Multiphysics, $L = 69$ mm, $H = 22$ mm, $h = 1$ mm, $d = 2.75$ mm, $Lm = 6.5$ mm, $Hg = 5$ mm.
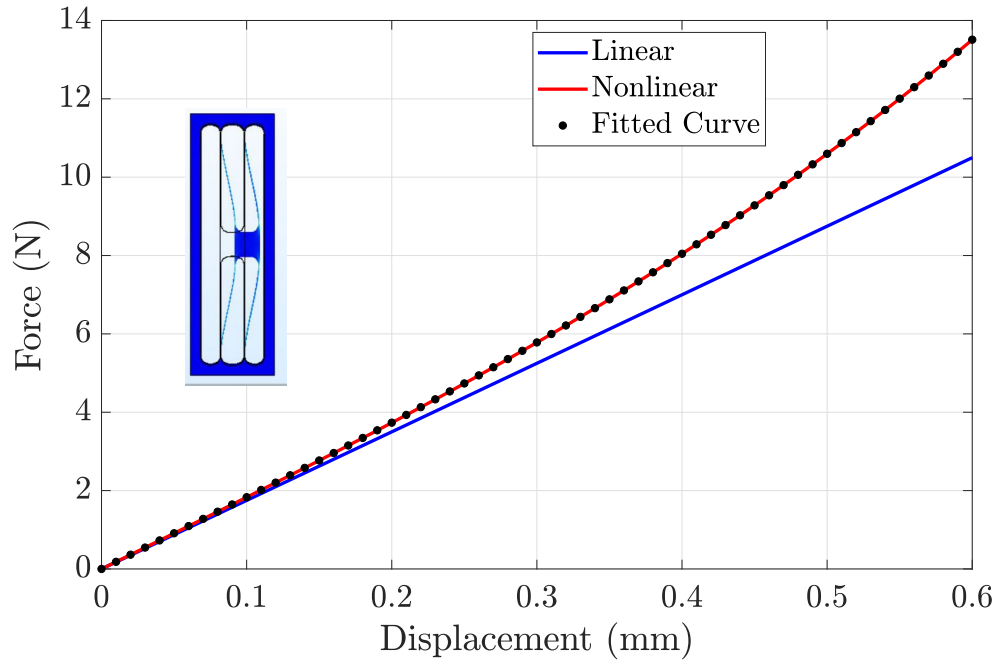
Figure 5.12: Determining the resonator nonlinear stiffness for the model; displacement-force curve measured in COMSOL and fitted curve.

natural frequency (the in plane natural frequency was determined in COMSOL Multiphysics and it is equal to 543.64 Hz) and highlighted in the shaded area in the figure. Particularly, the bandgap is located between 504.6-544.5 Hz. To further demonstrate the bandgap, we determine the transmissible curve of a chain consists of 50 cells and excited in the longitudinal direction. The transmission diagram is depicted in Fig. 5.14 and indicates clearly a significant drop in the transmissibility around the bandgap frequencies.

After demonstrating the bandgap in the infinite and finite structure (i.e., 50 cells chain), we conduct further nonlinear time dependent analyses using COMSOL Multiphysics. We excite the system by an input wave at a frequency, which lies within the long-wavelength limit (a frequency just after the bandgap in the optical mode). We selected this frequency to be ω=600 Hz and defined the input wave as

$$u_0 = \frac{U_0}{2}(H(t) - H(t - 2\pi Ncy/\omega))(1 - cos(\omega t/Ncy))sin(\omega t) \tag{5.51}$$

where $H(t)$ is the Heaviside function, and Ncy is the number of cycles in the input wave and it is equal to 30 in the current simulations. We first excite the system by a low wave amplitude $U_0 = 10\mu$m to investigate the behavior in the linear regime. The spectrogram of the short term Fourier transform for the temporal domain is depicted in Fig. 5.15 (a). The results indicate that the output wave has frequency content within the input frequency range. However, a frequency component with very low energy content appears at frequency above the input frequency range. This component is developed due to the extremely weak nonlinearity at this level of input wave's amplitude. Next, we excite our structure by a large amplitude wave $U_0 = 100\mu$m to reach the weekly nonlinear regime. The spectrogram of the output wave is shown in Fig. 5.15 (b). The results indicate the existence of high energy frequency components at frequency away from the input signal frequency. This demonstrates a significant frequency shift at the long-wavelength limit, which corroborates the analyti-
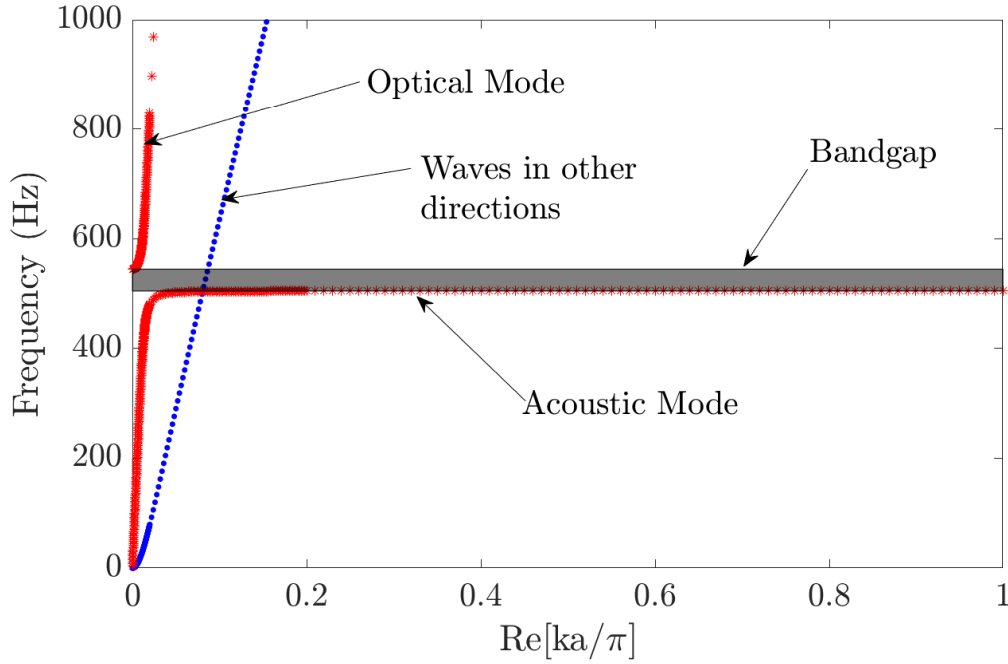
Figure 5.13: Band diagram of the structure by applying periodic boundary condition in COMSOL Multiphysics. Only the Brillouin zone of the longitudinal waves is considered here.

cal observations in the previous sections. Increasing the vibration amplitude further will result in further migration of the energy content to frequency components away from the input frequency component and diminishing the energy content of the linear component(i.e., component with frequency equal to the input frequency).

5.7 Experimental demonstration of significant frequency shift

A metastructure prototype consists of 50 cells (i.e., single cell is shown in Fig. 5.11) was fabricated from Multipurpose 6061 Aluminum Sheet with a thickness of 4.8 mm. A thin piezoelectric layer was installed on the resonator embedded in the last cell to simulate the
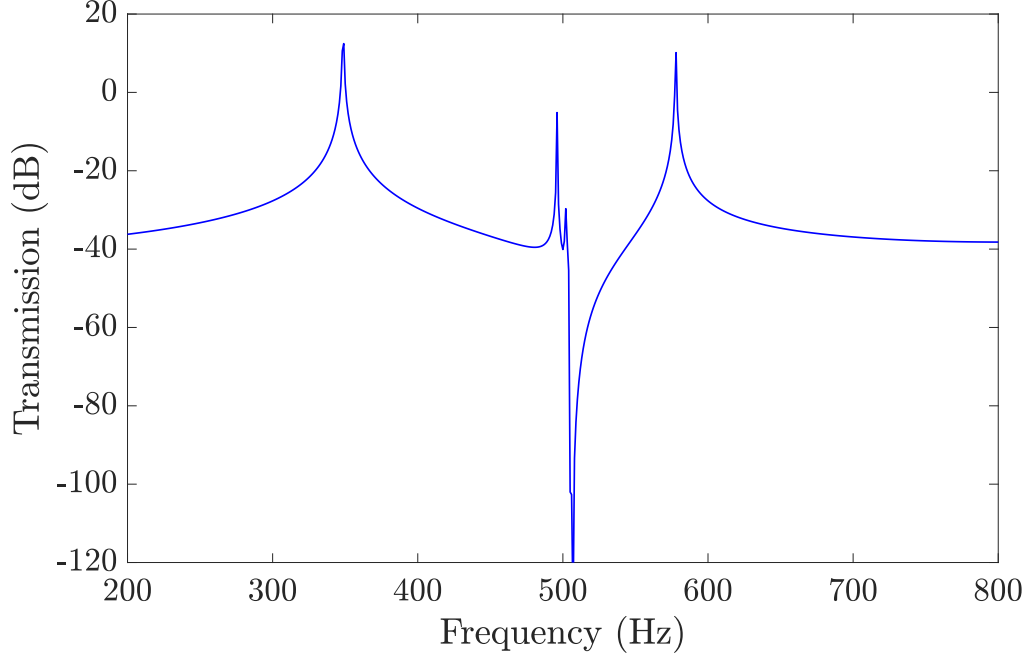
Figure 5.14: Transmission diagram of a structure consisting of 50 cells.
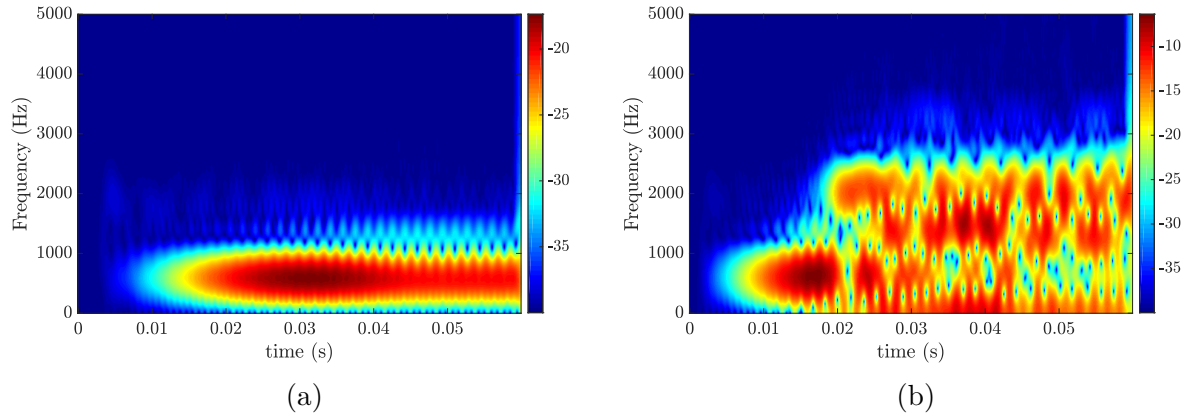
Figure 5.15: Spectrogram of the short term Fourier transform for the output wave: (a) Linear regime $U_0 = 5\mu$m; (b) Nonlinear regime $U_0 = 50\mu$m.

Figure 5.16: Experimental setup of the metastructure prototype: (a) Shaker, (b) prototype, (c) amplifier, (d) analyzer, (e) laser doppler, (f) shunted circuit.

weak electromechanical coupling and monitor the harvested voltage. To simulate a free condition at the top and the bottom, the metastructure is suspended using fishing wires, as shown in Fig. 8.15. The first cell of the metastructure is glued to an electromagnetic shaker (LDS V408) that is driven by an amplified signal generated through the analyzer (Polytec DAQ) according to the input wave profile defined in Eq. 5.51. This signal is further amplified using an amplifier (LPA100). The response of the free end of the structure is recorded using Polytec Laser Doppler Vibrometer (Polytec PSV-500). In addition, the piezoelectric layer is shunted to a load resistor (2.2 MΩ) and the voltage is recorded using a DAQ system.

We first determine the transmission of the metastructure to determine the frequency of the long wavelength limit that needs to be applied to the structure. A burst random
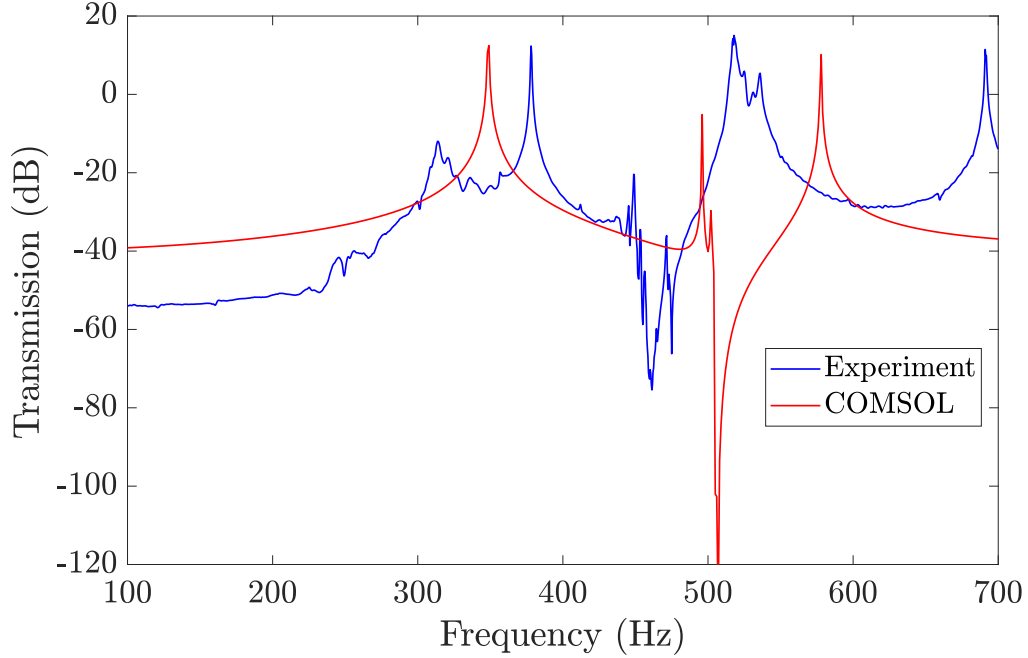
Figure 5.17: Experimental transmission diagram of a structure consists of 50 cells.

signal with 15 averages is used to obtain the transmission curve. The obtained transmission
curve is shown in Fig. 5.17 and compared with COMSOL results. From the figure, it can
be observed that there is a clear local resonance transmission dip at around 462 Hz. Due to
some imperfection in the manufacturing process, the experimental attenuation dip is slightly
different from that of the computational with around 9% percentage error. This shift in
the frequency value can also be attributed to gluing the structure to the shaker unlike the
free-free boundary conditions used in the computational simulations. Moreover, this shift
might also be attributed due to the holes made in the structure in order to facilitate the
manufacturing process. Based on this, we also anticipate shifting the long wavelength limit
to a lower frequency region. Therefore, we select 530 Hz as an excitation frequency to
demonstrate the frequency shift in the long wavelength limit.

Next, we applied an input wave with a frequency of 530 Hz and 30 cycles to the structure
and measure the harvested voltage. The measured voltage is further analyzed by determining

the short term Fourier transform of the signal, as shown in Fig. 5.18. At low amplitude input signal (i.e., 0.05 V, 0.1269 g), the results indicate that the harvested voltage is confined within the input frequency region and no frequency shift can be observed, as depicted in Fig. 5.18(a). This indicates that the metastructure is excited in the linear regime where the effect of nonlinearity is negligible. However, when we increase the input voltage to 0.5 V, multiple frequency components appears at frequencies different from the input frequency range with a significant energy content, as shown in Fig. 5.18(b). Indeed, this clearly demonstrates the significant frequency shift at the long-wavelength limit due to resonator nonlinearity when the system is excited in the nonlinear regime. Hence, the experimental observation corroborates both the analytical and computational findings i.e., the emergence of significant frequency shift in the long-wavelength domain. Therefore, these components with shifted frequency content can be utilized to design the electromechancial diode when coupled to a linear chain.
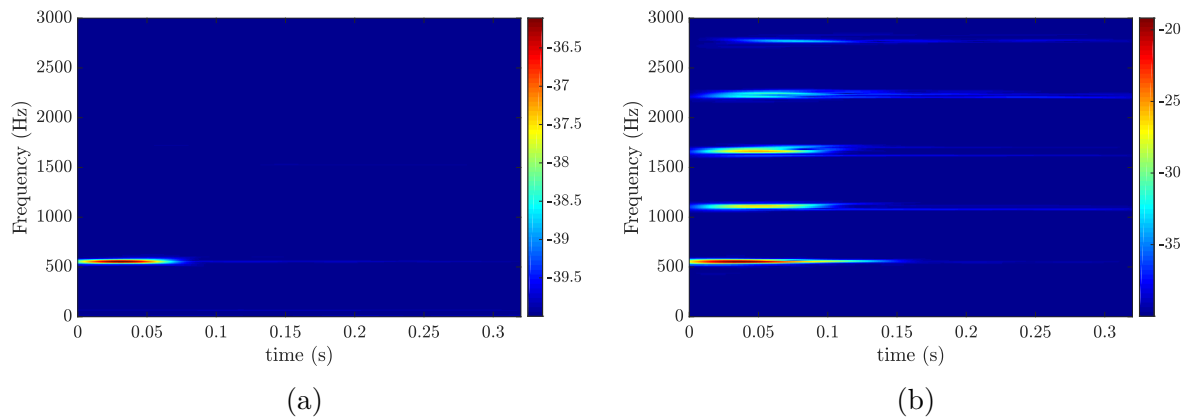
Figure 5.18: Spectrogram of the short term Fourier transform for the measured output voltage: (a) Linear regime 0.05 Volt; (b) Nonlinear regime 0.5 Volt.

Chapter 5. Substantial frequency conversion at long-wavelength limit in
metamaterial with weakly nonlinear local electromechanical resonators: Analytical
162   and computational study

Conclusion

In this paper, we investigated a metamaterial with nonlinear local electromechanical resonators for simultaneous energy harvesting and vibration attenuation. The metamaterial consists of a chain of masses connected by linear springs. A weakly nonlinear electromechanical resonator was coupled to each cell and shunted to a load resistor to harvest energy. The model of the electromechanical resonator was reduced to an equivalent nonlinear spring-mass system with an equivalent capacitance of the piezoelectric element and an equivalent coupling coefficient. An approximate closed-form solution for the dispersion relation was obtained by MMS. The analytical results indicated that the effect of nonlinearity is more pronounced at frequencies close to the resonance frequency of the electromechanical resonator. Therefore, it can appear at all wavelength limits, unlike the case of chain nonlinearity, where the effect of nonlinearity was concentrated at the short-wavelength limit only. Moreover, the results demonstrated that weakly electromechanical coupling has no effect on the bandgap size and dispersion curves. The electromechanical coupling affects only the attenuation level inside the bandgap without changing its size. Therefore, the proposed system can also be employed in energy harvesting applications without degrading the obtained bandgap size. On the other hand, a very strong electromechanical coupling can lead to a significant change in the band structure and merging the apart acoustics and optical mode into one dispersion curve.

To reveal more important characteristics of the nonlinear wave propagation in the proposed structure other than the cut-off frequencies, we conducted signal processing techniques on the numerical results to investigate the spectro-spatial features. The spatial wave profile of the signals demonstrated that propagating waves are subjected to severe wave distortion at all wavelength limits in the case of the nonlinear electromechanical resonator. In general, the effect of softening nonlinearity appears as a wave stretching over the chain,

while the effect of hardening nonlinearity appears as traveling localized component. The severity of wave distortion was significant at excitation frequencies close to the resonance frequency of the electromechanical resonator. In the acoustics mode, it was demonstrated that the traveling localized component has a harvested voltage higher than the linear case, thus hardening nonlinearity of the resonator can enhance sensing. The STFT also demonstrated the wave localization/stretching due to the hardening/softening nonlinearity at the medium and the short-wavelength limits in the acoustics mode and at the short wave length limit in the optical mode. However, the results demonstrated a significant frequency shift at medium wavelength limit in the optical mode for both types of nonlinearity. In particular, the output frequency components of the wave appeared at frequencies different than the input frequency and the energy content was concentrated into multiple component. Unlike the case of nonlinear chain, the nonlinearity of the electromechanical resonator surprisingly showed a significant frequency shift at long wavelength limit in the optical mode. This frequency shift can extend the application of metamaterials to the long-wavelength region in addition to medium and short wavelengths. Furthermore, we obtained the contour plot of 2D FFT to numerically reconstruct the dispersion curves. In addition to demonstrating the significant frequency shift, the results demonstrated that hardening nonlinearity has a localized component with a fix slope. This indicated that the localized traveling component is a solitary wave. Furthermore, we employed the contour plots to validate our analytical solution. The results demonstrated the limitations of the obtained analytical solution. Although our analytical solution showed a limitation in predicting the cut-off frequency, it can be effectively used in obtaining the most affected regions and wavelength limits by nonlinearity. Finally, we proved the existence of significant frequency shift computationally using COMSOL Multiphysics and experimentally. We designed a cell with week cubic nonlinearity. Upon exciting a chain of 50 cells at the long-wavelength limit, we were able to show a significant frequency shift in this limit with large amplitude waves.

Chapter 6

Effect of electromechanical coupling on locally resonant metastructures for simultaneous energy harvesting and vibration attenuation applications

This chapter is an edited version of: Bukhari, Mohammad A., Feng Qian, Oumar R. Barry, and Lei Zuo. "Effect of Electromechanical Coupling on Locally Resonant Metastructures for Simultaneous Energy Harvesting and Vibration Attenuation Applications." *In Dynamic Systems and Control Conference*, vol. 84287, p. V002T38A003. American Society of Mechanical Engineers, 2020. [32].

The study of simultaneous energy harvesting and vibration attenuation has recently been the focus in many acoustic metamaterials investigations. The studies have reported the possibility of harvesting electric power using electromechanical coupling; however, the effect of the electromechanical resonator on the obtained bandgap's boundaries has not been explored yet. In this chapter, we investigate metamaterial coupled to electromechanical resonators to demonstrate the effect of electromechanical coupling on the wave propagation analytically and experimentally. The electromechanical resonator is shunted to an external

164

load resistor to harvest energy. We derive the analytical dispersion curve of the system and show the band structure for different load resistors and electromechanical coupling coefficients. To verify the analytical dispersion relations, we also simulate the system numerically. Furthermore, experiment is carried out to validate the analytical observations. The obtained observations can guide designers in selecting electromechanical resonator parameters for effective energy harvesting from metamaterials.

6.1   INTRODUCTION

Unlike homogeneous structures, artificially structured crystals in special engineered config-
urations and patterns can exhibit a superior vibration control performance particularly at
low frequencies. These structures are called metamaterials [14, 84]. For instance, arrang-
ing crystals in periodic configuration can attenuate waves with wavelength near the lattice
constant from propagating through the structure. This phenomena is also known as Bragg
scattering [97, 98, 99, 159, 160, 178].

Controlling smaller structures with lattice constant much smaller than the wavelength
can be obtained by embedding local resonators inside the structure to form locally resonant
metamaterials [110]. This is a consequence of mode hybridization. Nevertheless, Bragg
scattering can still be observed in locally resonant metamaterials [4]. Formation of bandgaps
in locally resonant metamaterials depend on the local resonator's parameters [109].

By attaching a piezoelectric patch on the local resonator, electromechanical bandgap
can be formed due to the added stiffness to the system by the electromechanical coupling
[5, 13, 34, 173, 194]. Moreover, shunting the piezoelectric patch to an external resistor can
harvest the kinetic energy from wave propagating through the structure [74]. This offers
simultaneous energy harvesting and vibration attenuation in metamaterials. Inspiring by
metamaterials' flat frequency response [157], many researcher investigated energy harvest-
ing from local electromechanical resonators. This included models for discrete crystals [74]
and distributed parameter metamaterials [75]. Moreover, Hu et al., [76] suggested coupling
the local resonators in metamaterials to enhance the energy harvesting performance. Fur-
thermore, experimintal demonstration for energy harvesting and vibration attenuation in 3D
printed 2D structure can be found in [105]. Another application for 2D metamaterials in
energy harvesting is focusing propagating waves by lens for effective energy harvesting [175].
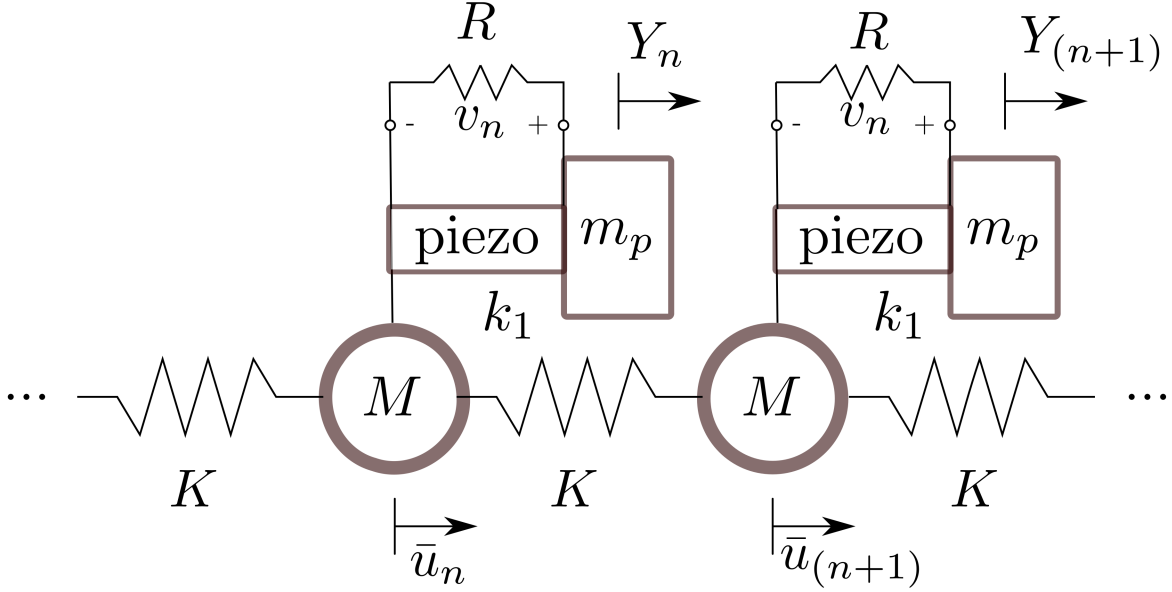
Figure 6.1: A schematic diagram for the locally electromechanical resonant metamaterial.

The aforementioned investigations have examined the concept of energy harvesting from metamaterials with electromechanical resonators. However, there were no studies that examines the effect of electromechanical coupling with load resistor on the band structure of locally resonant metamaterials. It is also unknown whether the energy harvesting degrades the performance of vibration attenuation in metastructure. This is the focus of the current study. In this chapter, we examine the wave propagation in a chain with local electromechanical resonators. The electromechanical resonator is shunted to an external load resistor to harvest the generated power. We present the governing equation of motions and then obtain the dispersion relation analytically. We also validate the obtained analytical results numerically. Moreover, we investigate the influence of different electromechanical coupling parameters on the band structure. Finally, we experimentally validate the observed analytical results with a finite structure.
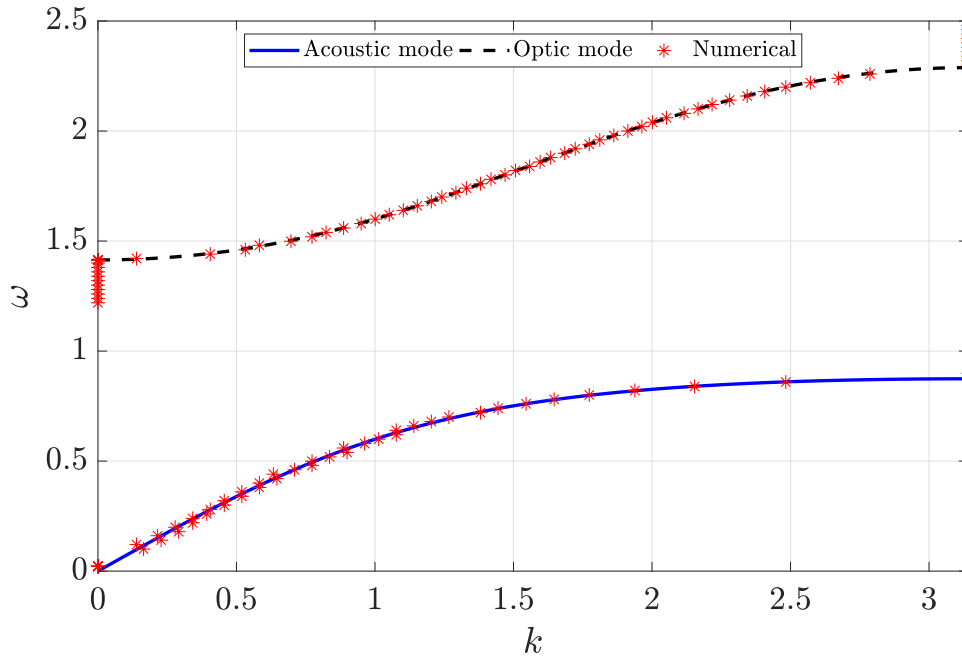
Figure 6.2: Analytical and numerical band structures for a chain with electromechanical resonator: $\omega_d = \omega_n = 1000$ rad/s^2, $k_1 = 10^6$ N/m, $\bar{k} = 1$, $\theta = 10^{-10}$ N/V, $C_p = 13.3 \times 10^{-9}$, and $R = 10^7 \Omega$.
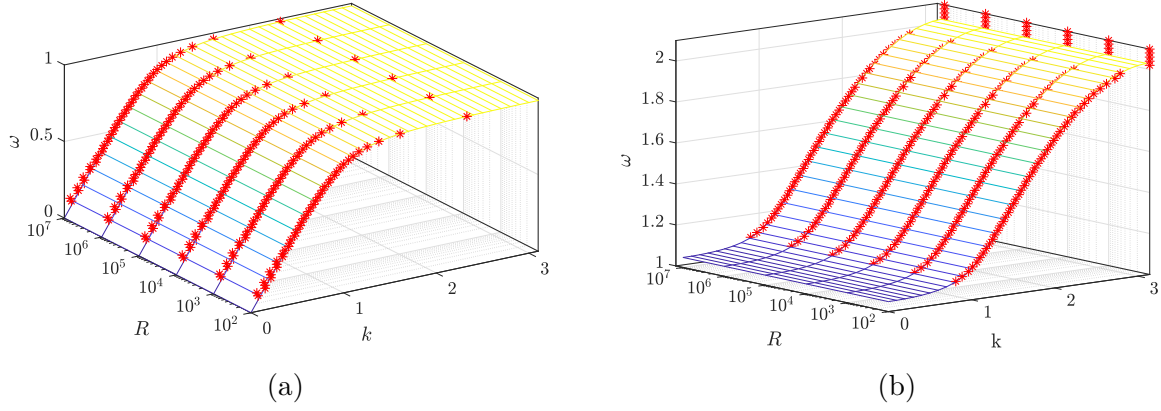
Figure 6.3: The effect of load resistor on the band structure: $\omega_d = \omega_n = 1000$ rad/s^2, $k_1 = 10^6$ N/m, $\bar{k} = 1$, $\theta = 10^{-10}$ N/V, $C_p = 13.3 \times 10^{-9}$, and $R = 10^2 - 10^7 \Omega$. (a): Acoustic mode; (b): Optical mode.

6.2 SYSTEM DESCRIPTION AND MATHEMATICAL MODELING

A schematic diagram for the locally electromechanical resonant chain is shown in Fig. 6.1. s periodic crystals with a mass, M, lattice constant, a, and connected by a linear spring with a coefficient, K. A local electromechanical resonator shunted to an external resistor R is embedded in each cell. The electromehanical resonator has an effective mass, m_p, effective stiffness, k_1, electromechanical coupling coefficient, θ, and capacitance of the piezoelectric element, C_p. The displacement of the nth cell is $\bar{u}_n$, the absolute displacement of the local resonator is Y_n, and the harvested voltage by the shunted resistor is $\bar{v}_n$.

The governing equation of motions for the nth crystal and its electromechanical local resonator can be expressed as

$$M\ddot{\bar{u}}_n + 2K\bar{u}_n - K\bar{u}_{n+1} - K\bar{u}_{n-1} + m_p(\ddot{\bar{y}}_n + \ddot{\bar{u}}_n) = 0 \tag{6.1}$$
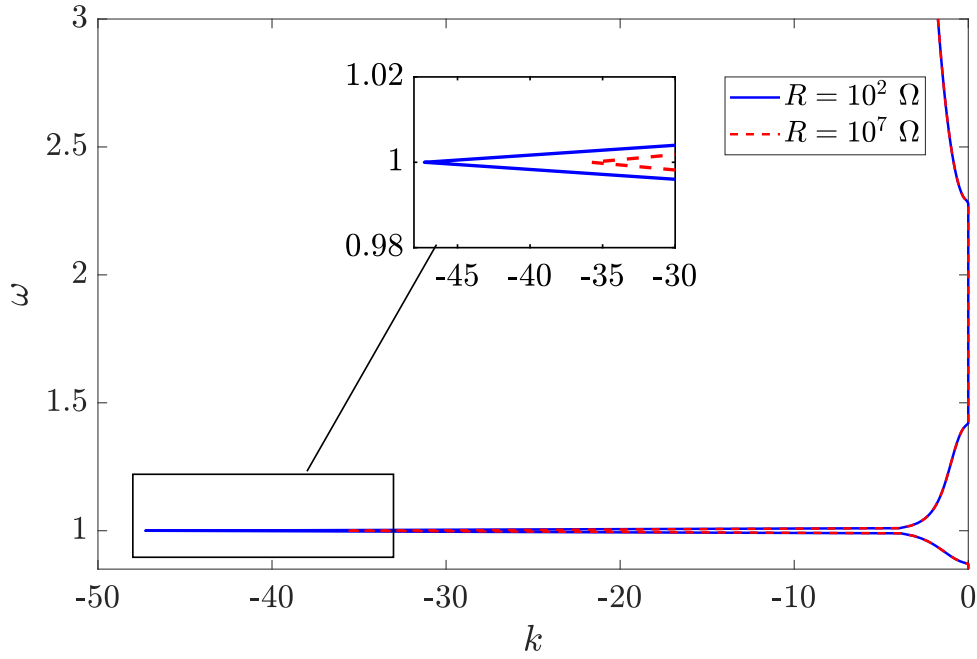
Figure 6.4: Imaginary part of the band structures for a chain with electromechanical resonator: $\omega_d = \omega_n = 1000$ rad/s^2, $k_1 = 10^6$ N/m, $\bar{k} = 1$, $\theta = 10^{-10}$ N/V, and $C_p = 13.3 \times 10^{-9}$ F.
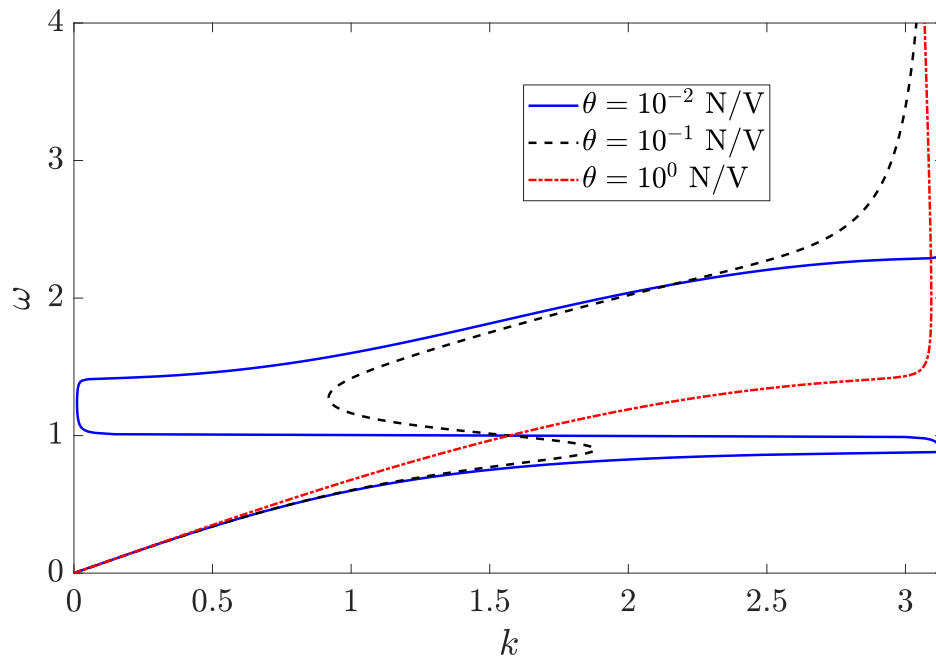
Figure 6.5: The effect of the electromechanical coupling coefficient on the band structures for a chain with electromechanical resonator: $\omega_d = \omega_n = 1000$ rad/s^2, $k_1 = 10^6$ N/m, $\bar{k} = 1$, $R = 10^2 \Omega$, and $C_p = 13.3 \times 10^{-9}$ F.

$$m_p \ddot{\bar{y}}_n + k_1 \bar{y}_n - \theta \bar{v}_n = -m_p \ddot{\bar{u}}_n \tag{6.2}$$

$$RC_p \dot{\bar{v}}_n + \bar{v}_n + R\theta \dot{\bar{y}}_n = 0 \tag{6.3}$$

where $\bar{y}_n = Y_n - \bar{u}_n$ is the net displacement of the nth electromechanical resonator, and the dots are the time derivatives.

Equations (1)-(3) can be rewritten in the dimensionless form as

$$\ddot{u}_n + 2u_n - u_{n+1} - u_{n-1} + \bar{k}\Omega_0^2(\ddot{y}_n + \ddot{u}_n) = 0 \tag{6.4}$$

$$\Omega_0^2 \ddot{y}_n + y_n - \alpha_1 v_n = -\Omega_0^2 \ddot{u}_n \tag{6.5}$$

$$\alpha_2 \dot{v}_n + v_n + \alpha_3 \dot{y}_n = 0 \tag{6.6}$$

where

$$\omega_n^2 = K/M, \omega_d^2 = k_1/m_p, \bar{k} = k_1/m_p, u_n = \bar{u}_n/U_0,$$
$$y_n = \bar{y}_n/y_0, v_n = \bar{v}_n/V_0, \Omega_0 = \omega_n/\omega_d, \alpha_1 = \theta V_0/k_1, \tag{6.7}$$
$$\alpha_2 = RC_p\omega_n, \alpha_3 = R\theta\omega_n y_0/V_0, \tau = \omega_n t$$

and U_0, y_0, and v_0, are normalized constants. The solution of the system can be expressed as

$$u_n = A e^{i(nk-\omega\tau)} \tag{6.8}$$

$$y_n = B e^{i(nk-\omega\tau)} \tag{6.9}$$

$$v_n = C e^{i(nk-\omega\tau)} \tag{6.10}$$

where ω is angular frequency and k is the normalized wavenumber.

Introducing Eqns. (9)-(10) into Eqn. (6) yields

$$-i\alpha_2\omega C + C - i\alpha_3\omega B = 0 \tag{6.11}$$

Rearranging Eqn. (11) leaves us with

$$C = \Gamma B \tag{6.12}$$

where Γ is complex and defined as

$$\Gamma = \frac{i\alpha_3\omega}{1 - i\alpha_2\omega} \tag{6.13}$$

Similarly, introducing Eqns. (8)-(10) and Eqn. (12) in Eqn. (5) leads to

$$B = K_\omega A \tag{6.14}$$

where K_ω is also complex and defined as

$$K_\omega = \frac{\Omega_0^2\omega^2}{1 - \alpha_1\Gamma - \Omega_0^2\omega^2} \tag{6.15}$$

By substituting Eqns. (8)-(9), and Eqn. (14), the dispersion relation of the system can be written as

$$-\omega^2 + (2 - 2\cos k) - \bar{k}\Omega_0^2\omega^2(1 + K_\omega) = 0 \tag{6.16}$$

6.3   EFFECT OF ELECTROMECHANICAL COUPLING ON THE BAND STRUCTURE

Upon calculating the roots of Eqn. (16) at a specific wave number, we get four complex roots with nonzero real part and one pure complex root. Two of the former are the passband positive frequencies while the other two roots are the passband negative frequencies. The fifth root is the frequency inside the bandgap. We plot the band structure of the system in Fig. 6.2. To check the accuracy of the analytical solution, we also plot the band structure obtained numerically in Fig. 6.2. The band structure can be obtained by numerically integrating a chain (i.e we use here 100 cells) excited at the middle point (at n = 50) by a harmonic force. Then, we determine the wave number by picking the maximum value of the 2-D spectrum; such that, the wave number is associated with the spatial frequency at the excitation frequency. To eliminate any reflected waves, the end condition is chosen to be a perfectly matched layer (PML) [133]. The numerical results shows a very good agreement with the analytical results in the presence of electromechanical coupling.

Next, we study the effect of load resistor on the band structure in a weakly electromechanical coupling case. Figure 6.3 shows the acoustic and optical modes for different load resistor (star lines) as compared to the case of mechanical local resonator without electromechanical coupling (mesh surface). The results indicate that neither the acoustic nor the optical mode are evidently affected by the electromechanical coupling. This indicates that metastructures can be used for simultaneous energy harvesting and vibration mitigation without degrading the bandgap boundary when the electromecanical coupling is weak. Moreover, installing piezoelectric patches on few local resonators can offer feasible energy harvesting in finite structures while preserving the vibration mitigation performance.

Although shunting the local resonator to a load resistor does not change the bandgap's

size, the load resistor affects the attenuation level inside the bandgap. This can be observed from the change in the imaginary part of the band structure as shown in Fig. 6.4.

For stronger electromechanical coupling coefficient θ, electromechanical coupling does not also change the shape of the band structure for $\theta \leq 10^{-3}$. However, increasing the electromechanical coupling further results in gradual deformation in the band structure. Indeed, the acoustic and optical modes starts emerging into a one dispersion curve as shown in Fig. 6.5. Therefore, the bandgap eventually disappears. It is noteworthy here that this observation in the bandgap is not feasible in most engineering applications since the electromechanical coupling coefficient depends on the piezoelectric coefficient which does not usually exceed the order of 10^{-10} [148].

6.4 EXPERIMENTAL VALIDATIONS

In this section, experiments are carried out to study the effect of energy harvesting on the vibration attenuation performance in a finite chain with electromechanical resonators as shown in Fig. 6.7. The finite chain consists of five unit cells and is implemented by an aluminum clamped free beam with length of 500 mm. The beam has a modulus of elasticity of 69 GPa, 25.4 mm width, a density of 2.7 g/cm^3, and a thickness of 3.25 mm. A local eletromechanical beam resonator is attached to each cell. The beam resonator is made of copper (i.e., has a 117.2 GPa modulus of elasticity and 8.912 g/cm^3 density) to obtain high mass ratio, which has a length of 85 mm, width of 16 mm, and thickness of 2 mm. Each beam resonator is sandwiched by two piezoelectric layers that stretched over 25 mm for the resonator length and polarized in the direction of the thickness. The piezoelectric layers are bounded to the copper resonator by an electric conductive adhesive.

The finite structure was mounted on an electromagnetic shaker (VG-100) to excite the

beam in the transverse direction. The shaker was driven by a Spider 80X dynamic analyzer (Crystal Instruments Inc.). The analyzer generates a closed loop controlled signal that has a constant excitation amplitude at different frequencies. The input excitation was recorded by an accelerometer (PCB356A16) and fed the closed loop controller. Another accelerometer was attached to the free end to record the output vibration. Each electromechanical resonator was shunted to a load resistor with different values ranging from the short circuit condition to the open circuit condition. The vibration of the free end along with the harvested voltage from each resonator were collected by the analyzer. The system was excited by a harmonic frequency sweep over the range of (20-300 Hz) with 0.1 g excitation amplitude. Within this frequency range, the analytical bandgap, bare structure, and electromechanical resonance frequency resonators are located.

To Validate the target frequencies for the host beam and the local resonators, we test these components using the same experimental setup. The 2nd-4th natural frequencies for the host beam are analytically determined as 66.4 Hz, 186.1 Hz, 366 Hz, respectively while the experimental results indicate that the corresponding frequencies are 63 Hz, 180.5 Hz, and 353 Hz, respectively. On the other hand, the natural frequency of the open circuit local resonator is analytically determined as 163 Hz while the experimental results show that the local resonator frequency is 158 Hz. The errors between the analytical and numerical results are less than 5% for all measurements, these error can be explained by the added mass from the accelerometer at the free end of the beams.

Next, we test the finite metastructure to obtain the experimental bandgap. For open circuit condition, we plot the analytical dispersion curve for the experimental setup in Fig. 6.7. Then, we plot the experimental vibration frequency response curve of the system with highlighting the boundaries of the analytical bandgap by the dashed vertical lines in Fig. 6.8. The results indicate that the experimental bandgap lies within the analytical bandgap;
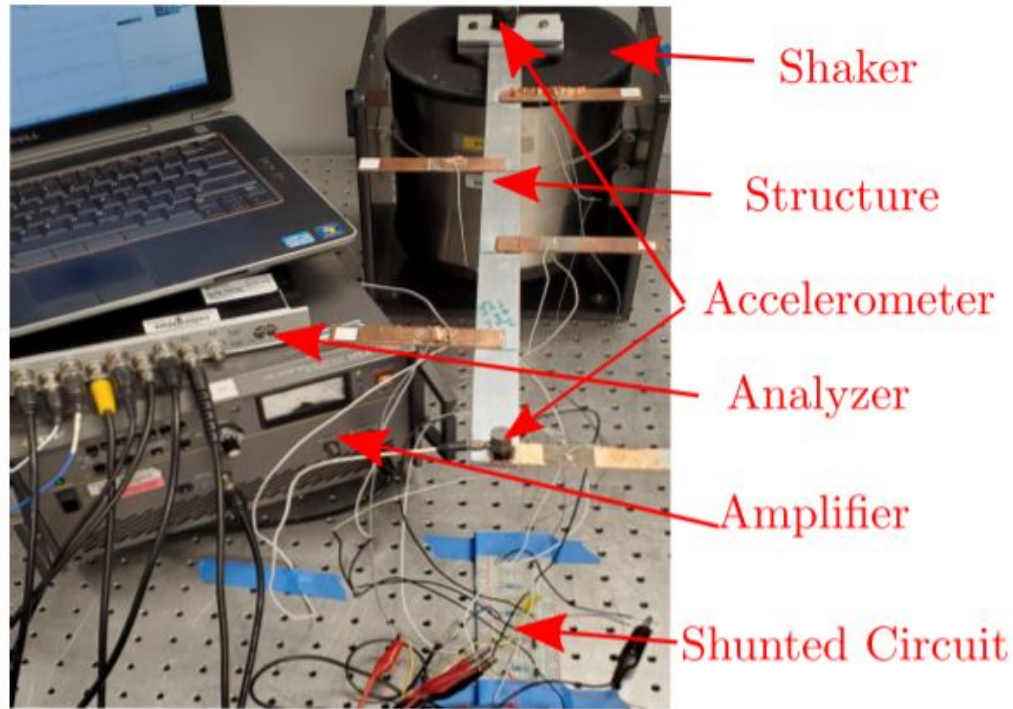
Figure 6.6: The experimental setup, a cantilever beam with 5 resonators.

however, there are multiple modes appearing in the middle of the bandgap. These modes are localized modes and are due to the low number of cells and existing boundary conditions. Therefore, these modes should be eliminated with increasing the number of cells in the model. To experimentally investigate the effect of energy harvesting on the boundaries of the bandgap, we plot the vibration frequency response curve of the finite structure in Fig. 6.9. As it was shown analytically, the shunted load resistor has no observaly effect on the bandgap size. Therefore, utilizing metastructure for energy harvesting applications does not degrade metastructure performance in terms of vibration attenuation.
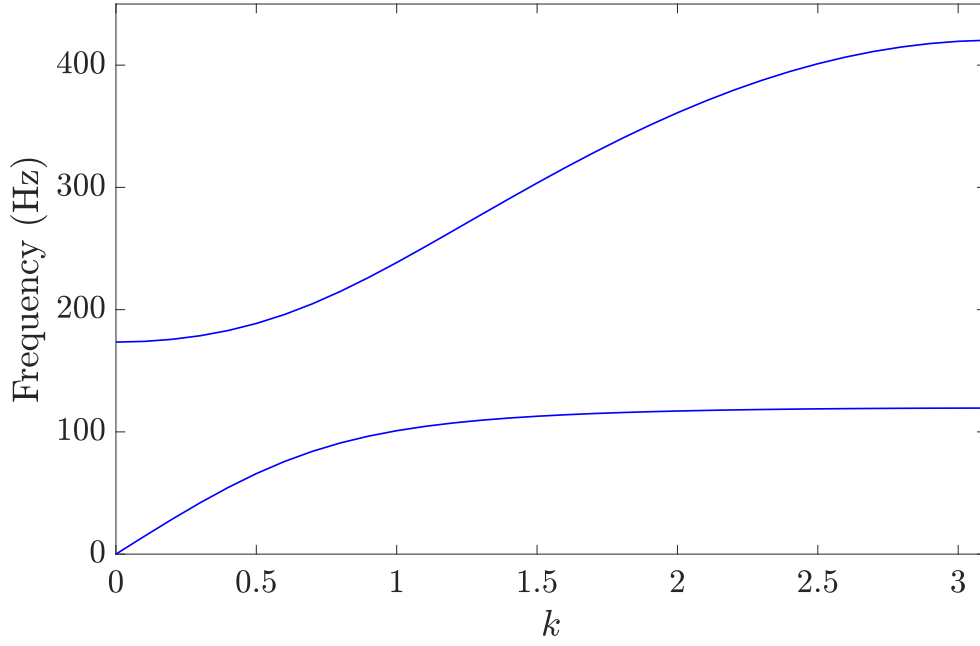
Figure 6.7: Analytical band structures for a chain with electromechanical resonator with parameters in the experimental setup: $\omega_d = 790$, $\omega_n = 1266$ rad/s^2, $k_1 = 6.788 \times 10^5$, $\bar{k} = 0.3581$.
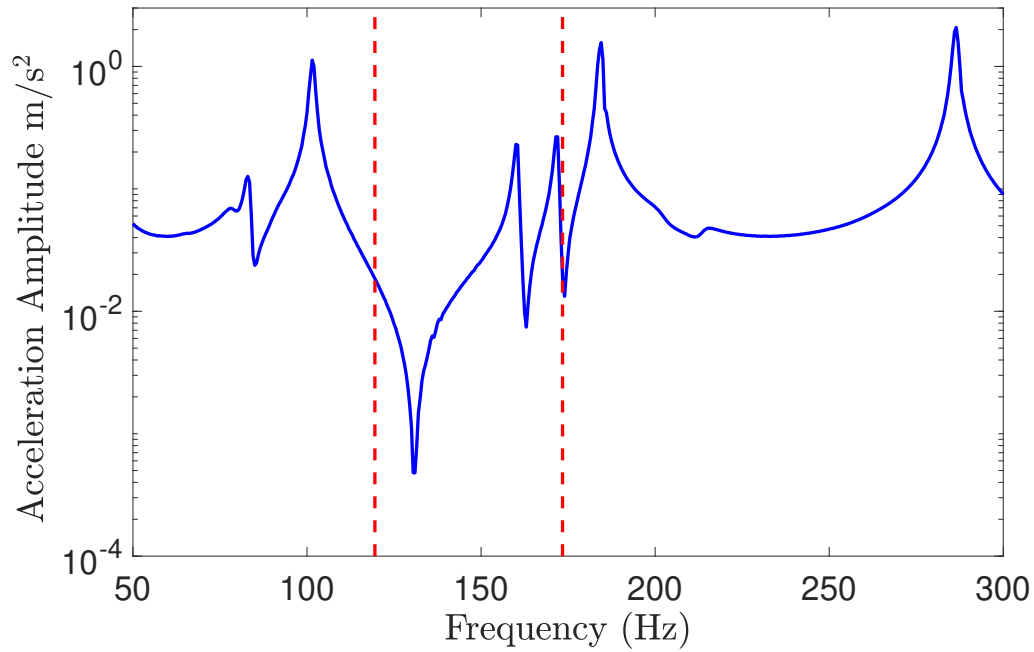
Figure 6.8: Vibration frequency response curve for a chain with electromechanical resonator with parameters in the experimental setup: $\omega_d = 790$, $\omega_n = 1266$ rad/s^2, $k_1 = 6.788 \times 10^5$, $\bar{k} = 0.3581$. Analytical bandgap is highlighted between the two vertical lines.
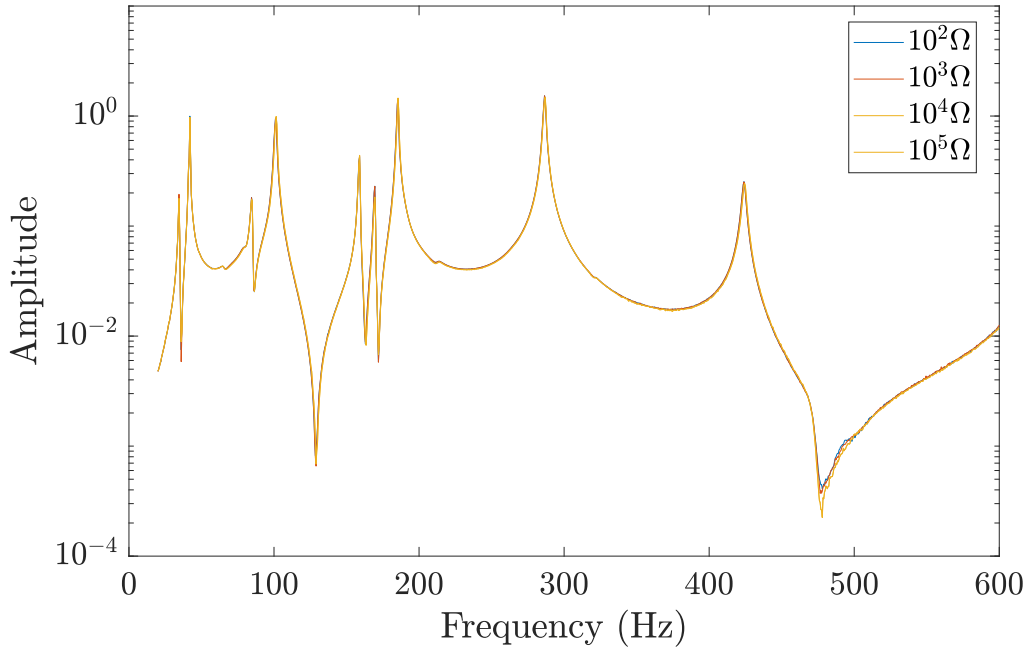
Figure 6.9: The effect of electromechanical coupling on the vibration frequency response curve for a chain with electromechanical resonator with parameters in the experimental setup: $\omega_d = 790$, $\omega_n = 1266$ rad/s^2, $k_1 = 6.788 \times 10^5$, $\bar{k} = 0.3581$.

6.5 CONCLUSION

In this chapter, we investigated the effect of energy harvesting on vibration attenuation performance in locally resonant metastructures. The system was represented by an infinite chain of spring-mass systems. Each unit cell (i.e., spring mass system) is connected to an electromechanical local resonator. The electromechanical resonator was modeled as a spring-mass system and is shunted to a load resistor. A dispersion relation and the band structure of the system for different load resistor were derived analytically. The analytical results demonstrated that locally resonant metastructures can be employed to harvest electric power without degrading the vibration attenuation performance for a weakly electromechanical coupling case. However, the load resistor reduces the attenuation constant inside the bandgap. Nevertheless, extremely strong coupling can deform the band structure and merge the dispersion curves of optical and accoustics mode. Experiments were conducted on a finite structure to demonstrate the observed phenomena for a weakly electromechanical coupling case. The experimental results indicated the exsitance of bandgap in the frequency response curve although the tested structure was finite. However, the effect of finite structure and boundary conditions appeared as localized modes inside the bandgap. Moreover, the test demonstrated that harvesting electrical power does not change the bandgap size.

Chapter 7

Broadband electromechanical diode: acoustic non-reciprocity in weakly nonlinear metamaterials with electromechanical resonators

This chapter is submitted for publication: Bukhari, M., and O. Barry. "Broadband electromechanical diode: acoustic non-reciprocity in weakly nonlinear metamaterials with electromechanical resonators".

Recent attention has been given to acoustic non-reciprocity in metamaterials with nonlinearity. However, the study of asymmetric wave propagation has been limited to mechanical diodes only. There is no work reported on electromechanical rectifiers or diodes. This problem is investigated here by analytically and numerically studying a combination of nonlinear and linear metamaterials coupled with electromechanical resonators. The nonlinearity of the system stems from the chain in one case and from the electromechanical resonator in another. The method of multiple scales is used to obtain analytical expressions for the dispersion curves. The obtained analytical results are validated numerically using Matlab built-in integrator. Numerical examples show potential for wider operation range

of electromechanical diode, considerable harvested power, and significant frequency shift. The observed frequency shift is demonstrated using spectro-spatial analyses and it is used to construct an electromechanical diode to guide the wave to propagate in one direction only. This only allows signal sensing for waves propagating in one direction and rejects any other signals. The performance of this electromechanical diode is evaluated by calculating the transmission ratio and the asymmetric ratio for a transient input signal. Design guidelines are provided to obtain the best electromechanical diode performance. The presented analyses show high asymmetry ratio for directional-biased wave propagation in the medium-wavelength limit for the case of nonlinear chain. Indeed, the present asymmetric and transmission ratios are higher than those reported in the literature for mechanical diode. The operation frequencies can also be broadened to the long-wavelength limit frequencies using the resonator nonlinearity.
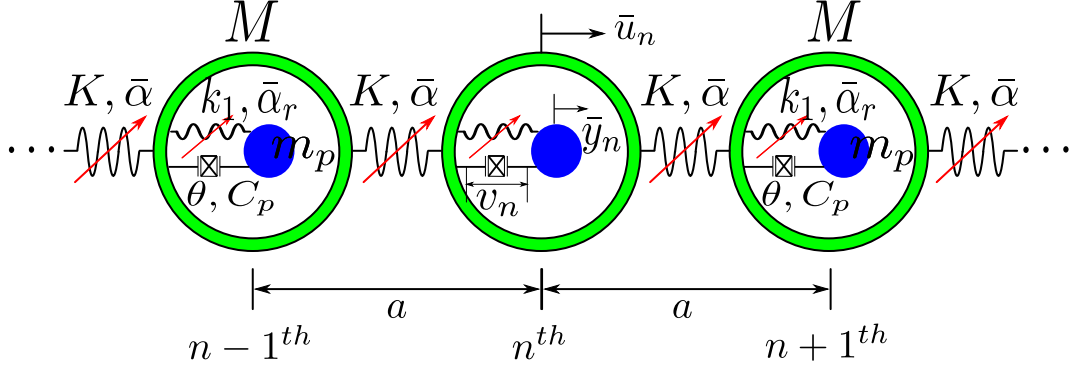
Figure 7.1: A schematic diagram for the nonlinear acoustic metamaterial with electrome-chanical resonators

7.1 INTRODUCTION

Metamaterials are artificially fabricated in special engineering configurations and constitutions. These configurations enable interesting dynamical properties that cannot be found in conventional homogeneous materials [14, 84]. These interesting unique properties make metamaterials perform incredibly in a wide pool of engineering applications (e.g., low frequency vibration mitigation, directional-biased wave propagation, wave focusing, and cloaking).

Metamaterials can be arranged in periodic patterns of cells also known as phononic crystals [97, 98, 99, 159, 160, 178]. Periodicity in phononic crystals can be represented by periodicity in material, geometry, and boundary conditions. These periodic crystals can reflect waves with a wavelength near the lattice constant due to Bragg scattering and hence they can be employed in low frequency vibration reduction applications. Nevertheless, the restriction on the lattice constant size limits this application to large structures only.

In order to extend the application of metamaterials to control smaller structures, researchers suggested embedding local resonators inside the cells [110]. This breaks the size constraint in Bragg scattering and allows hybridizing the resonance mode with the long-

wave nondispersive modes of the underlying medium, thus reflecting waves with wavelength much smaller than the lattice constant even in the absence of periodicity [4]. Indeed, both Bragg sccatering and mode hybridization can be observed in locally resonant metamaterials; however, each effect can be dominant at certain design parameters [109].

In addition to these unique low frequency vibration attenuation phenomena observed in linear metamaterials, nonlinearity in metamaterials can show further interesting wave propagation phenomena. This includes, but is not limited to, adjusted bandgap limits [117], solitons [95, 131], directional-biased wave propagation [107], and enhanced energy harvesting and sensing [26].

These interesting nonlinear wave propagation phenomena can be obtained through different analytical and numerical analyses. For analytical analyses, the type and the strength of nonlinearity determine how the problem can be tackled. For instance, weakly nonlinear systems can be handled using different perturbation approaches [134, 135]. The use of these techniques can be found in [133] for nonlinear chains, [195] for locally resonant metamaterials, and [27, 28, 30] for nonlinear chains with multiple linear and nonlinear local resonators. On the other hand, systems with strong nonlinearity should be handled using different techniques and closed form solution can be obtained in some cases analytically [90], or with the help of homotopy analyses [1]. However, numerical analyses should be employed when the approximate analytical solution of the problem is not accurate or when interesting nonlinear phenomena cannot be revealed by analytical analyses. These analyses include temporal space analyses and spectro-spatial analyses [27, 27, 28, 30, 63, 195].

The bandgap size in locally resonant metamaterials depends significantly on the added mass to the system, in that a wider bandgap requires a larger mass. Therefore, controlling vibrations in the structure may be limited by weight restrictions in many engineering applications. This restrictions can be overcome by adding a stiffness to the structure through

attaching piezoelectric patches to periodic patterns of cells [5, 13, 34, 173, 194]. In particular, electromechanical coupling can generate an electromechanical bandgap. The piezoelectric can also be used for energy harvesting and sensing. This is inspired by the flat frequency band in metamaterials and can be realized by shunting the piezoelectric material to a load resistor [74, 75, 76, 105, 157]. Consequently, metamaterials can be used for simultaneous energy harvesting and vibration reduction applications. For weak electromechanical coupling, it was analytically and experimentally shown that harvesting energy in metamaterials has no effect on the bandgap size [32]. The study of nonlinear systems also showed that the bandgap size is only affected by the nonlinearity in the chain in the case of weak electromechanical coupling.

The nonlinearity in metamaterials can lead to a significant wave distortion. This wave distortion results in frequency conversion, enabling output wave to appear at frequencies different from the input wave frequency. Indeed, when the nonlinear metamaterial is coupled to a linear metamaterial (i.e., the linear metamaterial has a bandgap tuned to the frequency conversion region in the nonlinear metamaterial), the energy content with shifted frequency can propagate in the forward configuration. However, waves propagating from the linear metamaterial side (backward configuration) will be tuned inside the linear metamaterial's bandgap. This is an indication that directional-biased wave propagation can be realized [16, 104, 106, 107, 115]. This wave non-reciprocity can also be observed in nonlinear granular structures [16] or nonlinear hierarchical internal structures [129]. Spectro-spatial analyses can be employed to examine the frequency conversion in nonlinear metamaterials. The spectro-spatial features can show a significant frequency shift at the medium-wavelength limit in both nonlinear chain and nonlinear local resonators metamaterials [26, 27, 195]. Unlike the case of nonlinear chain, nonlinear local resonator metamaterials can also show significant frequency shift at the long-wavelength limit in addition to the medium-wavelength limit

[27], [23]. Models of acoustic diodes are limited to the use of local mechanical resonators embedded within the periodic structure or simple coupling between linear and nonlinear metamaterials. To the best of our knowledge, there are no works in the literature investigating the use of electromechanical resonators in nonlinear metamaterials for designing electromechanical diodes except our preliminary work, recently published in a conference proceeding [29]. In addition, works in the literature did not harness the significant frequency shift at long wavelength limit for the case of nonlinear resonator to broaden the operation frequency of the electromechanical diode. Consequently, the asymmetric and transmission ratios are not relatively high for diodes reported in the literature. Furthermore, design guidelines for broadening the operation range of mechanical/electromechanical diode and increasing the asymmetry ratio are rarely found in the literature. These knowledge gaps form the core motivation of the current study.

In this paper, we study how a weakly nonlinear metamaterial with electromechanical local resonators can be used to maximize the performance of electromechanical diodes (i.e., increase both asymmetry and transmission ratios). The nonlinearity stems from the chain in one case and from the local electromechanical resonator in another, and is of a cubic type. These sources of nonlinearities can offer different operation frequency regions for the diode. The former can enable the diode to operate at medium wavelength limit, while the latter can broaden the operation frequency range since it can enable the diode to operate at both medium/long-wavelength limits. The system is simulated numerically and validated against other models in the literature. The numerical results are used to obtain the band structures and analyzed further by spectro-spatial analyses to demonstrate the frequency shift in the nonlinear proposed structure. This frequency shift is then used to design an electromechanical diode. The designed electromechanical diode is evaluated based on its transmission ratio and the asymmetric ratio for a transient input signal. The rest of the paper is as follows. In

Section 2, we present a mathematical model for the proposed weakly nonlinear metamaterial and the linear and nonlinear dispersion relations. In Section 3, we present the analytical and numerical band structures for different types of nonlinearities. Then, the significant frequency shift observed by analyzing the spectro-spatial features are presented in Section 4. This significant frequency shift is employed to design an electromechanical diode in Section 5. In Section 6, design guidelines for best electromechanical diode performance are provided. Finally, we summarize the main findings in the conclusion section.

7.2   SYSTEM DESCRIPTION AND MATHEMATICAL MODELING

A schematic diagram for the metamaterial chain with electromechanical resonators is shown in Fig. 7.1. The chain is constructed of s periodic cells with a mass, M, lattice constant, a, and connected by a linear or weakly nonlinear spring. The springs have linear coefficient, K, and nonlinear coefficient $\bar{\alpha}$. Attached to each cell, there is a local linear or nonlinear electromechanical resonator shunted to an external resistor R. The electromechanical resonator has effective mass, m_p, effective linear stiffness, k_1, effective nonlinear stiffness $\bar{\alpha}_r$, electromechanical coupling coefficient, θ, and capacitance of the piezoelectric element, C_p. It is noteworthy here that the system is reduced to a linear system when $\bar{\alpha} = 0$ and $\bar{\alpha}_r = 0$. Moreover, we set $\bar{\alpha}_r = 0$ for the case of nonlinear chain only, while we set $\bar{\alpha} = 0$ for the case of nonlinear resonator.

The equation of motions for the nth cell and its electromechanical resonator can be expressed as follows

$$M\ddot{\bar{u}}_n + 2K\bar{u}_n - K\bar{u}_{n+1} - K\bar{u}_{n-1} + \bar{\alpha}(\bar{u}_n - \bar{u}_{n+1})^3 +$$

$$\bar{\alpha}(\bar{u}_n - \bar{u}_{n-1})^3 + m_p(\ddot{\bar{y}}_n + \ddot{\bar{u}}_n) = 0 \tag{7.1}$$

$$m_p\ddot{\bar{y}}_n + k_1\bar{y}_n + \bar{\alpha}_r\bar{y}_n^3 - \theta\bar{v}_n = -m_p\ddot{\bar{u}}_n \tag{7.2}$$

$$RC_p\dot{\bar{v}}_n + \bar{v}_n + R\theta\dot{\bar{y}}_n = 0 \tag{7.3}$$

where $\bar{u}_n$ is the displacement of the nth cell, $\bar{y}_n = Y_n - \bar{u}_n$ is the net displacement of the nth electromechanical resonator, Y_n is the absolute displacement of the electromechanical resonator, $\bar{v}_n$ is the harvested voltage in the nth electromechanical resonator, and the dots are the derivative with respect to time.

We introduce the following dimensionless parameters in order to normalize Eqns. 7.1-7.3:

$$\omega_n^2 = K/M, \omega_d^2 = k_1/m_p, \bar{k} = k_1/K, u_n = \bar{u}_n/U_0,$$

$$y_n = \bar{y}_n/y_0, v_n = \bar{v}_n/V_0, \epsilon\alpha = \bar{\alpha}U_0^2/K, \epsilon\alpha_r = \bar{\alpha}_rU_0^2/k_1$$

$$\Omega_0 = \omega_n/\omega_d, \alpha_1 = \theta V_0/k_1, \alpha_2 = RC_p\omega_n, \tag{7.4}$$

$$\alpha_3 = R\theta\omega_n y_0/V_0, \tau = \omega_n t$$

where U_0, V_0, y_0 are the zeroth cell displacement, harvested voltage, and resonator displacement, respectively.

Substituting Eqn. 7.4 into Eqns. 7.1-7.3 yields the following normalized equations

$$\ddot{u}_n + 2u_n - u_{n+1} - u_{n-1} + \epsilon\alpha(u_n - u_{n+1})^3 + $$
$$\alpha(u_n - u_{n-1})^3 + \bar{k}\Omega_0^2(\ddot{y}_n + \ddot{u}_n) = 0 \tag{7.5}$$

$$\Omega_0^2\ddot{y}_n + y_n + \epsilon\alpha_r y_n^3 - \alpha_1 v_n = -\Omega_0^2\ddot{u}_n \tag{7.6}$$

$$\alpha_2\dot{v}_n + v_n + \alpha_3\dot{y}_n = 0 \tag{7.7}$$

(a)   (b)
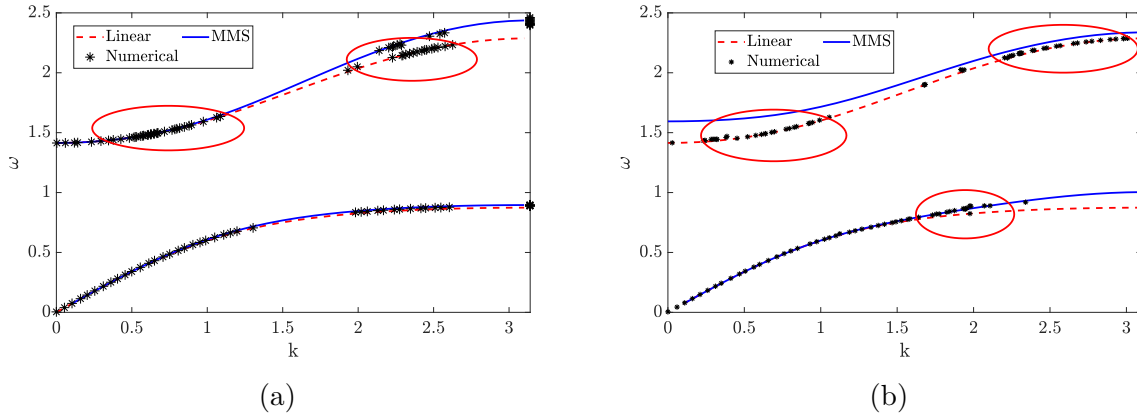
Figure 7.2: Band structure for linear and nonlinear metamaterials with electromechanical resonators obtained analytically and numerically: (a) Nonlinear chain case $\epsilon A^2\alpha = 0.06$, $\epsilon A^2\alpha_r = 0$; (b) Nonlinear resonator case $\epsilon A^2\alpha = 0$, $\epsilon A^2\alpha_r = 0.06$.

In order to obtain an approximate analytical solution, we need to expand the solution using the power series and separate the linear and nonlinear problems (see Appendix **??**).

Considering the linear problem (i.e., at order epsilon 0 in Appendix **??**) and following [26], we obtain the dispersion relation as

$$-\omega^2 + (2 - 2\cos k) - \bar{k}\Omega_0^2\omega^2(1 + K_\omega) = 0 \tag{7.8}$$

where $K_\omega = \frac{\Omega_0^2 \omega^2}{1 - \alpha_1 \Gamma - \Omega_0^2 \omega^2}$, and $\Gamma = \frac{i\alpha_3 \omega}{1 - i\alpha_2 \omega}$.

For the nonlinear problem (i.e., at order ϵ in Appendix **??**), one can write the nonlinear frequency equation, following [26], as

$$\omega_{nl} = \omega - \epsilon b' \tag{7.9}$$

where b' is the phase resulting from expressing A in the polar form (i.e., $A = ae^{ib}$) and is defined as

$$b' = c_1 a_0^2 \tag{7.10}$$

The constant c_1 is defined as

$$c_1 = -\frac{gl + fh}{h^2 + g^2} \tag{7.11}$$

where g, l, h, m, and f are defined in Appendix **??** for different sources of nonlinearity.

7.3   ANALYTICAL AND NUMERICAL BANDGAPS

To check our analytical dispersion relations, we plot the analytical and numerical band structure of the system with electromechanical resonator in Fig. 7.2. The numerical simulations are carried out by simulating a chain with 500 cells. The parameters of the metamaterial with electromechanical resonator are chosen to be: $\bar{k} = 1$, $\omega_n = \omega_d = 1000$, $k_1 = 10^6$ N/M, $C_p = 13.3 \times 10^{-9}$ F, $R = 10^7 \Omega$, and $\theta = 10^{-8}$ N/V. The system is excited by a transient wave packet and integrated numerically in MATLAB. To limit the propagation in one direction, we define the initial conditions as

$$u_m(0) = \frac{1}{2}(H(m-1) - H(m-1-N_{cy}2\pi/k))(1-$$
$$\cos(mk/N_{cy}))\sin(mk) \tag{7.12}$$
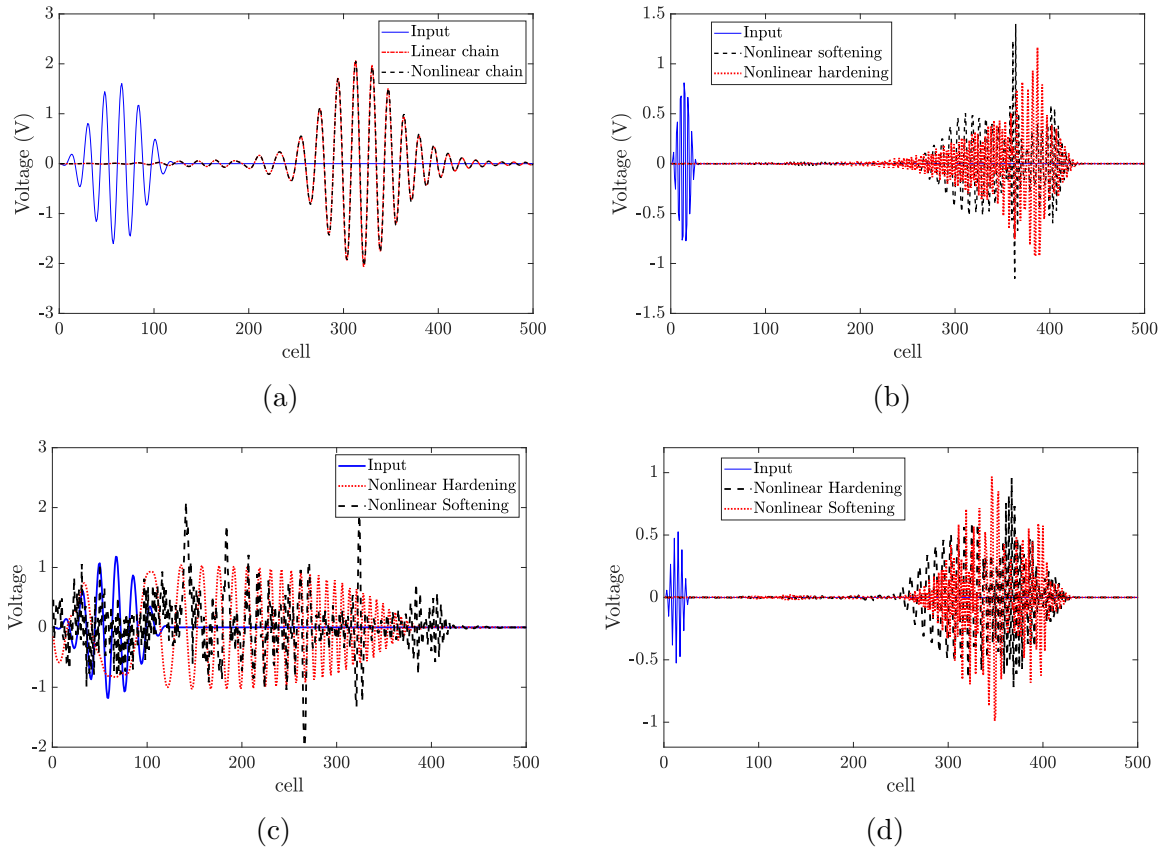
Figure 7.3: Spatial profile of the input/output voltage in the optical mode: (a) $k = \pi/9$, $|\epsilon A^2 \alpha| = 0.03$, $|\epsilon A^2 \alpha_r| = 0$; (b) $k = \pi/2$, $|\epsilon A^2 \alpha| = 0.03$, $|\epsilon A^2 \alpha_r| = 0$; (a) $k = \pi/9$, $|\epsilon A^2 \alpha| = 0$, $|\epsilon A^2 \alpha_r| = 0.03$; (b) $k = \pi/2$, $|\epsilon A^2 \alpha| = 0$, $|\epsilon A^2 \alpha_r| = 0.03$.

$$\dot{u}_m(0) = \frac{1}{2}(H(m-1) - H(m-1-N_{cy}2\pi/k))$$
$$(-\omega_n\omega/N_{cy}\sin(mk/N_{cy})\sin(mk) - \omega_n\omega(1- \tag{7.13}$$
$$\cos(mk/N_{cy}))\cos(mk))$$

$$y_m(0) = K_\omega u_m(0) \tag{7.14}$$

$$\dot{y}_m(0) = K_\omega \dot{u}_m(0) \tag{7.15}$$

$$v = \Gamma K_\omega u_m(0) \tag{7.16}$$

where $H(x)$ is the Heaviside function, and N_{cy} is the number of cycles and is chosen to be $N_{cy} = 7$ in this section.

Upon analyzing the simulation results by 2D Fast Fourier Transform (FFT), each point in the dispersion curves (frequency/wavenumber) belongs to the peak of 2D FFT. Then, the complete band structure can be obtained from sweeping the wavenumber over the first Brillouin zone at the acoustic and optical modes.

Figure. 7.2 (a) depicts the linear and nonlinear analytical band structures and the nonlinear numerical band structure for the nonlinear chain case. The results demonstrate that hardening nonlinearity shifts the dispersion curves up as compared to the linear curves. Moreover, the numerical integration results also demonstrate that the analytical solution can predict the boundary of the band structure, but fail to capture the significant frequency shift that is observed numerically at the medium wavelength limit in the optical mode. In

particular, input waves with frequencies within the medium wavelength limits appear inside the red circles on long and short wavelength limits, coinciding with the linear dispersion curves. This frequency shift will be used to design our electromechanical resonator and will be discussed further using the spectro-spatial analyses in the next section. Fig. 7.2 (b) shows the band structure for the nonlinear electromechanical resonator. The results demonstrate that hardening nonlinearity also shifts the dispersion curves up. This shift is more significant at frequencies near the fundamental frequency of the electromechanical resonator. Therefore, significant frequency shift near the long-wavelength limit in the acoustics mode can be realized, unlike the case of nonlinear chain where the frequency shift is limited to the medium-wavelength limit. For the case of resonator nonlinearity, input waves with frequencies within the medium and long-wavelength limits in the optical mode appear at different regions. These regions are highlighted inside the red circles and coincides with the linear dispersion curves. Therefore, the analytical solution fails to predict the band structure in these regions due to the significant frequency shift. Similar frequency shift appears at the short-wavelength limit in the acoustics mode, where the effect of the electromechanical resonator nonlinearity is maximum in this mode due to close tuning between the electromechanical resonator and frequencies in this region.

The results of band structures in Fig. 7.2 indicate the possibility of significant frequency shift; however, they do not reveal any further details on the the nature of the wave distortion, the output frequency content, and the spatial properties. Therefore, in the next section we employ different signal processing techniques to investigate the spectro-spatial features and obtain further detailed information.

7.4   SPECTRO-SPATIAL ANALYSES

To further demonstrate the significant frequency shift at the medium/long-wavelength limits in the optical mode for both types of nonlinearities, we analyze the numerical results further by utilizing different signal processing techniques.

We plot the spatial profile of the input and output voltage signals harvested by the electromechanical resonator at the end of the simulation in Fig. 7.3. At long-wavelength limit with chain nonlinearity (Fig. 7.3 (a), the results indicate that the chain nonlinearity has no effect on the output wave. In particular, the output wave is not distorted at all at this wavelength limit for chain nonlinearity. On the other hand, results at medium-wavelength limit demonstrate that the input signal is severely distorted and broken into several components, as shown in Fig. 7.3 (b). These components are: (1) one localized high-amplitude wave (solitary wave), and (2) two stretched and low-amplitude waves (dispersive waves). This indicates that the output wave appears at different frequencies other than the input frequency.

For nonlinear electromechanical resonator case, the results demonstrate that severe output wave distortion can be observed at long-wavelength limit (Fig. 7.3 (c)) and medium-wavelength limit (Fig. 7.3 (d)). Unlike the case of chain nonlinearity, severe wave distortion at long-wavelength limit due to resonator nonlinearity can be observed. Therefore, the input signal at this wavelength limit can appear at frequencies other than the input frequency. In addition, the wave distortion at medium wavelength limit due to resonator nonlinearity is similar to the distortion observed in the nonlinear chain case at the same wavelength limit. Although, the wave distortion in the case of nonlinear resonator is less severe than the distortion in the case of nonlinear chain, the case of nonlinear resonator can offer a significant frequency shift at the long-wavelength limit unlike the case of nonlinear chain.

Chapter 7. Broadband electromechanical diode: acoustic non-reciprocity in weakly nonlinear metamaterials with electromechanical resonators

196

The energy content of the frequency/wavenumber components are shown in Fig. 7.4. The figure presents the Short Term Fourier Transform (STFT) of the input/output signals' spatial components over the spatial domain. We use a Hann window with the size of the input signal to contain the propagating wave. For nonlinear chain case, the results indicate that the output voltage signal is broken into three components for hardening nonlinearity (Fig. 7.4 (a)) and into two components for softening nonlinearity (Fig. 7.4 (b)). For hardening nonlinearity, the first component appears at wavenumber/frequency above the input wavenumber/frequency window and it has the highest energy content. This is not surprising since the band structure figures showed that hardening nonlinearity shifts the dispersion curves up; therefore, the highest energy content component appears above the input frequency/wavenumber window. The second component appears inside the initial window and it has the lowest energy content. Finally, the third component is shifted below the initial window and its energy content is between the first and second components. Thus, most of the energy content of the input signal (i.e., inside the red ellipses on the figure) appears at output signal frequencies different than the input signal frequencies. This shows a good potential for using the proposed system to design an electromechanical diode. For softening nonlinearity, the first component appears outside the input frequency/wavenumber window and it has low energy content. The second component appears below the input window range and has the highest energy content. Although the case of softening nonlinearity shows also a significant frequency shift (i.e., inside the red ellipses on the figure), a significant portion of the energy content appears inside the input frequency/wavenumber window unlike the case of hardening nonlinearity. Therefore, we anticipate that hardening chain has better performance than softening chain in terms of non-reciprocal energy transmission.

For the case of nonlinear resonator, the results demonstrate a significant frequency shift at the long wavelength limit unlike the case of nonlinear chain. For softening nonlin-
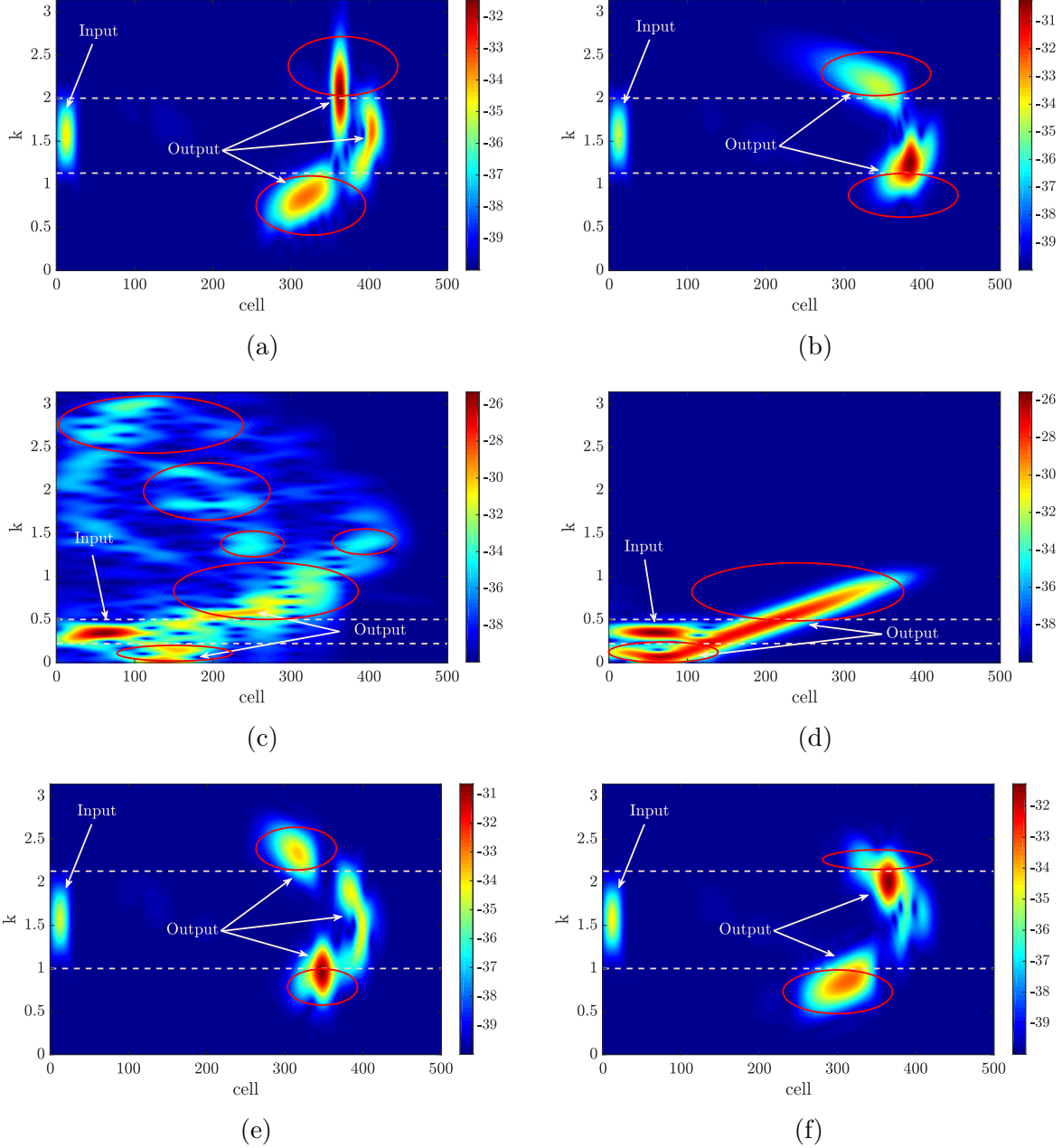
Figure 7.4: Spectrograms of the input/output voltage in the optical mode: (a)$k = \pi/2$, $\epsilon^2 A\alpha = 0.03$, $\epsilon^2 A\alpha_r = 0$; (b)$k = \pi/2$, $\epsilon^2 A\alpha = -0.03$, $\epsilon^2 A\alpha_r = 0$; (c)$k = \pi/9$, $\epsilon^2 A\alpha = 0$, $\epsilon^2 A\alpha_r = -0.03$; (d)$k = \pi/9$, $\epsilon^2 A\alpha = 0$, $\epsilon^2 A\alpha_r = 0.03$;(e)$k = \pi/2$, $\epsilon^2 A\alpha = 0$, $\epsilon^2 A\alpha_r = -0.03$; (f)$k = \pi/2$, $\epsilon^2 A\alpha = 0$, $\epsilon^2 A\alpha_r = 0.03$.
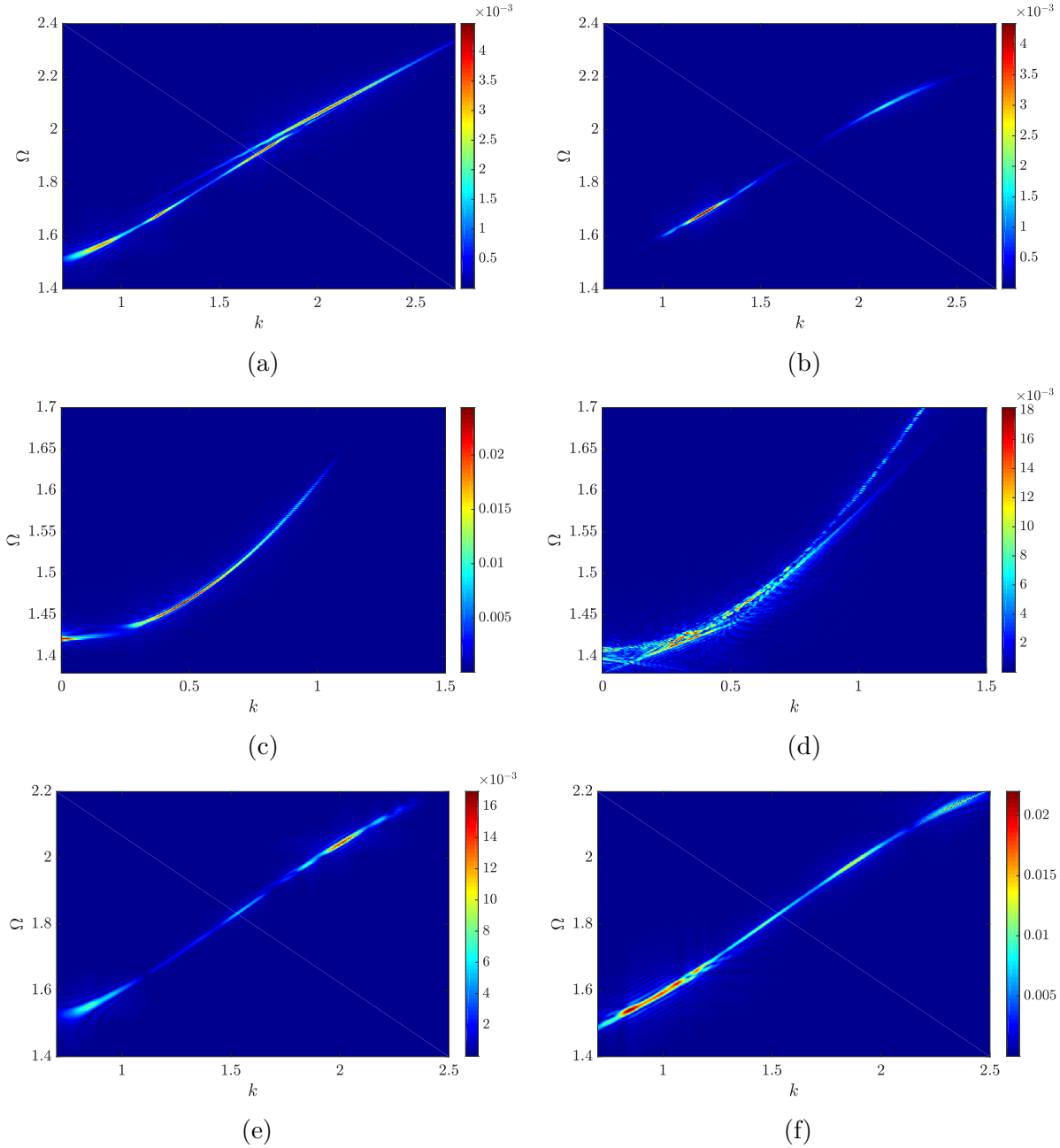
Figure 7.5: Images of the 2D FFT of the output voltage in the optical mode: (a)$k = \pi/2$, $\epsilon^2 A\alpha = 0.03$, $\epsilon^2 A\alpha_r = 0$; (b)$k = \pi/2$, $\epsilon^2 A\alpha = -0.03$, $\epsilon^2 A\alpha_r = 0$; (c)$k = \pi/9$, $\epsilon^2 A\alpha = 0$, $\epsilon^2 A\alpha_r = 0.03$; (d)$k = \pi/9$, $\epsilon^2 A\alpha = 0$, $\epsilon^2 A\alpha_r = -0.03$;(e)$k = \pi/2$, $\epsilon^2 A\alpha = 0$, $\epsilon^2 A\alpha_r = 0.03$; (f)$k = \pi/2$, $\epsilon^2 A\alpha = 0$, $\epsilon^2 A\alpha_r = -0.03$.
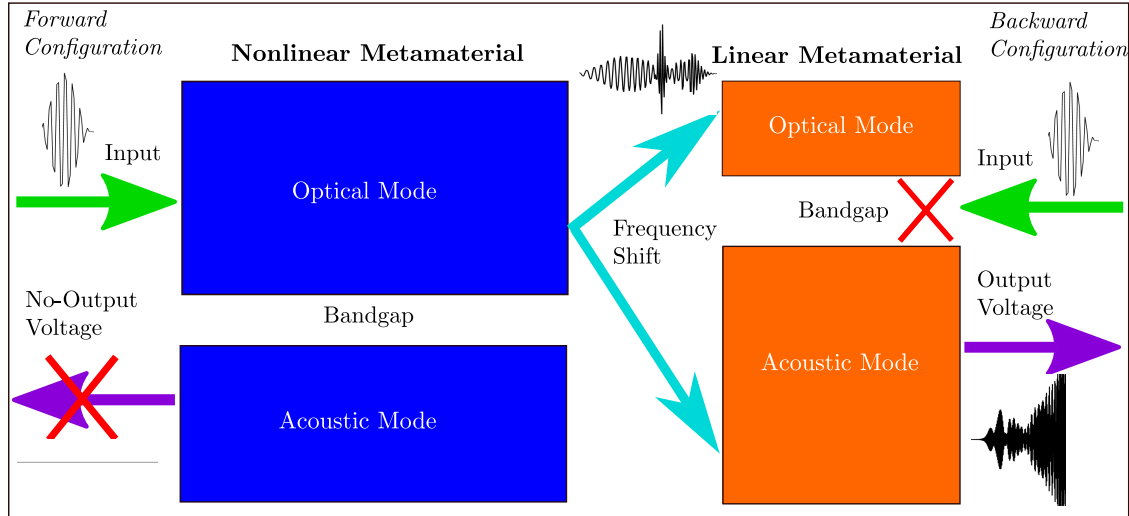
Figure 7.6: A schematic diagram for the electromechanical diode.

earity (Fig. 7.4 (c)), the STFT of the output voltage wave show the presence of multiple frequency/wavenumber components. These components stretch over a wide range of frequency/wavenumber. Most of those components appear outside the input frequency/wavenumber window (i.e., components confined inside the red ellipses). For hardening nonlinearity (Fig. 7.4 (d)), the energy content also extends outside the input frequency/wavenumber window. In particular, one of the output component stretches inside and outside the input window, while the other component is completely outside the input window. Therefore, hardening nonlinearity can also result in significant frequency shift at long-wavelength limit due to resonator nonlinearity. However, the frequency/wavenumber range at which the output signal stretches is narrower than that for the softening nonlinearity case. At medium-wavelength limit, the output signal is also broken into multiple components due to resonator nonlinearity similar to the case of nonlinear chain. For instance, softening nonlinearity breaks the output signal into three components, as shown in (Fig. 7.4 (e)). The highest energy content component appears below the input frequency/wavenumber window, while the lowest energy content component appears inside the input window. The third component has a moderate energy content and lies outside the input window. Since most of the output energy content

appears outside the input window (i.e., components confined inside the red ellipses), the resonator nonlinearity can also significantly shift the frequency content of the input signal at medium wavelength limit. Therefore, this type of nonlinearity is suitable to design an electromechanical diode at medium and long-wavelength limits. For hardening nonlinearity case (Fig. 7.4 (f)), resonator nonlinearity splits the output signal into two components. The first one has high energy content and is shifted up due to hardening nonlinearity, while the second has low energy content and appears below the input window. Since some of the energy content also appears outside the input window (highlighted by red ellipses in the figure), hardening nonlinearity can also show a significant frequency shift. However, this shift is not as significant as the shift in the case of softening nonlinearity for the resonator nonlinearity case.

Further demonstration of the significant frequency shift in the system can be obtained by plotting the contour of 2D FFT for the output signal as shown in Fig. 7.5. The results also indicate that the output signal frequency components are distributed over a wide range of frequencies, indicating the presence of significant frequency conversion. For instance, chains with hardening nonlinearity (Fig. 7.5 (a)) distribute the energy content over a wider range of frequencies as compared to the case of softening nonlinearity (Fig. 7.5 (b)). More-over, the high energy components are distributed over wavenumbers above and below the medium wavelength limit (i.e., wavelength of the input signal). In particular, most of the energy content is concentrated above the input signal frequency for hardening chains, while it is concentrated below the input signal frequency for softening chain. On the other hand, the results for resonator nonlinearity (Fig. 7.5 (c)-(f)) indicate similar significant frequency conversion at both long and medium-wavelength limits unlike the case of chain nonlinear-ity, which limits the frequency conversion to the medium-wavelength limit. For instance, hardening nonlinearity stretches the frequency content over a wide range of frequencies, as

shown in Fig. 7.5 (c). This stretch is even wider for the case of softening resonator frequency, as depicted in Fig. 7.5 (d). Beyond the significant frequency conversion obtained at long-wavelength limit, resonator nonlinearity can also show a significant frequency shift at medium wavelength limit. This shift is demonstrated by the clear stretch of the signal over wider range of frequencies for the hardening nonlinearity in Fig. 7.5 (e) and softening nonlinearity in Fig. 7.5 (f).

The discussion in this section emphasizes the presence of significant frequency shift (conversion) due to the nonlinearity in the proposed structure. This frequency conversion can be observed at medium-wavelength limit for both types of nonlinearity and at long-wavelength limit in the case of nonlinear resonator only. In the following section, we will then investigate how to design an electromechanical diode based on the observed direction. Moreover, we will also investigate the anticipated increase in the frequency band of the diode by the resonator nonlinearity since it shows a significant frequency shift at both long and medium-wavelength limits.

7.5 ELECTROMECHANICAL DIODE

Based on the significant frequency shift observed in the previous sections, we design an electromechanical diode for direction-biased waveguide applications. This diode allows waves to propagate in one direction; therefore, harvesting energy and sensing waves propagating in only one direction. A schematic diagram for the proposed electromechanical diode is shown in Fig. 7.6. The electromechanical diode is constructed from linear and nonlinear metamaterials. The nonlinear metamaterial with parameters defined above has a significant frequency region at medium wavelength limit in the optical mode for the case of nonlinear chain, and long/medium-wavelength limit for the case of the nonlinear resonator in the
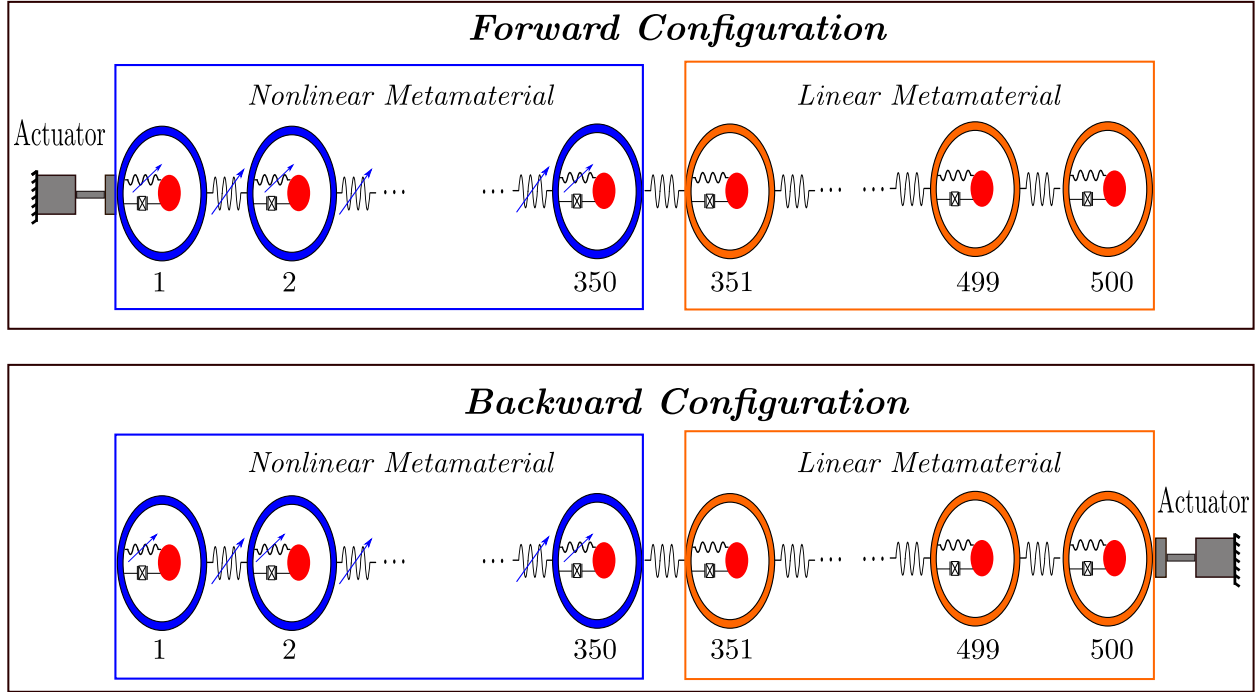
Figure 7.7: A schematic diagram for the forward and backward configurations.

optical mode. The linear metamaterial is designed to have a bandgap tuned to the medium or long-wavelength limit in the optical mode. Any wave with frequency in these regions and propagating in the nonlinear metamaterial has some energy content with frequencies different than the excitation frequency and outside these regions due to the significant frequency conversion. The output signal can propagate into another linear metamaterial since its bandgap is tuned to the input frequency. Therefore, voltage can be harvested in the forward configuration. On the other hand, a wave with the same frequency band does not propagate when it excites the linear metamaterial in the backward configuration. Therefore, voltage cannot be harvested in this configuration.

The combination of the linear and nonlinear chains constructing the electromechanical diode for forward and backward configurations is shown in Fig. 7.7. The nonlinear metamaterial consists of 350 cells with the same parameters defined in the previous sections and the nonlinearity stems from the chain or electromechanical resonator. The linear metamaterial

consists of 150 cells. The parameters of the linear metamaterial are chosen to tune the chain bandgap to the significant frequency shift region in the nonlinear metamaterial. It is note-worthy here that we chose the mass of the linear chain to be equal to the nonlinear chain mass to reduce the impedance mismatch. The linear chain has a stiffness, K_l, mass, M_l, local resonator stiffness, k_{1l}, and local resonator mass, m_{pl}. We assume that the linear chain has electromechanical coupling terms similar to those in the nonlinear chain. We define the following set of dimensionless parameters for the linear chain

$$\bar{k}_l = K_l/K; \bar{M}_l = M_l/M; \bar{k}_p = k_{1l}/k1; \bar{m}_p = m_{pl}/m_p \tag{7.17}$$

where $\bar{m}_p$ is set to 1 for all cases to reduce the impedance mismatch, and $N_{cy} = 60$ for all input signals.

We excite both configurations by a signal defined as

$$F_{ex} = \frac{1}{2}A[H(t) - H(t - \frac{2\pi\omega_n N_{cy}}{\omega\omega_d}][1-$$
$$cos(\frac{\omega_d\omega}{\omega_n N_{cy}}t)]sin(\frac{\omega_d\omega}{\omega_n}t) \tag{7.18}$$

where $N_{cy} = 60$.

To evaluate the performance of the electromechanical diode, we need to calculate the input and output energy harvested in the 1st and 500th cells. The power can be determined as

$$P_n = \frac{V_n^2}{R} \tag{7.19}$$

In each configuration the transmission ratio can be determined as

$$Tr_f = \frac{\int_0^\tau P_{500}}{\int_0^\tau P_1} \tag{7.20}$$

Chapter 7. Broadband electromechanical diode: acoustic non-reciprocity in weakly nonlinear metamaterials with electromechanical resonators

204
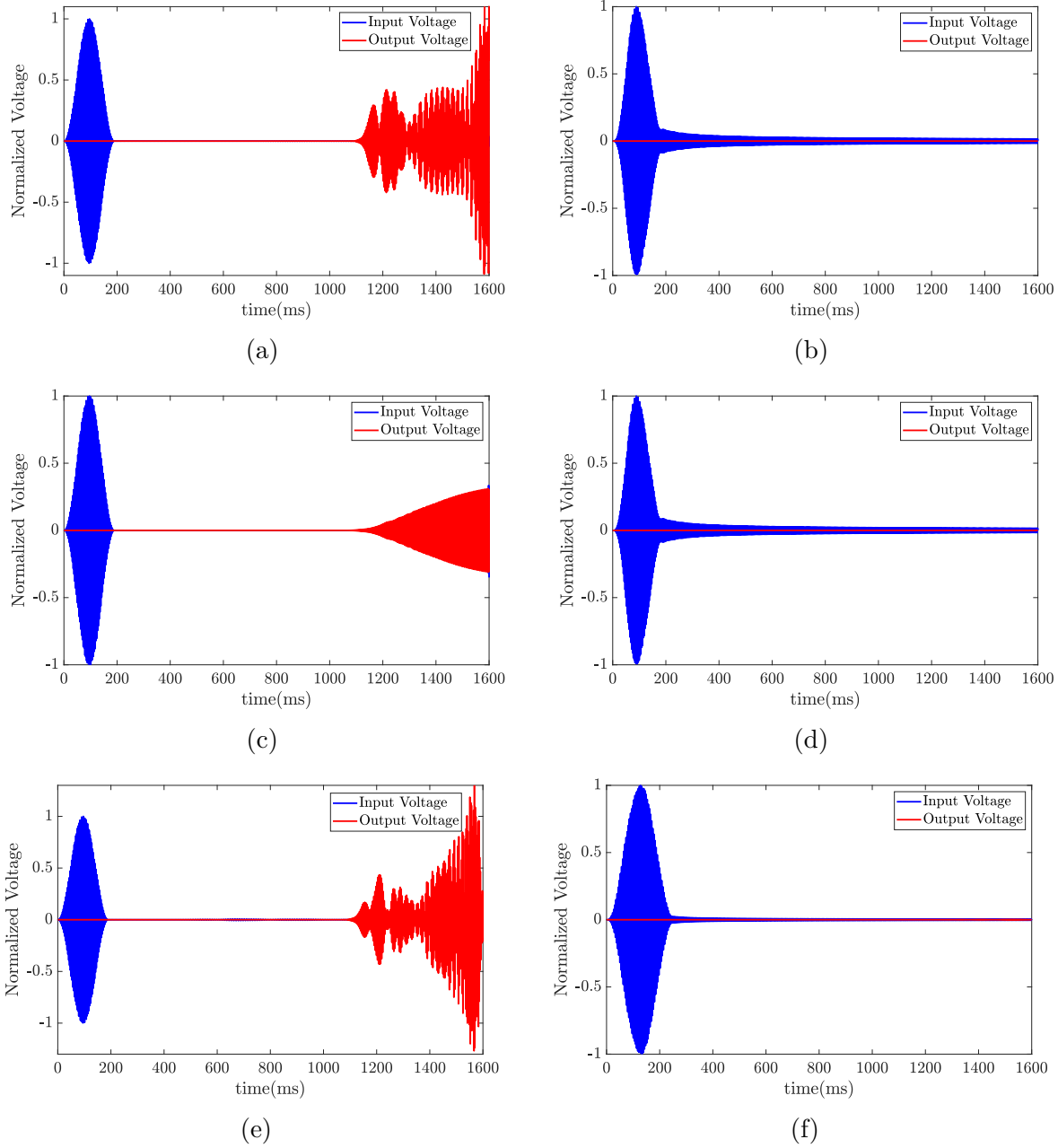
Figure 7.8: Time response of electromechanical diode in forward and backward configurations for the case of nonlinear chain: (a) Forward configuration, $\omega = 2$, $\bar{k}_l = 1.3$, $\bar{k}_p = 0.16$, $\bar{m}_p = 0.04$, $\epsilon^2 A\alpha = 0.03$, $\epsilon^2 A\alpha_r = 0$; (b) backward configuration, $\omega = 2$, $\bar{k}_l = 1.3$, $\bar{k}_p = 0.16$, $\bar{m}_p = 0.04$, $\epsilon^2 A\alpha = 0.03$, $\epsilon^2 A\alpha_r = 0$; (c) forward configuration, $\omega = 2$, $\bar{k}_l = 1.3$, $\bar{k}_p = 0.16$, $\bar{m}_p = 0.04$, $\epsilon^2 A\alpha = -0.03$, $\epsilon^2 A\alpha_r = 0$; (d) backward configuration, $\omega = 2$, $\bar{k}_l = 1.3$, $\bar{k}_p = 0.16$, $\bar{m}_p = 0.04$, $\epsilon^2 A\alpha = -0.03$, $\epsilon^2 A\alpha_r = 0$; (e) forward configuration, $\omega = 2$, $\bar{k}_l = 1.3$, $\bar{k}_p = 0.16$, $\bar{m}_p = 0.04$, $\epsilon^2 A\alpha = 0.06$, $\epsilon^2 A\alpha_r = 0$; (f) forward configuration, $\omega = 1.5$, $\bar{k}_l = 0.78$, $\bar{k}_p = 0.21$, $\bar{m}_p = 0.09$, $\epsilon^2 A\alpha = 0.03$, $\epsilon^2 A\alpha_r = 0$.

$$Tr_b = \frac{\int_0^\tau P_1}{\int_0^\tau P_{500}} \tag{7.21}$$

where Tr_f and Tr_b are the transmission ratios for the forward and backward configurations, respectively. Upon calculating the transmission ratios for each configuration, the asymmetric ratio can be calculated as

$$\sigma = \frac{Tr_f}{Tr_b} \tag{7.22}$$

For the case of nonlinear chain, the response of the forward and backward configurations for different types of nonlinearity is shown in Fig. 7.8. At medium wavelength limit, we excite the system by a signal with $\omega = 2$ with tuning the bandgap of the linear chain to the medium wavelength limit in the optical mode in the nonlinear chain. For hardening chain, the results indicate that the wave can propagate in the forward configuration (Fig. 7.8 (a)); therefore, voltage can be sensed on the other end. However, the input wave cannot propagate in the backward configuration, thus no voltage can be harvested and the system acts as direction-biased waveguide, as shown in Fig. 7.8 (b). For forward configuration, the transmission ratio is $Tr_f = 0.99$. The achieved transmission ratio in the forward configuration is high as compared to Ref. [16, 107]. The transmission ratio for the backward configuration is $Tr_b \approx 10^{-7}$. Moreover, the asymmetric ratio for the electromechanical diode is $\sigma \approx 6.4 \times 10^6$. These results show that the proposed electromechanical diode has a higher asymmetric ratio with higher transmission ratios than mechanical diodes reported in the literature. For instance, the asymmetric ratio in Refs. [16, 107] is $\sigma \approx 10^4$ and both reported low transmission ratios. For softening chain, the wave can also propagate in the forward configuration and voltage can be harvested on the other end, as shown in Fig. 7.8 (c). Moreover, waves cannot propagate in the backward configuration for softening nonlinearity as shown in Fig. 7.8 (d). This indicates that softening nonlinearity can also be used in designing electromechanical

Chapter 7. Broadband electromechanical diode: acoustic non-reciprocity in weakly
nonlinear metamaterials with electromechanical resonators
206

diodes. However, the harvested voltage on the other end is lower in this case as compared
to the hardening chain case in Fig. 7.8 (a). In particular, the transmission ratio for the
forward configuration is $Tr_f = 0.2457$, while the asymmetric ratio for the electromechanical
diode is $\sigma \approx 1.9 \times 10^6$. Increasing the strength of nonlinearity in the chain can increase
the transmission ratio for the forward configuration. For instance, increasing hardening
nonlinearity in the chain can significantly increase the output voltage with transmission ratio
$Tr_f \approx 1.3582$ and asymmetric ratio $\sigma \approx 8.8 \times 10^6$, as shown in Fig. 7.8 (e). It is noteworthy
that the transmission ratio for the voltage can exceed 1 as the voltage wave can be amplified
at some particular frequencies [26]. Finally, we excite our system with nonlinear chain at
frequency within the long-wavelength limit (i.e., $\omega = 1.5$) with linear chain's bandgap tuned
to this limit. The response of the forward configuration is shown in Fig. 7.8 (f). The result
indicates that the wave does not propagate within the long-wavelength limit; therefore,
voltage cannot be harvested at the other end. This is not surprising since we showed earlier
that the nonlinearity has no effect on the wave propagation at the long-wavelength limit in
the case of nonlinear chain.

For the case of nonlinear resonator, the response of the forward and backward configu-
rations for different types of nonlinearity is shown in Fig. 7.9. At medium wavelength limit,
we excite the system by a signal within the medium-wavelength limit in the optical mode
(i.e., $\omega = 2$) by tuning the bandgap of the linear chain to this region. For hardening nonlin-
earity, the results indicate that the nonlinear resonator case can also show non-reciprocity
in wave propagation. For instance, the wave can propagate in the forward propagation (Fig.
7.9 (a)) and get blocked in the backward configuration (Fig. 7.9 (b)). However, output
voltage in this case is lower as compared to the case of nonlinear chain. For this particular
case, the transmission ratio for the forward configuration is $Tr_f \approx 0.3467$ and asymmet-
ric ratio $\sigma \approx 1.9 \times 10^6$. At long wavelength limit (i.e., $\omega = 1.5$ and the linear bandgap
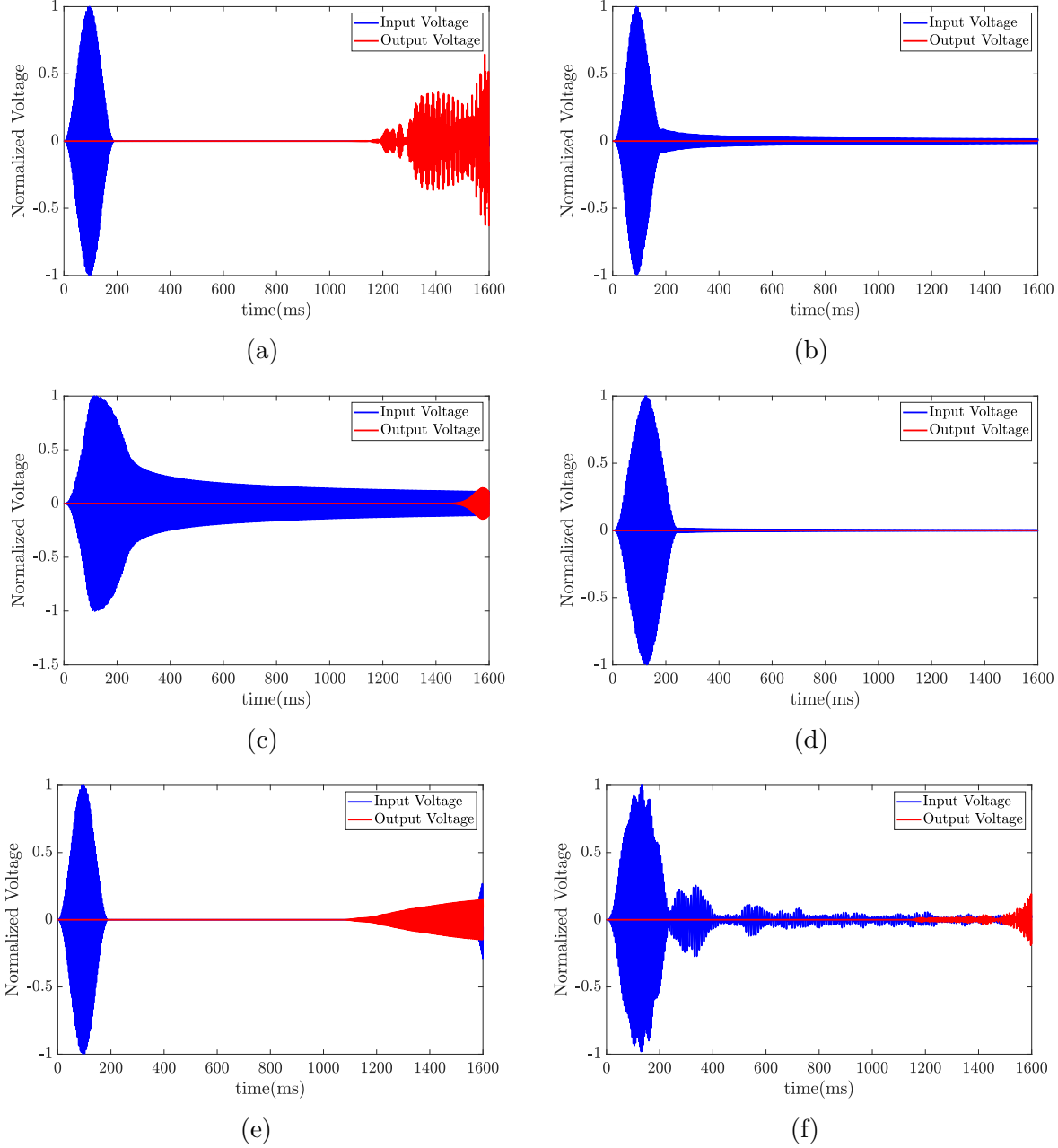
Figure 7.9: Time response of electromechanical diode in forward and backward configurations for the case of nonlinear resonator: (a) Forward configuration, $\omega = 2$, $\bar{k}_l = 1.3$, $\bar{k}_p = 0.16$, $\bar{m}_p = 0.04$, $\epsilon^2 A\alpha = 0$, $\epsilon^2 A\alpha_r = 0.03$; (b) backward configuration, $\omega = 2$, $\bar{k}_l = 1.3$, $\bar{k}_p = 0.16$, $\bar{m}_p = 0.04$, $\epsilon^2 A\alpha = 0$, $\epsilon^2 A\alpha_r = 0.03$; (c) forward configuration, $\omega = 1.5$, $\bar{k}_l = 0.78$, $\bar{k}_p = 0.21$, $\bar{m}_p = 0.09$, $\epsilon^2 A\alpha = 0$, $\epsilon^2 A\alpha_r = 0.03$; (d) backward configuration, $\omega = 1.5$, $\bar{k}_l = 0.78$, $\bar{k}_p = 0.21$, $\bar{m}_p = 0.09$, $\epsilon^2 A\alpha = 0$, $\epsilon^2 A\alpha_r = 0.03$; (e) forward configuration, $\omega = 2$, $\bar{k}_l = 1.3$, $\bar{k}_p = 0.16$, $\bar{m}_p = 0.04$, $\epsilon^2 A\alpha = 0$, $\epsilon^2 A\alpha_r = -0.03$; (f) forward configuration, $\omega = 1.5$, $\bar{k}_l = 0.78$, $\bar{k}_p = 0.21$, $\bar{m}_p = 0.09$, $\epsilon^2 A\alpha = 0$, $\epsilon^2 A\alpha_r = -0.03$.

is tuned to this limit), unlike the case of nonlinear chain, the wave can propagate in the forward configuration (Fig. 7.9 (c)), but it cannot propagate in the backward configuration (Fig. 7.9 (d)). The transmission ratio for this case is $Tr_f \approx 4 \times 10^{-3}$, and the asymmetric ratio is $\sigma \approx 2.2 \times 10^5$. Although the performance of the electromechanical diode in the case of nonlinear resonator at medium-wavelength limit is weaker than the case of nonlinear chain due to lower transmission and asymmetric ratios, the electromechanical diode can be operated at the long-wavelength limit in the case of nonlinear resonator unlike the case of nonlinear chain where no voltage can be sensed at the other end. This is not surprising since the spectro-spatial analysis showed the presence of significant frequency shift at the long-wavelength limit for the nonlinear resonator case. It is noteworthy that the input wave is also severely distorted at the long-wavelength limit since the effect of nonlinearity can appear in this region. For softening nonlinearity, an electromechanical diode can also be operated at medium/long-wavelength limits in the case of nonlinear resonator. For instance, Fig. 7.9 (e) shows that voltage can be sensed at the other end at medium-wavelength limit with transmission ratio $Tr_f \approx 0.059$ and asymmetric ratio is $\sigma \approx 3.85 \times 10^5$. On the other hand, Fig. 7.9 (f) shows that voltage can be sensed at the other end at long-wavelength limit with transmission ratio $Tr_f \approx 4.3 \times 10^{-3}$ and asymmetric ratio $\sigma \approx 2.4 \times 10^5$. The results of softening nonlinearity indicate that an electromechanical diode with softening nonlinearity outperforms diodes with hardening nonlinearity at long-wavelength limit. However, the presence of hardening nonlinearity in the resonator shows better performance at medium-wavelength limit.

In order to obtain a linear chain's bandgap tuned to the long-wavelength limit (e.g., the frequencies of the bandgap for linear chain ranges between 1.41-1.6), many options can be explored within a small margin of frequency change (± 0.01). We search for linear chain's bandgap limits within $\bar{k}_l = 0.5 - 1.5$, $\bar{k}_p = 0.01 - 1$, and $\bar{m}_p = 0.01 - 1$. Within these values
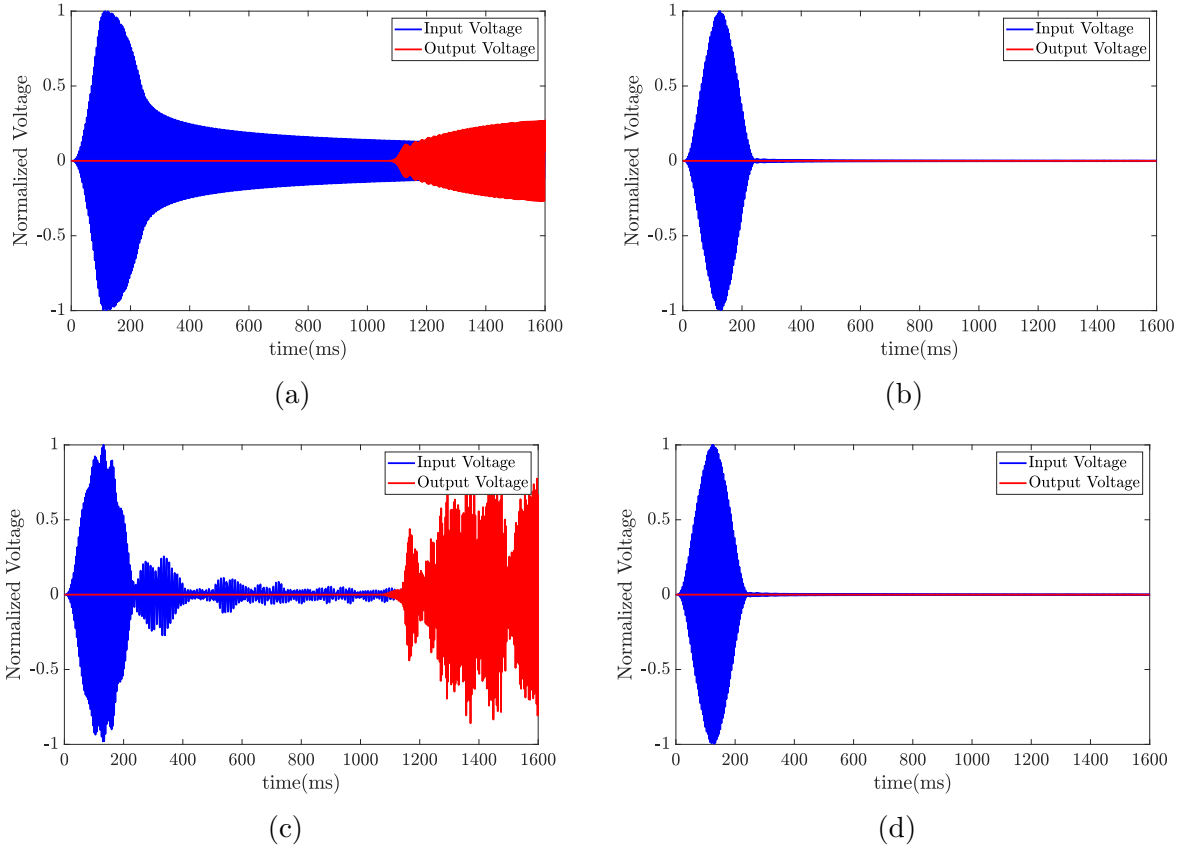
Figure 7.10: Time response of electromechanical diode in forward and backward configurations for the case of nonlinear resonator: (a) Forward configuration, $\omega = 1.5$, $\bar{k}_l = 1.5$, $\bar{k}_p = 0.37$, $\bar{m}_p = 0.17$, $\epsilon^2 A\alpha = 0$, $\epsilon^2 A\alpha_r = 0.03$; (b) backward configuration, $\omega = 1.5$, $\bar{k}_l = 1.5$, $\bar{k}_p = 0.37$, $\bar{m}_p = 0.17$, $\epsilon^2 A\alpha = 0$, $\epsilon^2 A\alpha_r = 0.03$; (c) forward configuration, $\omega = 1.5$, $\bar{k}_l = 1.5$, $\bar{k}_p = 0.37$, $\bar{m}_p = 0.17$, $\epsilon^2 A\alpha = 0$, $\epsilon^2 A\alpha_r = -0.03$; (d) backward configuration, $\omega = 1.5$, $\bar{k}_l = 1.5$, $\bar{k}_p = 0.37$, $\bar{m}_p = 0.17$, $\epsilon^2 A\alpha = 0$, $\epsilon^2 A\alpha_r = -0.03$.
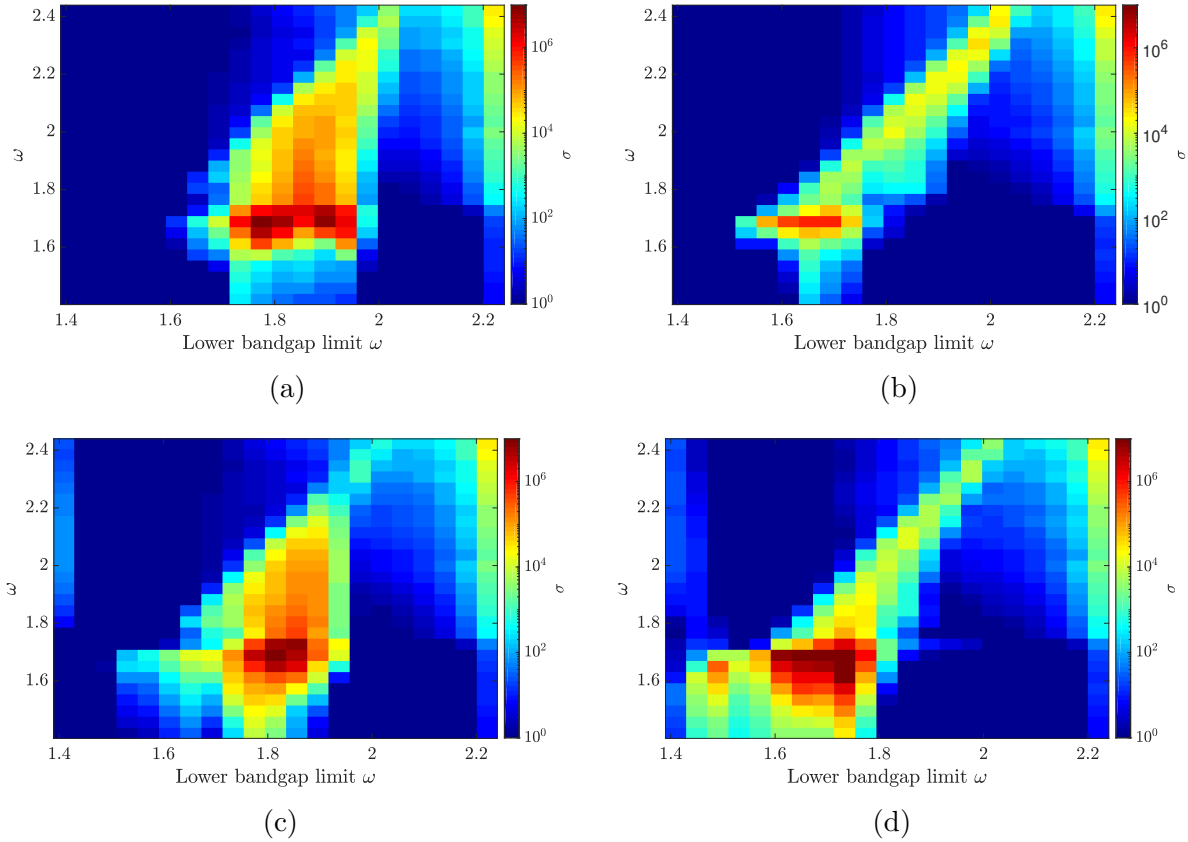
Figure 7.11: Asymmetric ratio for different linear chain designs with bandgap tuned within the whole optical mode of nonlinear chain. Upper boundary of the bandgap is fixed to the maximum frequency of optical mode of nonlinear chain and lower limit is swept over the optical mode: (a) Hardening nonlinear chain, $\epsilon^2 A \alpha_r = 0.03$, $\epsilon^2 A \alpha_r = 0$; (b) softening nonlinear chain, $\epsilon^2 A \alpha_r = -0.03$, $\epsilon^2 A \alpha_r = 0$; (c) hardening nonlinear resonator, $\epsilon^2 A \alpha = 0$, $\epsilon^2 A \alpha_r = 0.03$; (d) softening nonlinear resonator, $\epsilon^2 A \alpha = 0$, $\epsilon^2 A \alpha_r = -0.03$.
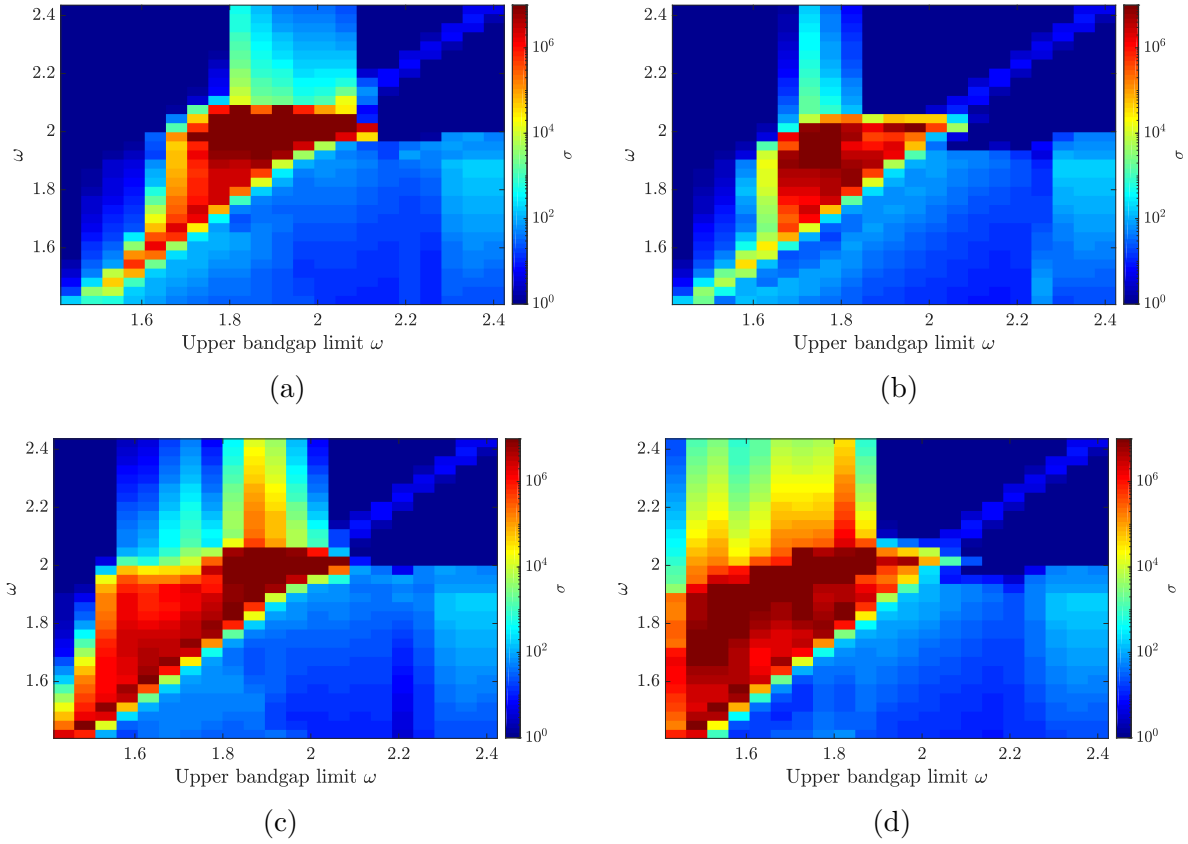
Figure 7.12: Asymmetric ratio for different linear chain designs with bandgap tuned within the whole optical mode of nonlinear chain. Lower boundary of the bandgap is fixed to the maximum frequency of optical mode of nonlinear chain and upper limit is swept over the optical mode: (a) Hardening nonlinear chain, $\epsilon^2 A\alpha_r = 0.03$, $\epsilon^2 A\alpha_r = 0$; (b) softening nonlinear chain, $\epsilon^2 A\alpha_r = -0.03$, $\epsilon^2 A\alpha_r = 0$; (c) hardening nonlinear resonator, $\epsilon^2 A\alpha = 0$, $\epsilon^2 A\alpha_r = 0.03$; (d) softening nonlinear resonator, $\epsilon^2 A\alpha = 0$, $\epsilon^2 A\alpha_r = -0.03$.

of parameters, we can obtain several options. We used the option with the lowest value of parameters to investigate the performance of the electromechanical diode in Figs. 7.8-7.9. The results in these figures demonstrate that the values of the transmission and asymmetric ratios are low at this wavelength as compared to results at medium-wavelength limit. This is because the lowest values that were chosen to plot the figures resulted in an optical mode stretching over a narrow range of frequencies. Therefore, only a few frequency components with low energy content from the output wave (i.e., its frequency content is converted into frequencies other than the input frequency) can propagate through the narrow optical mode. To increase the frequency components that can propagate through the optical mode, the range of optical mode frequencies needs to be increased by choosing parameters with highest values among all available options. This can result in the widest possible optical mode within the above assumed system's parameters ranges. For this case, we plot the responses of the forward and backward configurations in Fig. 7.10. For hardening nonlinearity in the resonator at long-wavelength limit (Fig. 7.10 (a)), the results indicate that the harvested voltage sensed at the other end is significantly higher than the case in Fig. 7.9 (c). Yet, the wave cannot propagate in the backward configuration as depicted in Fig. 7.10 (b). This can also be demonstrated from the values of transmission ratio $Tr_f \approx 0.1251$ and asymmetric ratio $\sigma \approx 1.5 \times 10^6$, which are also significantly higher. Therefore, the performance of the nonlinear resonator electromechanical diode at the long-wavelength limit is comparable to the performance of the nonlinear chain diode when the parameters of the linear chain are chosen carefully. Softening nonlinearity in the resonator with these linear chain's parameters can even provide better performance, and thus higher voltage can be sensed at the other end (Fig. 7.10 (c)), thus preventing any waves coming from the backward configuration from propagating through the structure (Fig. 7.10 (d)). This observation is also confirmed by the values of transmission ratio $Tr_f \approx 0.49$ and asymmetric ratio $\sigma \approx 6.2 \times 10^6$, which are also significantly higher than the case of hardening nonlinearity.

7.6 The effect of linear chain bandgap size on the performance of the electromechanical diode

In the previous section, we demonstrated that the proposed electromechanical diode can be used as a direction-biased waveguide. This direction-biased waveguide can be operated in the medium-wavelength limit for both nonlinear chain and nonlinear resonator cases. But the operation of this diode in the long-wavelength domain is limited to the nonlinear resonator case only. It should be noted that the parameters of the linear chain were chosen such that the bandgap of the linear chain is tuned to the operation frequency region to demonstrate the non-reciprocity. However, the effect of linear chain bandgap on the asymmetric ratio was not discussed in the previous section. Therefore, we present the asymmetric ratio for different linear chain's bandgap sizes and at different excitation frequencies.

In this section, we conduct our analyses by sweeping the bandgap size of the linear chain over either the whole frequency range of the nonlinear chain's optical mode frequencies or over a specific frequency range within the long/medium-wavelength limits of the nonlinear chain's optical mode. In order to define the linear chain parameters that satisfy the tested bandgap size, we sweep the chain's parameters over the ranges defined in the previous section and pick the largest parameters of the list that matches the bandgap requirement.

7.6.1 Sweeping the bandgap over the whole optical mode frequencies

For sweep over the whole optical mode, we set the upper boundary of the bandgap to the maximum frequency in this mode and sweep the lower boundary over other frequencies in the optical mode in one case, and fix the lower boundary to the minimum frequency in this mode

and sweep the upper in another case. For these two cases, we record the asymmetric ratio at different excitation frequency and bandgap boundaries and plot them in Figs. 7.11-7.12, respectively.

For the case of lower boundary being swept over the whole range of the optical mode (Fig. 7.11), the electromechanical diode has the highest asymmetry ratio when the lower bandgap boundary is close to frequencies near the medium-wavelength limit in the case of hardening chain nonlinearity as shown in Fig. 7.11 (a). In particular, the medium-wavelength limit is confined within the bandgap, and energy component associated with the shifted frequency can propagate through the passband below this bandgap. In addition, excitation frequencies near the medium-wavelength show higher symmetry ratio where significant frequency shift can be observed as shown in the previous sections for this type of nonlinearity. When the lower bandgap boundary is below the medium-wavelength limit (i.e., in the long-wavelength limit), the asymmetry ratio is very small and the electromechanical diode cannot be operated at all excitation frequencies within the optical mode. This is because all shifted frequencies lie within the bandgap (i.e., the band covers most of the optical mode); therefore, no waves will propagate in either the forward or backward directions. By moving the lower bandgap boundary above the medium-wavelength limit, the asymmetry ratio becomes lower since the frequency shift becomes also less significant in the short-wavelength limit. In general, only excitation frequencies within the bandgap shows directional-biased wave propagation for medium/short-wavelength limits, while no frequencies show directional-biased wave propagation in the long wavelength limit. For softening chain nonlinearity, similar observations can be deduced from Fig. 7.11 (b). However, both excitation frequencies and lower bandgap boundary have high symmetric ratio at frequencies lower than the hardening case. This is not surprising, since results in Fig. 7.4 (b) showed that the higher energy component is shifted below the medium-wavelength limit in the case of softening chain non-

linearity, unlike the case of hardening nonlinearity. For hardening resonator nonlinearity (Fig. 7.11 (c)), the regions of high symmetry ratios are similar to those of hardening chain; however, these regions are slightly extended to cover the long-wavelength region. This indicates that the operation range of electromechanical diode can be broaden by using resonator nonlinearity. The operation range of the electromechanical diode can further be increased if softening nonlinearity is used as shown in Fig. 7.11 (d), thus showing a good agreement with the observations in the previous section. Yet the significance of directional-biased wave propagation is not pronounced at this limit since the bandgap is tuned above this region due to fixing the higher bandgap boundary. Moreover, when the bandgap is tuned to this region, the bandgap covers most of the optical mode; therefore, the shifted frequency energy component cannot propagate in the forward configuration.

To obtain a bandgap that always covers the long-wavelength limit, we fix the lower bandgap boundary and sweep the upper boundary over the optical mode's frequencies. The asymmetry ratio for this case is shown in Fig. 7.12. For hardening chain (Fig. 7.12 (a)), the results indicate that with increasing the excitation frequency to get closer to the medium-wavelength limit, energy contents with shifted frequency components start to appear and directional-biased wave transmission can be observed. Yet the asymmetry ratio is not significant in the long-wavelength limit and start to increase rapidly as excitation frequencies approach the medium wavelength limit and the the bandgap covers this wavelength limit. It is noteworthy that the transmission ratios are higher in this case, which indicates that the frequency conversion shifts the signal frequency to a frequency above the bandgap and a significant energy content is associated with these shifted high frequencies. Consequently, upper bandgap boundary should be restricted to below short-wavelength region (just above frequencies within medium-wavelength limit, since a significant portion of the energy is shifted to the long-wavelength limit) for higher asymmetry ratio in designing linear chains.

These observations also hold for the softening chain case, as shown in Fig. 7.12 (b). However, the asymmetry ratio is lower at high frequencies since frequency conversion tends to shift the excitation frequencies to lower frequencies which lie within the bandgap, thus the transmitted energy is lower. For hardening resonator, Fig. 7.12 (c) shows a significant increase in the asymmetry ratio near the long wavelength limit as compared with cases in Figs. 7.12 (a)-(b). Yet high asymmetry ratios can still be observed in the medium-wavelength limit. In addition, the values of asymmetry ratios are significantly higher than the case of sweeping lower bandgap limit since the bandgap can cover the medium/long-wavelength limits with passband for frequencies at short-wavelength limit. This increase in asymmetry ratio become more pronounced with softening resonators, as shown in Fig. 7.12 (d). For the nonlinear resonator case, the directional-biased wave propagation can even be observed at high excitation frequencies where frequency components can also be shifted, as seen in Figs. 7.12 (c)-(d). However, the asymmetry ratio here is lower than other frequencies within medium/-long wavelengths limits. Finally, it is noteworthy that the asymmetry ratios are higher with sweeping the upper bandgap boundary, as compared to sweeping the lower boundary, since the short-wavelength limit is a passband in most cases where shifted excitation frequencies can propagate.

Based on the above discussions, the bandgap of the linear chain should not intersect with the long/medium-wavelength frequencies if the operation frequencies are confined within the short-wavelength limit. Moreover, the bandgap of the linear chain should not intersect with the short-wavelength frequencies if the operation frequencies are confined within the long/medium-wavelength limits. These considerations should be considered when designing an electromechanical diode. Furthermore, it is more beneficial to design the diode for operation range within the long/medium-wavelength limits since the asymmetry ratios are much higher in these regions as compared to the short-wavelength limit. After reaching

a conclusion about avoiding tuning the bandgap to the short-wavelength limit due to low asymmetry ratio, we should conduct a deeper investigation about tuning the bandgap to the long/medium wavelength limits.
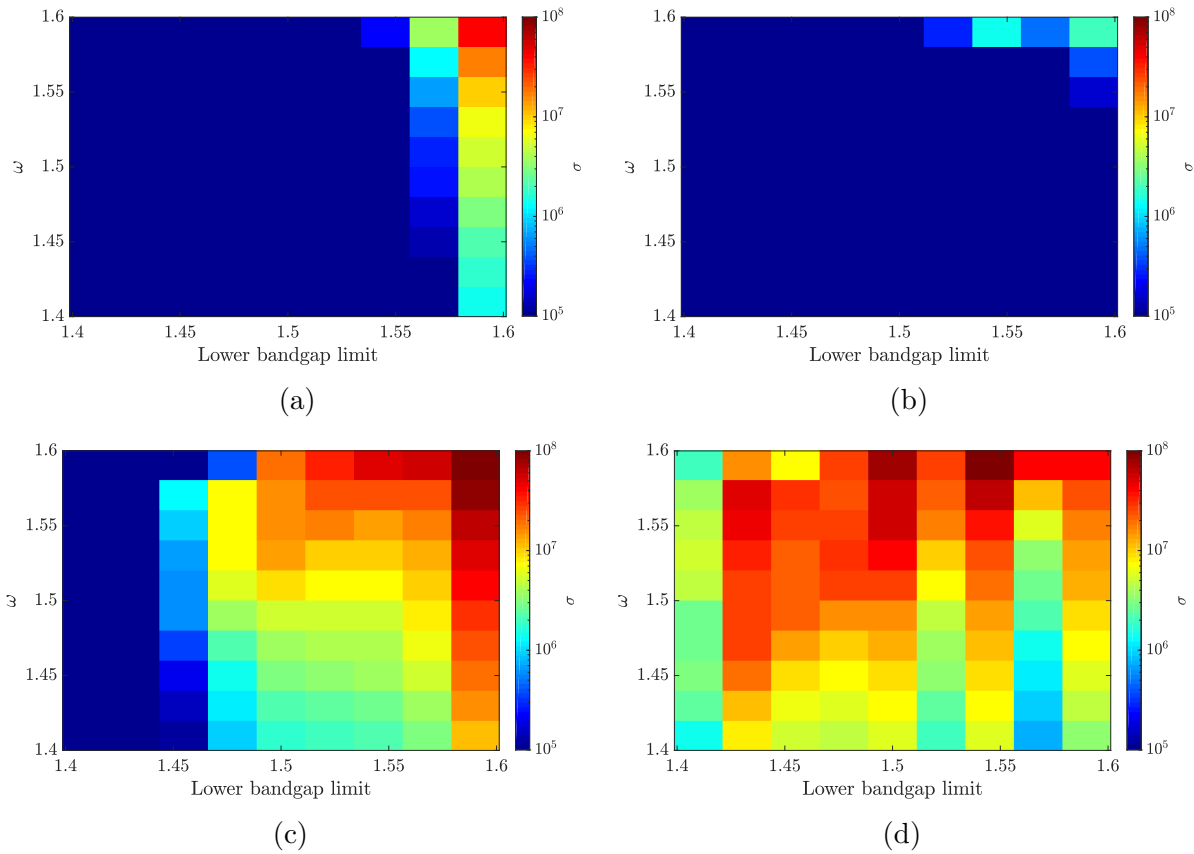
Figure 7.13: Asymmetric ratio for different linear chain designs with bandgap tuned within the long wavelength limit in the optical mode of nonlinear chain. Upper boundary of the bandgap is fixed to $\omega = 1.9$ optical mode of nonlinear chain and lower limit is swept over the long wavelength limit in the optical mode: (a) Hardening nonlinear chain, $\epsilon^2 A \alpha_r = 0.03$, $\epsilon^2 A \alpha_r = 0$; (b) softening nonlinear chain, $\epsilon^2 A \alpha_r = -0.03$, $\epsilon^2 A \alpha_r = 0$; (c) hardening nonlinear resonator, $\epsilon^2 A \alpha = 0$, $\epsilon^2 A \alpha_r = 0.03$; (d) softening nonlinear resonator, $\epsilon^2 A \alpha = 0$, $\epsilon^2 A \alpha_r = -0.03$.

Figure 7.14: Asymmetric ratio for different linear chain designs with bandgap tuned within the long wavelength limit in the optical mode of nonlinear chain. Lower boundary of the bandgap is fixed to $\omega = 1.4$ optical mode of nonlinear chain and upper limit is swept over the long wavelength limit in the optical mode: (a) Hardening nonlinear chain, $\epsilon^2 A \alpha_r = 0.03$, $\epsilon^2 A \alpha_r = 0$; (b) softening nonlinear chain, $\epsilon^2 A \alpha_r = -0.03$, $\epsilon^2 A \alpha_r = 0$; (c) hardening nonlinear resonator, $\epsilon^2 A \alpha = 0$, $\epsilon^2 A \alpha_r = 0.03$; (d) softening nonlinear resonator, $\epsilon^2 A \alpha = 0$, $\epsilon^2 A \alpha_r = -0.03$.

7.6.2 Sweeping the bandgap over the long-wavelength limit optical mode frequencies

In this section, we conduct further analyses to sweep the boundaries of the linear chain's bandgap over the long-wavelength and medium-wavelength limits separately. This can be done by conducting analyses similar to those conducted in Figs. 7.11-7.12. In particular, we fix the upper boundary and sweep the lower boundary in one case, while we fix the lower boundary and sweep the upper boundary in another. However, we sweep the bandgap only over the long-wavelength frequencies in one case (Fig. 7.13) and the medium-wavelength frequencies in another (Fig. 7.14). For analyses over the long-wavelength frequencies and fixing the bandgap's upper boundary, we plot the results in Fig. 7.13. For hardening and softening chains (Figs. 7.13 (a)-(b)), the results indicate that the asymmetry ratio is almost zero for all lower bandgap boundaries. However, the asymmetry ratio can be non zero when the lower bandgap boundary is near the medium-wavelength limit where the nonlinear chain show direction-biased wave propagation. In addition, the asymmetry ratio is higher for the case of hardening chain. On the other hand, the nonlinearity in the resonator shows a high asymmetry ratio for all lower bandgap boundaries at all excitation frequencies within this limit, as shown in Figs. 7.13 (c)-(d). Nevertheless, the lower bandgap boundary does not need to cover frequencies ($\omega \leq 1.48$ since the asymmetry ratio is very low in this region in the case of hardening resonator, as shown in Fig. 7.13 (c). However, the lower boundary can be extended to cover this region of frequencies in the case of softening resonator, as shown in Fig. 7.13 (d). For the case of the lower bandgap boundary being fixed Fig. 7.14, the results also show near zero asymmetry ratio in the cases of hardening and softening chain, as shown in Fig. 7.14 (a)-(b). In addition, sweeping the upper limit in this case is associated with lower asymmetry ratios for frequencies near the medium-wavelength limit as compared to the previous case shown in Figs. 7.13 (a)-(b). For hardening and softening

resonators (Figs. 7.13 (c)-(d)), high asymmetry ratios exist in the region on and above the diagonal (i.e., excitation frequency/upper bandgap boundary) line unlike the case of fixing the upper bandgap boundary where higher asymmetry ratios can be observed at wider range of excitation frequencies. This indicates that fixing the upper bandgap boundary is more beneficial than fixing the lower boundary. Therefore, when designing an electromechanical diode that shows high asymmetry ratio in the long-wavelength limit, the upper bandgap's boundary should be be tuned to a frequency near the lower frequencies within the medium-wavelength limit. On the other hand, the lower bandgap's boundary should be tuned to a frequency just above the lower frequencies within the optical mode in the presence of resonator nonlinearity.

7.6.3 Sweeping the bandgap over the medium-wavelength optical mode frequencies

Similarly, we focus on the sweep of linear chain bandgap's boundaries inside the medium-wavelength limit and plot the results in Figs. 7.15-7.16. For fixed upper bandgap boundary, the results indicate that the asymmetry ratio is almost zero for hardening chain (Fig. 7.15 (a)) and softening resonator (Fig. 7.15 (d)). However, the asymmetry ratio has significant values for softening chain (Fig. 7.15 (c)) and hardening resonator (Fig. 7.15 (d)). On the other hand, fixing the lower bandgap's boundary reveals significantly higher asymmetry ratio, as shown in Fig. 7.16. In particular, in the case of hardening chain Fig. 7.16 (a), the asymmetry ratio is significantly higher as compared to the case of sweeping the lower bandgap's boundary for this type of nonlinearity. Similarly, the asymmetry ratio is higher for the case of softening chain, as shown in Fig. 7.16 (b). However, the results indicate that sweeping the upper boundary shows higher asymmetry ratio at high frequencies as compared to the case of sweeping the lower boundary where high asymmetry is associated with low
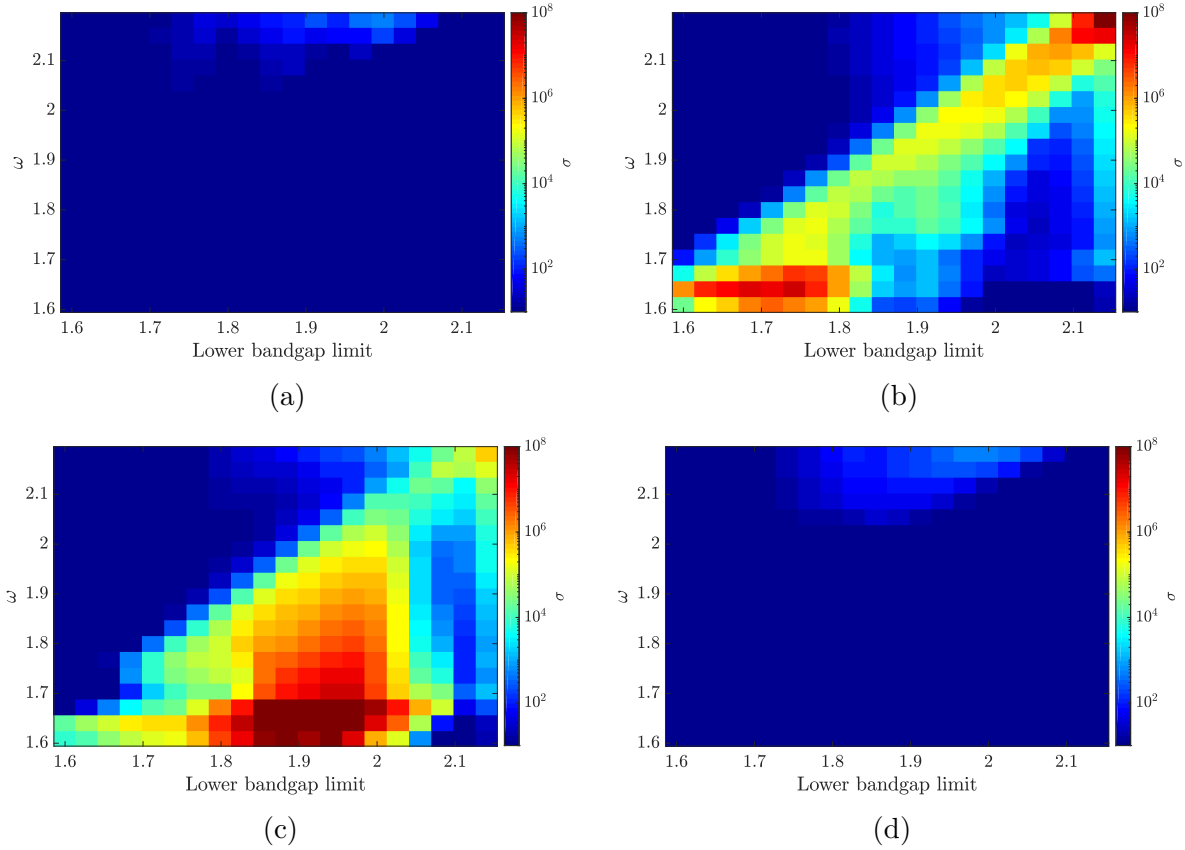
Figure 7.15: Asymmetric ratio for different linear chain designs with bandgap tuned within the medium wavelength limit in the optical mode of nonlinear chain. Upper boundary of the bandgap is fixed to $\omega = 2.2$ optical mode of nonlinear chain and lower limit is swept over the medium wavelength limit in the optical mode: (a) Hardening nonlinear chain, $\epsilon^2 A\alpha_r = 0.03$, $\epsilon^2 A\alpha_r = 0$; (b) softening nonlinear chain, $\epsilon^2 A\alpha_r = -0.03$, $\epsilon^2 A\alpha_r = 0$; (c) hardening nonlinear resonator, $\epsilon^2 A\alpha = 0$, $\epsilon^2 A\alpha_r = 0.03$; (d) softening nonlinear resonator, $\epsilon^2 A\alpha = 0$, $\epsilon^2 A\alpha_r = -0.03$.
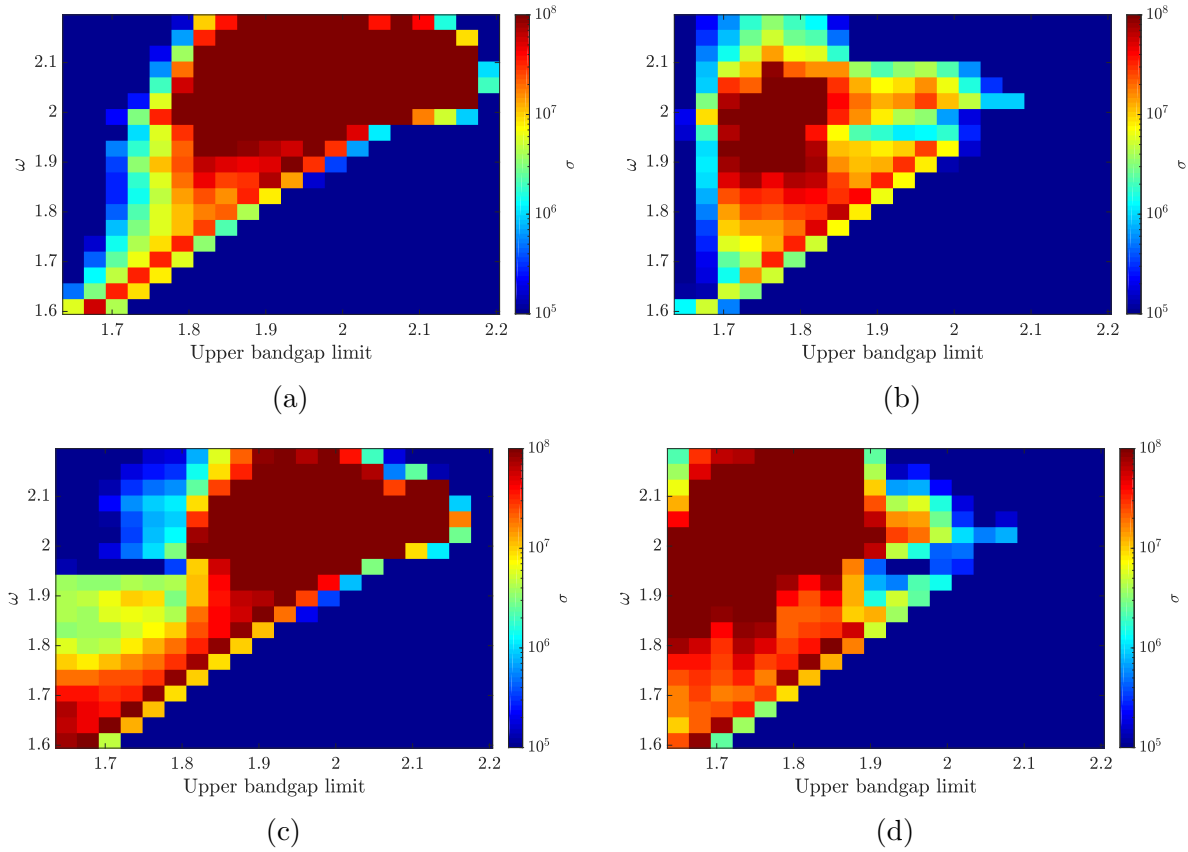
Figure 7.16: Asymmetric ratio for different linear chain designs with bandgap tuned within the medium wavelength limit in the optical mode of nonlinear chain. Lower boundary of the bandgap is fixed to $\omega = 1.9$ optical mode of nonlinear chain and upper limit is swept over the medium wavelength limit in the optical mode: (a) Hardening nonlinear chain, $\epsilon^2 A\alpha_r = 0.03$, $\epsilon^2 A\alpha_r = 0$; (b) softening nonlinear chain, $\epsilon^2 A\alpha_r = -0.03$, $\epsilon^2 A\alpha_r = 0$; (c) hardening nonlinear resonator, $\epsilon^2 A\alpha = 0$, $\epsilon^2 A\alpha_r = 0.03$; (d) softening nonlinear resonator, $\epsilon^2 A\alpha = 0$, $\epsilon^2 A\alpha_r = -0.03$.

frequencies. For the case of resonator nonlinearity Figs. 7.16 (c)-(d), we observe that fixing
the lower limit results in high asymmetry ratio at higher excitation frequencies within the
medium-wavelength limit as compared to fixing the upper boundary. It is noteworthy that
hardening nonlinearity provides high asymmetry ratio when the upper bandgap's boundary
is close to the upper end of the medium-wavelength limit's frequencies since signals tend
to be shifted to higher frequencies with hardening nonlinearity. The opposite is observed
when we set the upper bandgap's boundary to frequency below the higher frequencies of the
medium-wavelength limit. This is because signals tend to be shifted to lower frequencies
with softening nonlinearity.

The above analyses provide some guidelines in designing the linear chain in the elec-
tromechanical diode. The design guidelines depend on the operation frequency of the elec-
tromechanical diode and the type of nonlinearity. General guidelines include avoiding tuning
the bandgap to short-wavelength limit to allow shifted frequency components to propagate in
the forward direction. In addition, the lower boundary should be fixed just above the lowest
frequency in the optical mode for best performance at frequencies within the long-wavelength
limit and resonator nonlinearity should be used. For this operation range, the upper limit
should be set near the lower end of the medium-wavelength limit. Moreover, the lower
boundary should be tuned just below the medium-wavelength limit for best performance at
frequencies within the medium-wavelength limit and either resonator or chain nonlinearity
can be used. The upper boundary should be placed at the end of medium-wavelength in the
case of hardening nonlinearity and slightly below the short-wavelength limit in the case of
softening nonlinearity.

7.7   CONCLUSION

In this paper, a nonlinear metamaterial with electromechanical local resonators was inves-
tigated. The nonlinearity stemmed from the chain in one case and from the resonator in
another. The method of multiple scales was applied to the governing equations of motions to
obtain the dispersion relations. The analytical band structure was validated via comparison
with results obtained by direct numerical integration. The results show good agreement ex-
cept that the analytical results fail to predict some frequency regions within the optical mode
due to significant frequency shift, in particular, the medium-wavelength limit for the case of
nonlinear chain and the long/medium-wavelength limit for the nonlinear resonator. To fur-
ther demonstrate the frequency shift in these regions, we analyzed the numerical results by
spectro-spatial analysis. The spatial profiles indicated that the wave is severely distorted in
these regions and may split into localized and dispersive waves. Moreover, the spectrograms
and contour plots of 2D FFT demonstrated that most of the energy content of the output
voltage appears at frequencies outside the initial frequency band of the input signal. The ob-
served significant frequency shift was utilized to design an electromechanical direction-biased
waveguide (i.e., electromechanical diode). The proposed electromechanical diode was con-
structed by combining linear and nonlinear chains with electromechanical local resonators.
This diode showed the ability to harvest energy and sense the wave propagating in the for-
ward direction only and blocked any wave propagating in the backward configuration. This
direction-biased wave propagation can be observed only at the medium-wavelength limit in
the case of nonlinear chain. However, it can be observed at the medium/long-wavelength
limits in the case of nonlinear resonator. Therefore, the electromechanical diode can be
operated over a wider range of frequencies in the case of nonlinear resonator. Unlike me-
chanical diodes in the literature, the proposed diode does not only have a high asymmetric
ratio, it also has a high transmission ratio for the forward configuration. Yet the proposed

electromechanical diode can harvest energy and sense better than symmetric systems due to the birth of localized (solitary) waves. To draw guidelines on designing the linear chain's bandgap, we conducted analyses by sweeping the bandgap's boundaries over different frequency ranges and reported the asymmetry ratio of these simulations. The results indicated that it is more beneficial to tune the lower bandgap's boundary just above the minimum frequency of the optical mode of the nonlinear chain and fix the upper bandgap's boundary near the medium-wavelength limit for best performance in the long-wavelength limit for the case of nonlinear resonator. In addition, softening resonator should be used to realize high asymmetry ratio at low frequencies in the optical mode. Moreover, the results demonstrated that the lower bandgap's boundary should be tuned just above the long-wavelength limit to obtain high asymmetry ratio for excitation frequencies within the medium-wavelength limit for both types of nonlinearity. On the other hand, the results indicated that the upper bandgap's boundary should not go into the short-wavelength limit's frequencies, and should be fixed slightly lower in the case of softening nonlinearity. Finally, the bandgap's boundaries should be tuned around the operation frequency, in general, with avoiding extending its size to the short-wavelength region to allow shifted frequency component to propagate in the forward configuration.

Chapter 8

Towards a self-tuning sliding-mass metastructure

Passive vibration control systems are characterized by their simple practical design and independence of external power supplies. However, they are usually hindered by their narrow frequency band that cannot handle variable frequency disturbances. Recent research has demonstrated the capability of passive self-tuning resonators through the use of a sliding mass without the need for any external power sources. This work analytically and experimentally investigates the passive self-tuning of a vibration absorber consisting of a clamped-clamped beam with a sliding mass. The governing equations of motion show that the slider can be driven by Coriolis and centrifugal forces upon applying the excitation force on the structure. To improve the accuracy of our analytical simulations, we derive the exact instantaneous mode shapes and frequencies of the structure and feed them into an adaptive algorithm, which updates the spatial state of the system. Numerical simulations demonstrate that the proposed resonator can tune itself to the excitation frequency as the slider reaches the equilibrium position. This observation suggests that a significant vibration reduction can be obtained using the proposed resonator over a wide frequency band. Experiments are carried

out to validate the analytical findings. The proposed structure can be used in different vibration control applications (i.e., aerospace, automotive, and machining), and its model can further be extended to self-adaptive periodic structures (metamaterials).

8.1 Introduction

Many engineering structures are susceptible to unwanted vibrations from different environmental sources and disturbances. These vibrations can lead to different types of failures if left uncontrolled. These failures may result in structural damage, system malfunction, discomfort, and noise problems. Controlling these vibrations aims to mitigate or eliminate the system response to disturbances using several passive and active techniques. Linear passive vibration resonators have been extensively investigated and are widely employed in many engineering applications due to their low cost and simple design [52, 60]. Passive vibration resonators are tuned spring-mass systems that are installed on a structure to absorb undesired vibrations. To do so, the vibration resonator parameters are chosen so that the resonator will tune itself to a specific frequency, leading to vibration mitigation of the primary structure.

Since linear vibration resonators can be effective only near their design frequency, they fail to control vibrations that are not constant over time. Therefore, introducing mechanisms which can resonate at a wider range of frequencies has been the focus of researchers for many years. It has been observed that mechanisms with nonlinear resonators are more suitable for such purposes due to their wide bandwidth compared to linear resonators and the presence of secondary resonances [6, 67, 89, 112, 135, 140]. However, improvement resulted from nonlinear passive mechanisms are limited to a certain frequency regions, and it is often dependent on the initial disturbance to track the required energy orbit [179].

To overcome the narrow frequency band of passive resonators, researchers suggested the use of active frequency tuning techniques capable of adapting to the applied excitation frequency. However, due to the required external energy source, active tuning techniques are not practical and reliable in most applications [7]. On the other hand, passive self-

tuning mechanisms showed the ability to tune themselves to the applied excitation frequency. This self-tuning can be achieved through a sliding mass which moves freely along a beam. Particularly, Coriolis and centrifugal forces, resulting from the nonlinear interactions between the slider and the vibrating beam, move the mass till it reaches an equilibrium position. At this position, the resonator will be tuned to the excitation frequency and hence, achieving passive self-adaptive tuning. The study of these systems revealed substantial improvement in increasing the resonator's operating bandwidth in several applications including energy harvesting [3, 10, 18, 31, 37, 91, 94, 96, 123, 125, 130, 145, 165, 166, 167, 172, 182, 190, 191].

Investigations of energy harvesters with passive self-tuning mechanisms have recently drawn researchers' attention. Analytical investigations of self-tuning resonators' models can be found in the literature for stings [18], beams [123, 125, 172], and two-dimensional plates [182]. These analytical findings were further verified experimentally in several studies [37, 123, 125, 130, 145, 190, 191]. Interestingly, investigations of beam structures have shown the capability to obtain self-tuning by a slider regardless of the boundary conditions. For instance, a clamped-clamped system was investigated by Miller et al. and others [94, 123, 145, 190, 191], while a free-end system was studied by Mori et al. and others[37, 91, 125, 130]. The nonlinear dynamics of the system have also been investigated in-depth to reveal a further understanding of the system by Krack *et al.* [96]. These interesting findings motivated other researchers to extend the system in an array of several cantilever beams with sliders [165, 166, 167]. We emphasized that previous studies have reported the dynamic of self-tuning mechanisms with sliding mass for the resonator itself [125, 172], electromechanical energy harvesters [123], and electromagnetic energy harvesters [22]. However, to the best of our knowledge, there is no work in the literature which investigates the interaction between a passive self-tuning resonator and primary structure and studies how this resonator acts as a broadband vibration absorber. This tunable absorber can further be used in other

engineering applications like tunable metastructures and metamaterials. This is the focus of the current study. Given that the dynamic parameters of the system change as the slider moves along the resonator, the system dynamics evolve both in the spatial and the time domains. To handle these changes in both time and spatial domains, for first time, our current work also presents an adaptive algorithm to simulate the system dynamics by updating the spatial state as the system is being integrated over time.

In this paper, we investigate the performance of a self-tuning absorber installed on a structure. The self-tunability is targeted to be achieved through a sliding mass which moves along the resonator. We present the nonlinear governing equations of motion for the slider, resonator, and main structure, then obtain the exact linear frequency equation and the mode shapes of the continuous system. These mode shapes and linear frequencies are further used to discretize the partial differential equation using Galerkin's projection. Unlike conventional methods, we present an algorithm to feed the instantaneous system frequency in the spatial parameters to obtain more accurate results and guarantee the convergence of the slider to an equilibrium point. This algorithm is used to integrate the system numerically to solve for the system response and the slider position, thus, investigating the effect of self-tuning absorber on the system response. Parametric studies are also conducted to investigate the role of different parameters on the system response. Furthermore, the proposed system is examined experimentally to demonstrate the ability of the system to passively tune itself to the excitation frequency.

The rest of this paper is organized as follows: In Section 2, we present a description of the proposed system, its governing equations of motion, and discretize the partial differential equation. An adaptive algorithm to handle the dynamics evolve in the spatial domain is presented in Section 3. In Section 4, the simulation results with discussions about the ability of the resonator to tune itself are presented. This ability is further demonstrated through

experimental analyses in Section 5. Finally, we summarize our findings in the conclusion.

8.2   System description and mathematical modeling

A schematic of the primary structure along with the self-tuning resonator is depicted in Fig. 8.1. The primary structure is chosen to be a cantilever beam which is excited at its fixed end by a base excitation acceleration $\ddot{\bar{w}}_0$. The cantilever beam has a length of a, thickness t_m, width W_m, density ρ_m, and modulus of elasticity E_m. Embedding within the primary structure, there is a self-tuning resonator to mitigate the system resonance peaks. This resonator consists of a clamped-clamped beam with the length of a_r, thickness t_r, width W_r, density ρ_r and modulus of elasticity E_r. The self-tuning in the resonator is achieved by a sliding mass, attached to the fixed-fixed beam (as shown in Fig. 8.1), with a total mass of $M_.$. This mass is free to slide along the resonator beam due to Coriolis and centrifugal forces to tune the resonator. The governing equations of motion of the structure, the self-tuning resonator, and the slider can be expressed as:
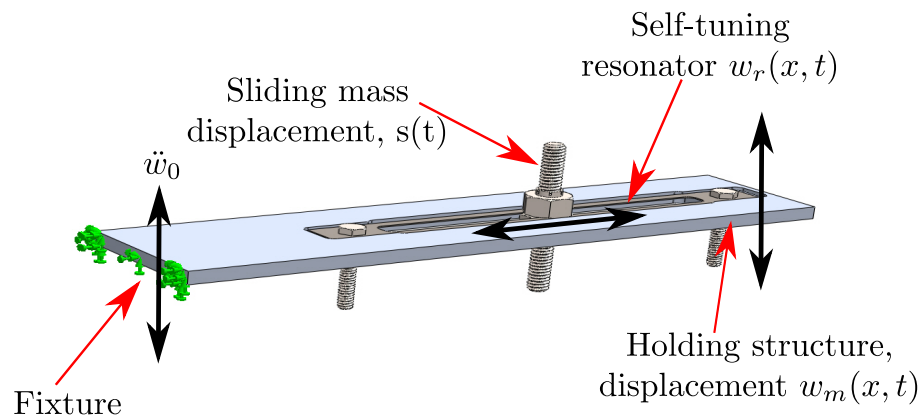
Figure 8.1: Key components of the self-tuning vibration absorber installed on a structure.

$$m_m\ddot{\bar{w}}_m + EI_m\bar{w}_m'''' = -m_m\ddot{\bar{w}}_0 \tag{8.1}$$

$$m\ddot{\bar{w}}_r + EI_r\bar{w}_r'''' + M[\ddot{\bar{w}}_r + 2\dot{\bar{s}}\dot{\bar{w}}_r' + \ddot{\bar{s}}\bar{w}_r' + \dot{\bar{s}}^2\bar{w}_r'']_{x=\bar{s}} = -m_r\ddot{\bar{w}}_0$$
$$-M\ddot{\bar{w}}_0\delta(x-\bar{s}) \tag{8.2}$$

$$M\ddot{\bar{s}} + M\bar{w}_r'[\ddot{\bar{w}}_r + 2\dot{\bar{s}}\dot{\bar{w}}_r' + \ddot{\bar{s}}\bar{w}_r' + \dot{\bar{s}}^2\bar{w}_r'']_{x=\bar{s}} = -M\bar{w}_r'\ddot{\bar{w}}_0\delta(x-\bar{s}) \tag{8.3}$$

where $\bar{w}_m$ is the displacement of the primary structure, $\bar{w}_r$ is the displacement of the res-onator, $\bar{s}$ is the displacement of the slider, δ is the Dirac delta function, $(\dot{})$ is the derivative with respect to time, and $(')$ is the derivative with respect to space. Note that the flexural rigidity EI_m, EI_r and the mass per unit length m_m, m_r vary along the structure. Further discussion on the flexural rigidity and the mass per unit length will be presented in Section 3. To normalize the system, the following dimensionless parameters are introduced

$$\omega_{nm}^2 = \frac{EI_m}{m_m a^4}, \omega_{nr}^2 = \frac{EI_r}{m_r a^4}, M_r = \frac{M}{m_r}, w_m = \bar{w}_m/a, w_r = \bar{w}_r/a, s = \bar{s}/a, \zeta = \bar{x}/a, \tau = \frac{t}{a^2}\sqrt{\frac{E_m}{m_m}},.$$
$$\tag{8.4}$$

substituting Eq. 8.4 into Eqs. 8.1-8.3 yields the following normalized equations

$$\ddot{w}_m + w_m'''' = -\ddot{w}_0 \tag{8.5}$$

$$\ddot{w}_r + \frac{\omega_{nr}^2}{\omega_{nm}^2}w_r'''' + M_r[\ddot{w}_r + 2\dot{s}\dot{w}_r' + \ddot{s}w_r' + \dot{s}^2 w_r'']_{\zeta=s} = -\ddot{w}_0 - M_r\ddot{w}_0\delta(\zeta-s) \tag{8.6}$$

$$\ddot{s} + w_r'[\ddot{w}_r + 2\dot{s}\dot{w}_r' + \ddot{s}w_r' + \dot{s}^2 w_r'']_{\zeta=s} = -w_r'\ddot{w}_0\delta(\zeta-s) \tag{8.7}$$

8.2.1   Galerkin's projection

In order to simulate our system numerically, we need to dicretize the partial differential equation given in Eqs. 8.5-8.6 into a system of ordinary differential equations. This can be done by Galerkin's projection, which further requires writing the solution of w_m, w_r as

$$w_m = \sum_{n=1}^{\infty} \phi_{nm}(\zeta) A_n(\tau) \tag{8.8}$$

$$w_r = \sum_{n=1}^{\infty} \phi_{nr}(\zeta) A_n(\tau) \tag{8.9}$$

where $A_n(\tau)$ is an unknown function of time for the nth mode, $\phi_{nm}(\zeta)$ is the nth mode shape of the primary structure, and $\phi_{nm}(\zeta)$ is the nth mode shape of the resonator. Substituting Eqs. 8.8-8.9 in Eqs. 8.5-8.6 yields

$$\sum_{n=1}^{\infty} \phi_{nm}(\zeta) \ddot{A}_n(\tau) + \sum_{n=1}^{\infty} \phi_{nm}^{iv}(\zeta) A_n(\tau) = -\ddot{w}_0 \tag{8.10}$$

$$\sum_{n=1}^{\infty} \phi_{nr}(\zeta) \ddot{A}_n(\tau) + \frac{\omega_{nr}^2}{\omega_{nm}^2} \sum_{n=1}^{\infty} \phi_{nr}^{iv}(\zeta) A_n(\tau) + M_r \Big[\sum_{n=1}^{\infty} \phi_{nr}(\zeta) \ddot{A}_n(\tau) + 2\dot{s} \sum_{n=1}^{\infty} \phi_{nr}'(\zeta) \dot{A}_n(\tau) +$$
$$\ddot{s} \sum_{n=1}^{\infty} \phi_{nr}'(\zeta) A_n(\tau) + \dot{s}^2 \sum_{n=1}^{\infty} \phi_{nr}''(\zeta) A_n(\tau) \Big]_{\zeta=s} = -\ddot{w}_0 - m_r \ddot{w}_0 \delta(\zeta - s) \tag{8.11}$$

$$\ddot{s} + \sum_{n=1}^{\infty} \phi_{nr}'(\zeta) A_n(\tau) \Big[\sum_{n=1}^{\infty} \phi_{nr}(\zeta) \ddot{A}_n(\tau) + 2\dot{s} \sum_{n=1}^{\infty} \phi_{nr}'(\zeta) \dot{A}_n(\tau) + \ddot{s} \sum_{n=1}^{\infty} \phi_{nr}'(\zeta) A_n(\tau) +$$
$$\dot{s}^2 \sum_{n=1}^{\infty} \phi_{nr}''(\zeta) A_n(\tau) \Big]_{\zeta=s} = -\sum_{n=1}^{\infty} \phi_{nr}'(\zeta) A_n(\tau) \ddot{w}_0 \delta(\zeta - s) \tag{8.12}$$

The reduced order equations can be obtained by multiplying Eq. 8.10 by $\phi_{pm}(\zeta)$ and Eq. 8.11 by $\phi_{pr}(\zeta)$, adding them together, integrating over the normalized length, and re-

calling the orthogonality conditions as

$$
\begin{aligned}
\ddot{A}_p + \omega_p^2 A_p + M_r \phi_p(s) [&\sum_{n=1}^{\infty} \phi_n(s)\ddot{A}_n(t) + 2\dot{s}\sum_{n=1}^{\infty} \phi_n'(s)\dot{A}_n(t) + \ddot{s}\sum_{n=1}^{\infty} \phi_n'(s)A_n(t) + \\
&\dot{s}^2 \sum_{n=1}^{\infty} \phi_n''(s)A_n(t)] = -\int_0^1 \phi_p(\zeta)\ddot{w}_0 d\zeta + m_1\phi_p(s)\ddot{w}_0
\end{aligned}
\tag{8.13}
$$

where $\ddot{w}_0 = w_0 \sin(2\pi ft)$, and ϕ_r, ϕ_p are the rth and the pth mode shape of the combined structure (i.e., the primary structure and the resonator), respectively.

After discretizing the system, the state space form of Eqs. 8.12-8.13 can be solved numerically in MATLAB. The resulting state-space model has a dimension $(2r+2)$, where r is the number of modes considered in the simulation. It is noteworthy here that the system is in the algebraic loop since each derivative is a function of the other derivatives. In order to solve this system, we need to break the loop by building a matrix for the coefficients of derivatives on the left hand of the state-space model, then multiplying the state-space model by the inverse of this matrix. Further, linear viscous damping is added to Eqs. 8.12-8.13 in the numerical simulation to achieve better convergence.

8.3   Adaptive linear mode shapes algorithm to simulate the system

In order to simulate the state-space model discussed in the above section, we need to obtain the space component (i.e., mode shapes) to integrate over the time only. The conventional approach to solve the current problem is to employ the mode shapes of the bare beam. This method is known as the assumed mode method and the associated error can be small if the

mass of attachment is small as compared to the primary beam. However, the error becomes significant for larger masses and hence, exact mode shapes and orthogonality conditions need to considered [9, 25, 70]. In the current study, the slider moves along the resonator till it reaches an equilibrium position. Therefore, the mode shapes and the resonance frequency of the system continuously change as the slider moves. Assuming a fixed mode shape throughout the numerical simulation may lead to erroneous results and the slider may not settle down at the correct equilibrium position that tunes the resonator to the excitation frequency.
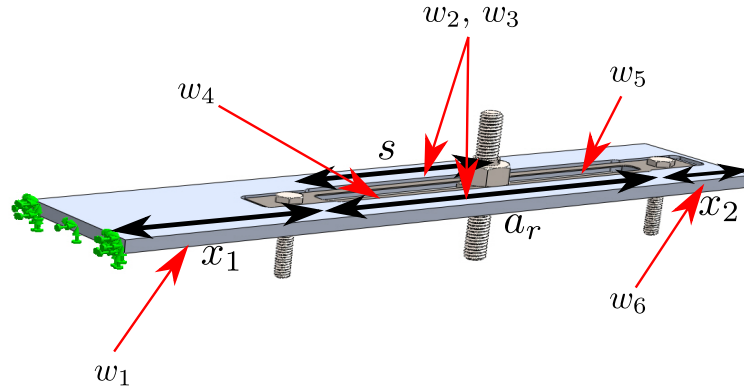
Figure 8.2: System portions used in determining the system instantaneous mode shapes.

To obtain the instantaneous exact linear mode shapes (i.e., at the instantaneous slider position) of the combined structure, the linear equation of motion corresponding to the free vibration for each portion of the system can be written as

$$\ddot{w}_i + \omega_i^2 w_i'''' = 0, \quad i = 1, \, 2, \, 3...6. \tag{8.14}$$

with

$$\omega_i^2 = \frac{E_i I_i}{m_i L_i^4} \tag{8.15}$$

where E_i is the modulus of elasticity, I_i is the second moment of area, m_i is the mass per unit length, and L_i is the length of the ith portion of the structure. To determine the system natural frequency, we divide the structure into 6 portions as shown in Fig. 8.2. The first portion stretches from the fixed end of the main structure to the first fixed point of the resonator. Therefore, it has a length of $L_1 = x_1$, modulus of elasticity $E_1 = E_m$, mass per unit length $m_1 = \rho_m t_m w_m$, and $I_1 = 1/12 t_m^3 w_m$. The second and the third portions of the system stretch parallel to the resonator along both sides on the main structure. These two portions will be identical and will have $L_2 = L_3 = a_r$, $E_2 = E_3 = E_m$, $m_2 = m_3 = \rho_m t_m w_{m2}$, and $I_2 = I_3 = 1/12 t_m^3 w_{m2}$, where w_{m2} is the width of each portion. The fourth and the fifth portions represent the resonator beam and they are divided by the instantaneous slider position s. Therefore, they both have $E_4 = E_5 = E_r$, $m_4 = m_5 = \rho_r t_r w_r$, and $I_4 = I_5 = 1/12 t_r^3 w_r$. However, their length depends on the instantaneous slider position, such that $L_4 = s$ and $L_5 = a_r - s$. In order to simplify the model of the resonator, we neglect the slot in which the slider moves. Finally, the last portion of the system stretches from the end of the resonator till the end of the structure beam with $E_6 = E_m$, $L_6 = x_2$, $m_6 = \rho_m t_m w_m$, and $I_6 = 1/12 t_m^3 w_m$.

8.3.1   Instantaneous linear mode shapes and frequencies

At each instantaneous slider position, we calculate the linear mode shapes and resonance frequencies by solving for the boundary and continuity conditions (i.e., in this case, we have 4×6=24 conditions). At the fixed end, the two boundary conditions can be defined as

$$w_1(0, \tau) = w_1'(0, \tau) = 0, \tag{8.16}$$

while at the free end, the other two boundary conditions can be expressed as

$$w_6''(1, \tau) = w_6'''(1, \tau) = 0. \tag{8.17}$$

The first set of the continuity conditions are defined at x_1 from the fixed end. In particular, these continuity conditions are defined between the end of the first portion (i.e., at x_1) and the beginning of the second, third, and fourth portion. These continuity conditions are

$$w_1(x_1, \tau) = w_2(x_1, \tau) = w_3(x_1, \tau) = w_4(x_1, \tau), \tag{8.18}$$

$$w_1'(x_1, \tau) = w_2'(x_1, \tau) = w_3'(x_1, \tau) = w_4'(x_1, \tau), \tag{8.19}$$

$$E_1 I_1 w_1''(x_1, \tau) = E_2 I_2 w_2''(x_1, \tau) + E_3 I_3 w_3''(x_1, \tau) + E_4 I_4 w_4''(x_1, \tau), \tag{8.20}$$

$$E_1 I_1 w_1'''(x_1, \tau) = E_2 I_2 w_2'''(x_1, \tau) + E_3 I_3 w_3'''(x_1, \tau) + E_4 I_4 w_4'''(x_1, \tau). \tag{8.21}$$

The second set of continuity conditions are defined between the fourth and the fifth portion at the slider position (i.e., $x_1 + s$). These conditions are

$$w_4(x_1 + s, \tau) = w_5(x_1 + s, \tau), \tag{8.22}$$

$$w_4'(x_1 + s, \tau) = w_5'(x_1 + s, \tau), \tag{8.23}$$

$$w_4''(x_1 + s, \tau) = w_5''(x_1 + s, \tau), \tag{8.24}$$

$$E_4 I_4 w_4'''(x_1 + s, \tau) = E_5 I_5 w_5'''(x_1 + s, \tau) + m_r \ddot{w}_4(x_1 + s, \tau). \tag{8.25}$$

Finally, the last set of continuity conditions are defined at the end of the resonator beam (i.e., $x_1 + a_r$). Particularly, between the beginning of the sixth portion and the end of

second, third, and fifth portion. The conditions are

$$w_6(x_1 + a_r, \tau) = w_2(x_1 + a_r, \tau) = w_3(x_1 + a_r, \tau) = w_5(x_1 + a_r, \tau), \qquad (8.26)$$

$$w_6'(x_1 + a_r, \tau) = w_2'(x_1 + a_r, \tau) = w_3'(x_1 + a_r, \tau) = w_5'(x_1 + a_r, \tau), \qquad (8.27)$$

$$E_6 I_6 w_6''(x_1 + a_r, \tau) = E_2 I_2 w_2''(x_1 + a_r, \tau) + E_3 I_3 w_3''(x_1 + a_r, \tau) + E_5 I_5 w_5''(x_1 + a_r, \tau), \quad (8.28)$$

$$E_6 I_6 w_6'''(x_1 + a_r, \tau) = E_2 I_2 w_2'''(x_1 + a_r, \tau) + E_3 I_3 w_3'''(x_1 + a_r, \tau) + E_5 I_5 w_5'''(x_1 + a_r, \tau). \quad (8.29)$$

Since the aim is to determine the instantaneous linear mode shapes, the solution of each portion can be written as

$$w_i = X_i(\zeta) \exp^{j\omega\tau} \qquad (8.30)$$

where $X_i(\zeta)$ is the linear mode shape and can be written as

$$X_i(\zeta) = A_i \sin(\beta_i \zeta) + B_i \cos(\beta_i \zeta) + C_i \sinh(\beta_i \zeta) + D_i \cosh(\beta_i \zeta) \qquad (8.31)$$

where $\beta_i = \sqrt{\omega_i \omega}$.

Upon imposing Eqs. 8.30-8.31 into Eqs. 8.16-8.29, the instantaneous mode shapes and frequencies of the system can be determined by solving the resulting system.

8.3.2   Adaptive algorithm to update the system spatial status

As mentioned in Sec. 2, the spatial parameters (i.e., the mode shapes and frequencies) need to be imposed in the system before integrating the system numerically over time. However, as the slider moves along the beam, the spatial parameters will change and hence, assuming a fixed value may result in erroneous results. Therefore, we need to update the value of

the spatial parameters to adapt the instantaneous slider position as the integration time evolves. To overcome this problem, one can determine the spatial parameters at each time step based on the instantaneous slider position inside an anonymous function that is called by MATLAB solver. Then, the calculated parameters will be fed into the state-space model and integrated numerically. However, this algorithm is computationally expensive since it needs to determine the system's natural frequency at each step. For a simple system with only one resonator, one can evaluate all possible frequencies and mode shapes by sweeping the slider position over the resonator with a small step and save the obtained data set prior to simulation. In addition, obtaining the data set can be done by parallel computation using multiple nodes. Since the slider may pass the same position at different time steps, determining the spatial parameter at each frequency step is computationally expensive. Instead, the data set can simply be called once for all time steps and the spatial parameters can be picked based on the instantaneous slider position from the previously obtained data set. The latter approach can reduce the computation time significantly for this simple case; however, it may not be practical to obtain the data set when we have multiple self-tuning resonator on the structure. Indeed, the size of the data set will be increased dramatically for the case of multiple resonators.

Another algorithm that can further reduce the computational effort is updating the spatial parameters at a time step larger than the simulation time step. For instance, if we run a simulation for 100 second with a time step 0.001 second (please note that the time step in MATLAB built-in integrator is adaptive, and it can be much smaller than this to get the simulation converging), we update the spatial parameters every 0.1 seconds. This assumption can be valid since the dynamic of the slider is usually slower than the dynamic of the system. Therefore, the simulation cost can be further reduced regardless of the algorithm used in the previous paragraph. Although this algorithm affects the accuracy of the transient

Table 8.1: System key parameters.

Parameter	Value	Unit	Parameter	Value	Unit
a	0.1397	m	ρ_r	7860	kg/m^3
t_m	0.0032	m	ρ_m	2700	kg/m^3
w_m	0.0318	m	E_m	68.9	GPa
a_r	0.0746	m	E_r	207	GPa
t_r	0.3048	mm	x_1	0.0494	m
w_r	9.5	mm	x_2	0.0156	m
M	7.4	g	w_{m2}	0.0103	m

response, it neither affects the equilibrium slider position nor the steady-state response.

8.4   Numerical demonstration

In this section, the results are presented for the combined structure shown in Figs. 8.1-8.2 to study the effect of self-tuning resonator on the structural vibration response. We also try to explore if the current model can represent an effective passive alternate system. The parameters of the simulated structure are shown in Table 8.1, where the primary structure is made from aluminum alloy while the resonator is made from spring steel.

8.4.1   Resonator and system linear frequencies

Based on the parameters listed in Table 8.1, we determine the resonance frequencies of the resonator beam with clamped-clamped ends and show the results in Fig. 8.3 for different slider positions. From Fig. 8.3, we can observe that the resonator beam can exhibit a wide range of frequencies at different vibration modes for different slider positions. For instance, it ranges from 82.2 Hz to 288.8 Hz at the first vibration mode for different slider positions (as shown in Fig. 8.3(a)). This observation further implies that the resonator can handle a wide range of frequency bands unlike conventional tuned spring-mass systems.

Moreover, the current model of the resonator also covers a wide frequency range at higher modes (as shown in Figs 8.3(b), (c), and (d)), while the frequency range where the resonator does not have any resonance frequency, in between the modes resonance frequency range, is narrow. This also indicates that the proposed resonator can be operated at a wider ranges of frequencies to cancel higher resonance peaks. It is noteworthy that the resonator has multiple potential equilibrium points at each point excluding frequencies at the local minima and maxima of the curve. These equilibrium positions depend on the initial conditions and the boundary condition of the resonator and resonator. The number of equilibrium positions for the clamped-clamped resonator could be up to twice the nth resonance mode. For instance, for the third vibration mode, there are six equilibrium positions, as shown in Fig. 8.3(c). Again, we neglected the slot inside the resonator beam in our simulations to simplify our model as our goal is to prove the self-tunability concept of our structure and record the achieved broadband vibration attenuation.

Next, we investigate the resonance frequencies for the whole structure (i.e., the cantilever beam with the self-tuning resonator). The frequencies corresponding to the first four modes of the combined structure are shown in Fig. 8.4 for all possible slider positions. These results demonstrate the significant dependency of the structure's resonance frequencies on the slider position. For instance, the first vibration mode of the structure ranges from 77.5 Hz to 136.4 Hz, as depicted in Fig. 8.4(a). This variance in the structure's resonance frequency may stretch over several hundred Hz at some vibration modes, as shown in Figs. 8.4-(b)-(c). These results also show the presence of multiple equilibrium positions at some frequency values. However, the slider will track the equilibrium positions of the single resonator to tune it as discussed below. Note that the frequency curve is not symmetric about the middle point of the resonator beam as the primary structure has different boundary conditions at each end, and the resonator's center point does not coincide with the center point of the
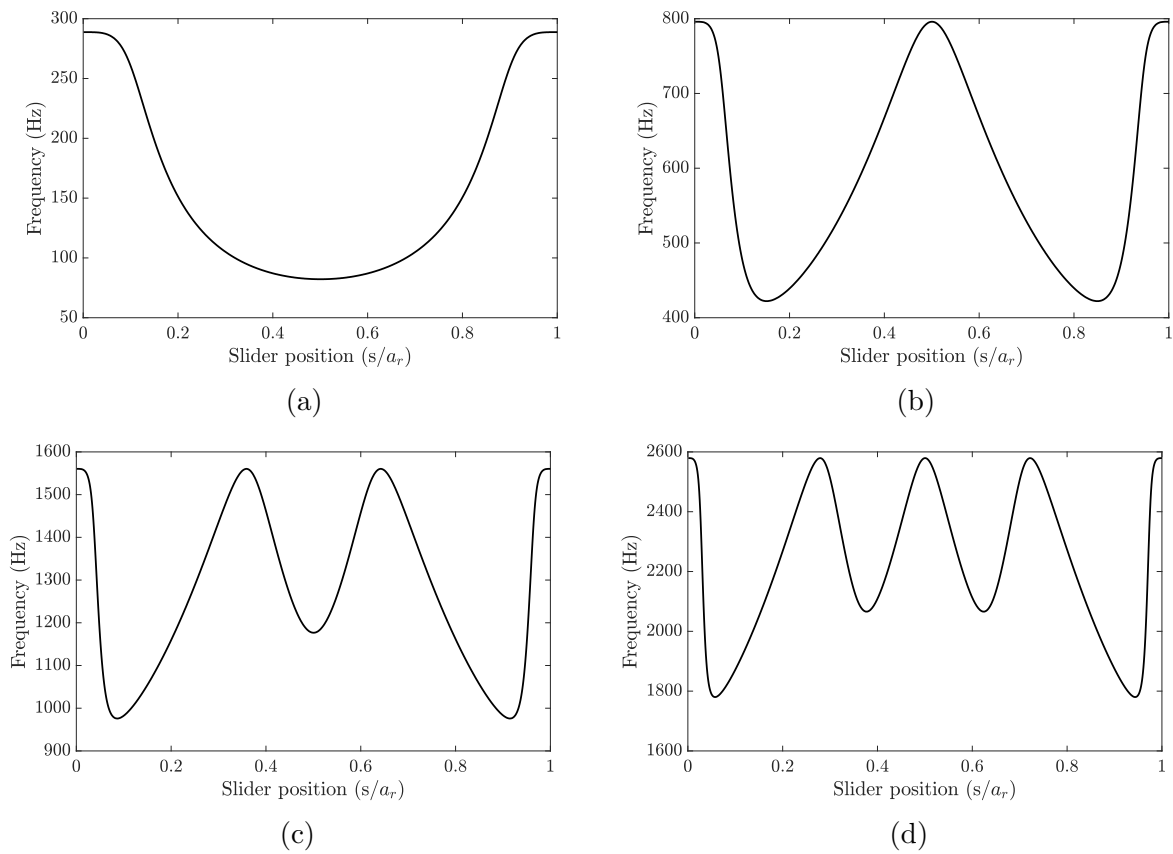
Figure 8.3: Resonance frequencies for resonator beam only at different slider positions: (a) First mode; (b) Second mode; (c) Third mode; (d) Fourth mode.

structure. Therefore, the system may exhibit more equilibrium points at lower vibration modes than higher modes at specific frequencies, as shown in Fig. 8.4(a). An example of the mode shape is shown in Fig. 8.5 for the first vibration mode corresponding to a specific slider position, $s = 0.5a_r$. At this position, the system has the minimum resonance frequency in the first vibration mode, as shown in Fig. 8.4-(a). Although the combined structure mode shape appears to have the first mode shape of a cantilever beam, the resonator mode shape seems to be different from the primary structure mode shape and has a vibration amplitude higher than any part of the primary structure.
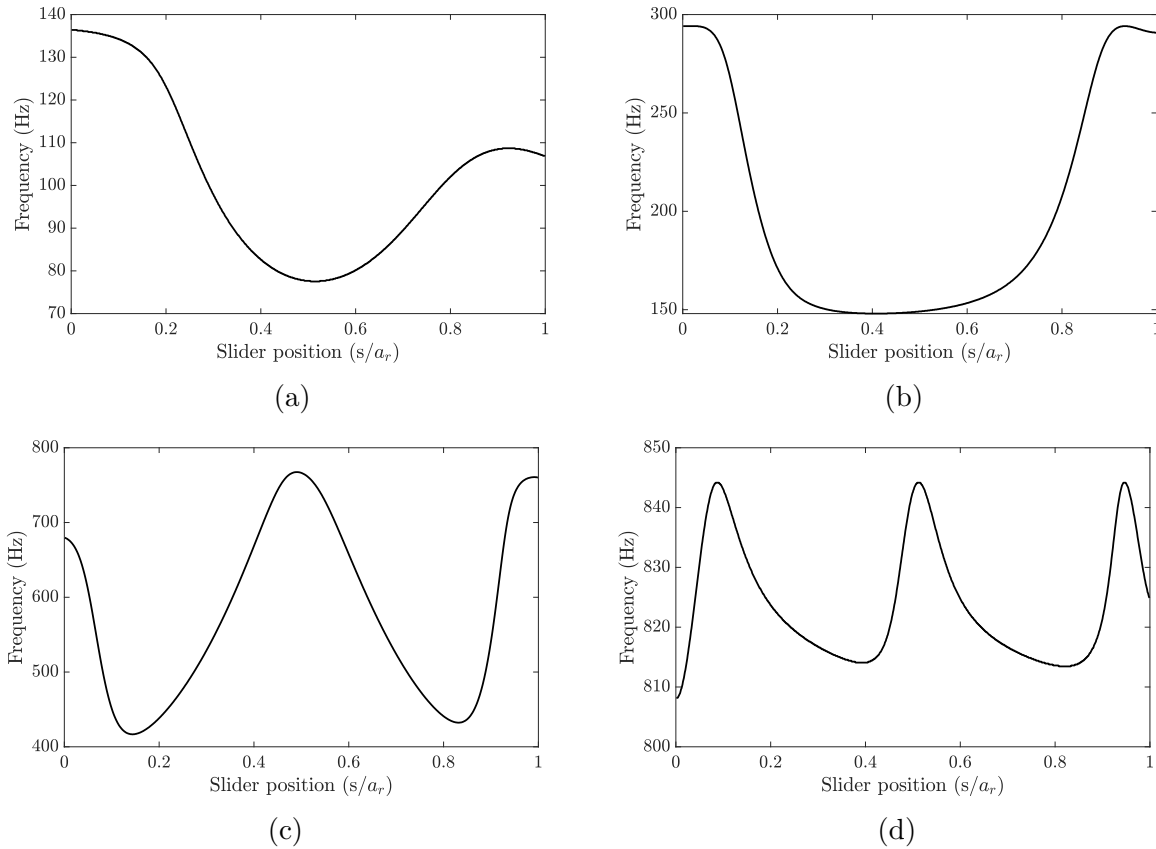
Figure 8.4: Resonance frequencies for the combined structure at different slider positions: (a) First mode; (b) Second mode; (c) Third mode; (d) Fourth mode.

Finally, we plot the resonance frequencies of the first and the second vibration modes of the combined structure and compare it with the first vibration mode of the resonator for
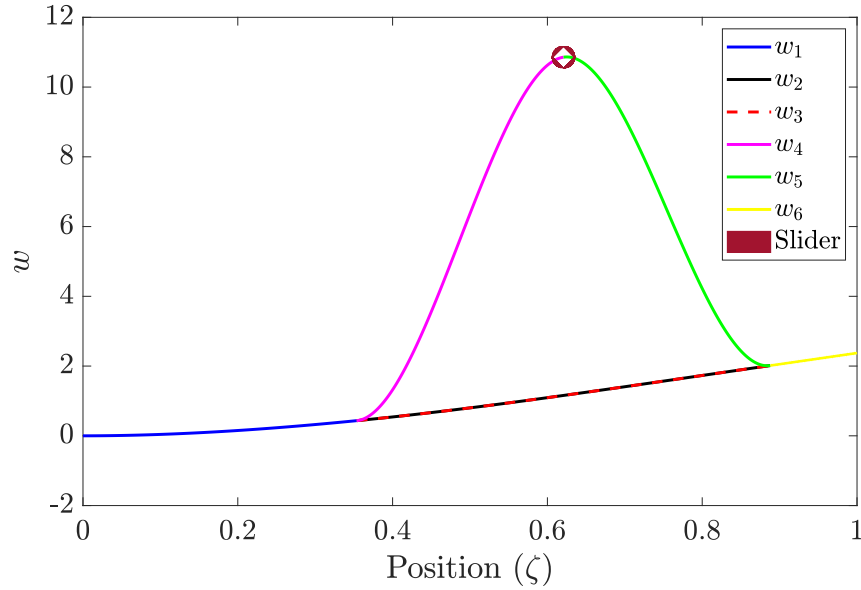
Figure 8.5: The first mode of the combined structure at slider position $s = 0.5a_r$; different system's portions highlighted in Fig. 8.2 (i.e., w_i are demonstrated in the legend in the addition to the slider; however, the y-axis represents the structure displacement (i.e., w).

different positions of the slider, as shown in Fig. 8.6. The result shows that the resonator resonance frequencies lie between the first and second vibration modes' of the structure. Indeed, the presence of the resonator can lead to a split in the first resonance peak of the bare structure (i.e, without the resonator) into the two modes as shown in Fig. 8.6. In addition, it can be observed that the resonance frequency curve of the resonator does not intersect with the resonance frequency curves of the structure. Therefore, if the resonator is tuned to the excitation frequency and the slider reaches the equilibrium position, the structure will not go under resonance as both resonance modes are away from the excitation frequency at this equilibrium position.
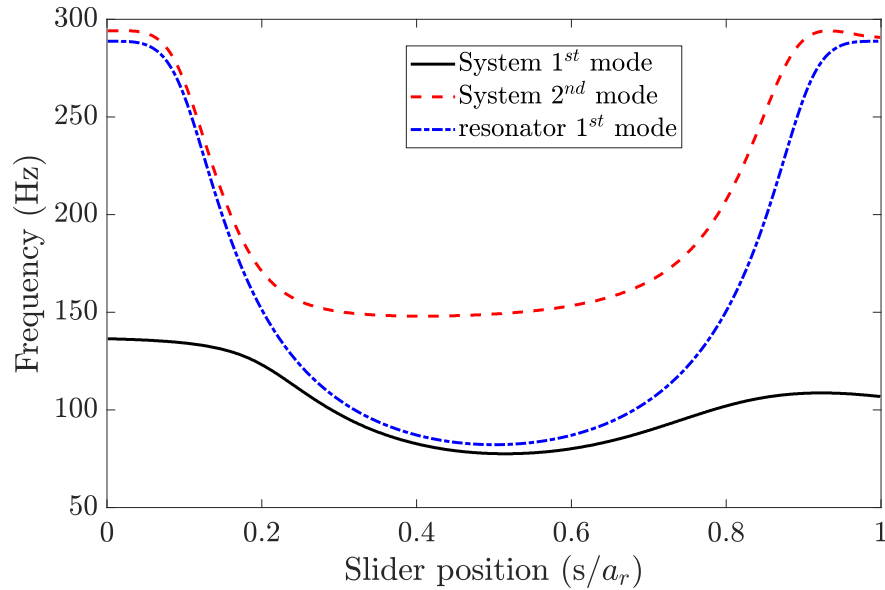
Figure 8.6: Comparison between the combined structure mode shapes and the resonator at different slider positions.

8.4.2 Simulation results

Based on the system parameters given in Table 8.1, we numericaly integrate the discretized system using the different algorithms discussed in Section 3.2. In this analysis, we focus on the first resonance mode of the resonator, which ranges from 82.2 Hz to 288.8 Hz.

Firstly, we determine the mode shapes and resonance frequency of the combined structure at the anticipated steady-state position (i.e., the equilibrium position) for a specific excitation frequency. Then, we numerically integrate the system by assuming a fixed mode shape. Secondly, we obtain the instantaneous linear frequencies and mode shapes and save them in a data set. Then, this data set is called in the numerical integration simulations at different excitation frequencies. Finally, we assume that the change in the slider position is slower than the system dynamics. Therefore, we update the mode shapes every 0.1 seconds and use the final state of this slow time step as initial conditions for the next simulation/time-step. The results of these three different methods for the slider position are shown in Fig. 8.7.

The results indicate that the assumed mode method may fail in determining the steady-state position of the slider accurately. Indeed, the assumed mode method shows that the slider can move to either ends of the slot i.e., either $s = 0.05a_r$ or $s = 0.95a_r$ (more details on the tracking of equilibrium position is discussed in the experimental section). On the other hand, the other algorithms show that the slider settles down almost at the same steady-state position with some discrepancies limited to the transient response. However, the simulation time for the semi-variable modes algorithm is significantly lower as compared to the variable mode method, which updates the instantaneous mode shapes at every time step. Therefore, we will use the semi-variable algorithm in all subsequent simulations in the current study.
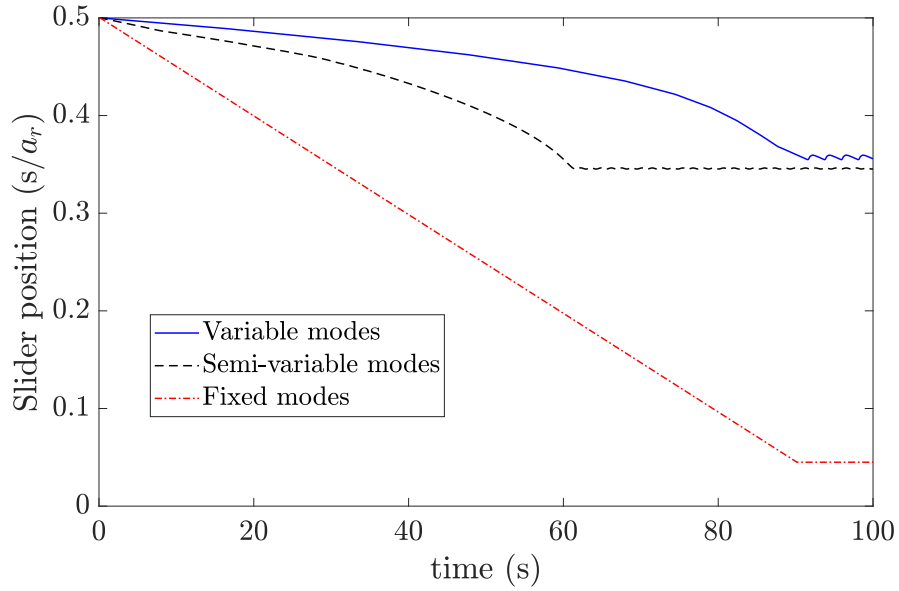
Figure 8.7: Comparison of equilibrium position of slider using different algorithms; Variable modes: updating the mode shapes at every time step, semi-variable modes: updating the modes at a larger time step, fixed modes: using assumed fixed mode shapes. Other parameters for simulation are $s_0 = 0.5/a_r$, $f = 90Hz$, $w_0 = 0.1g$, $n = 3$.

In order to determine the sufficient number of mode shapes that yield accurate results, we simulate the system with different numbers of mode shapes and plot the results in Fig. 8.8. The results demonstrate that including only one mode shape in the analyses yields inaccurate
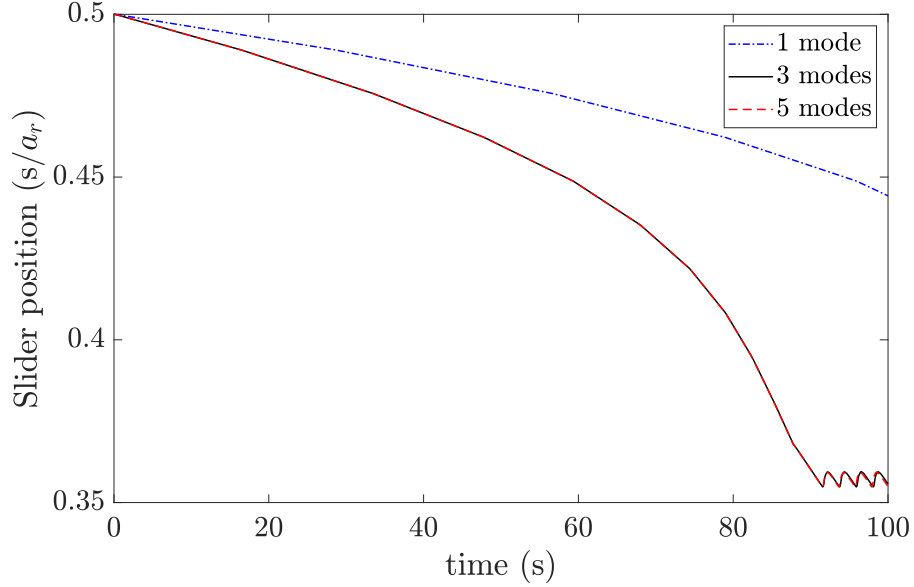
Figure 8.8: The effect of the considered mode shapes in the simulation on the results. Other parameters for simulation are $s_0 = 0.5/a_r$, $f = 90Hz$, $w_0 = 0.1g$.

results as compared to including three modes. However, increasing the number of considered modes beyond three does not significantly affect the simulation results except increasing the computation cost significantly. Thus, we will consider only the nearest three mode shapes from the excitation frequency in further analyses.

Having established the number of mode shapes required for simulations, next we investigate the slider response by dividing the frequency range of the resonator and the combined structure into three regions. For the low-frequency region, the variations in slider positions for different excitation frequencies are shown in Fig. 8.9. First, we excite the system at a frequency below the frequency ranges of both the resonator and the combined structure, as shown in Fig. 8.6. In this case, the slider does not track any equilibrium position within these frequency ranges; instead, it settles down near the free end of the structure, which represents a vibration anti-node of the structure, as shown in Fig. 8.9(a). Increasing the excitation frequency slightly to a frequency within the range of the combined structure and

outside the range of the resonator shows that the slider will track an equilibrium position near the middle of the resonator, as depicted in Fig. 8.9(b)-(c). It is noteworthy that the frequency does not hit the exact equilibrium position here due to numerical error in frequency calculations, where the frequency-position in this region has a small slope that differs the slider position significantly with small change in frequency calculations. This position tunes the structure to resonance instead of the resonator and results in a significant increase in the structure's tip displacement, as shown in Fig. 8.10(a). Increasing the excitation frequency to 85 Hz, which lies within the resonance frequency range of the resonator, shows that the slider starts to tune itself to the applied excitation frequency, as shown in Fig. 8.9(d). Although the steady-state position of the slider does not precisely coincide with the resonator frequency curve, it neither coincides with the resonance frequency curve of the structure. Thus, the tip displacement will be reduced significantly as the slider reaches its equilibrium position, as shown in Fig. 8.10(b).

Next, we focus on the frequency region close to the region where the structure does not have any resonance frequency and plot the slider positions and the tip displacements for different excitation frequency, and are shown in Figs. 8.11 and 8.12, respectively. As the frequency increases toward the region where the slider and the structure frequency-position curves start departing from each other, the slider tracks an equilibrium position which tunes itself to the resonance, as shown in Figs. 8.11(a)-(b). Note that this position is away from the equilibrium position that tunes the whole structure to resonance. This phenomenon will also lead to a gradual reduction in the tip displacement as the slider reaches its equilibrium position, as depicted in Fig. 8.12(a). The reduction observed in this figure is more significant as compared to the low-frequency region, as shown in Fig. 8.10(b). In Fig. 8.11, as we move our excitation frequency inside the region where only the resonator has resonance frequencies, we observe that the slider tracks the equilibrium positions which tunes it to
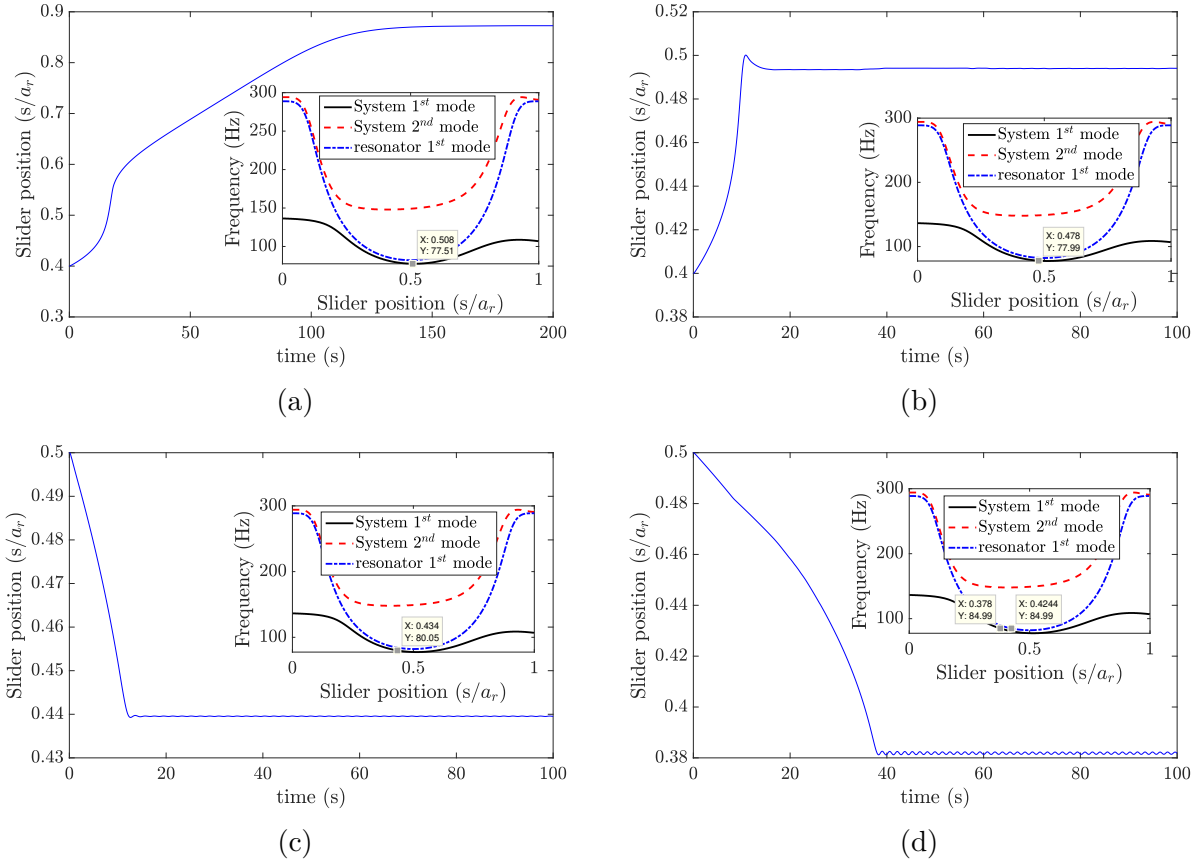
Figure 8.9: Slider position at different excitation frequencies: (a) f=77 Hz; (b) f=78 Hz; (c) f=80 Hz; (d) f=85 Hz, with $w_0 = 0.1g$.
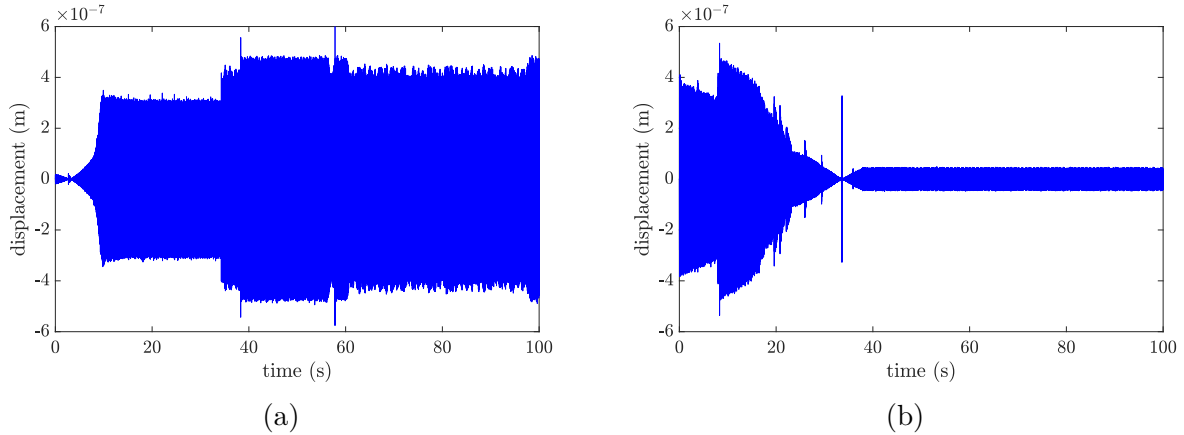
Figure 8.10: Tip displacement of the primary structure at different excitation frequencies: (a) f=78 Hz; (b) f=85 Hz, $w_0 = 0.1g$.

the applied excitation frequency. This observation is also supported by the absence of any resonance frequency for the combined structure for all possible slider positions in this region. Inside this region, the tip displacement becomes significantly low when the slider reaches the equilibrium position as compared to the response at other slider location, as can be seen in Fig. 8.12 b). As the excitation frequency increases above this range (see Figs. 8.11(e)-(f)), where the structure's second vibration mode does have resonance frequency along with the resonator, the slider still tracks an equilibrium position that tunes itself to the excitation frequency rather than the combined structure resonance frequency. However, the steady-state displacement of the system gradually increases at the equilibrium position as compared to other slider positions and the results in the low-frequency region (see Figs. 8.12 (c)-(d)).

Finally, we excite the structure at frequencies within the region where the slider and combined structure frequency-position curves are closer and the results are shown in Figs. 8.13-8.14. In this region, the slider still tracks equilibrium positions that tune it to the excitation frequency, as shown in Fig. 8.13(a)-(b). However, Fig. 8.13(c) demonstrates that the frequencies of the resonator and the combined structure become closer by increasing the excitation frequency to around 230 Hz. Yet the slider equilibrium position is closer to tune the resonator rather than the combined structure. This further leads to reducing the vibration attenuation recorded at the tip as the slider moves along the slot, as depicted in Fig. 8.14(a). Indeed, this increase in the steady-state response increases with the increase in the excitation frequency in this region. With further increase in the excitation (i.e., above 230 Hz), the slider does not track an equilibrium position anymore. Indeed, Figs. 8.13(e)-(f) indicates that the slider equilibrium position does not match the anticipated position highlighted in the small windows. Moreover, the slider's equilibrium position approaches the mid slot point, which might be close to an anti-node of higher vibration modes. This miss tuning yields a significant increase in the steady-state response as compared with the slider at other locations, as
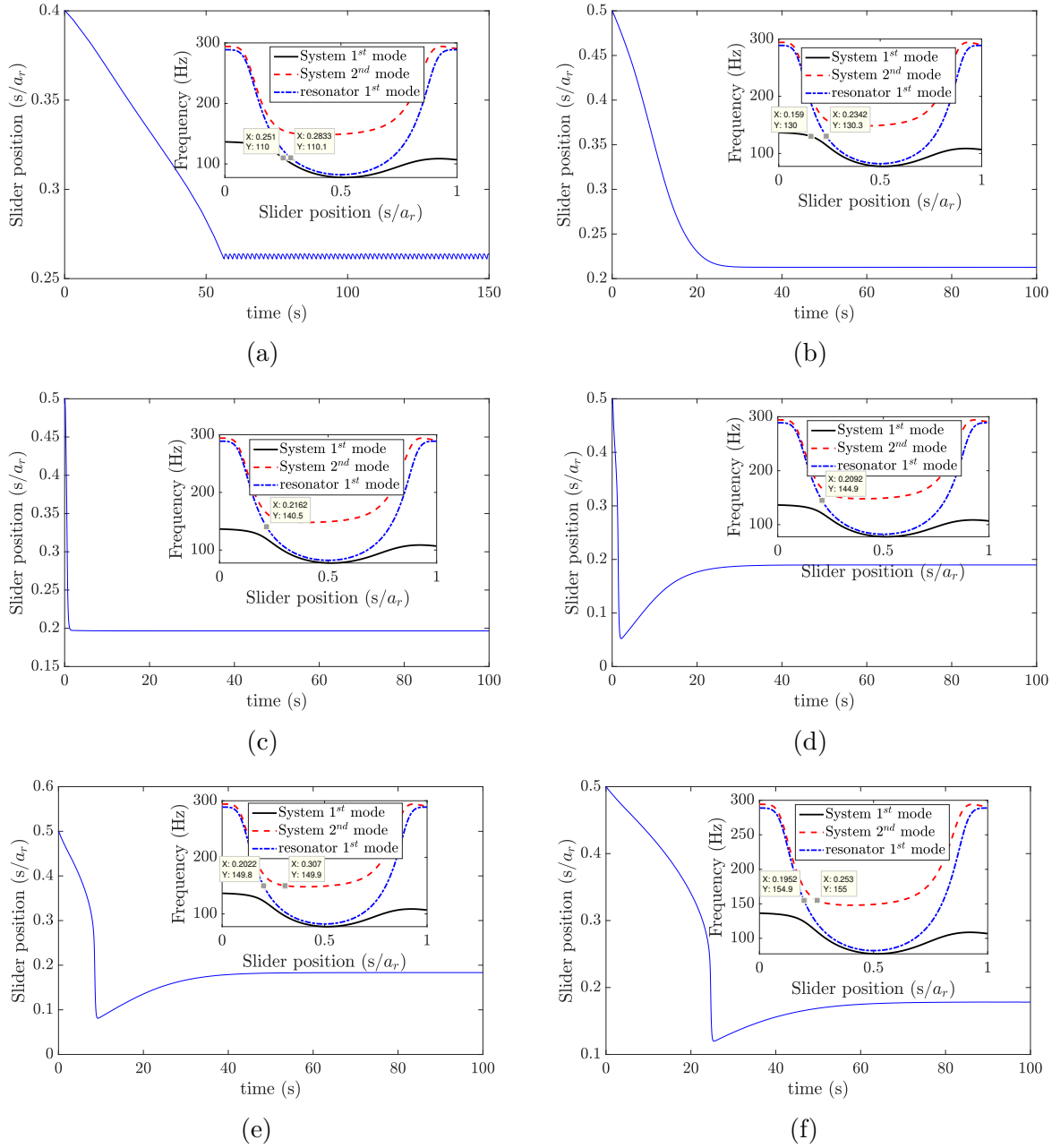
Figure 8.11: Slider position at different excitation frequencies: (a) f=110 Hz; (b) f=130 Hz; (c) f=140 Hz; (d) f=145 Hz; (e) f=150 Hz; (f) f=155 Hz, $w_0 = 0.1g$.
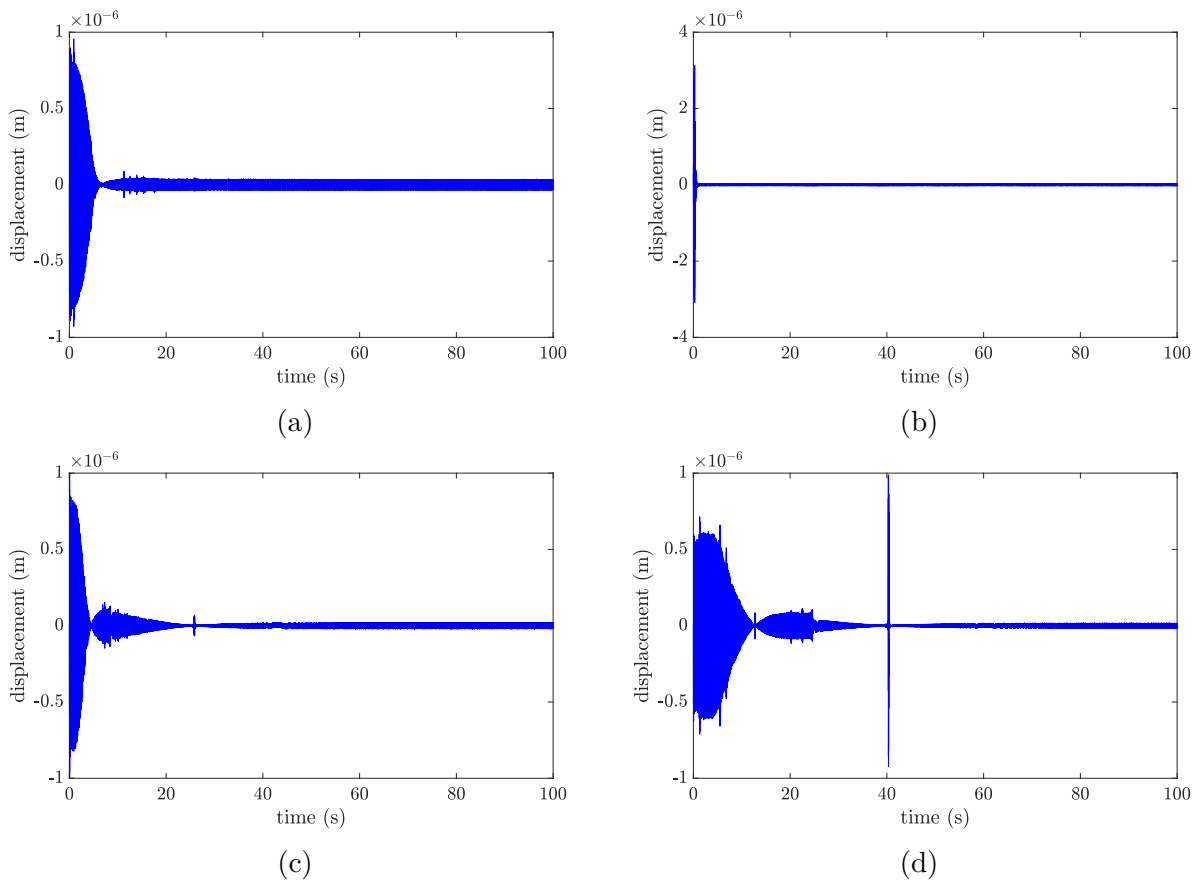
Figure 8.12: Tip displacement of the primary structure at different excitation frequencies: (a) f=130 Hz; (b) f=140 Hz; (c) f=150 Hz; (d) f=155 Hz, $w_0 = 0.1g$.

shown in Fig. 8.14(b).

8.5   Experimental demonstration of self-tunability

In order to verify the analytical observations, we conduct an experiment on a prototype representing the proposed structure. This prototype is shown in Fig. 8.1, and its dimensions are given in Table 8.1. It is noteworthy that we changed the total length of the primary structure to $a = 0.131$ m instead of the values given in Table 8.1. This change in length should shift the structure's frequencies up. As we recall from our analytical analyses, we neglected several parameters in our calculations. These parameters include the slot where the slider moves and the slider dimensions. However, we emphasize that these parameters should not significantly affect our qualitative study.

To study the effect of these parameters, we conduct frequency analyses using SolidWorks and report the resonance frequencies of the structure and the resonator only at different slider positions. The obtained resonance frequencies from both analytical simulations and Solidworks are tabulated in Table 8.2. Although neglecting the resonator parameters can cause some errors in both the structure and the resonator frequencies, the results show similar behavior in the frequency trend for both the structure and the resonator. In particular, the first resonance frequency increases with moving the slider toward the fixed end inside the slot, where it ranges from 70.65 Hz to 145.11 Hz. In addition, the second mode frequency also follows the same trend, where it ranges from 150.64 Hz to 377.84 Hz. It can be observed that the values of the second resonance frequency for the slider position between 0.25-0.5 a_r/a are close to each other. This observation can be explained by the plateau curve in this region, as it was observed in Fig. 8.6, in addition to numerical errors in simulations. In general, the upper limit of the frequencies for different modes went up due to a reduction in the length
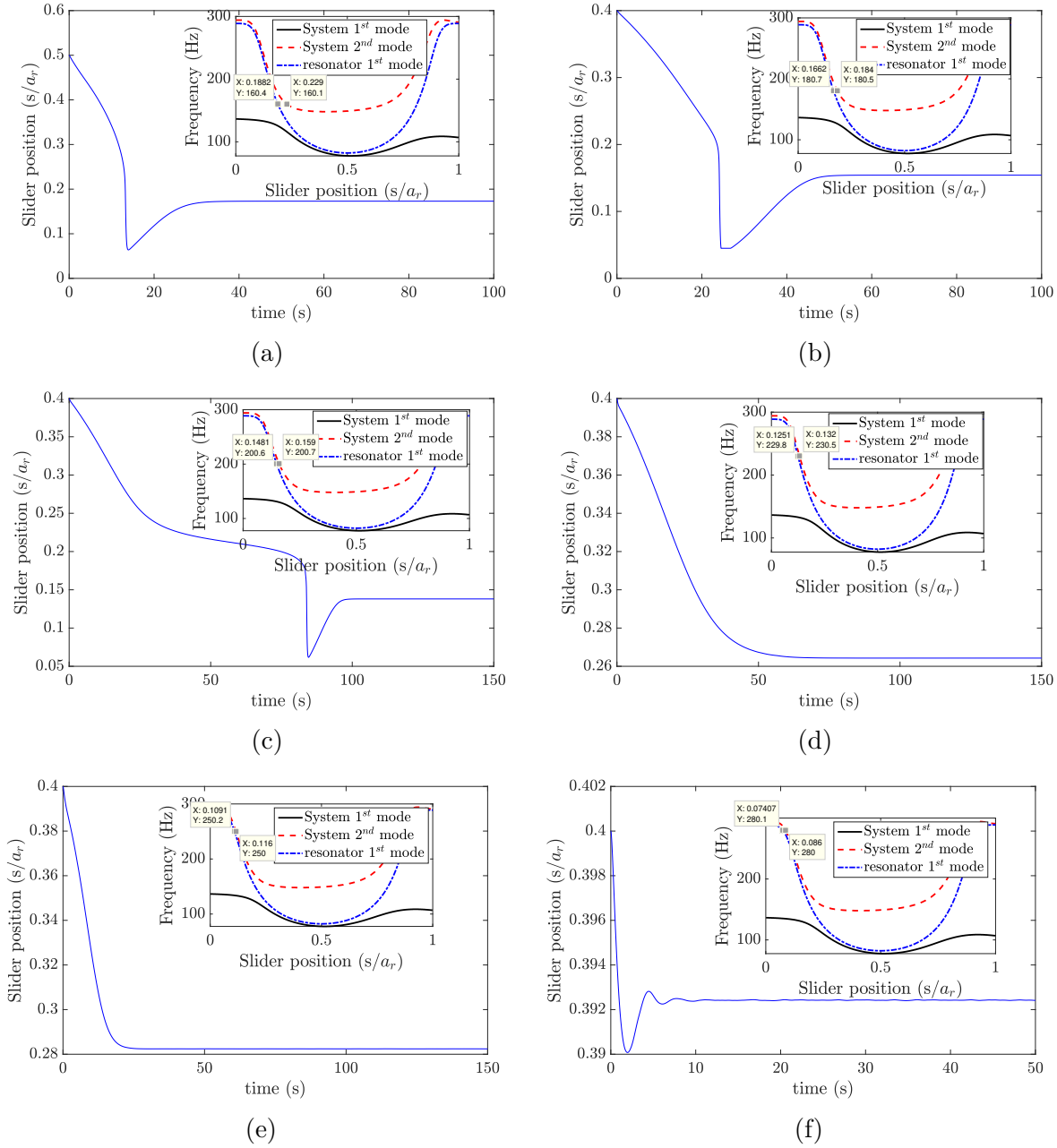
Figure 8.13: Slider position at different excitation frequencies: (a) f=160 Hz, $w_0 = 0.2g$; (b) f=180 Hz, $w_0 = 0.3g$; (c) f=200 Hz, $w_0 = 0.5g$; (d) f=230 Hz, $w_0 = 0.8g$; (e) f=250 Hz, $w_0 = 0.8g$; (f) f=280 Hz, $w_0 = 0.8g$.
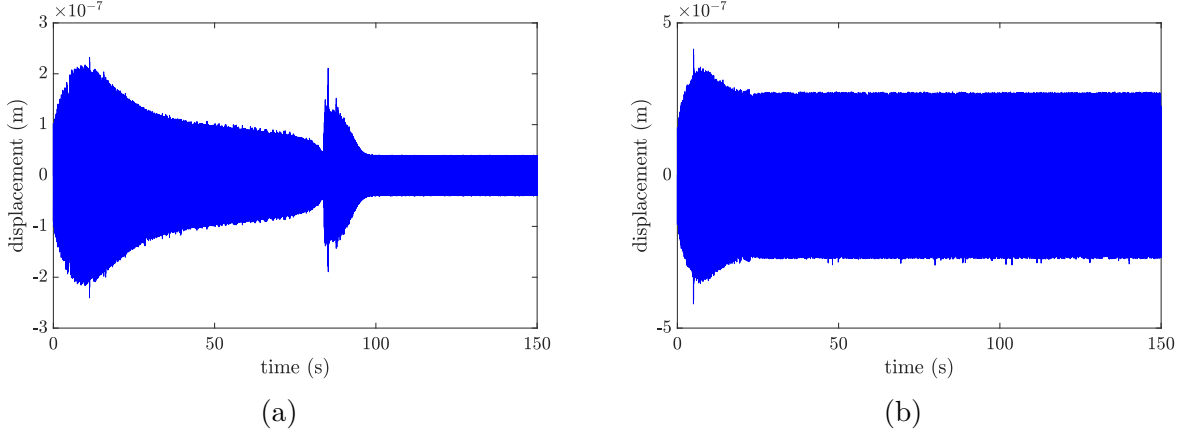
Figure 8.14: Tip displacement of the primary structure at different excitation frequencies: (a) f=200 Hz, $w_0 = 0.5g$; (b) f=250 Hz, $w_0 = 0.8g$.

of the primary structure, while the lower limit went down due to an increase in the mass ratio of the slider to the resonator as we remove the slotted mass and include the dimension of the slider in the simulation. On the other hand, the frequency region where the structure does not have any resonance frequencies (i.e., between the first and the second modes) was also reduced due to the reduction in the effective mass of the resonator by eliminating the slotted mass. However, the qualitative trends stayed similar to the analytical model.

The experimental setup of the proposed structure is shown in Fig. 8.15. The structure is excited by an electromagnetic shaker (LDS V408). This excitation is represented by a base excitation. The structure is fixed to the shaker from its fixed end using a fixture with a resonance frequency much higher than the investigated frequency range. The applied base excitation is measured by an accelerometer (PCB 356A16) fixed at the fixture. To avoid any mass addition on the free end of the structure, which may change the system frequency, we use a Polytec Laser Doppler Vibrometer (Polytec PSV-500) to record the structure response. The laser beam is pointed at the tip of the structure's free end. The velocity of the slider is also measured using Polytec Laser Doppler Vibrometer (Polytec PSV-500). This signal is further integrated to obtain the displacement of the slider by applying a low pass filter that

Table 8.2: Resonance frequencies for the primary structure and the resonator obtained by SolidWorks.

Position s/a_r	Structure 1st mode (Hz)		Structure 2nd mode (Hz)		Resonator 1st mode (Hz)	
	SolidWorks	Analytical	SolidWorks	Analytical	SolidWorks	Analytical
0.5	70.65	78.15	150.64	177	72.68	82.2
0.33	74.07	92.97	150.49	176	75.75	97.11
0.25	84.20	113.2	150.04	180.8	86.07	123.1
0.19	114.6	135.1	151.28	195.6	118.65	158.8
0	145.11	157	377.84	298.3	377.04	288.7

avoids error build-up in the integration due to noise. The signal generated by these sensors is recorded and analyzed using (Polytec DAQ). The DAQ is also used to generate the input profile which is amplified using an amplifier (LPA100) that drives the shaker.
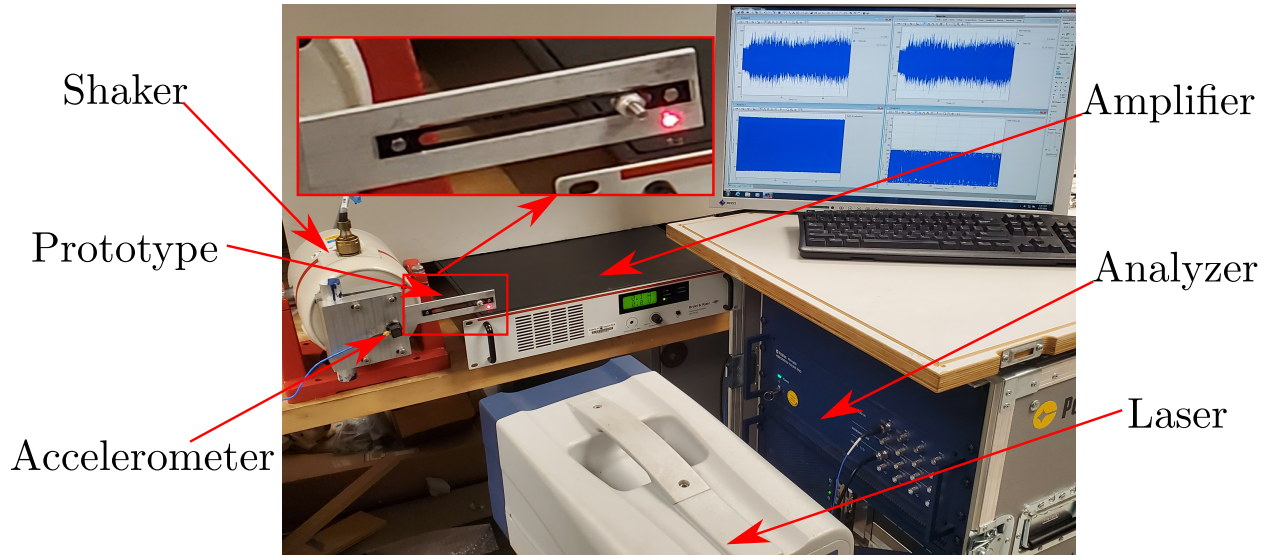
Figure 8.15: Key components of the experimental setup.

First, we record the slider displacement, which is free to move along the slot, by applying a sinusoidal signal with different frequencies and placing the slider at different initial positions. Note that we focus on demonstrating the qualitative analytical observations without paying attention to the exact quantitative part. This is because our analytical investigation neglected some design parameters and the effect of friction, which is beyond the scope of

the current analysis. The slider position is measured from its starting position till it reaches the equilibrium position. These measurements are shown in Fig. 8.16 for different excitation frequencies. For the low-frequency region, we conducted a test at 90 Hz. The results show that the slider settles down at the equilibrium position and stays there as time evolves, as can be seen in Fig. 8.16. Indeed, this new equilibrium position tunes the resonator to the applied excitation frequency and should result in significant decrease in the tip displacement (this observation is supported by experimental results for the tip displacement shown in Fig. 8.17). These results show a qualitative analogy with the analytical results shown in Figs. 8.9(d) and 8.10(b). Next, we examine the middle-frequency region by exciting the system at 110 Hz, 120Hz, and 130 Hz. With increase in the frequency, the slider tends to track an equilibrium position closer to the fixed end. This observation also shows a good agreement with the analytical results. Finally, we study the high-frequency region by exciting the system at 230 Hz. At this frequency, the slider tends to move to an equilibrium position near the other end of the beam. Yet it still tunes the system to the excitation frequency.
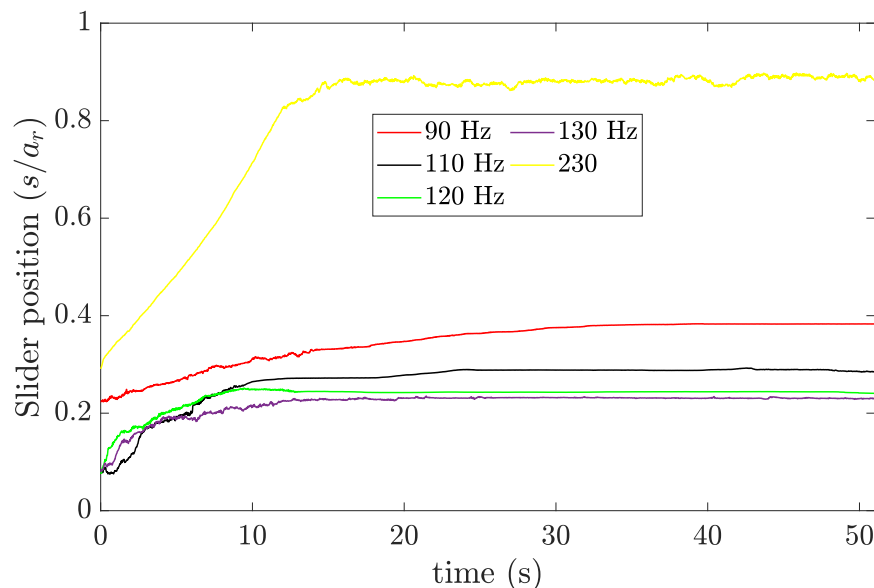
Figure 8.16: Measured slider position at different excitation frequencies.

Next, we report the the experimental time response of the tip displacement for various parameters in Fig. 8.17, where s_{start} is the initial position of the slider and s_{end} is the equilibrium position of the slider. For high-frequency region (Fig. 8.17(a)), the results indicate that the tip displacement increases as the slider reaches its equilibrium position. This observation can be justified as frequencies of both the resonators and the structure are close to each other in this region (see Fig. 8.6). Therefore, the slider keeps hitting the resonance frequency of the structure as it oscillates around its equilibrium position ($s_{end} = 0.9a_r$ in the case at 230 Hz), leading to high amplitude oscillations of the tip. This observation shows a good agreement with the analytical observation reported in Fig. 8.14(b). However, for regions where the frequencies of the slider and the structure are away from each other, one can observe a reduction in the response as the slider settles down at its equilibrium position, as shown in Fig. 8.17(b) for excitation frequency equal to 145 Hz. We emphasize here that the recorded reduction is not significant since the slider in this case approaches its equilibrium position from the left (its initial position is to the left from the equilibrium position as depicted in Fig. 8.6). Therefore, it does not hit any resonance frequency for the structure on its way. Moreover, the response for this initial position is lower. On the other hand, a significant reduction can be observed in the tip displacement as the slider approaches its equilibrium position from the right side, as shown in Figs. 8.17(c)-(d). By lowering the excitation frequency to 60 Hz (Fig. 8.17(e)), the slider tracks the middle point as an equilibrium position, indicating that the minimum frequency of the resonator obtained experimentally is around 60 Hz. At this frequency, a significant reduction can also be observed in the tip displacement as the slider settles down at its equilibrium position. Further, it can be observed from Figs. 8.17(a)-(e) that the final equilibrium position of the slider tends to move from $0.9a_r$ to $0.5a_r$ as we reduce the excitation frequency from 230 Hz to 60 Hz. This observation is similar to the experimental observations shown in Fig. 8.16 and the analytical observations shown in Figs. 8.9,8.11, and 8.13. In addition, the observed reduction in the structure displacement,

as the slider tunes the resonator, corroborates our analytical observations about the self-tuning capability of the proposed resonator, which was demonstrated in Figs. 8.10,8.12, and 8.14. Finally, we show the tip displacement of the system at frequency below the resonator frequency range (i.e., 55 Hz) in Fig. 8.17(f). The results show that the system response is not attenuated at all times and slider positions. In addition, the slider tracks an unanticipated equilibrium point. These two observations also show a good agreement with the analytical results in Fig. 8.9(a) and Fig. 8.10(a).

8.6   Discussion

Analytical and experimental investigations demonstrate the ability of the proposed self-tuning resonator to tune itself to the excitation frequency over a wide range of frequencies. This range can be controlled by optimizing the resonator and structure design. For instance, increasing the effective mass of the resonator can further split the resonance frequency modes of the structure. However, our analyses showed the presence of some frequencies, in particular very low and high-frequency regions (defined in the previous section), where the resonator may not be able to tune itself. Therefore, integrating the current passive system with an external actuator, which forces the resonator to perfectly tune itself and reduces its oscillation at the equilibrium position, may significantly widen the frequency band that can be controlled by this resonator. Assuming that the resonator can always tune itself to its equilibrium position (i.e., in perfect operation conditions), we determine the steady-state response of the proposed structure and compare it to the fixed frequency resonator. These FRFs are shown in Fig. 8.18. The results demonstrate the superiority of the self-tuning resonator as compared to the fixed frequency resonator in terms of structure response at a wide range of frequencies. Moreover, no sharp high amplitude peak can be observed within
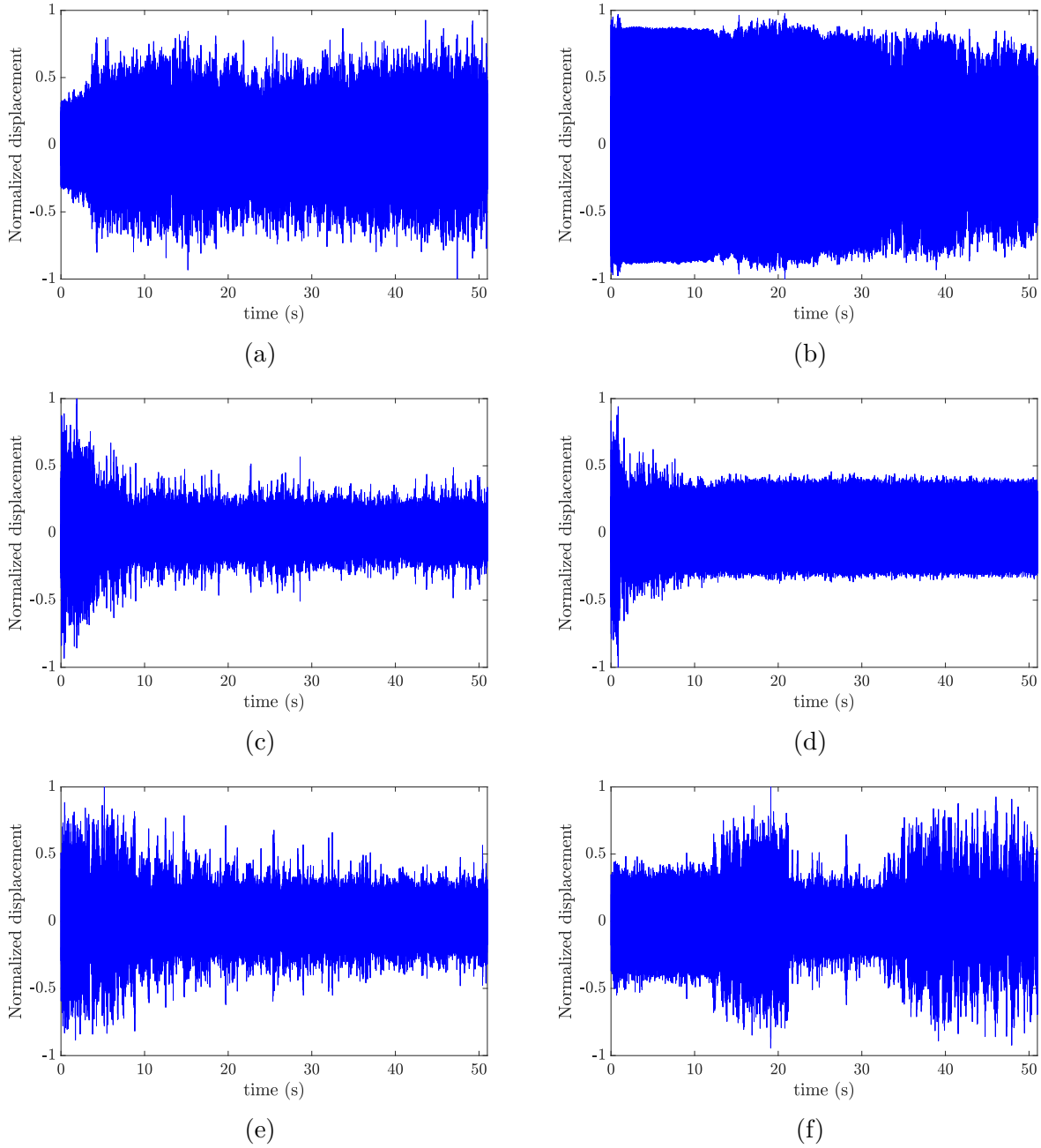
Figure 8.17: Test measurement of the tip displacement: (a) f=230 Hz, $s_{start} = 0.8a_r$, $s_{end} = 0.9a_r$, $w_0 = 6g$; (b) f=145 Hz, $s_{start} = 0.74a_r$, $s_{end} = 0.86a_r$, $w_0 = 0.6g$; (c) f=100 Hz, $s_{start} = a_r$, $s_{end} = 0.8a_r$, $w_0 = 1.37g$; (d) f=70 Hz, $s_{start} = 82a_r$, $s_{end} = 0.66a_r$, $w_0 = 1.44g$; (e) f=60 Hz, $s_{start} = 0.77a_r$, $s_{end} = 0.52a_r$, $w_0 = 1g$; (f) f=55 Hz, $s_{start} = 0.77a_r$, $s_{end} = 0.6a_r$, $w_0 = 1g$.

the target frequency. Finally, the present study is focused on the first mode resonance frequency range of the resonator; however, higher frequency modes are also worthy of investigation given that some of them can stretch over several hundred of hertz. Again, this range may be controlled by changing the design parameters.
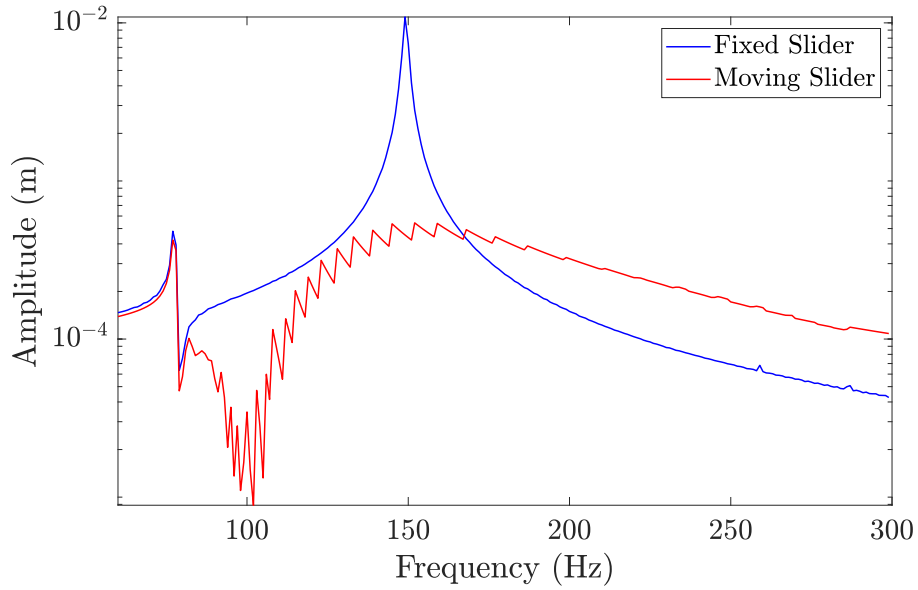
Figure 8.18: FRF comparison between the self-tuning resonator and the fixed resonatorat $0.5s/a_r$.

8.7   Conclusion

This paper detailed the analysis and modeling of a self-tuning resonator for vibration attenuation applications. This resonator takes the form of a fixed-fixed beam, which is integrated within a holding structure. The holding structure needs to be controlled in order to alleviate its dynamical response, with self-tuning facilitated by a sliding mass. This mass was free to move along a slot in the resonator's beam, changing the resonator's natural frequency. Therefore, it can tune the resonator to the applied excitation frequency once it settles down at an

equilibrium position. This can lead to broadband vibration attenuation in the holding struc-
ture. We presented the governing equation of motion for the primary structure, resonator,
and sliding mass. The system dynamics show the presence of coupling between the slider
and the resonator. The coupling terms that move the slider were defined as the Coriolis and
centrifugal forces. The system was then discretized in a system of ODEs using Galerkin's
projection. Unlike previous studies, we used exact linear instantaneous mode shapes and
frequencies in solving the problem to increase the accuracy. We also presented an adaptive-
mode shapes algorithm to tackle the problem. The algorithm was optimized to reduce the
simulation time and guarantee converging to an equilibrium position. Then, the system was
numerically simulated based on the proposed design parameters. The instantaneous system
frequencies showed that the resonator resonance frequencies can stretch over a wide range
of frequencies depending on the slider position. This demonstrated a good potential for the
proposed passive resonator to be used as a vibration absorber with a wide frequency band
as compared to other conventional passive mechanisms, which has narrow frequency band.
Over this wide frequency range, the slider showed the ability to settle down at equilibrium
position that tunes the resonator to the excitation frequency. The results also demonstrated
a significant reduction in the structure response as the slider reaches the equilibrium position.
Only very low and high frequency regions were excluded from this observation, where the
slider track equilibrium positions different from the anticipated equilibrium points. These
positions may be examined by including the investigation of higher modes unlike the current
study where it focused on the lower vibration mode only. The analytical observations of the
self-tunability was also supported by experimental results, particularly, in determining the
effective regions of the proposed absorber. Overall, the proposed passive absorber can work
over a wide frequency range as compared to conventional tuned spring-mass dampers with
completely eliminating the sharp peaks in frequency response.

Chapter 9

Conclusions and future work

9.1 Conclusion

This dissertation investigated the nonlinear wave propagation phenomena in nonlinear meta-materials by considering chain's and local resonator's nonlinearities. The research work dealt with three main topics. In the first part, nonlinear metamaterials with multiple local resonators were investigated. The second part of this dissertation discussed the electromechanical coupling in locally resonant nonlinear metamaterials and proposed a high symmetric electromechanical diode. The last part of this dissertation proposed a passive self-tuning metastructure using sliding mass mechanism. The major findings of these research topics, presented in this dissertation, are summarised as follows

- Nonlinear metamaterial consisting of a nonlinear chain with multiple nonlinear local resonators were studied. Analytical dispersion relations was derived using the method of multiple scales and validated numerically. These dispersion relations can provide an insight into the wavelength limits affected by the source and type of nonlinearity. The Spectro-Spatial wave features were also investigated by further processing the signals obtained numerically. The results demonstrated that the chain's nonlinearity could lead to the development of solitary waves and significant frequency shift limited to the medium-wavelength limit. On the other hand, the local resonator's nonlinearity can

also show the birth of solitary waves and significant frequency shift; however, this shift can be extended to the long-wavelength limit. Furthermore, the results demonstrated that the wave distortion associated with resonator nonlinearity can be controlled by tuning the nonlinear resonator frequency. These observations were further demonstrated by a computational study using ANSYS APDL.

• The effect of electromechanical coupling in the local resonator in nonlinear metamaterials was investigated. The study for both sources of nonlinearity (i.e., chain and local resonator) was presented.

• Analytical dispersion relation was obtained using perturbation techniques to study the effect of electromechanical coupling on the dispersion curves. Analytical results showed that the band structure can be altered only for a strong electromechanical coupling case. Therefore, a weak electromechanical coupling can allow the use of this metamaterials for simultaneous energy harvesting and vibration attenuation with no effect on the bangap size.

• Spectro-Spatial features investigations showed the birth of high amplitude localized solitary waves that can enhance energy harvesting and sensing for both sources of nonlinearity. However, these solitary waves were more pronounced in the case of chain nonlinearity. Spectro-Spatial analyses also demonstrated a substantial frequency shift in the output voltage signal for both sources of nonlinearity. In particular, the chain's nonlinearity can show a significant frequency shift limited to the medium-wavelength limit. However, the resonator's nonlinearity can demonstrate a similar shift at the long-wavelength limit and the medium-wavelength limit.

• The observations of significant frequency shift in nonlinear electromechanical metamaterials were employed for the design of electromechanical diode. This diode can allow

voltage harvesting from external disturbances in only one direction and block it in the other direction.

- The proposed electromechanical diode was constructed by combining the linear and nonlinear chains with electromechanical local resonators. The proposed diode does not only have a high asymmetric ratio, but also has a high transmission ratio for the forward configuration. Yet the proposed electromechanical diode can harvest energy and sense better than symmetric systems due to the birth of localized (solitary) waves.

- Different key parameters of the diode design were investigated. The results demonstrated that the operation range can be controlled through changing design parameters and selecting the source of nonlinearity. Particularly, the resonator's nonlinearity can exhibit a wider operation range within the long and medium-wavelength limits unlike the chain's nonlinearity, which limits the operation range to regions around the medium-wavelength limit.

- Design guidelines also showed that the bandgap's boundaries should be tuned around the operation frequency, in general, to avoid extending its size to the short-wavelength region and allow shifted frequency components to propagate in the forward configuration.

- A passive self-tuning resonator was investigated. The self-tunability was obtained by a sliding mass that moves along the resonator as the resonator vibrates. This slider moves itself to an equilibrium position to tune the resonator to the applied excitation frequency. Inspired by the capability of the self-tuning resonator, we integrated this resonator with a holding structure in order to investigate its vibration mitigation performance.

- The governing equations of motions of the holding structure, resonator, and the sliding

mass were presented and discretized into a system of ODE's using Galerkin's projection.

- Since the system spatial parameters (i.e., mode shapes and frequencies) vary over time as the slider moves toward its equilibrium position, an adaptive algorithm, to update the spatial parameters in numerical integration, was introduced to increase the simulation accuracy and minimize the simulation cost.

- Investigations of instantaneous exact mode shapes and frequencies revealed that the resonator's frequencies stretch over a wide range of frequencies as the slider moves along the resonator's beam.

- Analytical results indicate that the slider tracks an equilibrium position to tune the resonator to the applied excitation frequency. This can lead to significant vibration reduction in the system response for a wide range of frequencies. This reduction was also demonstrated experimentally to support the analytical findings.

9.2 Future work

Based on the research work and findings presented in this dissertation, the following insights are proposed for future work

- Analytical analyses have shown the possibility to widen the operation of electrome-chanical diode by considering resonator nonlinearity. I am planning on conducting experimental to demonstrate the performance of the electromechanical diode and the possibility of operating the system at the long-wavelength limit.

- Extending our investigations on nonlinear metamaterials to quasiperiodic metamaterials. This includes deriving the analytical expressions for nonlinear dispersion relations

and employing spectro-spatial analyses to reveal other interesting nonlinear wave prop-
agation phenomena.

- Studying the feasibility of energy harvesting in linear and nonlinear quasiperiodic struc-
  tures. This is motivate by the presence of localized mode shapes in quasiperiodic
  structures. Therefore, we anticipate harvesting most of the power by installing the
  harvester at the cells with high amplitude in the localized modes.

- Including the effect of slider friction in our model to enhance the accuracy of our model
  of self-tuning resonator.

- Integrating the passive self-tuning system with control system to enhance the stability
  and robustness of the slider while it tracks the best equilibrium position.

- Extending the single cell model of self-tuning resonator to periodic and quasiperiodic
  configurations in order to study the wave propagation in this structure and the possi-
  bility of developing self-tuning metamaterials.

- Integrating the self-tuning resonator in simultaneous vibration attenuation and en-
  ergy harvesting applications. This can also generate the required power to operate
  controllers for more robust tracking for the equilibrium position.

Bibliography

[1] Mohammad H Abedin-Nasab, Mary V Bastawrous, and Mahmoud I Hussein. Explicit dispersion relation for strongly nonlinear flexural waves using the homotopy analysis method. *Nonlinear Dynamics*, 99(1):737–752, 2020.

[2] Mohammad H Abedinnasab and Mahmoud I Hussein. Wave dispersion under finite deformation. *Wave Motion*, 50(3):374–388, 2013.

[3] Noha Aboulfotoh, Malte Krack, Jens Twiefel, and Jörg Wallaschek. A self-resonant system-experimental investigations of boundary and operating conditions. *Pamm*, 16 (1):253–254, 2016.

[4] Younes Achaoui, Vincent Laude, Sarah Benchabane, and Abdelkrim Khelif. Local resonances in phononic crystals and in random arrangements of pillars on a surface. *Journal of Applied Physics*, 114(10):104503, 2013.

[5] L Airoldi and M Ruzzene. Wave propagation control in beams through periodic multi-branch shunts. *Journal of Intelligent Material Systems and Structures*, 22(14):1567–1579, 2011.

[6] Mohammad A AL-Shudeifat, Alexander F Vakakis, and Lawrence A Bergman. Shock mitigation by means of low-to high-frequency nonlinear targeted energy transfers in a large-scale structure. *Journal of Computational and Nonlinear Dynamics*, 11(2), 2016.

[7] Rabih Alkhatib and MF Golnaraghi. Active structural vibration control: a review. *Shock and Vibration Digest*, 35(5):367, 2003.

[8] Muralidhar Ambati, Nicholas Fang, Cheng Sun, and Xiang Zhang. Surface resonant states and superlensing in acoustic metamaterials. *Physical Review B*, 75(19):195447, 2007.

[9] O Barry, DCD Oguamanam, and JW Zu. On the dynamic analysis of a beam carrying multiple mass-spring-mass-damper system. *Shock and Vibration*, 2014, 2014.

[10] Oumar Barry and Mohammad Bukhari. On the modeling and analysis of an energy harvester moving vibration absorber for power lines. In *ASME 2017 Dynamic Systems and Control Conference*, pages V002T23A005–V002T23A005. American Society of Mechanical Engineers, 2017.

[11] Jörg Baumgartl, Maria Zvyagolskaya, and Clemens Bechinger. Tailoring of phononic band structures in colloidal crystals. *Physical review letters*, 99(20):205503, 2007.

[12] Benjamin S Beck, Kenneth A Cunefare, Massimo Ruzzene, and Manuel Collet. Experimental analysis of a cantilever beam with a shunted piezoelectric periodic array. *Journal of Intelligent Material Systems and Structures*, 22(11):1177–1187, 2011.

[13] Andrea Bergamini, Tommaso Delpero, Luca De Simoni, Luigi Di Lillo, Massimo Ruzzene, and Paolo Ermanni. Phononic crystal with adaptive connectivity. *Advanced Materials*, 26(9):1343–1347, 2014.

[14] Katia Bertoldi, Vincenzo Vitelli, Johan Christensen, and Martin van Hecke. Flexible mechanical metamaterials. *Nature Reviews Materials*, 2(11):17066, 2017.

[15] Osama R Bilal and Mahmoud I Hussein. Trampoline metamaterial: Local resonance enhancement by springboards. *Applied Physics Letters*, 103(11):111901, 2013.

[16] Neil Boechler, Georgios Theocharis, and C Daraio. Bifurcation-based acoustic switching and rectification. *Nature Materials*, 10(9):665, 2011.

[17] Bernard Bonello, L Belliard, J Pierre, JO Vasseur, Bernard Perrin, and O Boyko. Negative refraction of surface acoustic waves in the subgigahertz range. *Physical Review B*, 82(10):104109, 2010.

[18] Arezki Boudaoud, Yves Couder, and M Ben Amar. A self-adaptative oscillator. *The European Physical Journal B-Condensed Matter and Complex Systems*, 9(1):159–165, 1999.

[19] Swinteck Bringuier, N Swinteck, JO Vasseur, J-F Robillard, K Runge, K Muralidharan, and PA Deymier. Phase-controlling phononic crystals: Realization of acoustic boolean logic gates. *The Journal of the Acoustical Society of America*, 130(4):1919–1925, 2011.

[20] J Bucay, E Roussel, JO Vasseur, Pierre A Deymier, AC Hladky-Hennion, Y Pennec, Krishna Muralidharan, B Djafari-Rouhani, and B Dubus. Positive, negative, zero refraction, and beam splitting in a solid/air phononic crystal: Theoretical and experimental study. *Physical Review B*, 79(21):214305, 2009.

[21] T Bückmann, M Thiel, M Kadic, R Schittny, and M Wegener. An elasto-mechanical unfeelability cloak made of pentamode metamaterials. *Nature communications*, 5(1): 1–6, 2014.

[22] M Bukhari, A Malla, H Kim, O Barry, and L Zuo. On a self-tuning sliding-mass electromagnetic energy harvester. *AIP Advances*, 10(9):095227, 2020.

[23] Mohammad Bukhari and Oumar Barry. Substantial frequency conversion at long-wavelength limit in metamaterial with weakly nonlinear local electromechanical resonators. *to appear in Journal of Mechanical systems and signal processing*, .

[24] Mohammad Bukhari and Oumar Barry. On the spectro-spatial wave features in nonlinear metamaterials with multiple local resonators. In *ASME 2019 International Design*

Engineering Technical Conferences and Computers and Information in Engineering Conference. American Society of Mechanical Engineers, 2019.

[25] Mohammad Bukhari and Oumar Barry. Exact nonlinear dynamic analysis of a beam with a nonlinear vibration absorber and with various boundary conditions. *Journal of Computational and Nonlinear Dynamics*, 15(1), 2020.

[26] Mohammad Bukhari and Oumar Barry. Simultaneous energy harvesting and vibration control in a nonlinear metastructure: A spectro-spatial analysis. *Journal of Sound and Vibration*, 473:115215, 2020.

[27] Mohammad Bukhari and Oumar Barry. Spectro-spatial analyses of a nonlinear metamaterial with multiple nonlinear local resonators. *Nonlinear Dynamics*, 99(2):1539–1560, 2020.

[28] Mohammad Bukhari, Eshagh Farzaneh Joubaneh, and Oumar Barry. Spectro-spatial wave features in nonlinear metamaterials: Theoretical and computational studies. *Journal of Vibration and Acoustics*, pages 1–45.

[29] Mohammad A Bukhari and Oumar R Barry. Electromechanical diode: acoustic non-reciprocity in weakly nonlinear metamaterial with electromechanical resonators. In *ASME 2020 International Design Engineering Technical Conferences and Computers and Information in Engineering Conference.* American Society of Mechanical Engineers Digital Collection, .

[30] Mohammad A Bukhari and Oumar R Barry. Nonlinear metamaterials with multiple local mechanical resonators: Analytical and numerical analyses. In *NODYCON 2019 The First International Nonlinear Dynamics Conference.* Springer, 2019.

[31] Mohammad A Bukhari, O Barry, and E Tanbour. On the vibration analysis of power lines with moving dampers. *Journal of Vibration and Control*, 24(18):4096–4109, 2018.

[32] Qian Feng Barry Oumar R Bukhari, Mohammad A and Lei Zuo. Effect of electromechanical coupling on locally resonant metastructures for simultaneous energy harvesting and vibration attenuation applications. In *ASME 2020 Dynamic Systems and Control Conference*. American Society of Mechanical Engineers Digital Collection.

[33] Wenshan Cai and Vladimir M Shalaev. *Optical Metamaterials*, volume 10. Springer, 2010.

[34] Filippo Casadei, Tommaso Delpero, Andrea Bergamini, Paolo Ermanni, and Massimo Ruzzene. Piezoelectric resonator arrays for tunable acoustic waveguides and metamaterials. *Journal of Applied Physics*, 112(6):064902, 2012.

[35] Ian L Cassidy, Jeffrey T Scruggs, and Sam Behrens. Design of electromagnetic energy harvesters for large-scale structural vibration applications. In *Active and Passive Smart Structures and Integrated Systems 2011*, volume 7977, page 79770P. International Society for Optics and Photonics, 2011.

[36] Francisco Cervera, L Sanchis, JV Sánchez-Pérez, R Martinez-Sala, C Rubio, F Meseguer, C López, D Caballero, and José Sánchez-Dehesa. Refractive acoustic devices for airborne sound. *Physical review letters*, 88(2):023902, 2001.

[37] Jaya Chandwani, Rohit Somkuwar, and Raghavendra Deshmukh. Multi-band piezoelectric vibration energy harvester for low-frequency applications. *Microsystem Technologies*, pages 1–11, 2019.

[38] Huanyang Chen and CT Chan. Acoustic cloaking in three dimensions using acoustic metamaterials. *Applied physics letters*, 91(18):183518, 2007.

[39] Liang-Shan Chen, Chao-Hsien Kuo, and Zhen Ye. Acoustic imaging and collimating by slabs of sonic crystalsmade from arrays of rigid cylinders in air. *Applied physics letters*, 85(6):1072–1074, 2004.

[40] Shengbing Chen, Gang Wang, Jihong Wen, and Xisen Wen. Wave propagation and attenuation in plates with periodic arrays of shunted piezo-patches. *Journal of Sound and Vibration*, 332(6):1520–1532, 2013.

[41] YY Chen, GK Hu, and GL Huang. An adaptive metamaterial beam with hybrid shunting circuits for extremely broadband control of flexural waves. *Smart Materials and Structures*, 25(10):105036, 2016.

[42] Johan Christensen and F Javier García de Abajo. Negative refraction and backward waves in layered acoustic metamaterials. *Physical Review B*, 86(2):024301, 2012.

[43] Johan Christensen, AI Fernandez-Dominguez, F de Leon-Perez, L Martin-Moreno, and FJ Garcia-Vidal. Collimation of sound assisted by acoustic surface waves. *Nature Physics*, 3(12):851–852, 2007.

[44] Manuel Collet, Morvan Ouisse, and Mohamed N Ichchou. Structural energy flow optimization through adaptive shunted piezoelectric metacomposites. *Journal of Intelligent Material Systems and Structures*, 23(15):1661–1677, 2012.

[45] Peter Constantinou and Saibal Roy. A 3d printed electromagnetic nonlinear vibration energy harvester. *Smart Materials and Structures*, 25(9):095053, 2016.

[46] Steven A Cummer and David Schurig. One path to acoustic cloaking. *New Journal of Physics*, 9(3):45, 2007.

[47] Steven A Cummer, Bogdan-Ioan Popa, David Schurig, David R Smith, John Pendry,

Marco Rahm, and Anthony Starr. Scattering theory derivation of a 3d acoustic cloaking shell. *Physical review letters*, 100(2):024301, 2008.

[48] Steven A Cummer, Johan Christensen, and Andrea Alù. Controlling sound with acoustic metamaterials. *Nature Reviews Materials*, 1(3):16001, 2016.

[49] Mohammed F Daqaq, Ravindra Masana, Alper Erturk, and D Dane Quinn. On the role of nonlinearities in vibratory energy harvesting: a critical review and discussion. *Applied Mechanics Reviews*, 66(4):040801, 2014.

[50] Amir Darabi, Ahmad Zareei, M-Reza Alam, and Michael J Leamy. Experimental demonstration of an ultrabroadband nonlinear cloak for flexural waves. *Physical Review Letters*, 121(17):174301, 2018.

[51] Bruce L Davis, Andrew S Tomchek, Edgar A Flores, Liao Liu, and Mahmoud I Hussein. Analysis of periodicity termination in phononic crystals. In *ASME International Mechanical Engineering Congress and Exposition*, volume 54945, pages 973–977, 2011.

[52] JP Den Hartog. Mechanical vibrations mcgraw-hill book company. *New York*, pages 122–169, 1956.

[53] Chang-Lin Ding and Xiao-Peng Zhao. Multi-band and broadband acoustic metamaterial with resonant structures. *Journal of Physics D: Applied Physics*, 44(21):215402, 2011.

[54] I El-Kady, RH Olsson III, and JG Fleming. Phononic band-gap crystals for radio frequency communications. *Applied Physics Letters*, 92(23):233504, 2008.

[55] Alper Erturk and Daniel J Inman. *Piezoelectric Energy Harvesting*. John Wiley & Sons, 2011.

[56] Víctor Espinosa, Víctor J Sánchez-Morcillo, Kestutis Staliunas, Isabel Pérez-Arjona, and Javier Redondo. Subdiffractive propagation of ultrasound in sonic crystals. *Physical Review B*, 76(14):140302, 2007.

[57] Xin Fang, Jihong Wen, Henri Benisty, and Dianlong Yu. Ultrabroad acoustical limiting in nonlinear metamaterials due to adaptive-broadening band-gap effect. *Physical Review B*, 101(10):104304, 2020.

[58] Mohamed Farhat, Sebastien Guenneau, and Stefan Enoch. Ultrabroadband elastic cloaking in thin plates. *Physical Review Letters*, 103(2):024301, 2009.

[59] Liang Feng, Xiao-Ping Liu, Yan-Bin Chen, Zhi-Peng Huang, Yi-Wei Mao, Yan-Feng Chen, Jian Zi, and Yong-Yuan Zhu. Negative refraction of acoustic waves in two-dimensional sonic crystals. *Physical Review B*, 72(3):033108, 2005.

[60] Hermann Frahm. Device for damping vibrations of bodies., April 18 1911. US Patent 989,958.

[61] Michael J Frazier and Dennis M Kochmann. Band gap transmission in periodic bistable mechanical systems. *Journal of Sound and Vibration*, 388:315–326, 2017.

[62] Matthew D Fronk and Michael J Leamy. Higher-order multiple scales analysis of weakly nonlinear lattices with implications for directional stability. In *International Design Engineering Technical Conferences and Computers and Information in Engineering Conference*, volume 51852, page V008T10A001. American Society of Mechanical Engineers, 2018.

[63] R Ganesh and Stefano Gonella. Spectro-spatial wave features as detectors and classifiers of nonlinearity in periodic chains. *Wave Motion*, 50(4):821–835, 2013.

[64] C Goffaux and JP Vigneron. Theoretical study of a tunable phononic band gap system. *Physical Review B*, 64(7):075118, 2001.

[65] Sébastien Guenneau, Alexander Movchan, Gunnar Pétursson, and S Anantha Ramakrishna. Acoustic metamaterials for sound focusing and confinement. *New Journal of physics*, 9(11):399, 2007.

[66] Bikash C Gupta and Zhen Ye. Theoretical analysis of the focusing of acoustic waves by two-dimensional sonic crystals. *Physical Review E*, 67(3):036603, 2003.

[67] Giuseppe Habib and Francesco Romeo. The tuned bistable nonlinear energy sink. *Nonlinear Dynamics*, 89(1):179–196, 2017.

[68] RL Harne, Z Wu, and KW Wang. Designing and harnessing the metastable states of a modular metastructure for programmable mechanical properties adaptation. *Journal of Mechanical Design*, 138(2), 2016.

[69] Ryan L Harne and Kon-Well Wang. *Harnessing Bistable Structural Dynamics: For Vibration Control, Energy Harvesting and Sensing*. John Wiley & Sons, 2017.

[70] PA Hassanpour, WL Cleghorn, JK Mills, and E Esmailzadeh. Exact solution of the oscillatory behavior under axial force of a beam with a concentrated mass within its interval. *Journal of Vibration and Control*, 13(12):1723–1739, 2007.

[71] Kin Ming Ho, Chun Kwong Cheng, Z Yang, XX Zhang, and Ping Sheng. Broadband locally resonant sonic shields. *Applied physics letters*, 83(26):5566–5568, 2003.

[72] Zhao Hong-Gang, Liu Yao-Zong, Wen Ji-Hong, Yu Dian-Long, Wang Gang, and Wen Xi-Sen. Sound absorption of locally resonant sonic materials. *Chinese Physics Letters*, 23(8):2132, 2006.

[73] Zhilin Hou, Fugen Wu, and Youyan Liu. Phononic crystals containing piezoelectric material. *Solid State Communications*, 130(11):745–749, 2004.

[74] Guobiao Hu, Lihua Tang, Arnab Banerjee, and Raj Das. Metastructure with piezo-electric element for simultaneous vibration suppression and energy harvesting. *Journal of Vibration and Acoustics*, 139(1):011012, 2017.

[75] Guobiao Hu, Lihua Tang, and Raj Das. Metamaterial-inspired piezoelectric system with dual functionalities: energy harvesting and vibration suppression. In *Active and Passive Smart Structures and Integrated Systems 2017*, volume 10164, page 101641X. International Society for Optics and Photonics, 2017.

[76] Guobiao Hu, Lihua Tang, and Raj Das. Internally coupled metamaterial beam for simultaneous vibration suppression and low frequency energy harvesting. *Journal of Applied Physics*, 123(5):055107, 2018.

[77] Xinhua Hu, Yifeng Shen, Xiaohan Liu, Rongtang Fu, and Jian Zi. Superlensing effect in liquid surface waves. *Physical Review E*, 69(3):030201, 2004.

[78] GL Huang and CT Sun. Band gaps in a multiresonator acoustic metamaterial. *Journal of Vibration and Acoustics*, 132(3):031003, 2010.

[79] Zi-Gui Huang and Tsung-Tsong Wu. Temperature effect on the bandgaps of surface and bulk acoustic waves in two-dimensional phononic crystals. *IEEE Transactions on Ultrasonics, Ferroelectrics, and Frequency Control*, 52(3):365–370, 2005.

[80] Mahmoud I Hussein and Michael J Frazier. Band structure of phononic crystals with general damping. *Journal of Applied Physics*, 108(9):093506, 2010.

[81] Mahmoud I Hussein, Gregory M Hulbert, and Richard A Scott. Hierarchical design

of phononic materials and structures. In *ASME International Mechanical Engineering Congress and Exposition*, volume 42258, pages 163–172, 2005.

[82] Mahmoud I Hussein, Gregory M Hulbert, and Richard A Scott. Dispersive elastodynamics of 1d banded materials and structures: analysis. *Journal of sound and vibration*, 289(4-5):779–806, 2006.

[83] Mahmoud I Hussein, Gregory M Hulbert, and Richard A Scott. Dispersive elastodynamics of 1d banded materials and structures: design. *Journal of Sound and Vibration*, 307(3-5):865–893, 2007.

[84] Mahmoud I Hussein, Michael J Leamy, and Massimo Ruzzene. Dynamics of phononic materials and structures: Historical origins, recent progress, and future outlook. *Applied Mechanics Reviews*, 66(4):040802, 2014.

[85] MI Hussein and R Khajehtourian. Nonlinear bloch waves and balance between hardening and softening dispersion. *Proceedings of the Royal Society A: Mathematical, Physical and Engineering Sciences*, 474(2217):20180173, 2018.

[86] KL Jim, CW Leung, ST Lau, SH Choy, and HLW Chan. Thermal tuning of phononic bandstructure in ferroelectric ceramic/epoxy phononic crystal. *Applied Physics Letters*, 94(19):193501, 2009.

[87] M Kafesaki, MM Sigalas, and N Garcia. Frequency modulation in the transmittivity of wave guides in elastic-wave band-gap materials. *Physical Review Letters*, 85(19): 4044, 2000.

[88] Manzhu Ke, Zhengyou Liu, Chunyin Qiu, Wengang Wang, Jing Shi, Weijia Wen, and Ping Sheng. Negative-refraction imaging with two-dimensional phononic crystals. *Physical Review B*, 72(6):064306, 2005.

[89] Gaetan Kerschen, Young Sup Lee, Alexander F Vakakis, D Michael McFarland, and Lawrence A Bergman. Irreversible passive energy transfer in coupled oscillators with essential nonlinearity. *SIAM Journal on Applied Mathematics*, 66(2):648–679, 2005.

[90] Romik Khajehtourian and Mahmoud I Hussein. Dispersion characteristics of a nonlinear elastic metamaterial. *Aip Advances*, 4(12):124308, 2014.

[91] Firoozeh Khalily, MF Golnaraghi, and GR Heppler. On the dynamic behaviour of a flexible beam carrying a moving mass. *Nonlinear Dynamics*, 5(4):493–513, 1994.

[92] A Khelif, B Djafari-Rouhani, JO Vasseur, and Pierre A Deymier. Transmission and dispersion relations of perfect and defect-containing waveguide structures in phononic band gap materials. *Physical Review B*, 68(2):024302, 2003.

[93] Abdelkrim Khelif, Abdelkrim Choujaa, Sarah Benchabane, Bahram Djafari-Rouhani, and Vincent Laude. Guiding and bending of acoustic waves in highly confined phononic crystal waveguides. *Applied physics letters*, 84(22):4400–4402, 2004.

[94] Hongjip Kim, Arthur Smith, Oumar Barry, and Lei Zuo. Self-resonant energy hearvester with a passively tuned sliding mass. In *Proceedings of the ASME 2019 Dynamic Systems and Control Conference*. ASME, 2019.

[95] Yuri S Kivshar and Nikos Flytzanis. Gap solitons in diatomic lattices. *Physical Review A*, 46(12):7972, 1992.

[96] Malte Krack, Noha Aboulfotoh, Jens Twiefel, Jörg Wallaschek, Lawrence A Bergman, and Alexander F Vakakis. Toward understanding the self-adaptive dynamics of a harmonically forced beam with a sliding mass. *Archive of Applied Mechanics*, 87(4): 699–720, 2017.

[97] Manvir S Kushwaha. Classical band structure of periodic elastic composites. *International Journal of Modern Physics B*, 10(09):977–1094, 1996.

[98] Manvir S Kushwaha, Peter Halevi, Leonard Dobrzynski, and Bahram Djafari-Rouhani. Acoustic band structure of periodic elastic composites. *Physical Review Letters*, 71(13): 2022, 1993.

[99] Manvir S Kushwaha, P Halevi, G Martinez, Leonard Dobrzynski, and Bahram Djafari-Rouhani. Theory of acoustic band structure of periodic elastic composites. *Physical Review B*, 49(4):2313, 1994.

[100] Vincent Laude, Mikaël Wilm, Sarah Benchabane, and Abdelkrim Khelif. Full band gap for surface acoustic waves in a piezoelectric phononic crystal. *Physical Review E*, 71(3):036607, 2005.

[101] Boyan Stefanov Lazarov and Jakob Søndergaard Jensen. Low-frequency band gaps in chains with attached non-linear oscillators. *International Journal of Non-Linear Mechanics*, 42(10):1186–1193, 2007.

[102] Jensen Li, Lee Fok, Xiaobo Yin, Guy Bartal, and Xiang Zhang. Experimental demonstration of an acoustic magnifying hyperlens. *Nature materials*, 8(12):931–934, 2009.

[103] Jing Li, Zhengyou Liu, and Chunyin Qiu. Negative refraction imaging of acoustic waves by a two-dimensional three-component phononic crystal. *Physical Review B*, 73 (5):054302, 2006.

[104] Xue-Feng Li, Xu Ni, Liang Feng, Ming-Hui Lu, Cheng He, and Yan-Feng Chen. Tunable unidirectional sound propagation through a sonic-crystal-based acoustic diode. *Physical Review Letters*, 106(8):084301, 2011.

[105] Ying Li, Evan Baker, Timothy Reissman, Cheng Sun, and Wing Kam Liu. Design of mechanical metamaterials for simultaneous vibration isolation and energy harvesting. *Applied Physics Letters*, 111(25):251903, 2017.

[106] B Liang, XS Guo, J Tu, D Zhang, and JC Cheng. An acoustic rectifier. *Nature Materials*, 9(12):989, 2010.

[107] Bin Liang, Bo Yuan, and Jian-chun Cheng. Acoustic diode: Rectification of acoustic energy flux in one-dimensional systems. *Physical Review Letters*, 103(10):104301, 2009.

[108] Sz-Chin Steven Lin, Tony Jun Huang, Jia-Hong Sun, and Tsung-Tsong Wu. Gradient-index phononic crystals. *Physical Review B*, 79(9):094302, 2009.

[109] Liao Liu and Mahmoud I Hussein. Wave motion in periodic flexural beams and characterization of the transition between bragg scattering and local resonance. *Journal of Applied Mechanics*, 79(1):011003, 2012.

[110] Zhengyou Liu, Xixiang Zhang, Yiwei Mao, YY Zhu, Zhiyu Yang, Che Ting Chan, and Ping Sheng. Locally resonant sonic materials. *Science*, 289(5485):1734–1736, 2000.

[111] Ming-Hui Lu, Liang Feng, and Yan-Feng Chen. Phononic crystals and acoustic metamaterials. *Materials Today*, 12(12):34–42, 2009.

[112] Zheng Lu, Zixin Wang, Ying Zhou, and Xilin Lu. Nonlinear dissipative devices in structural vibration control: A review. *Journal of Sound and Vibration*, 423:18–49, 2018.

[113] R Lucklum and J Li. Phononic crystals for liquid sensor applications. *Measurement Science and Technology*, 20(12):124014, 2009.

[114] Ralf Lucklum, Manzhu Ke, and Mikhail Zubtsov. Two-dimensional phononic crystal sensor based on a cavity mode. *Sensors and Actuators B: Chemical*, 171:271–277, 2012.

[115] Chu Ma, Robert G Parker, and Benjamin B Yellen. Optimization of an acoustic rectifier for uni-directional wave propagation in periodic mass–spring lattices. *Journal of Sound and Vibration*, 332(20):4876–4894, 2013.

[116] Guancong Ma and Ping Sheng. Acoustic metamaterials: From local resonances to broad horizons. *Science Advances*, 2(2):e1501595, 2016.

[117] James M Manimala and CT Sun. Numerical investigation of amplitude-dependent dynamic response in acoustic metamaterials with nonlinear oscillators. *The Journal of the Acoustical Society of America*, 139(6):3365–3372, 2016.

[118] James Mathew Manimala. *Dynamic behavior of acoustic metamaterials and metaconfigured structures with local oscillators.* PhD thesis, Purdue University, 2014.

[119] Kevin Manktelow, Michael J Leamy, and Massimo Ruzzene. Multiple scales analysis of wave–wave interactions in a cubically nonlinear monoatomic chain. *Nonlinear Dynamics*, 63(1-2):193–203, 2011.

[120] Rosa Martínez-Sala, J Sancho, Juan V Sánchez, Vicente Gómez, Jaime Llinares, and Francisco Meseguer. Sound attenuation by sculpture. *Nature*, 378(6554):241–241, 1995.

[121] Julien Meaud. Multistable two-dimensional spring-mass lattices with tunable band gaps and wave directionality. *Journal of Sound and Vibration*, 434:44–62, 2018.

[122] Jun Mei, Guancong Ma, Min Yang, Zhiyu Yang, Weijia Wen, and Ping Sheng. Dark acoustic metamaterials as super absorbers for low-frequency sound. *Nature communications*, 3(1):1–7, 2012.

[123] Lindsay M Miller, Pit Pillatsch, Einar Halvorsen, Paul K Wright, Eric M Yeatman, and Andrew S Holmes. Experimental passive self-tuning behavior of a beam resonator with sliding proof mass. *Journal of Sound and Vibration*, 332(26):7142–7152, 2013.

[124] Graeme W Milton, Marc Briane, and John R Willis. On cloaking for elasticity and physical equations with a transformation invariant form. *New Journal of Physics*, 8 (10):248, 2006.

[125] Erik Carl Miranda and Jon Juel Thomsen. Vibration induced sliding: theory and experiment for a beam with a spring-loaded mass. *Nonlinear Dynamics*, 16(2):167–186, 1998.

[126] Saeed Mohammadi and Ali Adibi. On chip complex signal processing devices using coupled phononic crystal slab resonators and waveguides. *AIP Advances*, 1(4):041903, 2011.

[127] Saeed Mohammadi, Ali Asghar Eftekhar, Abdelkrim Khelif, William D Hunt, and Ali Adibi. Evidence of large high frequency complete phononic band gaps in silicon phononic crystal plates. *Applied Physics Letters*, 92(22):221905, 2008.

[128] Saeed Mohammadi, Ali Asghar Eftekhar, William D Hunt, and Ali Adibi. High-q micromechanical resonators in a two-dimensional phononic crystal slab. *Applied Physics Letters*, 94(5):051906, 2009.

[129] Keegan J Moore, Jonathan Bunyan, Sameh Tawfick, Oleg V Gendelman, Shuangbao Li, Michael Leamy, and Alexander F Vakakis. Nonreciprocity in the dynamics of coupled oscillators with nonlinearity, asymmetry, and scale hierarchy. *Physical Review E*, 97(1):012219, 2018.

[130] Kotaro Mori, Tadashi Horibe, Shigekazu Ishikawa, Yasuhide Shindo, and Fumio Narita. Characteristics of vibration energy harvesting using giant magnetostrictive cantilevers with resonant tuning. *Smart Materials and Structures*, 24(12):125032, 2015.

[131] Neel Nadkarni, Chiara Daraio, and Dennis M Kochmann. Dynamics of periodic mechanical structures containing bistable elastic elements: From elastic to solitary wave propagation. *Physical Review E*, 90(2):023204, 2014.

[132] Damiano Nardi, Elisa Zagato, Gabriele Ferrini, Claudio Giannetti, and Francesco Banfi. Design of a surface acoustic wave mass sensor in the 100 ghz range. *Applied Physics Letters*, 100(25):253106, 2012.

[133] Raj K Narisetti, Michael J Leamy, and Massimo Ruzzene. A perturbation approach for predicting wave propagation in one-dimensional nonlinear periodic structures. *Journal of Vibration and Acoustics*, 132(3):031001, 2010.

[134] Ali H Nayfeh. *Introduction to Perturbation Techniques*. John Wiley & Sons, 2011.

[135] Ali H Nayfeh and Dean T Mook. *Nonlinear Oscillations*. John Wiley & Sons, 2008.

[136] Andrew N Norris. Acoustic cloaking theory. *Proceedings of the Royal Society A: Mathematical, Physical and Engineering Sciences*, 464(2097):2411–2434, 2008.

[137] Andrew N Norris. Acoustic metafluids. *The Journal of the Acoustical Society of America*, 125(2):839–849, 2009.

[138] Andrew N Norris and William J Parnell. Hyperelastic cloaking theory: transformation elasticity with pre-stressed solids. *Proceedings of the Royal Society A: Mathematical, Physical and Engineering Sciences*, 468(2146):2881–2903, 2012.

[139] Andrew N Norris and Alexander L Shuvalov. Elastic cloaking theory. *Wave Motion*, 48(6):525–538, 2011.

[140] F Nucera, Alexander F Vakakis, DM McFarland, LA Bergman, and Gaëtan Kerschen. Targeted energy transfers in vibro-impact oscillators for seismic mitigation. *Nonlinear Dynamics*, 50(3):651–677, 2007.

[141] John B Pendry and Jensen Li. An acoustic metafluid: realizing a broadband acoustic cloak. *New Journal of Physics*, 10(11):115032, 2008.

[142] Yan Pennec, Bahram Djafari-Rouhani, JO Vasseur, Abdelkrim Khelif, and Pierre A Deymier. Tunable filtering and demultiplexing in phononic crystals with hollow cylinders. *Physical Review E*, 69(4):046608, 2004.

[143] Yan Pennec, Jérôme O Vasseur, Bahram Djafari-Rouhani, Leonard Dobrzyński, and Pierre A Deymier. Two-dimensional phononic crystals: Examples and applications. *Surface Science Reports*, 65(8):229–291, 2010.

[144] Connor Daniel Pierce, Carson L Willey, Vincent Chen, James Hardin, John Daniel Berrigan, Abigail Juhl, and Kathryn H Matlack. Adaptive elastic metastructures from magneto-active elastomers. *Smart Materials and Structures*, 2020.

[145] Pit Pillatsch, LM Miller, Einar Halvorsen, PK Wright, Eric M Yeatman, and Andrew S Holmes. Self-tuning behavior of a clamped-clamped beam with sliding proof mass for broadband energy harvesting. In *Journal of Physics: Conference Series*, volume 476, page 012068. IOP Publishing, 2013.

[146] H Policarpo, MM Neves, and AMR Ribeiro. Dynamical response of a multi-laminated periodic bar: Analytical, numerical and experimental study. *Shock and Vibration*, 17 (4, 5):521–535, 2010.

[147] Bogdan-Ioan Popa, Lucian Zigoneanu, and Steven A Cummer. Experimental acoustic ground cloak in air. *Physical review letters*, 106(25):253901, 2011.

[148] Shashank Priya and Daniel J Inman. *Energy Harvesting Technologies*, volume 21. Springer.

[149] Chunyin Qiu, Xiangdong Zhang, and Zhengyou Liu. Far-field imaging of acoustic waves by a two-dimensional sonic crystal. *Physical Review B*, 71(5):054302, 2005.

[150] Don Richards and Darryll J Pines. Passive reduction of gear mesh vibration using a periodic drive shaft. *Journal of Sound and Vibration*, 264(2):317–342, 2003.

[151] J-F Robillard, O Bou Matar, JO Vasseur, Pierre A Deymier, M Stippinger, A-C Hladky-Hennion, Y Pennec, and B Djafari-Rouhani. Tunable magnetoelastic phononic crystals. *Applied Physics Letters*, 95(12):124104, 2009.

[152] Vicente Romero-García, Juan Vicente Sánchez-Pérez, and LM Garcia-Raffi. Tunable wideband bandstop acoustic filter based on two-dimensional multiphysical phenomena periodic systems. *Journal of applied physics*, 110(1):014904, 2011.

[153] Cory J Rupp, Martin L Dunn, and Kurt Maute. Switchable phononic wave filtering, guiding, harvesting, and actuating in polarization-patterned piezoelectric solids. *Applied Physics Letters*, 96(11):111902, 2010.

[154] M Ruzzene and A Baz. Control of wave propagation in periodic composite rods using shape memory inserts. *Journal of Vibration and Acoustics*, 122(2):151–159, 2000.

[155] Massimo Ruzzene, Fabrizio Scarpa, and Francesco Soranna. Wave beaming effects in two-dimensional cellular structures. *Smart materials and structures*, 12(3):363, 2003.

[156] Juan V Sánchez-Pérez, D Caballero, Rosa Mártinez-Sala, Constanza Rubio, José Sánchez-Dehesa, Francisco Meseguer, Jaime Llinares, and F Gálvez. Sound attenuation by a two-dimensional array of rigid cylinders. *Physical Review Letters*, 80(24): 5325, 1998.

[157] Li Shen, Jiu Hui Wu, Siwen Zhang, Zhangyi Liu, and Jing Li. Low-frequency vibration

energy harvesting using a locally resonant phononic crystal plate with spiral beams. *Modern Physics Letters B*, 29(01):1450259, 2015.

[158] Jinjie Shi, Sz-Chin Steven Lin, and Tony Jun Huang. Wide-band acoustic collimating by phononic crystal composites. *Applied Physics Letters*, 92(11):111901, 2008.

[159] M Sigalas and Eleftherios N Economou. Band structure of elastic waves in two dimensional systems. *Solid State Communications*, 86(3):141–143, 1993.

[160] Michael M Sigalas and Eleftherios N Economou. Elastic and acoustic wave band structure. *Journal of Sound and Vibration*, 158:377–382, 1992.

[161] MM Sigalas. Elastic wave band gaps and defect states in two-dimensional composites. *The Journal of the Acoustical Society of America*, 101(3):1256–1261, 1997.

[162] MM Sigalas. Defect states of acoustic waves in a two-dimensional lattice of solid cylinders. *Journal of Applied Physics*, 84(6):3026–3030, 1998.

[163] Mariantonieta Gutierrez Soto and Hojjat Adeli. Tuned mass dampers. *Archives of Computational Methods in Engineering*, 20(4):419–431, 2013.

[164] Alessandro Spadoni and Chiara Daraio. Generation and control of sound bullets with a nonlinear acoustic lens. *Proceedings of the National Academy of Sciences*, 107(16): 7230–7234, 2010.

[165] LGH Staaf, E Köhler, PD Folkow, and P Enoksson. Smart design piezoelectric energy harvester with self-tuning. In *Journal of Physics: Conference Series*, volume 922, page 012007. IOP Publishing, 2017.

[166] LGH Staaf, AD Smith, E Köhler, P Lundgren, PD Folkow, and P Enoksson. Achieving increased bandwidth for 4 degree of freedom self-tuning energy harvester. *Journal of Sound and Vibration*, 420:165–173, 2018.

[167] LGH Staaf, AD Smith, P Lundgren, PD Folkow, and P Enoksson. Effective piezo-electric energy harvesting with bandwidth enhancement by assymetry augmented self-tuning of conjoined cantilevers. *International Journal of Mechanical Sciences*, 150: 1–11, 2019.

[168] A Sukhovich, B Merheb, Krishna Muralidharan, JO Vasseur, Y Pennec, Pierre A Deymier, and JH Page. Experimental and theoretical evidence for subwavelength imaging in phononic crystals. *Physical review letters*, 102(15):154301, 2009.

[169] Alexey Sukhovich, Li Jing, and John H Page. Negative refraction and focusing of ultrasound in two-dimensional phononic crystals. *Physical Review B*, 77(1):014301, 2008.

[170] N Swinteck, J-F Robillard, S Bringuier, J Bucay, Krishna Muralidharan, JO Vasseur, K Runge, and Pierre A Deymier. Phase-controlling phononic crystal. *Applied Physics Letters*, 98(10):103508, 2011.

[171] Xiudong Tang and Lei Zuo. Simultaneous energy harvesting and vibration control of structures with tuned mass dampers. *Journal of Intelligent Material Systems and Structures*, 23(18):2117–2127, 2012.

[172] Jon Juel Thomsen. Vibration suppression by using self-arranging mass: effects of adding restoring force. *Journal of Sound and Vibration*, 197(4):403–425, 1996.

[173] O Thorp, Massimo Ruzzene, and A Baz. Attenuation and localization of wave prop-agation in rods with periodic shunted piezoelectric patches. *Smart Materials and Structures*, 10(5):979, 2001.

[174] S Tol, FL Degertekin, and A Erturk. Gradient-index phononic crystal lens-based

enhancement of elastic wave energy harvesting. *Applied Physics Letters*, 109(6):063902, 2016.

[175] S Tol, FL Degertekin, and A Erturk. Phononic crystal luneburg lens for omnidirectional elastic wave focusing and energy harvesting. *Applied Physics Letters*, 111(1):013503, 2017.

[176] Daniel Torrent and José Sánchez-Dehesa. Acoustic metamaterials for new two-dimensional sonic devices. *New journal of physics*, 9(9):323, 2007.

[177] MDEF Torres, FR Montero De Espinosa, D Garcia-Pablos, and N Garcia. Sonic band gaps in finite elastic media: surface states and localization phenomena in linear and point defects. *Physical Review Letters*, 82(15):3054, 1999.

[178] JO Vasseur, B Djafari-Rouhani, L Dobrzynski, MS Kushwaha, and P Halevi. Complete acoustic band gaps in periodic fibre reinforced composite materials: the carbon/epoxy composite and some metallic systems. *Journal of Physics: Condensed Matter*, 6(42): 8759, 1994.

[179] Jiahua Wang and Wei-Hsin Liao. Attaining the high-energy orbit of nonlinear energy harvesters by load perturbation. *Energy Conversion and Management*, 192:30–36, 2019.

[180] Yi-Ze Wang, Feng-Ming Li, Wen-Hu Huang, Xiaoai Jiang, Yue-Sheng Wang, and Kikuo Kishimoto. Wave band gaps in two-dimensional piezoelectric/piezomagnetic phononic crystals. *International Journal of Solids and Structures*, 45(14-15):4203–4210, 2008.

[181] Yi-Ze Wang, Feng-Ming Li, Kikuo Kishimoto, Yue-Sheng Wang, and Wen-Hu Huang. Elastic wave band gaps in magnetoelectroelastic phononic crystals. *Wave Motion*, 46 (1):47–56, 2009.

[182] YR Wang and CY Lo. Design of hybrid dynamic balancer and vibration absorber. *Shock and Vibration*, 2014, 2014.

[183] Rab Wilson, Julien Reboud, Yannyk Bourquin, Steven L Neale, Yi Zhang, and Jonathan M Cooper. Phononic crystal structures for acoustically driven microfluidic manipulations. *Lab on a Chip*, 11(2):323–328, 2011.

[184] Ying Wu, Yun Lai, and Zhao-Qing Zhang. Effective medium theory for elastic meta-materials in two dimensions. *Physical Review B*, 76(20):205313, 2007.

[185] Yiwei Xia, Massimo Ruzzene, and Alper Erturk. Dramatic bandwidth enhancement in nonlinear metastructures via bistable attachments. *Applied Physics Letters*, 114(9): 093501, 2019.

[186] Xianchen Xu, Miles V Barnhart, Xin Fang, Jihong Wen, Yangyang Chen, and Guoliang Huang. A nonlinear dissipative elastic metamaterial for broadband wave mitigation. *International Journal of Mechanical Sciences*, 164:105159, 2019.

[187] Eli Yablonovitch. Inhibited spontaneous emission in solid-state physics and electronics. *Physical Review Letters*, 58(20):2059, 1987.

[188] Suxia Yang, John H Page, Zhengyou Liu, Michael L Cowan, Che Ting Chan, and Ping Sheng. Focusing of sound in a 3d phononic crystal. *Physical review letters*, 93(2): 024301, 2004.

[189] Jia-Yi Yeh. Control analysis of the tunable phononic crystal with electrorheological material. *Physica B: Condensed Matter*, 400(1-2):137–144, 2007.

[190] Liuding Yu, Lihua Tang, Liuyang Xiong, Tiejun Yang, and Brian R Mace. A passive self-tuning nonlinear resonator with beam-slider structure. In *Active and Passive Smart*

Structures and Integrated Systems XII, volume 10967, page 109670K. International Society for Optics and Photonics, 2019.

[191] Liuding Yu, Lihua Tang, and Tiejun Yang. Experimental investigation of a passive self-tuning resonator based on a beam-slider structure. *Acta Mechanica Sinica*, pages 1–14, 2019.

[192] Valentina Zega, Priscilla B Silva, Marc GD Geers, and Varvara G Kouznetsova. Experimental proof of emergent subharmonic attenuation zones in a nonlinear locally resonant metamaterial. *Scientific reports*, 10(1):1–11, 2020.

[193] Xiangdong Zhang and Zhengyou Liu. Negative refraction of acoustic waves in two-dimensional phononic crystals. *Applied Physics Letters*, 85(2):341–343, 2004.

[194] Wanlu Zhou, You Wu, and Lei Zuo. Vibration and wave propagation attenuation for metamaterials by periodic piezoelectric arrays with high-order resonant circuit shunts. *Smart Materials and Structures*, 24(6):065021, 2015.

[195] WJ Zhou, XP Li, YS Wang, WQ Chen, and GL Huang. Spectro-spatial analysis of wave packet propagation in nonlinear acoustic metamaterials. *Journal of Sound and Vibration*, 413:250–269, 2018.

[196] Jie Zhu, Johan Christensen, Jesper Jung, Luis Martin-Moreno, X Yin, Lee Fok, Xiang Zhang, and FJ Garcia-Vidal. A holey-structured metamaterial for acoustic deep-subwavelength imaging. *Nature physics*, 7(1):52–55, 2011.

[197] R Zhu, XN Liu, GK Hu, CT Sun, and GL Huang. A chiral elastic metamaterial beam for broadband vibration suppression. *Journal of Sound and Vibration*, 333(10): 2759–2773, 2014.

[198] Lei Zuo and Xiudong Tang. Large-scale vibration energy harvesting. *Journal of Intelligent Material Systems and Structures*, 24(11):1405–1430, 2013.

Appendices

Appendix A

A.1

In order to handle the problem using the method of multiple scales, we assume the system is weakly nonlinear (i.e., assuming $\alpha = \epsilon\alpha$, and $\alpha_r = \epsilon\alpha_r$). Therefore, the first order expansion can be written as

$$u_n(t, \epsilon) = u_{n0}(T_0, T_1) + \epsilon u_{n1}(T_0, T_1) + o(\epsilon^2) \tag{A.1}$$

$$y_n(t, \epsilon) = y_{n0}(T_0, T_1) + \epsilon y_{n1}(T_0, T_1) + o(\epsilon^2) \tag{A.2}$$

$$v_n(t, \epsilon) = v_{n0}(T_0, T_1) + \epsilon v_{n1}(T_0, T_1) + o(\epsilon^2) \tag{A.3}$$

where $T_0 = \tau$ and $T_1 = \epsilon\tau$ are the fast and slow time scales, respectively, while ϵ is a small dimensionless parameter.

In addition, the partial derivative with respect to the defined time scales can be expressed using the chain rule as

$$(\dot{\ }) = D_0 + \epsilon D_1 + ... \tag{A.4}$$

$$(\ddot{\ }) = D_0^2 + 2\epsilon D_0 D_1 + ... \tag{A.5}$$

Substituting Eqns. (A.1)-(A.5) into Eqns. (7.5)-(7.7) and separating the terms of similar

coefficient at orders ϵ^0 and ϵ leads to

order ϵ^0

$$D_0^2 u_{n0} + 2u_{n0} - u_{(n-1)0} - u_{(n+1)0} + \bar{k}\Omega_0^2 D_0^2(y_{n0} + u_{n0}) = 0 \qquad \text{(A.6)}$$

$$\Omega_0^2 D_0^2 y_{n0} + y_{n0} - \alpha_1 v_{n0} = -\Omega_0^2 D_0^2 u_{n0} \qquad \text{(A.7)}$$

$$\alpha_2 D_0 v_{n0} + v_{n0} + \alpha_3 D_0 y_{n0} = 0 \qquad \text{(A.8)}$$

order ϵ^1

$$D_0^2 u_{n1} + 2u_{n1} - u_{(n-1)1} - u_{(n+1)1} +$$
$$\bar{k}\Omega_0^2 D_0^2(y_{n1} + u_{n1}) = -2\bar{k}\Omega_0^2 D_0 D_1(y_{n0} + u_{n0}) - \qquad \text{(A.9)}$$
$$2D_0 D_1 u_{n0} - \alpha(u_{n0} - u_{(n-1)0})^3 - \alpha(u_{n0} - u_{(n+1)0})^3$$

$$\Omega_0^2 D_0^2 y_{n1} + y_{n1} - \alpha_1 v_{n1} = -\Omega_0^2 D_0^2 u_{n1} - 2\Omega_0^2 D_0 D_1 u_{n0} -$$
$$\alpha_r y_{n0}^3 - 2\Omega_0^2 D_0 D_1 y_{n0} \qquad \text{(A.10)}$$

$$\alpha_2 D_0 v_{n1} + v_{n1} + \alpha_3 D_0 y_{n1} = -\alpha_2 D_1 v_{n0} - \alpha_3 D_1 y_{n0} \qquad \text{(A.11)}$$

A.2

In order to determine the nonlinear frequency correction coefficient b', the solvability condition needs to be solved to eliminate secular unbounded terms. After some algebric manipulations, the values of g, h, l, f for the case of nonlinear chain can be expressed as

$$g = -\frac{1}{2}\omega \left(\alpha_2\omega \left(\Omega_0^2 \left(\bar{k}\left(\alpha_1(-\text{Im}[\Gamma]\text{Im}[K_\omega] + (\alpha_1\text{Re}[\Gamma] - 2)\,\text{Re}[K_\omega] - 2) + 2\omega^2\right) - 2\right)\right.\right.$$
$$\left.\left.+ 2\Omega_0^2\bar{k}\text{Im}[K_\omega] - \alpha_1\alpha_3\omega \left(\Omega_0^2\bar{k}\left(\text{Re}[K_\omega] + 2\right) + 2\right)\right)\right)$$

$$h = \frac{1}{2}\omega \left(\Omega_0^2 \left(\bar{k}\left(\text{Re}[K_\omega]\left(\alpha_1\alpha_2\text{Im}[\Gamma]\omega - 2\right) + \omega\text{Im}[K_\omega]\left(\alpha_2\left(\alpha_1\text{Re}[\Gamma] - 2\right) - \alpha_1\alpha_3\right) - 2\right) + 2\omega^2\right) - 2\right)$$

$$f = \frac{3}{2}\alpha ccc \left(\omega^2\Omega_0^2 - 1\right) \tag{A.12}$$

$$l = \frac{1}{2}(-3)\alpha ccc\omega \left(\alpha_2\left(\omega^2\Omega_0^2 - 1\right) - \alpha_1\alpha_3\right) \tag{A.13}$$

while for the case of nonlinear resonator these values can be expressed as

$$g = -\frac{1}{2}\omega \left(\alpha_2\omega \left(\Omega_0^2 \left(\bar{k}\left(\alpha_1(-\text{Im}[\Gamma])\text{Im}[K_\omega] + (\alpha_1\text{Re}[\Gamma] - 2)\,\text{Re}[K_\omega] - 2\right) + 2\omega^2\right) - 2\right) \right. \tag{A.14}$$
$$\left. + 2\Omega_0^2\bar{k}\text{Im}[K_\omega] - \alpha_1\alpha_3\omega \left(\Omega_0^2\bar{k}\left(\text{Re}[K_\omega] + 2\right) + 2\right)\right) \, ,$$

$$h = \frac{1}{2}\omega \left(\Omega_0^2 \left(\bar{k}\left(\text{Re}[K_\omega]\left(\alpha_1\alpha_2\text{Im}[K_\omega]\omega - 2\right) + \omega\text{Im}[K_\omega]\left(\alpha_2\left(\alpha_1\text{Re}[\Gamma] - 2\right) - \alpha_1\alpha_3\right) - 2\right) \right.\right. \tag{A.15}$$
$$\left.\left. + 2\omega^2\right) - 2\right) \, ,$$

$$f = \frac{3}{8}a^3\alpha\omega^2\Omega_0^2\bar{k} \left(\alpha_2\omega\text{Im}[K_\omega]^3 - 3\alpha_2\omega\text{Im}[K_\omega]\text{Re}[K_\omega]^2 + 3\text{Im}[K_\omega]^2\text{Re}[K_\omega] - \text{Re}[K_\omega]^3\right) \, ,$$
$$\tag{A.16}$$

$$l = \frac{1}{8}(-3)a^3\alpha\omega^2\Omega_0^2\bar{k}\left(3\alpha_2\omega\text{Im}[K_\omega]^2\text{Re}[K_\omega] + 3\text{Im}[K_\omega]\text{Re}[K_\omega]^2 - \text{Im}[K_\omega]^3 - \alpha_2\omega\text{Re}[K_\omega]^3\right).$$

$$\text{(A.17)}$$

It is noteworthy that in the presence of both nonlinearities (i.e., chain and resonator nonlinearities), the nonlinear frequency correction coefficient can be written as

$$b' = b'_{ch} + b'_{res} \tag{A.18}$$

where b'_{ch} is the correction coefficient for the case of nonlinear chain case and b'_{res} is the correction coefficient for the nonlinear resonator case.